

BOND- AND MODE-SPECIFIC REACTIVITY OF METHANE ON Ni(100)

THÈSE N° 3335 (2005)

PRÉSENTÉE À LA FACULTÉ SCIENCES DE BASE

Institut des sciences et ingénierie chimiques

SECTION DE CHIMIE ET GÉNIE CHIMIQUE

ÉCOLE POLYTECHNIQUE FÉDÉRALE DE LAUSANNE

POUR L'OBTENTION DU GRADE DE DOCTEUR ÈS SCIENCES

PAR

Plinio MARONI

laurea in fisica, Università di Pisa, Italie
et de nationalité italienne

acceptée sur proposition du jury:

Dr R. Beck, directeur de thèse
Prof. J. Barth, rapporteur
Prof. H. Brune, rapporteur
Prof. Th. Rizzo, rapporteur
Prof. G. Scoles, rapporteur

Lausanne, EPFL
2005

Abstract

In this work, the state-resolved reactivity of methane excited to different C-H stretch vibrations have been measured on a Ni(100) surface. Two kinds of experiments have been performed.

In the first series of experiments, we have measured the reactivity of dideutero methane (CD_2H_2) excited in two different C-H stretch vibrational states which are nearly iso-energetic, but have different vibrational amplitudes. We observed that CD_2H_2 excited with two quanta of vibrational energy in one C-H bond were more reactive (by as much as a factor 5) than molecules excited with one quantum in each of two C-H bonds.

This was the first time that state specificity has been observed in a gas-surface reaction. Our results clearly exclude the possibility of statistical models correctly describing the mechanisms of the methane chemisorption and highlight the importance of the dynamical calculations. We rationalize our results in terms of a spectator model and *bond-specific* reactivity, where the laser excited bond is broken in the reaction with the surface and the difference in reactivity of the two vibrational states is explained in terms of vibrational energy localized in a single C-H bond.

Additionally, we have measured the state-resolved reactivity of CH_4 in its totally symmetric C-H stretch vibration (ν_1) on Ni(100). The methane molecules were excited to ν_1 by stimulated Raman pumping prior the collision with the surface. We observed that the reactivity of the ν_1 excited CH_4 is about an order of magnitude higher than that of methane excited to the isoenergetic antisymmetric stretch (ν_3) reported by Juurlink *et al.* [Phys. Rev. Lett. **83**, 868 (1999)] and is similar to that we have previously observed for the excitation of the first overtone ($2\nu_3$).

Since all four bonds initially carry vibrational amplitude for both ν_1 and ν_3 , the difference in reactivity between the symmetric and antisymmetric vibrations cannot simply be explained in terms of bond-specific laser excitation. We refer to this reactivity difference as *mode-specific*. In this case, the relative reactivity between two different vibrational states does not only depend on the quantity of vibrational energy contained in each bond, but it is also influenced by the symmetry of the vibrational state excited. Our results are consistent with predictions of a vibrationally adiabatic model of the methane reaction dynamics [Halonen *et al.*, J. Chem. Phys. **115**, 5611 (2001)].

Version abrégée

Au cours de mon travail de thèse, j'ai étudié la réactivité résolue en états quantiques du méthane et de l'un de ses isotopes sur la surface de Ni(100). Deux types d'expériences ont été réalisées.

Tout d'abord, nous avons mesuré la réactivité des molécules de méthane dideutérées (CD_2H_2) excitées selon deux états de vibration d'élongation C-H différents et quasi iso-énergétiques, mais correspondant à des déplacements de noyaux différents. Nous avons observé que les molécules de CD_2H_2 excitées avec deux quanta d'énergie de vibration dans une seule liaison C-H étaient plus réactives (jusqu'à un facteur 5) que celles excitées avec un quantum de vibration dans chaque liaison C-H. C'est la première fois que la spécificité de vibration est observée pour une réaction entre un gaz et une surface. Nos résultats excluent clairement la possibilité d'utiliser un modèle statistique pour décrire correctement les mécanismes de cette réaction et soulignent l'importance des calculs dynamiques. Ces résultats ont été expliqués avec le "spectator model" et le concept de la réactivité sélective d'une liaison. Dans ce modèle, la liaison excitée par le laser est rompue pendant la réaction avec la surface et la différence de réactivité entre les deux états de vibration est expliquée en terme d'énergie de vibration localisée sur une liaison C-H.

Puis nous avons mesuré la réactivité résolue en état quantique sur le Ni(100) des molécules de méthane (CH_4) excitées dans le mode de vibration d'élongation symétrique C-H (ν_1). Ces molécules ont été préparées avant la collision avec la surface dans ν_1 par pompage Raman stimulé. Nous avons observé que la réactivité du méthane excité selon ν_1 est approximativement un ordre de grandeur plus élevée que celle du méthane excité selon l'élongation antisymétrique (ν_3) publiée par Juurlink [Phys. Rev. Lett. **83**, 868 (1999)]. De plus la réactivité du méthane préparé dans ν_1 est similaire à celle que nous avons précédemment observé pour l'excitation de la première harmonique ($2\nu_3$).

Etant donné que pour les deux états considérés (ν_1 et ν_3) l'amplitude de vibration est répartie dans les quatre liaisons C-H, la différence de réactivité entre les élongations symétrique et antisymétrique ne peut pas être expliquée en terme d'excitation spécifique d'une liaison. Dans ce cas, nous parlons de réactivité spécifique au mode de vibration. La réactivité relative entre deux états de vibration ne dépend pas seulement de la quantité d'énergie de vibration contenue dans une liaison, mais elle est aussi influencée par la symétrie de l'état de vibration qui a été excité. Nos résultats sont en accord avec les prédictions obtenues par un modèle dynamique de la réaction du méthane sur le nickel qui considère que la molécule arrive sur la surface de

manière adiabatique pour les vibrations [Halonen *et al.*, J. Chem. Phys. **115**, 5611 (2001)].

Contents

1	Introduction	1
1.1	Motivation	1
1.2	Molecule-surface interactions	1
1.3	Gas-surface reaction dynamics	4
1.4	State specific reactivity in the gas-phase	8
1.5	Methane chemisorption on metal surfaces	10
1.6	Outline	17
2	Experimental setup	19
2.1	Our sticking coefficient measurements	19
2.2	Overall view of experimental setup	20
2.3	Pulsed molecular beam source	22
2.3.1	Theory of supersonic expansions	25
2.3.2	Molecular beam characterization	27
2.4	Surface-science chamber	38
2.4.1	Auger spectrometer	39
2.4.2	LEED spectrometer	44
2.4.3	Sample cleaning	45
2.5	Pulsed infrared laser setup	46
2.6	Cavity ring-down setup.	49
2.7	Stimulated Raman pumping laser setup	50

3	State-resolved reactivity of CD₂H₂ on Ni(100)	57
3.1	Introduction	57
3.2	CD ₂ H ₂ laser-off sticking coefficient	58
3.3	The CD ₂ H ₂ molecule	61
3.3.1	Rotational energy levels of an asymmetric-top rotor	62
3.3.2	Vibrational transitions of CD ₂ H ₂	64
3.4	State-resolved sticking coefficients	71
3.4.1	CD ₂ H ₂ rotational temperature	73
3.4.2	Number of molecules excited in the molecular beam	76
3.4.3	Calculation of state-resolved sticking coefficients	80
3.5	Results and discussion	81
4	State-resolved reactivity of CH₄(ν_1) on Ni(100)	87
4.1	Introduction	87
4.2	The CH ₄ molecule	88
4.2.1	Molecular rotations	89
4.2.2	Molecular vibrations	91
4.3	Sticking coefficient of CH ₄ (ν_1) on Ni(100)	93
4.3.1	CH ₄ rotational temperature	97
4.3.2	Number of molecules excited in the molecular beam	102
4.3.3	Calculation of the state-resolved sticking coefficients	112
4.4	Results and discussion	113
5	Discussion and outlook	119
5.1	Discussion	119
5.2	Improving the apparatus	125
5.3	Outlook	128
 APPENDICES		
A	Rotational energy levels of an asymmetric rotor	131
B	Measurement of the IR beam intensity distribution	133
C	The T and T_d group	135

D Stimulated Raman pumping	137
D.1 SRS: classical description	138
D.2 SRS: quantum-mechanical description	142
E Program for saturation curve fitting	147
F Methane vibrational energy levels	151

Introduction

1.1 Motivation

A microscopic description of the dissociation of small alkanes on metal surfaces has been the subject of research within surface science over the past three decades because of its importance for industrial catalysis. The reaction of methane on a nickel catalyst to form surface-bound methyl and hydrogen is the rate-limiting step in steam reforming, which is the principal process for industrial hydrogen production as well as the starting point for the large-scale synthesis of many important chemicals such as ammonia, methanol, and higher hydrocarbons. Because of its importance, the dissociation of methane on nickel has been considered a prototype reaction for chemical bond formation between a polyatomic molecule and a solid surface. In this thesis, we investigate how the reactivity of CH_4 on a nickel surface changes by preparing the methane molecules in different rovibrational states. The results obtained in this work can be helpful for the understanding of the dynamics of the dissociative chemisorption of CH_4 on nickel surfaces.

1.2 Molecule-surface interactions

When atoms or molecules approach a metal surface, they experience forces due to electrostatic and van der Waals interactions between the nuclei and electrons that constitute the approaching molecules or atoms and the surface. The term *adsorption* refers to the binding of molecules or atoms on the surface due to this gas-surface interaction. For large distance from the surface (several Å), the interaction molecule-surface is due to the van der Waals' force and molecules held

on the surface in this way are said to be *physisorbed* (binding energy $\sim 5 - 500$ meV/atom). At smaller molecule-surface distance, the electronic orbitals of the molecule and metal surface start to overlap giving rise to repulsion or attraction and the interaction becomes of more “chemical” nature. The electron distribution changes enough to form a chemical bond between the surface and the molecule and the intramolecular bonds can weaken or eventually be broken. Molecules or atoms bound to a surface in this way are said to be *chemisorbed* (binding energy $\sim 1 - 10$ eV/atom).

The interaction between the surface and a molecule can be represented by the potential energy U , where the bound state corresponds to the local minima of U . The potential energy can be written as a function of the coordinates of the nuclei of the system using the Born-Oppenheimer approximation, which assumes that the motion of the nuclei is much slower than that of the electrons. For molecule-surface interactions, a diatomic molecule over a surface is the simplest case that we can consider. Under this condition, the potential energy can be written as $U(x, y, z, d, \gamma, \phi, \{u_i\})$, where (x, y, z) are the coordinates of the molecular center of mass relative to some point on the surface, d is the intramolecular bond length, γ is the polar angle of the bond with respect to the surface normal \hat{z} , ϕ the azimuth angle, and u_i the displacement of the surface atom i with respect to its unperturbed equilibrium position. U is referred to as a potential energy surface (PES). To stress its multi-dimensionality, U is usually called potential energy hyper-surface.

Even the case of a diatomic molecule interacting with a surface shows a quite complicated PES, which depends on six degrees of freedom. Since the full dimensional PES is very time consuming to calculate, gas-surface interaction are usually discussed in terms of reduced dimensionality models. In 1932, Lennard-Jones proposed a simple model for a molecule-surface interaction where the PES is considered as a 1-dimensional potential $U(z)$ depending only on the molecule-surface distance as shown in Fig. 1.1.¹ The gray curve (2) represents the potential energy of a diatomic molecule AB as a function of the surface-molecule distance z . The minimum at z_p is the bottom of the physisorption well. The gray curve (1) is the potential of the molecule-constituent atoms which are chemisorbed on the surface at z_c . At large z , i.e. in the gas phase, the difference in energy between the two curves is the internal binding energy D of the molecule. Under adiabatic conditions, where the energy levels are not allowed to cross, the curves (1) and (2) are combined and give rise to two new PESs (dashed line) which are referred as adiabatic curves. The lower one represents the electronic ground state and is more relevant for the description of gas-surface dynamics. A molecule impinging on the surface with sufficiently high kinetic energy

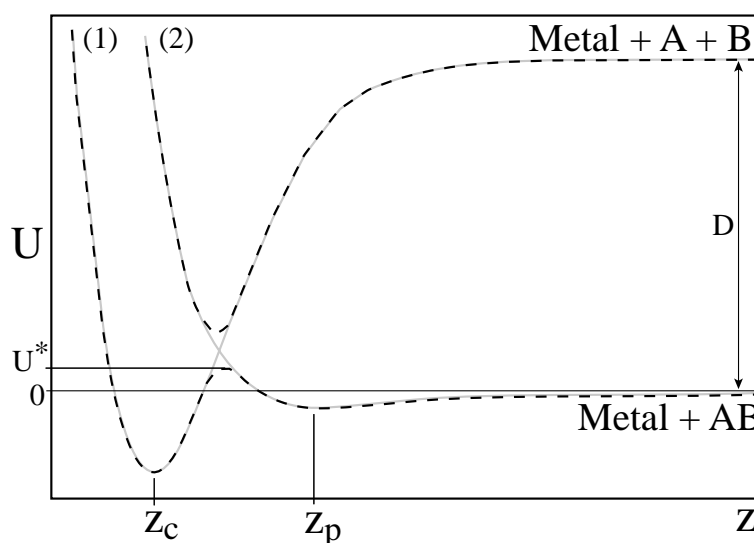


Figure 1.1: Lennard-Jones one-dimensional PES describing the dissociative adsorption of a diatomic molecule on a surface¹. The gray curve (1) and (2) represent the diabatic potential curves describing the interaction of the molecule AB as well as its constituent atoms with a metal surface. The dashed line are the adiabatic curves, the lower one represent the electronic ground state.

can overcome the barrier U^* and reach the bottom of the chemisorption well at z_c where the intermolecular bond is broken and two atom-surface bonds are formed. However, such a PES is not realistic because it does not take into consideration the length changes of the molecular bond as the molecule approaches the surface. Thus, in order to account for the dissociation of the molecule at the surface, the interatomic distance d is the next coordinate included in the PES. The inclusion of d in the PES allows also for considering the effects that molecular vibrations have in the reaction with the surface. Two-dimensional PESs are often visualized by means of contour plots, where equipotential lines are plotted vs. the two coordinates. One example of a two-dimensional PES used for modelling H_2 dissociative adsorption² is shown in Fig. 1.2a. The dashed line in Fig. 1.2a represents the minimum energy path, which defines the reaction coordinate. The PES in Fig. 1.2a exhibits a saddle point. A cut of the PES along the reaction path is shown in Fig. 1.2b. The configuration of the system at the saddle point is called transition state (TS).

Mapping out a PES requires solving the electronic Schrödinger equation for many nuclear configurations. This is very time consuming and one typically calculates a reasonable number of points and then fits the surface to some analytical form. The techniques used to calculate the

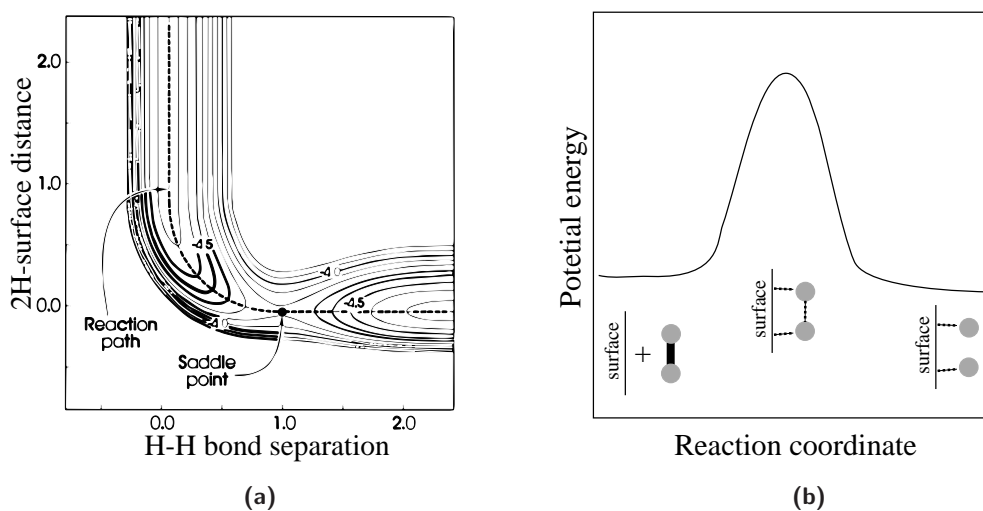


Figure 1.2: Contour plot of a two-dimensional PES (a) used for modelling the H_2 dissociative adsorption (from Halstead *et al.*²) and potential energy along the reaction path (b).

PESs can be classified into ab-initio and semi-empirical methods. Ab initio methods calculate the PES by solving the electronic Schrödinger equation for the multi-electron system. As example, we can mention the Hartree-Fock and the density functional methods. However, these methods are time consuming for a good accuracy and become expensive and difficult to calculate the entire PES. A solution is to limit the calculation to fewer degrees of freedom along the reaction path. Semi-empirical methods make gross approximations to reduce the complexity of the problem, e.g. by considering the interaction between nuclei as Morse oscillators. The PES is then generated by the knowledge of the asymptotic states and interpolation through the reactive region.

1.3 Gas-surface reaction dynamics

Chemical reaction dynamics is concerned with the microscopic kinetics of chemical reactions. The goal of molecule-surface reaction dynamics is the detailed study of molecule-surface reactions, such as the dissociative chemisorption, at the molecular level. One aim of this field is to answer questions that are related to the topic of chemical control: “can the reaction be promoted by changing the internal quantum state of a reacting molecule?”, or “is the orientation of the reactive molecule relative to the surface important in determining the reaction probability?”.

John Polanyi (Nobel prize in 1986) is one of the pioneers in the field of chemical reaction

dynamics. Polanyi *et al.* have used classical trajectory simulations for the gas-phase system $A + BC$ in order to identify the general features of the potential energy surface that affect the energy consumption and disposal in bimolecular reaction^{3,4}. They showed that one of the key features of the PES is the location of the saddle point with respect to the entrance and exit valley. One can distinguish between an “early” or “attractive” potential, for which the transition state is located within the entrance channel (mainly along the coordinate representing the separation between reactants A and BC), and a “late” or “repulsive” potential, where the saddle point is located in the “exit valley”, along the coordinate representing the separation of the product AB and C. By performing a large number of classical trajectory calculations and by averaging the outcome over the distributions of initial conditions (vibrational excitation, vibrational phase, incidence angle ...) they were able to predict the experimentally observed energy consumption and disposal in bimolecular reactions. They found that an early barrier is more easily surmounted by initial translational energy and favors the creation of vibrationally excited products. On the other hand, a late barrier can be overcome more easily by initial vibrational energy and causes energy release to be mainly into translation. This can be visualized using the model PESs shown in in Fig. 1.3. Surface I and II represents an early and late barrier respectively. The barrier height is 29 kJ/mol in both cases. For the early barrier (surface I), 37 kJ/mol of kinetic energy alone are sufficient to drive the reactants over the barrier to form vibrationally excited AB (Fig. 1.3(a)). Conversely, reactants having 60 kJ/mol of vibrational energy and 6 kJ/mol of translational energy are unable to cross the early barrier (Fig. 1.3(b)). For the late barrier (surface II), vibrational excitation drives the chemical reaction (Fig. 1.3(c)), whereas translational energy does not (Fig. 1.3(d)). For vibrationally excited reactants, one observes that the phase of the vibration must be taken into account as the reactant approaches the barrier. Quantitative information are obtained by averaging a large number of trajectories with different impact parameters. The actual outcome of reactive encounters on a PES depends strongly on the details of the gradients along the various coordinates, and merely looking at the shape of the PES is not sufficient to make quantitative predictions of the reactivity. A more accurate description can be obtained from quantum-mechanical wavepacket propagation on the PES, which may also account for the tunneling of light atoms.

For the dissociative adsorption of a molecule on a surface, the problem becomes more complicated because of the many degrees of freedom involved. Progress made by electronic structure theories in computing the interaction of a molecule with a metal surface can be monitored by comparisons of experimental and theoretical dynamics studies. As stated in the previous sec-

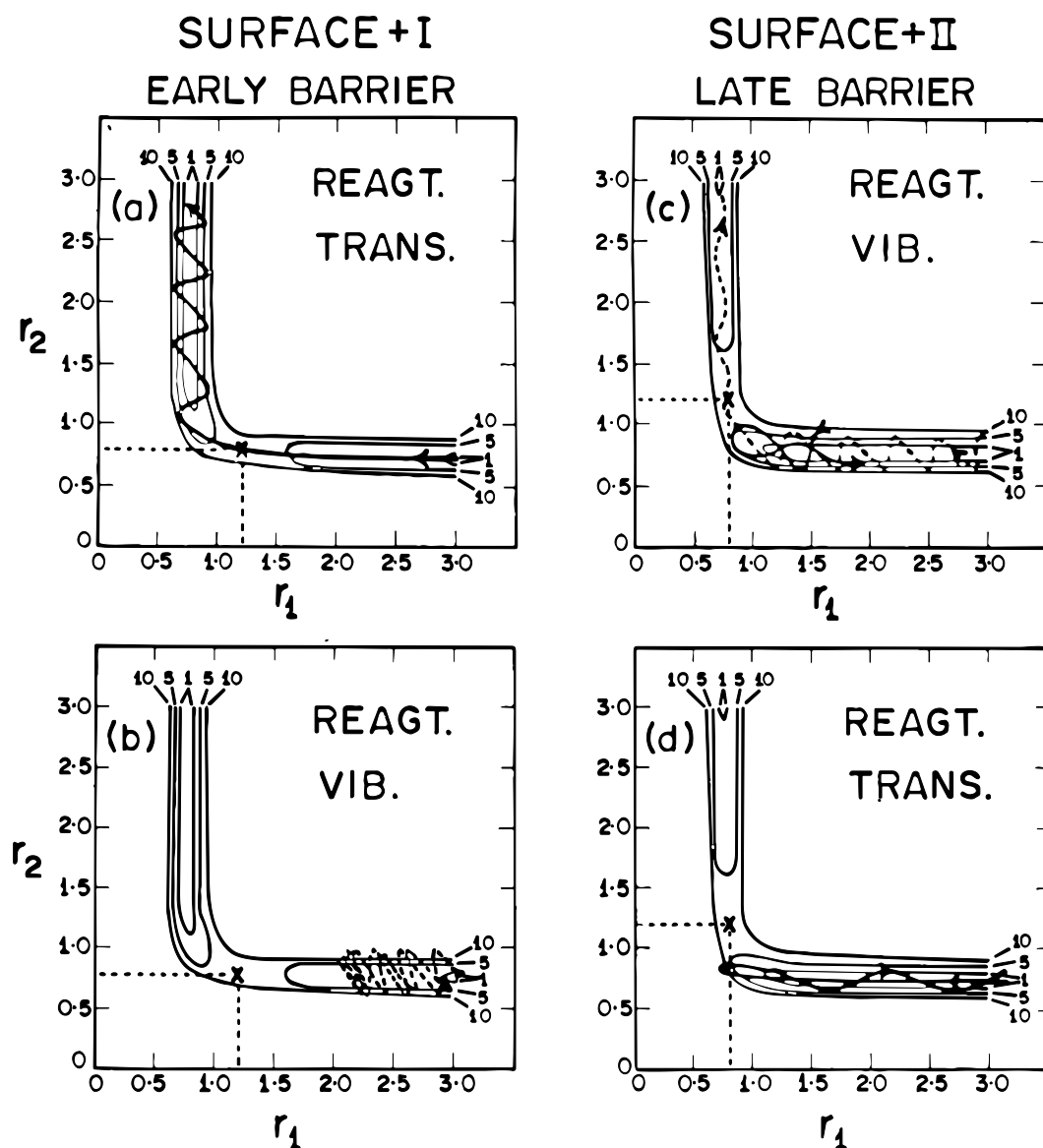


Figure 1.3: Classical trajectories on different types of PES for reactions of the type $A + BC \rightarrow AB + C$. Coordinates r_1 and r_2 represent the internuclear separation A-B and B-C respectively. From the work of Polanyi⁴.

tion, the simplest case that we can consider is that of a diatomic molecule interacting with a surface. To gain deeper insight into the reaction mechanisms, benchmark systems are needed for which experimental and theoretical studies can be performed. Because of the availability of a wide range of experimental data and its relative “simplicity” for a molecule-surface process, the

dissociative chemisorption of H_2 on metal surfaces has represented a good benchmark system. For the chemisorption of H_2 on $\text{Pd}(100)$ ⁵, on $\text{Cu}(100)$ ^{6,7}, or $\text{Cu}(111)$ ⁸, calculations including all six molecular degrees of freedom have started to appear only recently. For the non-activated dissociation of H_2 on Pd, the calculations^{5,9} are in quantitative agreement with experimental results¹⁰, where the reaction probability first decreases and then increases again with increasing collision energy. The high surface reactivity at low energy is explained by a “steering” effect: for molecules that approach with low kinetic energy, the forces exerted by the surface steer the molecule to sites and orientations that are favorable to reaction. At higher kinetic energy, there is not enough time for the forces exerted by the surface to redirect or reorient the molecule by the time it hits the surface. For the same reason, the calculations predict that rotationally excited H_2 molecules are less easily steered into favorable orientations than nonrotating molecules. This was experimentally confirmed in experiments of H_2 on $\text{Pd}(111)$ ¹¹. For the activated dissociation of H_2 on $\text{Cu}(100)$, six-dimensional quantum dynamics calculations⁷ predicted a much enhanced reactivity of vibrationally excited ($v = 1$) H_2 , which is in agreement with experimental results¹². A comparison with state-to-state probabilities for scattering experiments of vibrationally excited H_2 ($v = 1, j = 1$) on $\text{Cu}(100)$ ¹³ shows good agreement for the probability that H_2 remains in the same rovibrational state. However, a discrepancy is observed on how the energy loss is divided up among the available channels. A possible source of errors in the theory is an accurate description of the anisotropy of the molecule-surface interaction in the region in which the molecule is approaching the barrier.

Overall, these studies have shown that for a wide range of initial conditions, dynamical effects govern the chemisorption. Consequently, dynamical models are needed to correctly understand dissociative chemisorption processes, and calculation of the transition state alone is not sufficient to predict real-world reactivities at surfaces. The success of the theoretical approach described here for dissociative chemisorption of hydrogen calls for extensions of the approach to more challenging systems, such as polyatomic molecules. An important question that can be addressed for polyatomic molecules is: which vibrational modes of the molecule are effective in promoting the reaction? In this context, the dissociative chemisorption of CH_4 on metal surfaces has become a new benchmark for quantum reaction dynamics studies. However, this system is more complex than the chemisorption of diatomic molecules. Methane has 9 vibrational degrees of freedom and H_2 only one! Until computational power allows for full dimensionality calculations, one way to treat such complexity is to develop reduced dimensionality models. If the reaction path proceeds principally along a restricted set of coordinates, then a reduced-dimensionality

model that considers only those coordinates may capture the essential dynamical features.

Since the dissociative chemisorption of CH_4 on a nickel surface involves the breaking of a C-H bond¹⁴⁻¹⁶, the first reduced-dimensionality quantal calculations treated CH_4 as a pseudo-diatomic RH ($\text{R}=\text{CH}_3$) and modelled one C-H stretch vibration¹⁷⁻¹⁹. The results obtained from these calculations are in qualitative agreement with molecular beam experiments²⁰. However, the calculated reactivity of vibrationally excited CH_4 disagrees with the experimental results obtained from state-resolved molecular beam experiments of CH_4 prepared in the antisymmetric stretch (ν_3)²¹ and its overtone ($2\nu_3$)²² prior to the collision. This lack of agreement indicates the need for a quantum dynamical model treating more than one molecular vibrational motion. Whereas calculations including more than one vibrational degree of freedom start to be feasible²³⁻²⁵, in parallel to theoretical calculations, more experimental data must be collected to test the theoretical results. In this respect, we focus our effort toward the effect of molecular vibrations other than the antisymmetric stretch in the dissociative chemisorption of CH_4 on nickel.

1.4 State specific reactivity in the gas-phase

For chemical reactions that occur completely in the gas phase, state specific reactivity has been already observed. The first experimental evidence of a laser controlled chemical reaction has been found by the group of Fleming Crim^{26,27}. In one of their experiments, they studied the reaction $\text{Cl} + \text{H}_2\text{O} \rightarrow \text{HCl} + \text{OH}$ and observed how the product state distribution changes for excitation of different O-H stretching overtones. They prepared the water molecules in the $|13\rangle^-$, $|04\rangle^-$, $|02\rangle^-|2\rangle$ and $|03\rangle^-$ local mode states. The notation $|n, m\rangle$ means n quanta of excitation in one O-H stretch and m quanta in the other one. Because the vibrational wavefunctions must reflect the symmetry of the molecule, the eigenfunctions of the zeroth-order Hamiltonian for the local mode stretching states are the symmetrized functions $|n, m\rangle^\pm = 1/\sqrt{2} \cdot (|n, m\rangle \pm |m, n\rangle)$. The notation $|nm\rangle^\pm|l\rangle$ means that there are l quanta of excitation in the bending motion. They found that the reaction of water molecules excited to the $|04\rangle^-$ state predominately produces $\text{OH}(v=0)$ while reaction from the $|13\rangle^-$ state forms mostly $\text{OH}(v=1)$. For the vibrational states $|02\rangle^-|2\rangle$ and $|03\rangle^-$, which have similar total energies but correspond to different distributions of vibrational excitation, they measured that the $|03\rangle^-$ state promotes the reaction much more efficiently than the $|02\rangle^-|2\rangle$. Using HOD excited to the third overtone of the O-H stretch, they observed that the reaction with chlorine atoms produces at least an eightfold excess of OD over OH. This result

can be interpreted with a simple spectator model, where Cl reacts with the most excited O-H bond and the rest of the molecule does not participate in the reaction. These results show that molecular vibrations can be used to preferentially break one bond instead of another one. The selected abstraction of the vibrationally excited O-H bond can be rationalized in terms of bond-specific reactivity. In this picture, the most vibrationally excited O-H bond is predominantly broken in the reaction.

Experiments on CD_2H_2 reacting with chlorine atoms to form methyl and HCl have shown that the excitation of the first C-H stretch overtone leads to a preference for hydrogen abstraction, whereas the excitation of the first C-D overtone reverses this preference²⁸. The same kinds of experiments have shown that the reaction of CD_2H_2 prepared in a local mode state containing two quanta of stretch in one C-H bond $\text{CH}_2\text{D}_2(|20\rangle^-)$ or in a local mode containing one quantum in each of the C-H bonds $\text{CH}_2\text{D}_2(|11\rangle)$ lead to different product states. Methyl radicals in the vibrational ground state are predominantly obtained for the reaction of Cl with $\text{CH}_2\text{D}_2(|20\rangle^-)$, whereas the reaction with $\text{CH}_2\text{D}_2(|11\rangle)$ produces methyl radicals with the C-H bond excited. These results are compatible with the spectator model and with the idea of bond-specific reactivity.

Yoon *et al.* studied experimentally and theoretically the relative reactivity of CH_3D molecules with excited symmetric (ν_1) and antisymmetric (ν_4) C-H stretching vibrations in the reaction with photolytic chlorine atoms. Their results show that the symmetric C-H stretching vibration ν_1 promotes the reaction seven times more efficiently than the antisymmetric C-H stretching vibration ν_4 ^{29,30}. Since the ν_1 and ν_4 modes have similar energies and vibrational motions that differ primarily by the phase of the C-H bond stretches, the difference in reactivity of the symmetric and antisymmetric C-H stretching vibrations could not be explained in terms of a spectator model and bond-specific reactivity as in the case of water and CD_2H_2 . Thus, they performed ab-initio calculations of the vibrational eigen-states for different Cl- CH_3D distances and found that, in the vibrationally adiabatic limit, the ν_1 vibration of CH_3D becomes localized into the vibrational excitation of the C-H bond pointing toward the Cl atom during the approach of the reactants, promoting the abstraction reaction. Conversely, energy initially in the ν_4 vibration flows into the C-H bonds pointing away from the approaching Cl atom and remains unperturbed during the reaction.

In a similar experiment, Yoon *et al.* determined the relative reactivity of the stretch-bend combination vibrations of CH_4 in the reaction with chlorine³¹. They found that vibrational excitation of the symmetric stretch-bend combination ($\nu_1 + \nu_4$) state promotes the reaction more

efficiently than excitation to the antisymmetric stretch-bend combination ($\nu_3 + \nu_4$) by a factor of two. These results are consistent with calculations that find strong coupling of the ν_1 symmetric stretch mode to the reaction coordinate³²⁻³⁴. We use the term mode-specific reactivity when two vibrational states with similar vibrational amplitudes have different reactivities. In these cases, the vibrational specificity has a more profound sense than that shown in the experiments with water and CD₂H₂. The difference in reactivity between two different vibrational states does not only depend on the quantity of vibrational energy contained in each bond, but is influenced also by the symmetry of the vibrational state excited. In the adiabatic limit, the excitation of the reactant in two vibrational states with different symmetries leads to different vibrational energy localizations in the transition-state complex.

1.5 Methane chemisorption on metal surfaces

The chemisorption of methane on transition metal surfaces has been the subject of many works. This section reviews previous experiments on methane chemisorption on transition metals with their major results.

In 1975, Stewart *et al.* have found that the dissociative chemisorption of CH₄ on rhodium surfaces can be initiated by heating the source of an effusive beam of methane to temperatures around 700 K³⁵. For gas temperatures in the range of 600-710 K, they measured that the reactivity of CD₄ is at least one order of magnitude smaller than for CH₄ under the same conditions. Since the kinetic energy distribution of the molecules from one effusive beam depends only on the temperature of the source and not on the molecular mass, they concluded that vibrational energy was the degree of freedom effective in dissociation at the surface and that the barrier to dissociation of the molecules was located in the exit valley of the potential energy surface. One year later, Winters observed the kinetic isotope effect in bulb experiments and proposed a precursor model including a tunneling mechanism that involves the vibrational excitation³⁶.

In 1979, two experiments were devoted to search for vibrational activation in the chemisorption of methane^{37,38}. Yates *et al.* and Brass *et al.* tried to initiate the chemisorption of static methane on Rh(111) by infrared He-Ne laser excitation of methane vibrations. The sensitivity of both experiments was too low to measure any enhancement in the sticking of CH₄ on Rh. Yates *et al.* gave an upper limit of $5 \cdot 10^{-5}$ for the sticking probability of methane excited in the ν_3 and $2\nu_4$ (first overtone of the antisymmetric bend) states. Brass *et al.* have found that the reaction probability of methane excited in the ν_3 and $2\nu_3$ are less than $1 \cdot 10^{-4}$ and $7 \cdot 10^{-2}$ respectively.

Both experiments suggested that the vibrational energy alone was not sufficient to account for the enhancement on sticking observed in previous experiments.

Starting from 1985, experiments with supersonic molecular beams allowed the study of methane chemisorption under better control of the distribution of energy between translation and vibrational modes^{39,40}. Rettner *et al.* found that the initial chemisorption probability of CH₄ on W(110) increases by $\sim 10^5$ on raising of incident translational energy from 5 to 100 kJ/mol.³⁹ Shortly thereafter, the same authors investigated the vibrational energy dependence of the dissociative chemisorption probability of CH₄ on W(110)⁴⁰. They changed the degree of vibrational excitation of the incident CH₄ molecules, while the incident kinetic energy was held constant, by varying the beam source temperature and seed ratio. Rettner *et al.* found that vibrational excitation enhances the initial chemisorption probability of CH₄ on W(110), but, on average, this enhancement is not significantly larger than for an equivalent amount of energy placed into kinetic energy normal to the surface⁴⁰. While their observations were consistent with all previous experiments, they could not exclude the possibility that individual vibrational modes contribute disproportionately to the observed average sticking probability.

In 1986, Lee *et al.* studied the dynamics of the activated dissociative chemisorption of CH₄ on Ni(111) by molecular beam techniques^{14,15}. For a surface temperature of 150 K, they observed adsorbed methyl as product of the chemisorption reaction by high resolution electron energy loss spectroscopy. As the surface temperature was increased to 475 K, the methyl radical was observed to decompose to a -CH species¹⁴. Their experiments also showed that the reactivity of methane on nickel increased exponentially with the normal component of the incident molecule's translational energy and with vibrational excitation¹⁵. They observed that the vibrational energy is as effective as the translational energy in promoting the chemisorption. They interpreted these results by proposing a deformation ("splats") model: the normal component of the translational energy promotes deformation of the molecule upon impact resulting in the proper configuration for the transition state that leads to the dissociated products. This deformation serves to push the hydrogen atoms out from between the surface and the carbon atom in the same way as vibrational excitation of the symmetric (ν_2) and antisymmetric (ν_4) bending modes, thereby exposing the carbon atom to the Ni surface. Due to the large kinetic isotope effect and the exponential dependence of the dissociation probability on energy, they suggested that the tunneling also plays a role in the final C-H bond breaking step¹⁵.

Beebe *et al.* have measured the probability of the methane decomposition reaction on Ni(111), Ni(100), and Ni(110) as a function of coverage under high incident flux conditions of 1 Torr

methane⁴¹. They compared thermal sticking coefficients with the result of molecular beam experiments of CH₄ on Ni(111)^{14,15} and Ni(100)⁴². Their results were in good agreement with the measurement of Lee *et al.*, but not with the results published by Hamza *et al.* for Ni(100). This discrepancy was attributed to the significant vibrational excitation of the methane molecules in the molecular beam experiments. The effect of the vibrational energy in the reaction probability was not accounted in the work of Hamza *et al.*, whereas Lee *et al.* have taken care to identify the vibrational contribution to the reactivity.

Luntz *et al.* and Oakes *et al.* reported molecular beam measurements of the dissociative chemisorption probability for methane on more reactive Pt surfaces^{43,44}. In both experiments, they found large increases in the chemisorption probability with increases in the normal component of translational energy, the vibrational energy of methane molecules, and surface temperature.

Such a large amount of experimental data has triggered theoretical efforts toward the understanding of the reaction mechanisms by calculating transition state structures. Anderson and Maloney⁴⁵ studied the reaction of methane on metal clusters using the atom superposition and electron delocalization molecular orbital semi-empirical method. They found that a 10-atom cluster model of Ni(111) predicted a transition state with a C-H bond elongated by 0.51 Å. Ab-initio calculation on a 13-atom cluster of Ni(100) also predicted an elongation of the C-H bond in the transition state at the atop site⁴⁶. Yang and Whitten¹⁶ calculated the transition state of methane on Ni(111) with larger metal clusters and proposed a lowest energy path involving a stretched CH₃-H geometry. They concluded that stretching the C-H bond is the only likely mechanism for chemisorption of CH₄ on the surface. Burghgraef *et al.*⁴⁷⁻⁵⁰ calculated the transition state of methane on a 13-atom Ni and Co clusters using density functional theory, and found that methane in an highly deformed configuration in which a single C-H bond is stretched. The results of these calculations contradict the “splats” model proposed by Lee *et al.*¹⁵ and highlight the importance of the vibrational stretching modes.

In 1991, Luntz and Harris developed a theoretical model describing the dissociation of CH₄ on metal surfaces by treating nuclear dynamics on a reduced dimensionality potential energy surface, with methane behaving like a quasidiatomic molecule R-H (R=CH₃)¹⁷. In 1995, Luntz adapted the model for the CH₄ chemisorption on Ni(100). In this model, the interaction between the surface and the molecule is considered as simple semi-empirical 2-dimensional PES $V(z, d)$, where z is the molecule surface distance and d is the R-H bond distance. In order to simulate the surface temperature dependence of the reaction probability, the PES is coupled to the recoil

of the vibrating surface via an harmonic oscillator: $V(z - y, d)$, where y represents the deviation of the oscillating surface from its equilibrium position. These calculations showed that the methane reactivity dependencies on the translational energy, nozzle temperature, and surface temperature could have been rationalized with a direct chemisorption mechanism.

The same year, Holmblad *et al.* reported a detailed molecular beam study of the dissociative sticking of methane on Ni(100)²⁰. As has been observed earlier for CH₄ on other metal surfaces, the sticking coefficient shows a strong dependence on the translational energy normal to the surface (activated direct chemisorption): the reaction probability increases between 2 and 3 orders of magnitude as the translational energy for fixed vibrational temperature is raised from 20 to 120 kJ/mol. They observed also a dramatic effect of vibrational energy on the reactivity, e.g., at a fixed translational energy of 40 kJ/mol, the sticking coefficient increases 2 orders of magnitude as the vibrational temperature is raised from 550 to 1050 K. This vibrational enhancement is more pronounced than that observed on W and Pt. Following the quasidiatomic dynamical model by Luntz, they analyzed their data in terms of an empirical state-resolved model based on “S-shape” curves describing the sticking probability as a function of kinetic energy, where the observed effect of vibrational energy is distributed amongst the $v=0, 1$ and 2 states of the stretching modes of methane. This model was used to compare the results from molecular beam experiments with the deposition rates observed under thermal equilibrium, suggesting that the same direct dissociative mechanism is dominant under equilibrium conditions (bulb experiments)⁵¹. The strong dependence of the sticking coefficient on the vibrational energy was attributed to the barrier dislocation mainly located along the vibrational coordinates of the potential energy surface (“late barrier”).

In contrast with the quasidiatomic model proposed by Luntz, Ukraintsev and Harrison have developed a statistical model for activated dissociative adsorption of methane on metal surfaces using microcanonical, unimolecular rate theory⁵². This model assumes that the initial vibrational energy in methane is randomized as the molecule transiently resides in a local “hot-spot” and interacts with a limited number of surface atoms. Consequently, the rotational, vibrational and translational energy normal to the surface are strictly equivalent in driving the system over the reaction barrier. Since both statistical and dynamical models reproduced the experimental data, the question of whether the surface reaction mechanism is governed by statistical or dynamical behavior could not be resolved.

In 1999, Juurlink *et al.* reported for the first time state-resolved sticking coefficient measurements of methane on Ni(100) as a function of kinetic energy^{21,53}. By combining molecular

beam techniques with laser excitation, they measured the reactivity of methane prepared in the antisymmetric stretch vibration (ν_3) on Ni(100). Their results show that the excitation of one quantum of ν_3 (36 kJ/mol) is about as effective as an equivalent amount of translational energy in promoting the reaction. They estimated that methane excited to ν_3 contributes less than 2% to the reactivity measured by hot-nozzle molecular-beam experiments²⁰. They argued that vibrational modes other than ν_3 must play a significant role in the chemisorption. In 2002, we reported the sticking probability of methane excited to the first overtone of the antisymmetric stretch ($2\nu_3$) on Ni(100)^{22,54}. Our data showed that energy in the $2\nu_3$ is less efficient than the translational energy in promoting the reaction. Our measurements also showed that the reactivity of vibrationally excited methane increases less rapidly than that of ground state molecules as the kinetic energy increases. These results are in contradiction to what has been determined from the molecular beam experiment of Holmblad *et al.*²⁰. Their data analysis was based on the quasi-diatomic model of Luntz and Harris. Their results of state-resolved curves were determined from globally fitting an empirical “S-shape” curves to vibrationally-averaged measurements and the good fit of the data did not prove the validity of the assumptions of the quasi-diatomic model. For this reason, our state-resolved measurements, together with those of Juurlink *et al.*, provide a more accurate benchmark for testing theoretical models of CH₄ chemisorption.

Higgins *et al.* have measured the state-resolved reactivity of methane excited to the $2\nu_3$ state on Pt(111)⁵⁵. They observe that, at low incident energy (5.4 kJ/mol), the reactivity of the vibrationally excited molecules is 30 times larger than molecules in the ground state. This correspond to an efficacy of 40% compared to the translational energy.

These state-resolved results have triggered new theoretical efforts toward the understanding of methane chemisorption. In particular, efforts have been made to consider more than one vibrational degree of freedom of methane. Milot *et al.* performed wave packet simulations including all nine internal vibrations²³ and calculated the inelastic scattering of CH₄ molecules from a flat surface in the translational energy range from 32 to 128 kJ/mol. They found that the scattering from the surface is more inelastic when three hydrogen nuclei point towards the surface and that the energy loss after the scattering shows the following trend for the initial vibrational excitations of the modes: symmetric stretch>antisymmetric stretch>antisymmetric bend>ground state. Even though they did not describe the dissociation itself, the scattering simulations yield indications for the role of vibrational excitation in the dissociation of methane. Their simulations show that initial vibrational excitation favors translational kinetic-energy

transfer toward intramolecular vibrational energy. That is, the energy lost during the inelastic scattering process is transferred to vibrational stretching modes at the turnaround point. Based on this, they concluded that the excitation of the symmetric stretch ν_1 is the most effective for enhancing the dissociation probability.

In 2001, Halonen *et al.* performed four-dimensional variational calculations which model the energy flow between methane stretching vibrational energy states as the molecule adiabatically approaches a flat metallic surface²⁴. The isolated methane molecule is modelled with a local mode Hamiltonian. The interaction with the surface is modelled with a London-Eyring-Polanyi-Sato potential and occurs only via a single C-H bond which is pointing towards the surface. By comparing the relative decrease of the vibrational eigenenergies of methane as it approaches the transition state, they predict a larger increase in reactivity for the symmetric stretch state compared to the antisymmetric stretch. Specifically, the symmetric stretch fundamental adiabatically correlates with the localized excitation in the unique C-H bond pointing towards the surface. Conversely, the antisymmetric stretch correlates with vibrations in the CH₃ radical pointing away from the surface, and therefore, when the methane molecule is close to the surface, the vibrational energy is “quarantined” into the CH₃ group. The authors investigated as well the effect of the incident velocity on the adiabatic dynamical picture. They found that, for approaching speed of 1000 m/s, both adiabatic and non-adiabatic pathways are possible: the vibrational energy may flow between the symmetric and antisymmetric stretch modes as the molecule approaches the surface. Although the predictive capabilities of the vibrationally adiabatic model alone may be limited due to its strongly simplifying assumptions, it is reinforced by calculations that have been made for reactions that occur entirely in the gas phase. In these cases, more realistic dynamical calculations find that the symmetric stretch vibration is generally more efficient than the antisymmetric stretch in promoting reactions^{29, 33, 34, 56–60}, and this has been confirmed, in part, by experiments^{29, 31}.

In a recent work, Mortensen *et al.* reported the measurements of dissociative adsorption and associative desorption for CH₄ on Ru(0001)⁶¹. For dissociative adsorption, they found the typical translational and vibrational activation characteristic of CH₄ on transition metals and their data are in good agreement with what reported by Larsen *et al.*⁶². As remarkable results, the authors found that the thermally averaged vibrational energy efficacy is 1.5 times more efficient than the translational energy ($\eta_\nu \geq 1$). However, 2D adiabatic dynamic (quasi-diatom molecule) requires $\eta_\nu \leq 1$ ⁶³. Mortensen *et al.* deduced that this efficacy larger than one can be due to the coupling with the lattice, e.g. as “dynamic recoil”¹⁷, or to the contribution of

many vibrational modes to the vibrational activation. For the associative desorption measurements, they have shown that neither the quasi-diatomic dynamic model nor the statistical model proposed by Ukraintsev and Harrison⁵² are able to reproduce the time of flight profile of the laser desorbed molecules. These models represent two extremes of possible dissociation behavior, low-dimensionality direct dynamics, and purely statistical dissociation. The experimental results show that the reality is in between these two extremes and point out the necessity to develop a theoretical model incorporating more dimensionality in the dynamics.

Overall, these studies have shown that methane chemisorption on metal surfaces is a direct process where the reaction mechanism involves the breaking of a single C-H bond on the surface. Molecular beam experiments have shown that the reactivity has a strong dependence on translational energy normal to the surface and on the nozzle temperature (thermally averaged vibrational states). However, these experiments could not determine if certain vibrational modes contribute disproportionately to the enhancement of the reactivity. State-resolved experiments have shown that the excitations of CH₄ to the ν_3 and to the $2\nu_3$ states enhance the reactivity of methane molecule on Ni(100). These experiments have found also that energy in ν_3 promotes the reaction with similar efficacy as kinetic energy along the surface normal. By comparing the molecular-beam experiment results and the state-resolved data, it has been shown that CH₄ molecules excited to the ν_3 contribute less than 2% to the activated chemisorption of thermally excited methane²¹. Consequently, other vibrational modes than ν_3 must play a significant role in methane reactivity under thermal condition. Statistical⁵² and dynamical^{17,19,23,24} models have been developed to understand methane chemisorption on metal surfaces. Despite having opposed assumptions, both statistical and dynamical approaches claim to reproduce existing experimental data. Whereas some dynamical calculations suggest that the reactivity of methane on nickel should depend on the precise nature of the vibrational mode^{23,24}, the statistical models exclude the possibility of such effects. Although associative desorption experiments have shown that the desorption of CH₄ from metal surfaces seems to deviate from a purely statistical model⁶¹, the experimental results reported thus far do not exclude either approaches, because there is no reported evidence for mode specificity in the reaction of methane with metal surfaces.

In this thesis, we investigate how the excitation of different vibrational C-H stretching states influences the reactivity of CH₄ on Ni(100). We perform state-resolved reaction probability measurements by selectively exciting different vibrational states of the CH₄ molecules in a molecular beam using pulsed laser radiation.

The experiments presented in this thesis serve to establish if the chemisorption of methane on

nickel has to be treated with statistical or dynamical models. In order to test for vibrational mode-specificity for a gas-surface reaction, we perform state-resolved reactivity measurements of CD_2H_2 on Ni(100) with the molecules prepared in two different C-H stretch vibrational states which are nearly iso-energetic, but have different motion of the nuclei.

Recent calculations suggest mode specific reactivity for methane chemisorption on Ni, where the symmetric stretch is predicted to be more efficient than the antisymmetric in promoting the reaction^{23,24}. To test these predictions, we perform state-resolved reaction probability measurements of methane on Ni(100), where the molecules are prepared in the symmetric C-H stretching state, and our results are compared with the state-resolved sticking coefficients for the antisymmetric stretch, $S_0(\nu_3)$, reported by Juurlink *et al.*^{21,64}, as well as our previous measurements²² of $S_0(2\nu_3)$.

Our results allow for rigorous testing of the calculations to come. The precise control over the initial state of the reactant achieved in these experiments provides useful information about the multidimensional potential energy surface for full-dimensionality calculations of the reaction dynamics.

1.6 Outline

The material in this thesis is presented as follows. In Chapter 2, we describe the experimental setup. In the first part of Chapter 2, we explain the experimental approach that we use to measure the reactivity of methane on nickel and we show an overview of the experimental setup which is divided in several subsystems. In the second part of Chapter 2, we describe in detail each subsystem, with a strong focus on how the experimental conditions are determined and controlled.

In Chapter 3, we report the measurements of the reactivity of CD_2H_2 on Ni(100) as a function of the kinetic energy normal to the surface, with the impinging molecules prepared via IR excitation in two vibrational states that have almost the same energy, but correspond to different motions of nuclei. In the same chapter, we show also how we calculate the state-resolved sticking coefficient.

Chapter 4 describes how we determine the sticking coefficient of CH_4 on Ni(100) with the molecules excited to the symmetric stretch ν_1 ($\text{CH}_4(\nu_1)$). Since this transition is IR inactive, we use stimulated Raman pumping to excite the molecules. A different data analysis is reported in this chapter compared to what has been described in Chapter 3. In the final part of Chapter

4, we compare the reactivity of $\text{CH}_4(\nu_1)$ with those of methane excited to the fundamental antisymmetric stretch⁶⁴ (ν_3) and its first overtone²² ($2\nu_3$).

In Chapter 5, we summarize the most important results of this work and make suggestions for future experiments.

The appendices cover supplementary material that is referred to in Chapters 2-4. In particular, Appendix D explains the origin of the stimulated Raman scattering using both classical and quantum mechanical treatments.

Experimental setup

2.1 Our sticking coefficient measurements

We determine the laser-off sticking coefficient of CH_4 on Ni(100) by performing a timed exposure of the clean crystal surface to a molecular beam containing methane. Once the deposition is finished, surface carbon produced by methane chemisorption is quantified by Auger electron spectroscopy (AES). The initial sticking coefficient S_0 for chemisorption is defined as the probability of CH_4 to dissociate on the surface in the zero coverage limit and is given by:

$$S_0 = \frac{N_{\text{adsorbed}}}{N_{\text{collided}}}, \quad (2.1)$$

where N_{adsorbed} is the number of CH_4 molecules dissociated on the surface, and N_{collided} is the total number of CH_4 molecules that have impinged on the surface. In our experiments, N_{adsorbed} is less than 10% of a monolayer (ML). By modelling the carbon uptake curve on Ni(100) with a second order kinetic process⁶⁵, we calculate that the sticking coefficients determined with carbon coverage in the range of 5 – 10% ML are 90 – 80% of the sticking coefficient in the limit of zero coverage, respectively. Since our sticking coefficient measurements have uncertainties of 30 – 40%, we neglect the effect of the carbon coverage on the reaction probability measured.

The primary products of methane chemisorption on a nickel surface are adsorbed CH_3 and adsorbed hydrogen atoms, as observed by high resolution electron energy loss (HREELS) vibrational spectroscopy on Ni(111) held at 150 K^{14,66}. During our timed exposure to the molecular beam, we maintain the crystal temperature at 473 K. At this temperature the methyl groups dehydrogenate and only carbon atoms are left on the surface with no evidence for accumulation

of CH_2 or CH^{67} . It should be pointed out that the validity of the determination of S_0 using equation 2.1 is guaranteed only if there is a one-to-one correspondence between the number of CH_4 molecules dissociated and the number of carbon atoms on the surface. Since nickel is a good methanation catalyst, one should address the question of whether adsorbed CH_3 can recombine with adsorbed hydrogen to form CH_4 that is subsequently desorbed. If the reverse reaction of dissociation occurs, the one-to-one correspondence between the carbon atoms on the surface and the chemisorbed CH_4 is not guaranteed. However, temperature programmed desorption (TPD) experiments⁶⁸ show that for low CH_3 coverage (< 0.09 ML) no CH_4 is formed. The reason for that resides in the different activation energies for the methanation and dehydrogenation reactions, which are 10 ± 1 kcal/mol and 3 ± 0.4 kcal/mol respectively.

To control the incident kinetic energy of CH_4 molecule in the molecular beam, CH_4/H_2 mixtures are used. For the kinetic energies we investigate, H_2 is known to dissociate with high probability on nickel surfaces ($S_0 \sim 0.5$)^{42,69,70}. The adsorbed hydrogen atoms may block the surface sites where CH_4 chemisorbs and may induce methanation reaction resulting in errors on the determination of initial sticking probability. However, TPD experiments have shown that the adsorbed hydrogen atoms leave the surface by recombinative desorption for temperatures higher than 410 K⁶⁶. In a previous Ph.D thesis, Schmid⁷¹ has calculated the net rate of hydrogen adsorption on Ni(100) assuming that H_2 molecules are periodically supplied from the molecular beam pulses. He found that under our experimental conditions the molecular beam produces a steady state hydrogen coverage of $\sim 0.3\%$ ML on the Ni(100) surface. The calculation shows that the amount of hydrogen on the surface does not perturb the determination of methane S_0 , but it does not address the issue of methanation. In some experiments⁷²⁻⁷⁴, hydrogen at relatively high pressure (~ 1 Torr) is observed to reduce the carbon coverage on a C saturated Ni(100) surface. However, in those studies, a hydrogen dose of 4 orders of magnitude larger than the total surface exposure of our molecular beam experiments is used to reduce the carbide coverage to $1/e$ of its initial value. Additionally, we verified that seeding CH_4 in H_2 does not perturb the measurements by observing that the S_0 obtained with a CH_4/He mixture was equal to that measured using CH_4/H_2 mixture for the same methane kinetic energy⁷¹.

2.2 Overall view of experimental setup

The overall scheme of our experimental setup is shown in Fig.2.1. The apparatus can be divided in 6 parts:

1. pulsed molecular beam source,
2. ultra high vacuum (UHV) surface science chamber,
3. time-of-flight setup for molecular beam speed determination,
4. pulsed infrared laser setup,
5. cavity ring-down setup,
6. stimulated Raman pumping laser setup.

The ultra high vacuum (UHV) surface-science chamber is equipped for surface analysis and product detection, and it is connected to the molecular beam source (center part of the figure). The pulsed molecular beam source is used to accelerate methane molecules to a well-defined kinetic energy, and the molecules are collided with the clean nickel surface. The speed of the molecules in the molecular beam is controlled by changing the CH_4/H_2 seed ratio or via the valve temperature. We determine the kinetic energy of CH_4 molecules using a time-of-flight setup (TOF). For these measurements, the crystal is moved out of the molecular beam path and the beam enters directly into the ion source of a quadrupole mass spectrometer (QMS). We also use the QMS to monitor the molecular beam intensity throughout the molecular beam exposure. After a given exposure time, the molecular beam is stopped and the quantity of surface carbon atoms is probed via AES.

Quantum state-resolved measurements are performed by exciting a specific rovibrational transition of the incident methane with intense laser pulses, and thereby preparing a fraction of the incident beam in an excited state with well defined quantum numbers v and J . We can excite infrared (IR) active transitions using an infrared pulsed-laser setup (left-hand side of Fig.2.1). Part of the radiation produced by the pulsed IR laser setup is reflected into a jet expansion cavity ring-down (CRD) spectroscopy setup that is used to tune the IR laser frequency in resonance with the transition that we want to excite in the molecular beam.

For infrared inactive transitions, a two-photon process called stimulated Raman pumping (SRP) is used to prepare the molecules in the molecular beam in the desired rovibrational state. The SRP laser system setup is installed on the opposite side of the surface-science UHV chamber with respect to the IR pulsed laser setup as shown in Fig.2.1. Detailed descriptions of the two laser systems will be given later in this chapter.

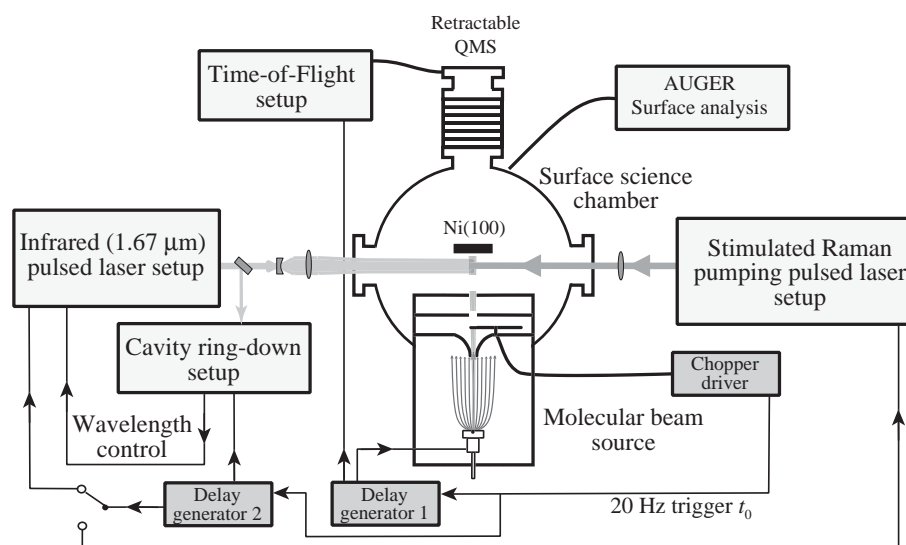


Figure 2.1: Overall scheme of our experimental setup.

2.3 Pulsed molecular beam source

Our pulsed molecular beam source (Thermionics, MSC-9800) consists of three differentially pumping stages as shown in Fig. 2.2. The first chamber (supersonic expansion chamber) contains a temperature-controlled solenoid valve (General Valve, nozzle $\varnothing = 1$ mm) and a replaceable skimmer (Beam Dynamics, hole $\varnothing = 1$ mm). The skimmer extracts the cold core of the supersonic expansion and is designed to minimally disturb the flow of the gas. The distance between the valve and the skimmer opening is ~ 20 mm and is adjusted to maximize the gas throughput into the second differential pumping stage. A 1000 l/s turbo pump (Balzers, TMU1000), backed by a 65 m³/h mechanical pump (Balzers, Duo 65), ensures sufficiently high pumping speed and maintains the residual pressure in the chamber of about $5 \cdot 10^{-4}$ mbar when the valve is operating at 20 Hz.

The second and the third chambers provide for chopping and collimation of the molecular beam and are evacuated each by a 500 l/s turbo pump (Balzers TMU520, Pfeiffer TMU521 P) backed by dry membrane pumps (Pfeiffer MDT4). With the valve running at 20 Hz, typical pressures in the chambers 2nd and 3rd are $4 \cdot 10^{-6}$ and $9 \cdot 10^{-8}$ mbar, respectively. A manually operated valve separates the second and third pumping stage, so that the molecular beam source can be vented for servicing without breaking the vacuum in the UHV chamber. While the presence of the second and third pumping stages minimize the gas load from source chamber into the

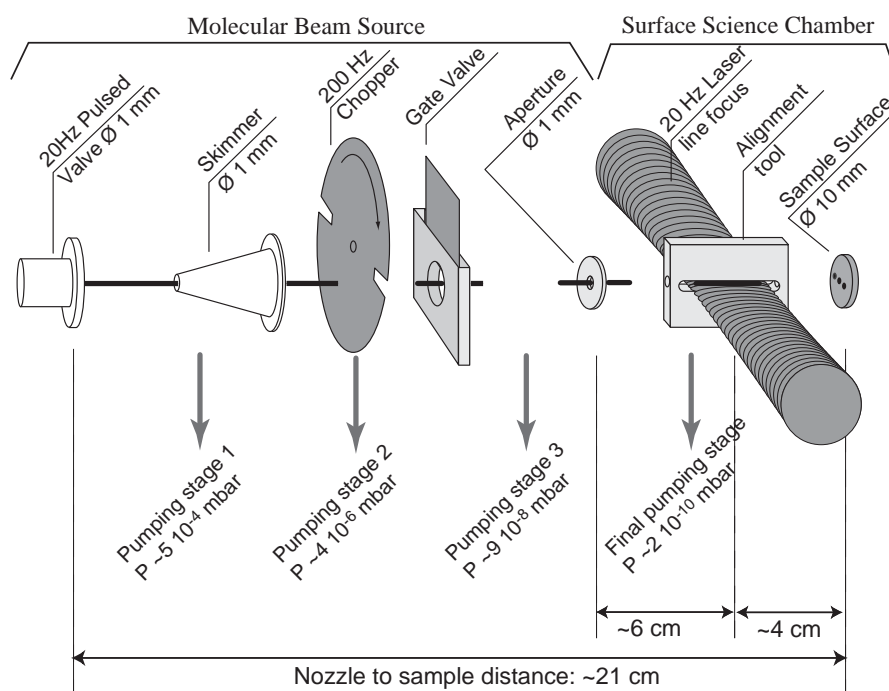


Figure 2.2: Schematic overview of the molecular beam source connected to the UHV surface science chamber. In the first chamber the supersonic jet expansion is skimmed. In the second and third chambers the gas pulses are chopped and collimated. Finally the molecular beam pulses enter in the UHV surface science chamber and, before the collision onto the crystal, the molecules are prepared in the desired rovibrational quantum state by pulsed laser beam irradiation (20 Hz).

UHV chamber, the short distance (~ 21 cm) between the valve and the crystal maximizes the molecular beam intensity on the crystal surface.

In order to maximize the fraction of excited molecules in the beam prepared by the pulsed laser, the spatial length of the molecular beam pulses is reduced by a rotating chopper wheel located in the second chamber. The 127 mm diameter chopper wheel contains 2 pairs of opposing slits of 2 mm and 25 mm width. An optocoupler (not shown in Fig. 2.2) installed opposite to the skimmer hole (see Fig. 2.5) detects the passages of the slits. A homemade chopper driver controls an AC synchronous motor that spins the chopper wheel at 200 ± 0.08 Hz. The optocoupler generates a reference signal consisting of a sequence of short ($\approx 30 \mu\text{s}$) and long ($\approx 330 \mu\text{s}$) pulses with a periodicity of 400 Hz. A timer circuit can be set to filter either the long or the short pulses, and a divider ($\div 20$) reduces the frequency to 20 Hz. In this way, a 20 Hz signal, referenced to the transit of the narrow or wide slits through the optocoupler, is generated

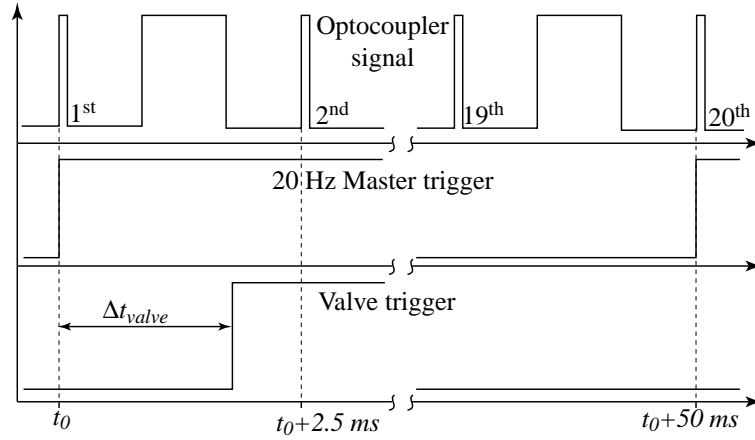


Figure 2.3: Timing diagram of the optocoupler signal, the master trigger, and the valve trigger. A timer circuit filters out the long slit optocoupler signal and a TTL pulse is emitted each 20th transits of the narrow slit generating the 20 Hz master trigger. The valve opening trigger is delayed of Δt_{valve} with respect to the master trigger.

which serves as the master trigger of the experiment. Figure 2.3 shows the optocoupler signal and the 20 Hz master trigger signal as a function of time; in Fig. 2.3 the master trigger is referenced to the transit of the narrow slit.

To transmit the molecular beam pulse through the narrow or wide slits, the opening of the valve must be properly synchronized. If we assume that the chopper driver is set to generate the master trigger pulse at t_0 when the narrow slit transits in front of the optocoupler, the same slit will transit in front of the skimmer hole at $\sim t_0 + 2.5 \text{ ms}$. Due to mechanical delay of the pulsed valve opening and to the flight time of the molecules from the valve orifice to the chopper wheel position, the valve opening must be delayed less than 2.5 ms relative to the master trigger if we want that the molecular beam pulse reaches the chopper wheel when the slit aperture passes in front of the skimmer hole (see Fig. 2.3). The delay time between the master trigger and the valve opening (Δt_{valve}) can be adjusted with a Stanford Research System DG 535 delay generator (delay generator 1 in Fig. 2.1). Δt_{valve} depends on the speed of the molecules and it is adjusted to maximize the throughput in the UHV chamber. For a supersonic expansion of 12% CH_4 in H_2 at 423 K we use a Δt_{valve} of 1.9 ms.

The open time of our solenoid valve can be adjusted. We found that running the valve at short open time ($< 200 \mu\text{s}$) can cause a leak in the valve. This effect occurs because the short drive pulses apply just enough force to nudge the poppet from its sealed position. The leak may persist when the valve driver is switched off, which might be interpreted erroneously as a faulty

poppet. Instead of replacing the poppet, it may actually suffice to run the valve with longer open time. We determined the duration of the gas pulses by measuring the pressure rise in the third chamber as a function of Δt_{valve} . We have found that if we increase the valve open time from 220 μs to 350 μs the pulse width increases from 340 μs to 500 μs .

Transmitting the molecular beam through the wide or the narrow slits reduces the pulse duration to 333 μs or 26.6 μs FWHM respectively.

Since the fraction of molecules excited in the molecular beam depends on the ratio between the volume illuminated by the laser and the total volume of the molecular beam pulse, the production of short molecular beam pulses is critical in the context of our chemisorption experiments. If the gas pulses are too long, the excited fraction of molecules in the molecular beam will be small and the chemisorption of the unexcited molecules can dominate the observed carbon signal on the surface hiding the effect produced by the laser excitation.

2.3.1 Theory of supersonic expansions

For our state-resolved reaction probability measurements, the reactant molecules have to be prepared under well-defined initial conditions. In particular, our initial sticking probability results are measured as a function of the excited vibrational states and incident kinetic energy. Supersonic beam sources provide good control of the velocity of the expanded molecules ($\Delta v/\langle v \rangle \sim 0.1$ for CH_4 expansion, $T_{\parallel} = 15$ K) compared to bulb experiments where static gas samples are used ($\Delta v/\langle v \rangle \sim 1$ for static CH_4 at 300 K). Moreover, with molecular beam sources, we have control of the direction of the velocity (incident angle), and we can produce molecules in a collisionless environment. Where the excited quantum states are long lived limited only by spontaneous emissions.

When a gas escapes from a high-pressure region (P_0) into vacuum through an orifice of diameter larger than the molecular mean free path at P_0 , a supersonic expansion is produced. The expansion converts the random thermal energy of the gas into directed mass flow of a supersonic jet. Typically, the gas expansion is treated as ideal; viscosity and heat conduction are neglected. These are good approximations for high-speed flow when the characteristic flow time is short compared with the diffusion times for non-equilibrium processes. The expansion is then isentropic, which means that along any streamline the total enthalpy per unit of mass h_0 is conserved and we can write:

$$h + v^2/2 = h_0, \quad (2.2)$$

where h and v are the enthalpy per unit mass and the velocity of the molecules at some point in the expansion. For an ideal gas $dH = C_p dT$ and:

$$v^2 = 2(h_0 - h) = 2 \int_T^{T_0} C_p dT, \quad (2.3)$$

where C_p is the heat capacity per unit mass at constant pressure and T_0 is the gas temperature in the reservoir. If C_p is constant over the temperature range of interest, then $v = \sqrt{2C_p(T_0 - T)}$. For an ideal gas $C_p = \gamma/(\gamma - 1)k/m$, where $\gamma = C_p/C_v$, k is the Boltzmann constant and m is the mass of the molecule. If the gas is cooled substantially in the expansion ($T \ll T_0$), we obtain the maximum or terminal velocity rewriting eq. 2.3⁷⁵:

$$v_\infty = \sqrt{\frac{2k}{m} \frac{\gamma}{\gamma - 1} T_0}. \quad (2.4)$$

The expansion is called *supersonic* because the flow velocity v exceeds the local speed of sound $a = \sqrt{\gamma k T / m}$, where T is the local temperature of the molecules. With polyatomic molecules, one must consider the internal degrees of freedom as well as the translational degrees of freedom. In the early expansion close to the nozzle, where the gas is dense enough that the collisions are still frequent, energy is transferred from vibration and rotation into translation. However, because the gas is expanding and the density is decreasing, the molecules experience only a finite number of collisions (typically of the order of $10^2 - 10^3$) and there are not enough collisions for the internal degrees of freedom to approach the equilibrium with translation. Since rotational relaxation is faster than vibrational relaxation, the molecules are in a non-equilibrium distribution where $T_{translations} < T_{rotations} < T_{vibrations}$.

The velocity distribution of the supersonically expanded molecules can be described by a flux weighted and shifted Maxwell-Boltzmann distribution⁷⁵:

$$f(v) \propto v^3 \exp \left[-\frac{m}{2kT_{\parallel}} (v - v_0)^2 \right], \quad (2.5)$$

where T_{\parallel} is the translational temperature and v_0 is the stream velocity of the expansion. The maximum of this distribution is at

$$v_{max} = \frac{1}{2} \left(v_0 + \sqrt{v_0^2 + 6 \frac{2kT_{\parallel}}{m}} \right). \quad (2.6)$$

Under our experimental conditions, $v_0 \sim 1000$ m/s and $T_{\parallel} \sim 10$ K. Using these values, we have that $v_0^2 \gg \frac{2kT_{\parallel}}{m}$ and v_0 approximately represents the most probable velocity.

The accessible range of kinetic energies can be extended considerably by seeding, i.e. by mixing the gas of interest in a lighter or heavier carrier gas. Due to collisions, all species in the expansion tend to move with nearly the same velocity; the heavier molecules are accelerated by the lighter ones and vice versa. In this case, the terminal velocity is determined by replacing m and γ with the average molar mass ($\bar{m} = \sum_i X_i m_i$) and the average molar gamma ($\bar{\gamma} = \sum_i X_i \gamma_i$) in eq. 2.4, where X_i , m_i and γ_i are the fractional molar concentration, the mass and the ratio C_p/C_v of the species i in the gas mixture, respectively.

2.3.2 Molecular beam characterization

Molecular beam velocity

Since the reaction probability of CH_4 on a nickel surface increases nearly-exponentially with respect to the kinetic energy normal to the surface, accurate velocity determinations are important for the experiments presented here. Additionally, the determination of the speed of the molecules is needed for the synchronization of the laser pulses with the transit of the molecular beam through the excitation region.

The time-of-flight (TOF) technique is commonly used for the determination of molecular beam velocities and its basic principle is simple; knowing the interval of time (Δt_{flight}) that a molecule requires to fly across a distance (L), the speed of the molecule (v) can be calculated as $v = L/\Delta t_{flight}$.

Our TOF setup for the determination of molecular beam kinetic energy is schematically represented in Fig. 2.4. Here, the free flight distance L is the distance between the chopper wheel and the center of the ionizer of the QMS. The QMS detects the arriving molecules and a multi-channel scaler (MCS) monitors the number of arriving molecules per unit of time as a function of the elapsed time after the trigger signal (t_0). The velocity distribution $f(v)$ shown in eq. 2.5 is transformed in the TOF distribution $g(t)$ using $v = L/t$:

$$g(t)dt = f\left(\frac{L}{t}\right) dv(t) = -\frac{L}{t^2} f\left(\frac{L}{t}\right) dt, \quad (2.7)$$

due to normalization, the minus sign and L in the multiplying factor can be dropped. This equation gives the distribution in terms of molecular flux ($flux = v \cdot density$). Since the QMS

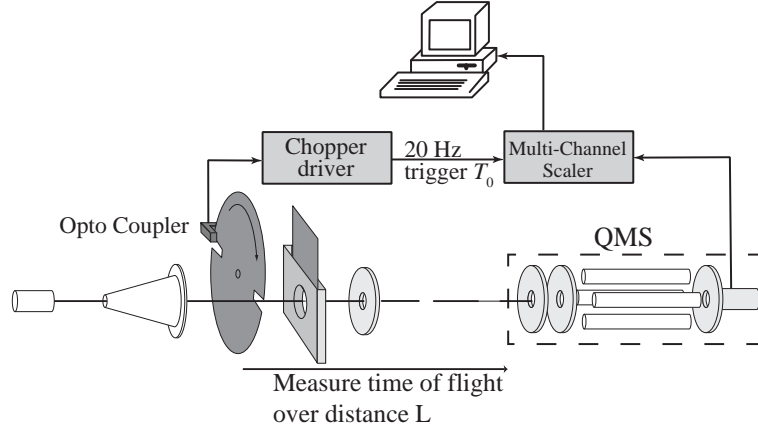


Figure 2.4: TOF setup. The QMS is installed collinear to the molecular beam. The molecules enter in the QMS ionizer with an initial velocity v_0 .

measures the particle density, the right hand of eq. 2.7 must be divided by v :

$$g_{den}(t)dt \propto \frac{1}{t} f\left(\frac{L}{t}\right) dt, \quad (2.8)$$

Replacing $f(v)$ with eq. 2.5 we find the TOF distribution:

$$g(t)_{den}dt \propto \frac{1}{t^4} \exp\left[-b\left(\frac{L}{t} - v_0\right)^2\right] dt, \quad (2.9)$$

with $b = m/2kT_{\parallel}$. For a more detailed analysis of the TOF distribution, the transmission function of the chopper wheel $O(t)$ must be considered. In an ideal experiment $O(t) \sim \delta(t)$, in reality $O(t)$ will be approximately trapezoidal. As a consequence, the experimentally measured TOF distribution will be the convolution of $g_{den}(t)$ and the chopper transmission function $O(t)$:

$$G(t) \propto \int_{-\infty}^{\infty} O(t - \tau) g_{den}(\tau) d\tau. \quad (2.10)$$

We approximate the transmission function $O(t)$ with a trapezoidal shape. Where the rise and fall times are set equal to $8 \mu\text{s}$ and the plateau time is $19 \mu\text{s}$. The experimental setup used to determine these values is shown in Fig. 2.6, and will be described in more detail below.

The average velocity of the molecules v_0 in the molecular beam and the translational temperature T_{\parallel} are determined by fitting eq. 2.10 to the measured TOF distribution.

Calibration of TOF velocity measurements

To determine the beam velocity from the TOF measurement, we need to calibrate the TOF setup. The elapsed time t recorded by the MCS includes the TOF of the neutral molecules t_{TOF} and several delays. The time t can be written as

$$t = \Delta t_{\text{chop.}} + \Delta t_{\text{ions}} + t_{\text{TOF}}, \quad (2.11)$$

where $\Delta t_{\text{chop.}}$ is the chopper delay time. It represents the delay between the master trigger signal t_0 and the time at which the molecular beam pulse is generated, that is when the narrow slit is centered to the molecular beam hole (see Fig. 2.5 right-hand side). Δt_{ions} represents the flight time of the ions from the ionizer to the detector.

The calibration of the TOF setup consists of the determination of $\Delta t_{\text{chop.}}$, Δt_{ions} , and the flight distance L in eq. 2.9

$\Delta t_{\text{chop.}}$: chopper delay time determination. Since the opto coupler is installed approximately at 180° relative to the molecular beam aperture (see Fig. 2.5), the time interval between the trigger signal at t_0 and the time when the chopper wheel is centered on the molecular beam aperture (t_1) corresponds approximately to a half of a rotation of the chopper wheel (~ 2.5 ms). Figure 2.6 schematically depicts how we determined $\Delta t_{\text{chop.}}$. The solenoid pulsed valve is replaced with a glass window and a He-Ne laser beam is aligned through the molecular beam path. The nickel crystal is used to reflect the laser beam on a photodiode outside the UHV chamber and an oscilloscope records the master trigger and the photodiode signals. The slits in the chopper wheel transmit the laser beam and the photodiode measures the intensity of the transmitted He-Ne laser beam and senses the transits of the slits. The time interval between the master trigger signal and the centroid of the chopper wheel transmission function determines $\Delta t_{\text{chop.}}$. The photodiode signal shown in Fig. 2.7 consists of two peaks that represents the passage of the He-Ne laser beam through the narrow slits of the chopper wheel. In order to show more clearly the shape of the transmitted intensities of the narrow slits, the horizontal axes is cut in two intervals. The peak generated by the large slit is in between the two narrow slit peaks, and it is omitted in the graph.

We measure $\Delta t_{\text{chop.}}$ to be 2.5143 ± 0.0005 ms, where the error is determined by monitoring the jitter of the chopper slit signal with the oscilloscope. The full width at half maximum of the narrow slit transmission function is $26.6 \mu\text{s}$. We use the shape of the narrow slit peak to

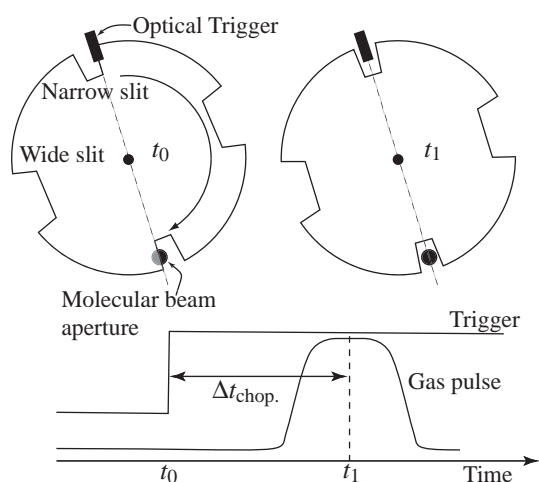


Figure 2.5: Left-hand side: chopper wheel position when the master trigger signal is generated (t_0). Right-hand side: chopper wheel position corresponding to the starting time for the real TOF (t_1).

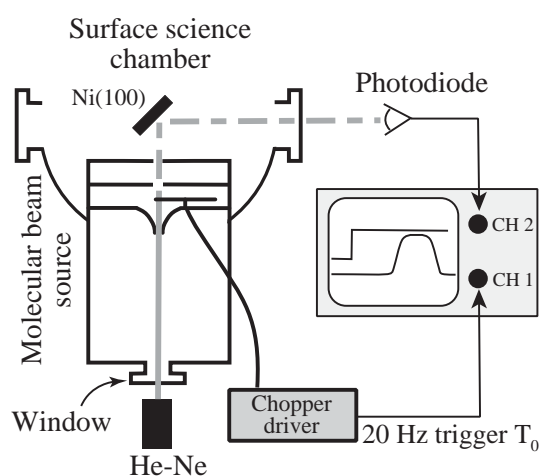


Figure 2.6: Experimental setup used to determine $\Delta t_{chopper}$. The He-Ne laser beam follows the molecular beam path. The oscilloscope detects the trigger and the photodiode signals.

determine the parameters of the trapezoidal chopper transmission function mentioned earlier in this section (see Fig. 2.8).

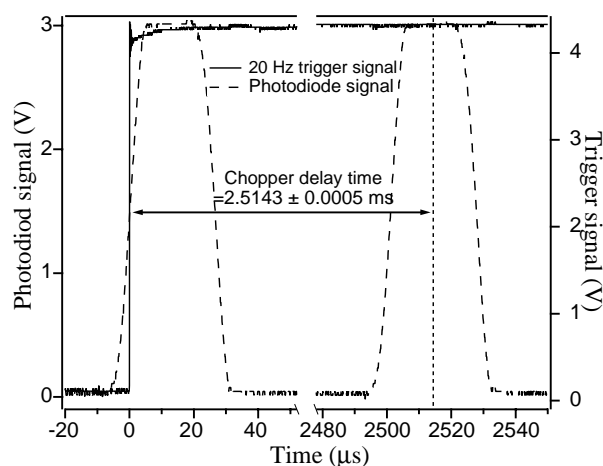


Figure 2.7: Transmitted He-Ne laser beam intensity detected by the photodiode and trigger signal as a function of time. The photodiode senses the transit of the narrow and large slits of the chopper wheel.

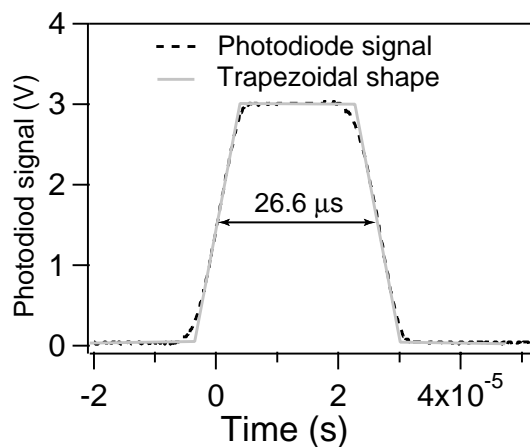


Figure 2.8: Transmission function of the narrow slit (dashed line) as measured with the He-Ne laser. The grey solid line is the trapezoidal function used for the convolution in eq. 2.10.

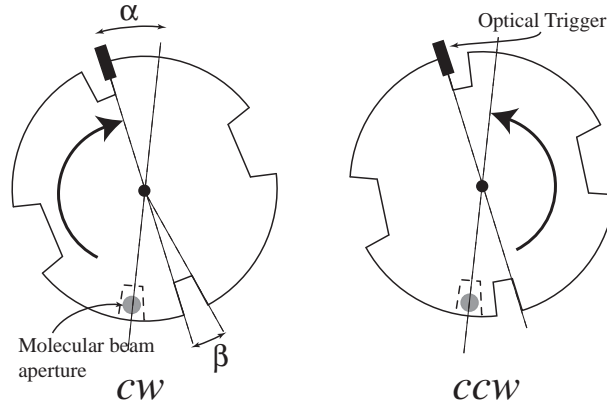


Figure 2.9: Schematic view of the chopper wheel with the optocoupler and the molecular beam angularly misaligned by α . By spinning in the clockwise (left-hand) and counter-clockwise (right-hand) directions, the chopper wheel has to rotate different angles to reach the opening position (narrow slit drawn with dashed line in front of the molecular beam aperture).

Our chopper driver can spin the wheel both clockwise (*cw*) and counter-clockwise (*ccw*). The delay time previously reported is measured with the chopper wheel spinning in the *cw* direction.

Changing the direction of rotation of the chopper wheel will cause a shift in the recorded TOF profiles if the opto coupler is not installed exactly at 180° relative to the molecular beam aperture. We recorded TOF distributions of 100% CH_4 at 120°C for the two directions, and the TOF recorded with the chopper wheel spinning in the *ccw* direction arrives $9.8 \pm 1 \mu\text{s}$ earlier than that with the chopper wheel spinning in *cw* direction. From this difference in time ($\Delta t_{\text{arrival}}$), we calculate the misalignment of the optocoupler. Figure 2.9 shows the schematic view of the chopper wheel with the optocoupler and the molecular beam angularly misaligned of α . If the chopper wheel spins in the *ccw* direction (right-hand of Fig.2.9), it has to rotate of $\pi - \alpha + \beta/2$ to reach the position where the molecular beam hole is centered on the slit (right-hand side). For the other spinning direction, it has to rotate of $\pi + \alpha + \beta/2$ (left-hand side). Where β is the angular aperture of the narrow slit. Since the spinning velocity of the wheel ω_0 is the same for the two directions, the difference in the arrival time of the two TOF will be $\Delta t_{\text{arrival}} = 2\alpha/\omega_0$. The resulting α is 0.006 ± 0.0003 radian, corresponding to a misalignment of 0.4 mm. We can calculate $\Delta t_{\text{chop.}}$ for the *cw* direction from the $\Delta t_{\text{arrival}}$ observing that

$$\Delta t_{\text{chop.}} = \frac{T}{2} + \frac{\Delta t_{\text{arrival}}}{2} + \frac{\beta}{2\omega_0} - \Delta t_{\text{elec.}}, \quad (2.12)$$

where T is the period of rotation, and $\Delta t_{elec.}$ is the electronic delay time between the transit of the slit in the optocoupler and the delivering of the 20 Hz master trigger signal pulse. Using the oscilloscope, we find $\Delta t_{elec.} = 2.5 \pm 0.5 \mu s$. For $\beta/(2\omega_0) = 26.6/2 \mu s$, from eq. 2.12 we find $\Delta t_{chop.} = 2.515 \pm 0.002$ ms, which is in good agreement with what we have determined with the He-Ne laser.

Δt_{ions} : ion TOF. Once the molecules are ionized in the ion source of the QMS, the ions are accelerated by an electric potential (cage voltage). Subsequently, the charged particles travel for ~ 20 cm through the quadrupole mass filter and arrive at the detector (channeltron). The flight time of the ions is called ion TOF (Δt_{ions}) and can be expressed by:

$$\Delta t_{ions} = \frac{d}{\sqrt{v_0^2 + \frac{2qU}{m}}}, \quad (2.13)$$

where d is the flight distance of the ions, v_0 is the initial velocity of the neutral particles when entering the ionizer, q and m are the charge and the mass of the ions respectively, and U is the cage voltage. The distance d is determined by recording the TOF arrival time for different values of U and by fitting the obtained experimental points with the following equation:

$$h_{fit}(U) = A + \frac{d}{\sqrt{v_0^2 + \frac{2qU}{m}}}, \quad (2.14)$$

where the fitting parameters are A and d . The term A represents the shift in time due to the neutral TOF. The initial velocity v_0 used in the fitting equation is determined either theoretically (eq. 2.4) or experimentally. We experimentally determine v_0 by translating the QMS, that is we record TOF profiles for different QMS-chopper distances and we plot the arrival time as a function of the position of the QMS. We perform a linear fit to the data points and we extract v_0 from the slope resulted from the linear regression. In Table 2.2 the measured v_0 of Ar, He and CH₄ expansions at 393 K (v_0 exp.) are shown together with the theoretical values obtained using eq. 2.4. We can note that the values of v_0 exp. are larger than the calculated terminal velocities. This is probably due to some systematic errors in our experimental technique. However, we will show below that these errors have a small influence ($\sim 1\%$) in the determination of d .

The graph in Fig. 2.10 shows the result of the fitting of the experimental points acquired by expanding 100% Ar with a nozzle temperature (T_{nozzle}) of 393 K. The measurement is repeated for 100% CH₄ and 100% He for $T_{nozzle} = 393$ K and the results are reported in Table 2.2. The

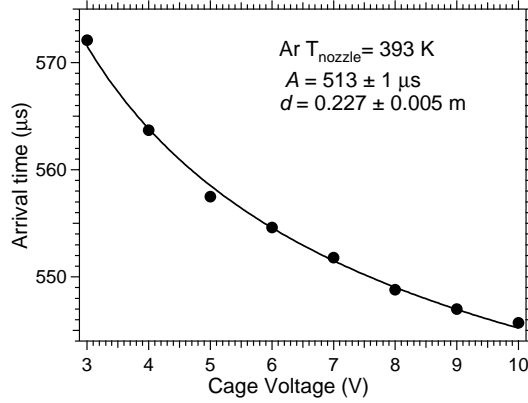


Figure 2.10: Arrival time of the Ar supersonic expansion with $T_{nozzle} = 393$ K as a function of the cage voltage. The solid line is the best fit obtained using eq. 2.14. A and d are the parameters resulting from the fit.

gas (T_{nozzle})	v_0 exp. (m/s)	v_0 theoretical (m/s)	Ion TOF (μ s)	d (m)
Ar (393 K)	656 ± 6	639	32.6 ± 0.9	0.227 ± 0.005
CH ₄ (393 K)	1286 ± 10	1278	20.6 ± 0.5	0.233 ± 0.005
He (393 K)	2050 ± 20	2020	10.3 ± 0.3	0.221 ± 0.005
Average				0.227 ± 0.006

Table 2.1: Ion TOF fit results for different gasses. The value reported in the column labelled “ v_0 exp.” are the velocities measured by translating the QMS and are the values used for the determination of d . The column “ v_0 theoretical” are the theoretical velocities calculated using eq 2.4. The “Ion TOF” corresponds to the time the ions spend inside the QMS when the cage voltage is set to 10 V.

average value of the ion flight distance is 0.227 ± 0.006 m. Using the theoretical values of v_0 in equation 2.14 we find an average d of 0.225 ± 0.009 .

Neutral TOF distance L . By inserting Δt_{chop}^{cw} and d in the equations 2.11 and 2.13, we can write the TOF of the neutral molecules t_{TOF} as a function of the time recorded by the MCS t :

$$\Delta t_{TOF} = t - 2.5143 \cdot 10^{-3} [\text{s}] - \frac{0.227 [\text{m}]}{\sqrt{v_0^2 + \frac{2qU}{m}}}. \quad (2.15)$$

The parameter L is determined by fitting the experimental TOF distributions obtained for Ar, He and CH₄ at 393 K. As fitting function, we use the convolution of $g_{den}(t_{TOF})$ (eq.2.9) and

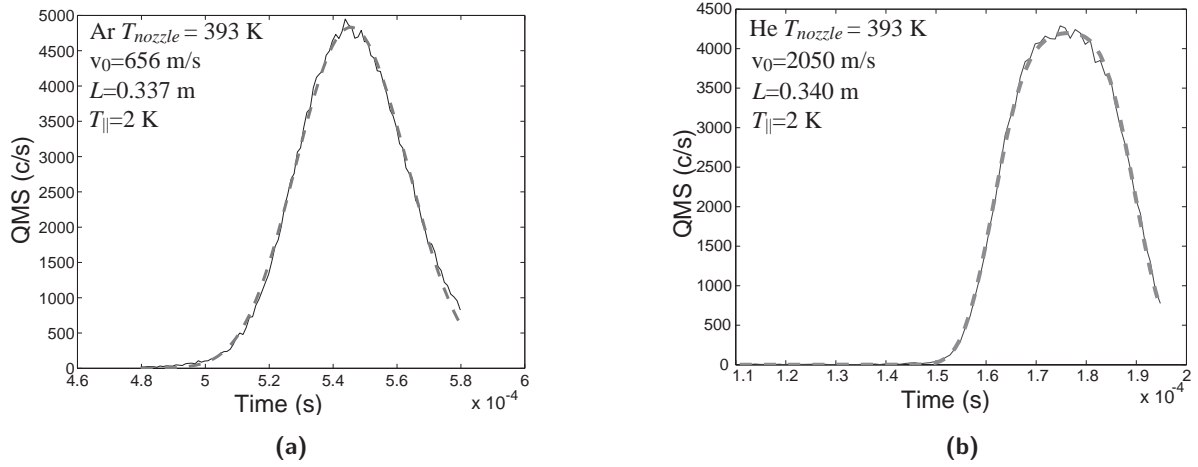


Figure 2.11: Ar (a) and He (b) TOF distributions are shown in solid line. The dashed lines are the best fit results. The fitting function is obtained by the convolution between the $g_{den}(t_{TOF})$ (2.10) and the chopper transmission function $O(\tau)$.

the chopper transmission function $O(t)$ (eq.2.10). The fitting parameters are the neutral flight distance L , the translational temperature T_{\parallel} and an intensity normalization factor. The dashed lines in Fig. 2.11a and 2.11b are the best fits for the TOF of Ar and He supersonically expanded at 393 K. v_0 is the velocity used in the fitting function for the determination of L .

Since the molecular beam pulses arriving at the QMS have a diameter ($\varnothing \sim 4$ mm) larger than the exit hole of the ion source ($\varnothing = 3$ mm) (see Fig. 2.12), a certain number of molecules collide around the exit hole (light grey part in the drawing) and are scattered inside the ion source. As a consequence, the falling part of the TOF distribution is distorted by an exponentially decaying tail. The decay time of is the pump-out time of the ion source. We apply two changes to the setup to reduce the effect of the tail on the TOF distribution. First, we decrease the stagnation time of the molecules inside the ion source by removing the entrance aperture of the ions source (see figure) in order to decrease the pump-out time. Second, to minimize the fraction of scattered molecules, we reduce the diameter of the molecular beam by inserting an aperture of 1 mm diameter in the molecular beam. The aperture is attached to the sample manipulator and can be positioned accurately in the molecular beam. The distance between the aperture and the ion source is ~ 20 cm. The position of the aperture with respect to the molecular beam and the ionizer exit hole is adjusted to reduce as much as possible the contribution of scattered molecules in the TOF profile. However, a small fraction of the molecules in the molecular beam

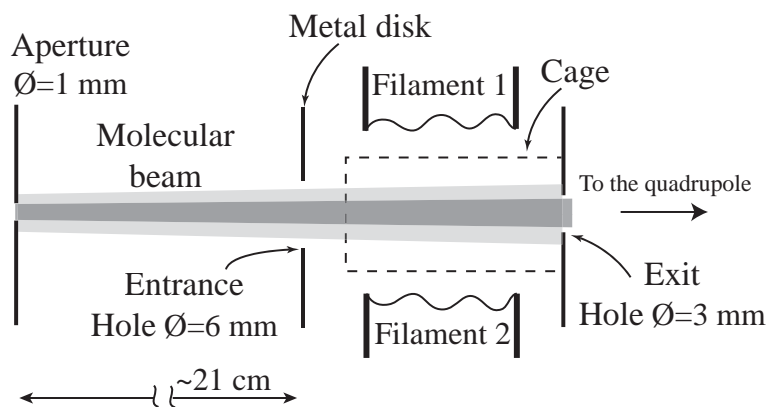


Figure 2.12: Schematic view of the ion source installed in our QMS. The molecular beam pulse moves from left to right. The 1 mm diameter aperture is installed below our sample holder and reduces the size of the molecular beam. Without the aperture, the molecular beam diameter (part drawn in light grey) would be larger than the exit hole of the ion source, and molecules would scatter around the hole causing a pressure rise inside the source.

gas (T_{nozzle})	v_0 exp. (m/s)	v_0 theoretical (m/s)	$T_{ }(K)$	L (m)
Ar (393 K)	656 ± 6	639	~ 2	0.337
CH ₄ (393 K)	1286 ± 10	1278	~ 2	0.335
He (393 K)	2050 ± 20	2020	~ 2	0.340
Average				0.337 ± 0.003

Table 2.2: Neutral flight distance calibration results.

are still scattered by the cage of the ion source and a small tail is still present on the TOF distribution. Equation 2.10 would not properly fit this part of the TOF and for this reason we cut the falling part of the recorded TOF distribution at 20% of the maximum intensity.

Table 2.2 reports the values of L and $T_{||}$ determined using Ar, He, and CH₄. The average value for L is 0.337 ± 0.003 m. Using v_0 theoretical instead the v_0 exp. gives an averaged distance L of 0.333 ± 0.003 , which is in good agreement with that reported in Table 2.2.

Once the calibration is performed, the average molecular beam velocity can be determined by fitting the experimental TOF distribution with eq.2.10. Now, the fitting parameters become the velocity v_0 and $T_{||}$. As example, the TOF of a mixture CH₄/H₂ with nominal methane concentration of 1.3% is reported in Fig. 2.13. The measured velocity is 3190 ± 58 m/s, and the error is evaluated by propagating the uncertainty of the calibration parameters. The shape of this TOF distribution is more trapezoidal compared to that shown in Fig. 2.11a and Fig.

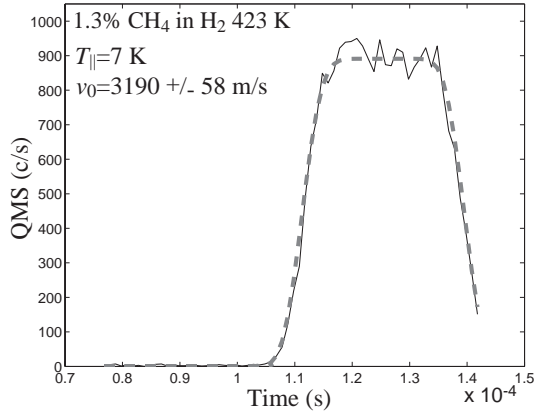


Figure 2.13: Example of velocity determination of a mixture of CH₄ in H₂ with a nominal methane concentration of 1.3%. The dashed line is the best fit to the experimental data.

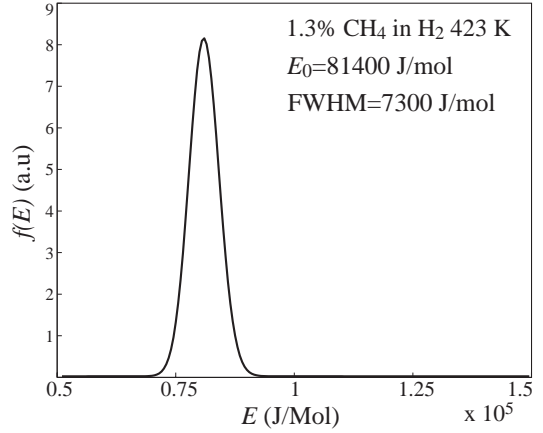


Figure 2.14: Energy distribution of the TOF shown in Fig.2.13. E_0 is the average energy.

2.11b. This is due to the convolution in eq. 2.10; as the TOF becomes shorter, the molecules in the beam pulse with different velocities spread less and the chopper transmission function dominates over $g_{den}(t)$.

Finally, the average kinetic energy of the molecules in the molecular beam pulses can be calculated from the energy distribution

$$i(E)dE = f\left(\sqrt{\frac{2E}{m}}\right)dv(E) = \frac{1}{m\sqrt{\frac{2E}{m}}}f\left(\sqrt{\frac{2E}{m}}\right)dE, \quad (2.16)$$

as determined from the measured TOF distribution. The energy distribution corresponding to the TOF in Fig. 2.13 is shown in Fig.2.14. Since the energy distributions we determined are almost symmetric with respect to the maximum position at E_0 , the average energy is calculated as $E_0 = 1/2mv_0^2$. The FWHM of the energy distributions depend on the translational temperature determined from the TOF fit. For expansion of pure He and Ar, we calculate translational temperatures on the order of 2 K, which corresponds to a kinetic energy spread $\Delta E/E$ of ~ 0.13 . For the mixtures of CH₄ in H₂, the kinetic energy spread decreases from 30% to 12% when decreasing the seed ratio from 25% to 1.3%.

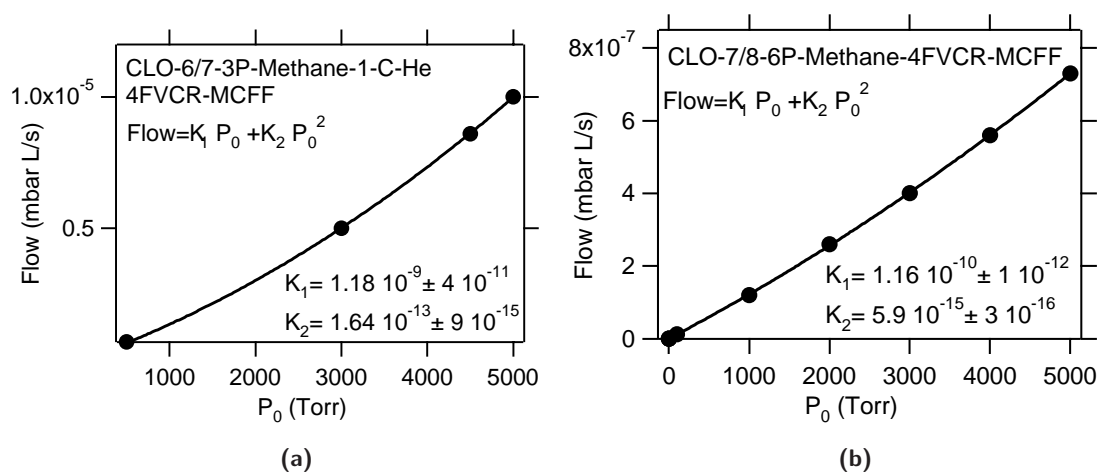


Figure 2.15: Factory calibration data points for the CLO-6/7 (a) and CLO-7/8 (a) crimped calibrated leak standards. The values between the calibration data points are determined by fitting a second order polynomial equation. The best fit results are reported in the graph with their errors. The units for K_1 and K_2 are (mbar L)/(s Torr) and (mbar L)/(s Torr²) respectively.

Molecular beam intensity

The number of CH₄ molecules per unit time incident on the nickel surface during a deposition experiment is determined by monitoring the methane partial pressure rise in the UHV chamber using our QMS. The QMS signal (counts/s) is calibrated in terms of molecules per second using a crimped capillary leak standard (Vacuum Technology Inc. Accuflow Variable leak). This device is factory calibrated to produce a known throughput in (mbar·l)/s as a function of backing pressure. In order to cover the methane flow range used in our experiments, two capillary calibrated leaks are installed on the UHV chamber. Since the flow rate from capillary leak elements into vacuum depends on the square of the backing pressure⁷⁶, the factory calibration data points are interpolated using second order polynomials. The interpolation functions and their coefficients are shown in Fig. 2.15a and Fig. 2.15b. The factory calibration data points are shown as bullets. The flow rates have been converted from mbar·l/s (at a specified temperature) to molecules/s according to the ideal gas law. The pressure behind the calibrated leak is measured with a capacitance manometer (MKS, Baratron 722A-1000 Torr). These measurements rely on the assumption that the pumping speed of our UHV chamber is independent of pressure among the calibration points and does not change between the calibration and the molecular beam experiment, which is reasonable for UHV chamber pumped by a turbomolecular pump.

In order to compensate for the decrease in sensitivity of the QMS channeltron, we regularly recalibrate the QMS response to a known flow. The statistical error in the flow calibration is evaluated from the propagation of the confidence limits of the fitting parameters K_1 and K_2 .

For the sticking coefficient calculation, the flux in molecules/(s·cm²) of reagent molecules is required. Since the molecular beam is slightly divergent, the flux on the crystal surface depends on the position of the crystal along the beam axis. During the deposition experiments, the crystal is placed at a distance of 103 mm from the aperture that transmits the molecular beam pulses into the UHV chamber (manipulator position: $X = 0.930''$, $Y = 1.000''$, $Z = 9.245''$, $\theta = 98^\circ$). Under this condition, the diameter of the molecular beam on the crystal surface is 1.9 mm and it is determined by recording Auger spectra over the spot of adsorbed carbon produced via a deposition experiment. Details on the surface analysis with Auger spectroscopy will be reported later in this chapter.

Typical molecular beam intensities measured during deposition experiments are $1 \cdot 10^{14} \pm 3\%$ and $1 \cdot 10^{15} \pm 3\%$ molecules/(s·cm²) using the narrow and wide slits respectively (12 % CH₄/H₂, $T_{nozzle} = 150$ °C).

2.4 Surface-science chamber

Our custom-built UHV surface science chamber is pumped by a 1000 l/s turbo pump (Pfeiffer, TMU 1000P), backed by a mechanical pump (Pfeiffer, Duo 10) equipped with a catalyst trap to avoid back streaming of oil vapor. The base pressure of the UHV chamber is of $5 \cdot 10^{-11}$ mbar. The design of the chamber is based on three levels. The lowest level holds the vacuum gauges (Balzers, IKR 070 and IKR 020), two calibrated leaks, and a load lock which enable us to replace the crystal without breaking vacuum in the chamber. The second level, where the molecular beam enters, is for deposition experiments as well as molecular beam characterization with a quadrupole mass spectrometer (Hiden, HAL 301/3FPIC). The third level is used for surface cleaning and analysis. It is equipped with an Auger electron spectrometer (AES) (Omicron, CMA 150), a low energy electron diffraction (LEED) spectrometer (Omicron, SPECTALEED) and an ion sputter gun (Omicron, ISE 10).

The sample surface is mounted on a commercial four axis manipulator, providing for translation along the vertical Z axis (16'' travel, repeatability of 0.0005''), X and Y displacements in the horizontal plane with $\pm 0.8''$ travel and 0.0001'' precision. The manipulator includes rotation about the Z axis for control of the incident angle of the molecular beam as well as for the

orientation of the sample in front of the different analysis tools. A doubly differentially pumped rotation stage with three spring-loaded Teflon seals permits free rotation of the manipulator. All connections to the manipulator (electrical and cooling by liquid nitrogen) are made via the rotating top flange, preventing in vacuum flexing of tubing and electrical connections.

Our 10 mm diameter nickel single crystal is mounted on a removable sample platen that attaches to a copper dewar-heater assembly. The platen, including a K -type thermocouple spot welded to the edge of the sample, can be transferred from the copper dewar with a magnetically coupled rotary-linear feedthrough (Thermionics Laboratory Inc, FLRE series), through a load lock chamber.

The sample can be heated by electron impact and cooled by flowing liquid nitrogen through the dewar. The heating system is commercially available (Thermionics, STLC-TTC platen) and includes the power supply (SPS series) and the PID controller (Omron, E5AK). Electron bombardment heating is provided by a 0.3 mm tungsten filament situated behind the crystal sample. With the sample grounded, the electrons are accelerated by a negative potential (filament HV) applied to the filament (max 2 kV). The PID controller regulates the temperature of the sample either by changing the filament HV (“HV Regulation”) or by controlling the alternating current used to heat the filament (“Current Regulation”). In our measurements, we prefer stabilizing the temperature using the “Current Regulation” because it avoids rapid variations of the filament HV that could induce noise in the Auger measurements. For crystal heating around 500 K, the HV and the filament current are limited to -500 V and 11 A respectively and the temperature regulation is stable within 1 K. At higher temperature (1100 K) the HV is limited to -1.5 kV. While the crystal is heated, liquid nitrogen continuously flows through the dewar. The lowest achievable sample temperature is 99 K and can be reached in around 15 min starting from 300 K.

2.4.1 Auger spectrometer

After deposition, the amount of carbon atoms on the nickel surface is quantified by Auger electron spectroscopy (AES).

The basic Auger process starts with the removal of an atomic inner shell electron to form a vacancy. The inner shell vacancy is filled by a second atomic electron from a higher shell. Energy must be simultaneously released, then a third electron (Auger electron) escapes carrying the excess energy in a radiationless process. The process of an excited ion decaying into a doubly charged ion by ejection of an electron is called the Auger process. Since the kinetic energy of

Element	Energy (eV)	Auger Transition
C	273	KLL
O	510	KLL
Ni	848	LMM

Table 2.3: Auger transition for the atomic species that we detect on the surface.

the Auger electrons ejected depends only on the level spacing of the parent atoms, it is possible to unequivocally detect all atomic species other than hydrogen and helium.

In the AES technique, an electron beam (primary electrons with 1 – 5 keV of kinetic energy) is used to produce the atomic inner shell electron vacancies. An advantage of Auger spectroscopy for surface studies is that the low-energy Auger electrons (20-2000 eV) are able to penetrate only few atomic layers (3 – 20 Å) of the solid. Thus, while the primary electrons penetrate $\sim 1 \mu\text{m}$ into the surface, only those Auger electrons produced in the first five atomic layers escape to the surface to reach the analyzer⁷⁷. Auger spectra are often recorded as the derivative of the Auger electron current versus the electron kinetic energy using a lock-in amplifier. The acquisition of the derivative of the Auger electron current eliminates the slowly varying background signal, which is produced from inelastically scattered primary electrons as well as secondary electrons.

We use Auger spectroscopy to assess the cleanliness of our sample surface and to quantify the amount of adsorbed carbon atoms on the surface after the deposition. The atomic species we usually detect on the surface are carbon, oxygen, and nickel. Table 2.3 reports the Auger transitions used and their respective energies.

Our Auger spectrometer (Omicron CMA 150) has a single stage cylindrical mirror analyzer (CMA) and an integrated e^- -gun (EKI 25). The detection limit of the CMA, as specified by the manufacturer, is 0.5% of a monolayer under the following experimental conditions: primary electron energy $E_0 = 3 \text{ keV}$, primary electron beam current $I_0 = 10 \mu\text{A}$, modulation = 5 V_{pp} , lock-in dwell time 2 s/eV. The setup is shown in Fig.2.16. Primary electrons (3 kV) are produced by the electron gun, their energy and the emission current I_0 is adjusted by the e^- -gun controller. Since the number of the Auger electrons is proportional to the current of the primary electrons, we monitor the I_0 output from the electron gun controller (0 – 10 V for current range of 0 – 50 μA) by the analog-to-digital converter (ADC) input of a National Instruments data acquisition card Lab-PC+ (DAQ in Fig. 2.16) installed in a PC computer. This input has an acquisition range of 0 – 10 V (gain = 10), thus the maximum I_0 we can monitor is 5 μA . The Auger electrons

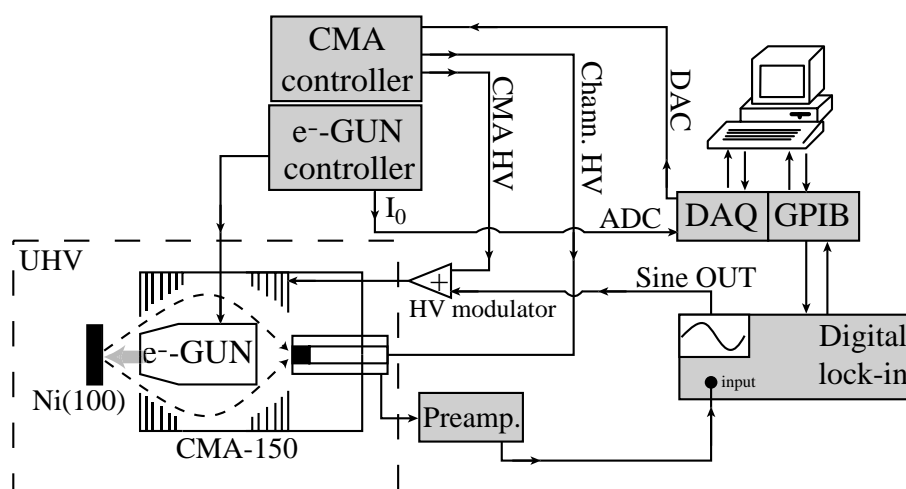


Figure 2.16: Schematic view of the Auger spectrometer that we use to quantify the carbon product amount and to verify the cleanliness of the surface.

(dashed curves in figure) are emitted from the Ni(100) crystal, and enter the CMA where they are filtered in energy. The energy of the transmitted electrons depends on the voltage applied between the cylindrical mirrors (CMA HV in the figure) and is remotely controlled via a 0 to 10 V digital-to-analog converter output (DAC) of the DAQ card. The CMA controller supplies high voltage (1.5 kV) for the channeltron (Chann. HV in the figure), which detects the arriving Auger electrons. The derivative of the Auger-electron current relative to the Auger-electron kinetic energy is recorded by modulating (HV modulator) the CMA HV with a sinusoidal signal ($5.5 V_{pp}$, 9.7 kHz) generated by the oscillator included in the digital lock-in. The Auger signal coming from the channeltron is pre-amplified (gain= $\times 300$) and detected by a digital dual-phase lock-in amplifier (SR830). The digital lock-in amplifier can be remotely controlled by the computer via a GPIB interface.

Since small changes in the sample position (~ 0.1 mm) produce apparent energy shifts in the Auger electrons (~ 2 eV)⁷⁸, we optimize the crystal position by observing the elastically scattered electrons produced at a well known kinetic energy (3 keV). The lock-in phase of 2.58° is determined by maximizing the carbon signal at 273 eV.

To reduce the electron induced carbon formation on the surface, a low primary electron current ($0.4 - 0.8 \mu\text{A}$) is used to record our Auger spectra. Under this condition, the typical carbon accumulation rate is ≈ 0.04 ML/h.

By convention, Auger intensities are measured as the difference between the maxima and the minima of the peaks. The locations on the kinetic energy scale are read at the valley position.

	Carbon	Nickel	Survey scan
Scan interval (eV)	260 – 290	825 – 870	50 – 950
Scan step (eV)	1	1	2
Dwell time (s)	1	0.1	0.3
Time constant (s)	1	0.1	0.1
Sensitivity (mV)	20	200	200

Table 2.4: Auger parameters used in each region we scan for surface analysis. Time constant and sensitivity are parameters set in the lock-in amplifier.

To verify the cleanliness of the surface, we acquire an Auger spectrum in the interval 50 – 960 eV (survey scan) using the settings shown in Table 2.4. Figure 2.23 (upper trace) shows the Auger spectrum of a new Ni(100) sample after transfer into the UHV chamber before the cleaning. The lower trace shows the same sample surface after the cleaning treatment. For comparison with other different spectrometers and to compensate possible variations in collection efficiency, the amount of carbon on the surface is determined as the ratio between the carbon and nickel peak intensities. When we analyze the surface for carbon determination, we record two spectra in the regions of 260 – 290 eV, for the detection of carbon KLL transition, and 825 – 870 eV for the most intense LMM nickel transition (see Table 2.4). We usually detect a small quantity of carbon (< 10% of ML) and, under this condition, the carbon Auger peak intensity is one order of magnitude smaller than that of the nickel peak. In order to optimize the acquisition time and the signal to noise ratio, we scan the two regions at different dwell times and sensitivities. For the carbon region, we use a dwell time of 1 s and a sensitivity of 20 mV. For nickel, the dwell time and the sensitivity are 0.1 s and 200 mV respectively. As example the Auger spectra of carbon and nickel on Ni(100) used for adsorbate detection are reported in Fig. 2.17.

Automated sample motion

The spatially resolved carbon concentration on the crystal surface is obtained by recording the carbon and nickel Auger peaks as a function of the crystal position relative to the primary electron beam (C/Ni surface scan). The crystal is displaced along the Z and X axis (directions perpendicular to the Auger spectrometer) of the manipulator. The X -axis micrometer and the Z -axis drive of the manipulator are equipped with stepper motors for automated motions; RS Components, 5 V, 0.5 A, 200 steps/turn for the X -axis and RS Components, 5 V, 1 A, 200 steps/turn for the Z -axis. These motors are computer controlled via a series of TTL pulses

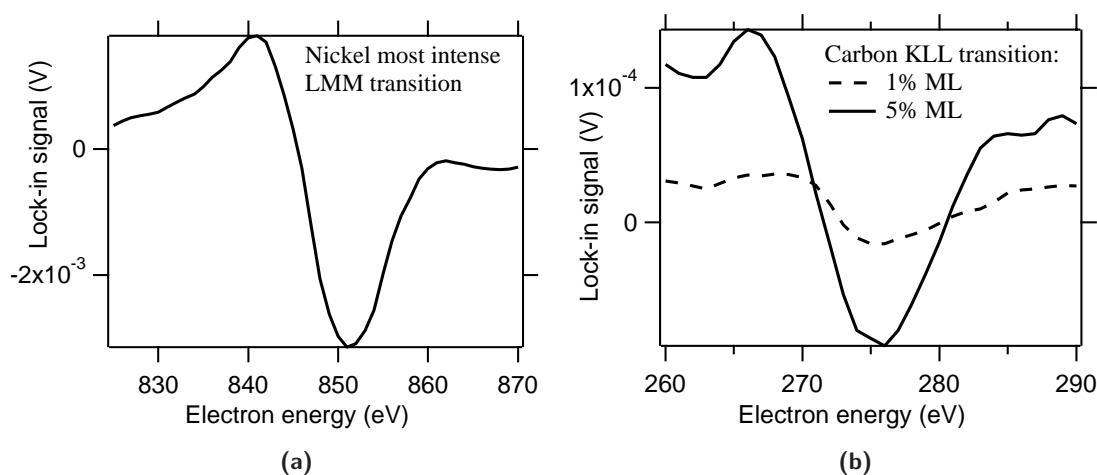


Figure 2.17: Auger spectra of the most intense LMM nickel transition (a) and the KLL carbon transition (b). For carbon we show two spectra acquired at different carbon coverages. The signal displayed in the graphs is not normalized with respect to the primary electron current.

generated by two hardware clocks installed on the DAQ card. The TTL pulse frequency is limited to 300 Hz to avoid motor stalling. The rotation direction of the motors is controlled by the digital output of the same DAQ card. The spatial resolutions for motion along the X - and Z -axis are 0.0001" and 0.0005" respectively. A set of micro-switches on the manipulator prevents the X -axis motor from applying force on the micrometer screws before the maximum travel is reached. A LabVIEW program that controls the stepper motors and the Auger spectrometer is used for automated acquisition of Auger spectra across the surface.

In order to analyze the part of the crystal where the deposition with the molecular beam has been performed, we need to find the relations that transform the deposition coordinates into the analysis coordinates. Since the molecular beam axis, which is parallel to the X -axis of the manipulator, is perpendicular to the primary electron beam of the Auger, we know that the Y -axis deposition coordinates ($Y_{dep.}$) transform into the X -axis analysis coordinates (X_{Auger}). The map of the crystal surface in term of the deposition and analysis coordinates is shown in Fig. 2.18.

We determine the size of our Auger electron beam by scanning across a tantalum wire ($\varnothing = 50 \mu\text{m}$) and across the edges of the sample surface. We found an optimized electron beam diameter of 140 μm FWHM.

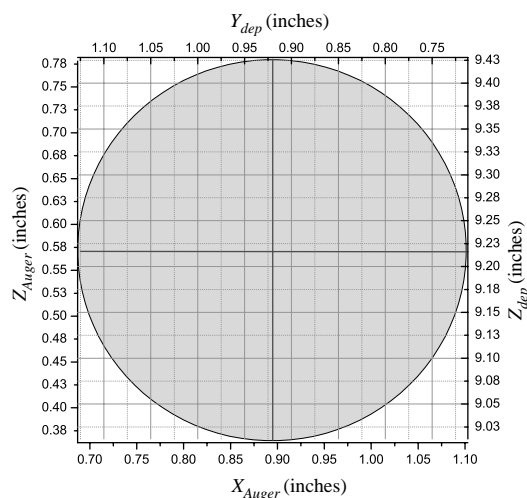


Figure 2.18: Crystal surface mapped in term of deposition coordinates ($Z_{dep.}$, $Y_{dep.}$) and Auger analysis coordinates (Z_{Auger} , X_{Auger}).

Auger spectrometer calibration. Absolute quantification of adsorbed carbon can be obtained by measuring the Auger signal for a known carbon coverage. We can obtain a defined quantity of carbon on the surface by knowing that ethylene produces at most half ML of carbon on Ni(100)^{79–81}. Ethylene is leaked into the chamber at a static pressure in the 10^{-8} mbar range, while the temperature of the surface is kept at 475 K to promote the recombinative desorption of hydrogen. We record the uptake curve of C on Ni(100) by scanning the sample surface along the X axis in front of the Auger system. For each sample position corresponding to a different exposure time, we take Auger spectra for C and Ni and plot the peak ratio in the form of an uptake curve shown in Fig. 2.19. The average C/Ni Auger peak ratio at surface saturation is 0.14, which corresponds to 0.5 ML ($1.6 \cdot 10^{15}/2$ atoms/cm²).

2.4.2 LEED spectrometer

We use low energy electron diffraction (LEED) to have qualitative information on the surface structure of our sample and to verify the integrity of the surface structure after ion sputtering. Our nickel single crystal sample is cut to within 0.1° of the (100) plane. The LEED pattern of our Ni(100) sample recorded after argon ion sputtering (1.5 kV, 20 μ A, 5 minutes) and subsequent annealing (1123 K for 5 minutes) for surface cleaning is shown in Fig. 2.20⁷¹. The picture clearly shows the pattern produced from an fcc(100) surface, confirming that the annealing process reconstructs the surface in its original configuration.

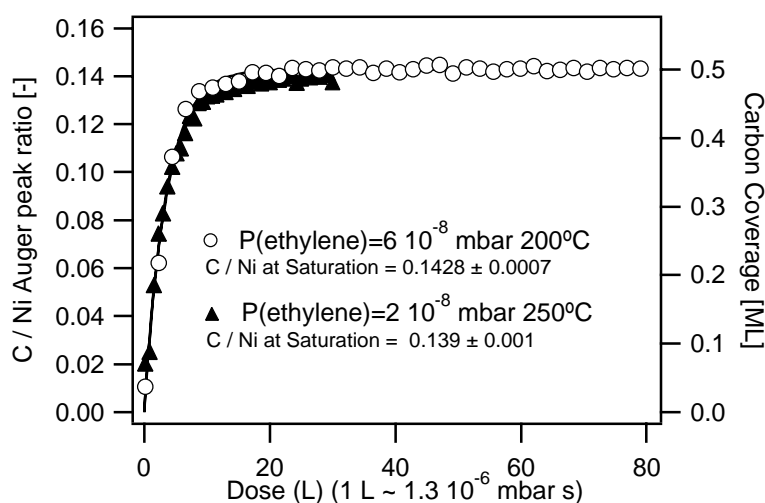


Figure 2.19: Self-limiting chemisorption of ethylene on Ni(100). The saturation value correspond to 0.5 ML on Ni(100) (graph taken from Schmid Ph.D. thesis⁷¹).

Terborg et al.⁸² have found that at a coverage smaller than 0.15 ML the carbon atoms on the surface occupy simple undistorted hollow sites. At higher coverage the adsorbates induce a substrate reconstruction. In particular, when Ni(100) is saturated with carbon (0.5 ML), the surface has a structure of Ni(100)-Cp4g phase, which has been shown to involve a *clock* reconstruction of the outermost nickel layer⁸³. In this structure the top layer nickel atoms are displaced parallel to the surface, by alternate clockwise counter-clockwise rotation about the carbon atoms in such a way that the hollow sites occupied by the atoms are enlarged (see Fig. 2.21). The LEED pattern of the carbon saturated Ni(100) is shown in Fig. 2.22. It was identified and correctly interpreted by Onuferko et al.⁸³, and it corresponds to a pattern of a primitive (2×2) with missing spots (highlighted with circles). Onuferko et al. showed that the missing spots acquire intensities if the electron beam is normal to the surface, then the LEED pattern shown in Fig. 2.22 is obtained by slightly tilting the surface⁷¹.

2.4.3 Sample cleaning

Before every sticking coefficient determination, the surface must be free from contaminations.

We clean our Ni(100) crystal by bombardment with energetic argon ions from a commercial ion gun (Omicron, ISE 10). We sputter the sample with a total current leaving the gun of 20 μA , which corresponds to $\sim 2 \mu\text{A}$ on the 19 mm diameter of the crystal holder. The ion dose in this condition is 10^{15} ions/ cm^2 after 5 minutes of sputter cleaning. During the sputtering,



Figure 2.20: LEED pattern of a clean Ni(100) acquired using an electron beam energy of 103 eV (picture from Schmid Ph.D. thesis⁷¹).

the Ar pressure in the UHV chamber is $5.5 \cdot 10^{-7}$ mbar. After sputtering, the crystal structure is restored by annealing the surface for 5 minutes at 1173 K⁸⁴. The upper trace in Fig. 2.23 shows the Auger spectrum of a new Ni(100) sample after transfer into the UHV chamber before the cleaning. The lower trace shows the Auger spectrum of the same sample after the cleaning treatment.

When the sputtering is not enough to remove the impurities, we alternate argon ion bombardment and annealing with oxidation and reduction cycles. The chemical treatment is performed using the following recipe:

1. Cover the surface with oxygen at room temperature ($P_{O_2} = 1 \cdot 10^{-7}$ mbar for 30 s).
2. Heat the sample in vacuum to 1073 K.
3. Reduce the sample for 15 minutes with H_2 ($1 \cdot 10^{-6}$ mbar) maintaining the surface temperature at 1073 K.

It is important to avoid heating the surface with oxygen in the UHV, which would cause O to dissolve into the bulk of the crystal.

2.5 Pulsed infrared laser setup

In order to prepare a significant fraction of molecules of the molecular beam pulses in a selected rovibrational state via overtone or combination transitions, we generate tunable infrared (IR)

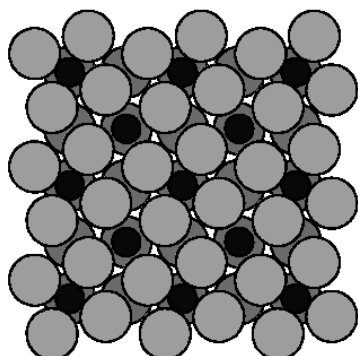


Figure 2.21: $(2 \times 2)p4g$ reconstruction produced by 0.5 ML of carbon. The light grey circles represent the top rotated nickel layer atoms, the black circles are the carbon atoms and the dark grey circles are the nickel atoms of the second layer.

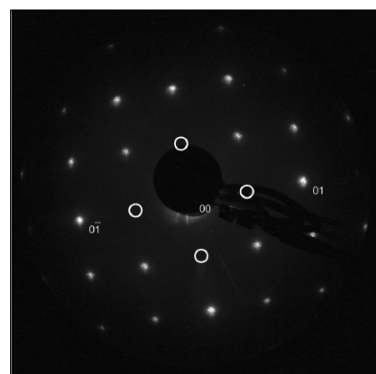


Figure 2.22: LEED pattern of a carbon saturated Ni(100) recorded with electron energy of 103 eV (picture from Schmid Ph.D. thesis⁷¹). The diffraction pattern is similar to the $p(2 \times 2)$ structure with missing spots marked using circles.

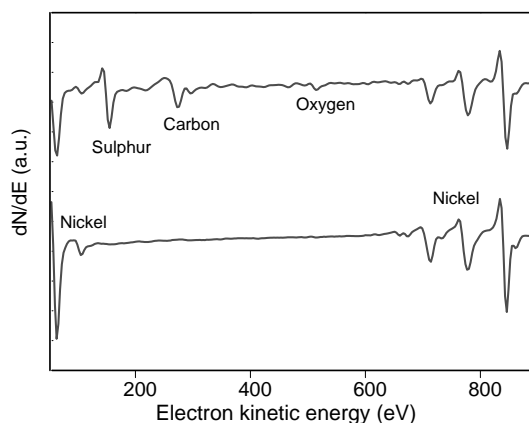


Figure 2.23: Auger electron spectra of a contaminated (upper trace) and clean (lower trace) Ni(100). The surface is cleaned by a combination of argon ion sputtering, annealing (1173 K) and oxidation/reduction cycles.

radiation with narrow bandwidth and high pulse energy. Figure 2.24 shows a schematic view of our optical system. In this setup, non-linear optical techniques are used to produce IR radiation tunable around $1.7 \mu\text{m}$. The second harmonic of an injection-seeded single-mode Nd:YAG laser (Spectra Physics, GCR 270-20, maximum output $> 400 \text{ mJ}$ at 532 nm, 8 ns pulse duration) is used to pump a tunable, narrow bandwidth (0.02 cm^{-1}) dye laser with intra-cavity etalon (Lambda Physik, Scanmate 2E). The dye laser produces $\sim 50 \text{ mJ}$ pulses vertically polarized

(see Fig. 2.24) at 650 nm using Exciton DCM dye in 20% propylene carbonate/methanol; oscillator: $5.1 \cdot 10^{-4}$ M, amplifier: $1.25 \cdot 10^{-4}$ M. A Bethune cell ($\varnothing = 3.5$ mm) installed in the amplification stage of the dye laser produces a circular beam profile that is expanded with a telescope to match the 1 cm diameter of 1064 nm of the Nd:YAG. The Nd:YAG fundamental

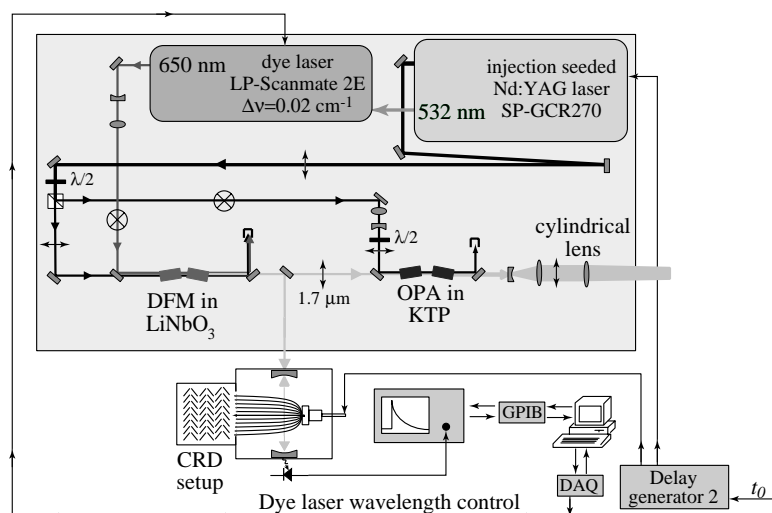


Figure 2.24: Infrared laser setup used to excite CH_4 overtone and combination CH stretch transitions around $1.7 \mu\text{m}$. We perform difference frequency mixing (DFM) in a LiNbO_3 crystal between the fundamental of an injection-seeded Nd:YAG and 650 nm generated by the dye laser. The $\sim 1.7 \mu\text{m}$ produced is amplified by an optical parametric amplifier (OPA) with two KTP crystals. The vertical and horizontal polarizations with respect to the plane of the optic table are represented with the symbols \otimes and \longleftrightarrow respectively.

is split in two parts via a half-waveplate and a polarizing cubic prism beam splitter. The weaker beam (120 mJ/pulse , $\Delta\nu=0.003 \text{ cm}^{-1}$), with horizontal polarization, is used to perform difference frequency mixing (DFM) with the 650 nm light in a LiNbO_3 crystal (Cstech) to produce $2 - 3 \text{ mJ}$ of IR radiation at $\sim 1.7 \mu\text{m}$. The crystal is installed in a commercial angle-tracking system (Inrad, Autotracker II), allowing for continuous tuning of the IR radiation. After the DFM stage, the residual 1064 nm and 650 nm are separated from the $1.67 \mu\text{m}$ by reflection with a dielectric mirror and a silicon plate respectively. 30% of the DFM output is directed to the cavity ring-down setup for acquiring jet absorption spectra and for tuning the IR frequency onto the desired molecular transition. The remaining 1.3 mJ/pulse are amplified in an optical parametric amplifier (OPA).

The OPA system consists of two 25 mm long KTiOPO_4 (KTP) crystals cut at $\theta = 67.5^\circ$ $\phi = 0^\circ$ and arranged in a walkoff-compensated configuration⁸⁵. The KTP crystals are used in

the *ooe* configuration, meaning that the pump (1064 nm) and the seed (1670 nm) beams have ordinary polarization, and that the idler (3000 nm), at the output of the OPA, has extraordinary polarization⁸⁶.

The 1064 nm vertically polarized beam reflected by the beam splitter is used as pump in the OPA stage. In order to match the 1 cm diameter of the 1.67 μm , the pump beam diameter is reduced with a telescope. The pump beam polarization is rotated onto the ordinary plane of the KTP crystals via a half-waveplate.

Once the output of the DFM is tuned into resonance with the target transition, the angles of the OPA crystals are adjusted manually to maximize the output energy. After the OPA stage, the 1064 nm pump radiation and the idler beam are separated from the amplified seed beam by dichroic mirrors. By pumping the OPA with 500 mJ/pulse at 1064 nm, we can produce IR pulses at 1670 nm with energies up to 150 mJ. The 1.67 μm beam is expanded by a telescope to a diameter of 40 mm, and a cylindrical lens with a focal length of 160 cm focuses the tunable IR beam to a line within the UHV chamber where it is carefully overlapped with the molecular beam with the aid of an IR-sensitive video camera and an alignment tool installed between the crystal sample and the aperture of the molecular beam (see Fig. 2.2). During the deposition experiment, the IR power transmitted through the alignment tool is measured using a laser power meter.

Throughout the deposition, we monitor the CRD signal to verify that the laser stays resonant with the molecular transition. We found that the frequency of the IR radiation is sufficiently stable that it is not necessary to actively lock it to the CRD signal.

A delay generator synchronizes (Delay generator 2 in Fig. 2.24) the IR laser pulses with the transit of the molecular beam pulses in the alignment tool.

2.6 Cavity ring-down setup.

For the state-resolved reaction probability measurements, we need to determine the number of excited molecules in the molecular beam. This depends on the population of the starting level of the targeted transition and on the laser intensity. During the supersonic expansion, the molecules are rotationally cooled. Therefore, the rotational temperature of the molecules must be measured in order to determine the populations of the rotational levels. The rotational temperatures are determined by analyzing the intensities of the Q-branch transitions in a vibrational band. For this purpose, we perform cavity ring-down (CRD) spectroscopy in jet expansion using an

auxiliary setup that reproduces the expansion condition of our molecular beam source.

The auxiliary vacuum chamber (base pressure $1 \cdot 10^{-6}$ mbar) is equipped with the same temperature controlled solenoid valve as installed in the molecular beam source. A 85 cm long cavity is formed by two high reflective plano-concave mirrors (Tiger Optics, 99.999% at $1.7 \mu\text{m}$) with a radius of curvature $r = 1$ m. The cavity longitudinal and transverse mode spacings are 170 MHz and about 80 MHz respectively. 30% of the DFM output at $1.67 \mu\text{m}$ (8ns, 0.02 cm^{-1} FWHM) is directed towards the cavity and the transmitted intensity is measured as a function of time with a fast InGaAs photodiode (Hamamatsu, G8373-01). The time-dependent transmitted intensity follows an exponential decay with a ring-down time constant τ given by⁸⁷:

$$\tau = \frac{d}{c(1 - R + \sigma nl)}, \quad (2.17)$$

where d is the length of the cavity, c the speed of light, σ is the absorption cross section of the sample molecules, n their number density, l the length of the sample and R the reflectivity of the mirrors. When the cavity is empty, the decay time is dominated by finite reflectivity of the mirrors. If an absorbing sample is introduced in the cavity, an additional loss is introduced and the ring-down time decreases. CRD spectra are recorded by monitoring the ring-down time as a function of the laser frequency. Practically, the photodiode signal is recorded as a function of time by an oscilloscope (Lecroy 9350A) and 20 traces are averaged internally to increase the signal to noise ratio. The averaged trace is transferred to a PC computer via a GPIB interface (see Fig. 2.24). A LabVIEW program determines the cavity ring-down time by fitting the experimental trace with an exponential decay function. With an empty cavity, we record a ring-down time up to $146 \mu\text{s}$, which corresponds to an effective reflectivity of 99.998%. The dye laser frequency is controlled by the PC computer via a DAQ card and a serial port interface (RS-232, not shown in Fig.2.24).

The rotational temperature of the jet-cooled CH_4 can be estimated by comparing the relative intensities of the transitions Q(1) and Q(2) of the $2\nu_3$ band. Table 2.5 shows the rotational temperatures for methane under different expansion conditions.

2.7 Stimulated Raman pumping laser setup

If the derivative of the molecular dipole moment with respect to a normal mode coordinate is zero, it is not possible to excite the vibrational transition associated to that normal mode using

Gas mixture	Nozzle Temperature (K)	Rotational Temperature (K)
CH ₄	373	26
CH ₄	313	14
3% CH ₄ /H ₂	373	6
3% CH ₄ /H ₂	313	9

Table 2.5: Rotational temperatures of CH₄ in pulsed jet expansion under various expansion conditions.

IR light. In the case of CH₄ molecules, the symmetric C-H stretch ν_1 is IR inactive. However, ν_1 can be excited using Raman scattering. The basic physics behind the Raman scattering process resides in the polarizability of the molecule. When one applies an electric field to a distribution of charges such as a molecule, the field will polarize the charges, giving rise to an induced dipole moment. If the applied field is not too strong, the induced dipole moment will be proportional to the applied field:

$$\mu_i = \alpha_{ij} E_j, \quad (2.18)$$

where α is the proportionality constant between the electric field and the induced dipole moment and is called *polarizability*. In a molecule, the nuclei are engaged in vibrational motions and the dipole moment induced by an external electric field will be a function not only of the external field, but also of the instantaneous nuclear positions. As a consequence, the polarizability is a function of the normal coordinates X_ν and can be expressed as a power series:

$$\alpha_{ij} = [\alpha_{ij}]_0 + \sum_{\nu} \left[\frac{\partial \alpha_{ij}}{\partial X_{\nu}} \right]_0 X_{\nu} + \dots \quad (2.19)$$

The first term in the right-hand side of this equation is responsible for the Rayleigh scattering and the second term originates the Raman scattering. Consequently, a vibrational transition associated to a normal mode X_ν is Raman active when $[\partial \alpha_{ij} / \partial X_\nu]_0 \neq 0$.

Raman scattering is a two-photon process which involves the inelastic scattering of the incident radiation with matter. When the scattered photon has a frequency lower than the incident one, leaving the molecule in an excited state, the process is called Stokes scattering (Fig. 2.25a). If the scattered photon has a higher energy than the incident one, then the scattering is called anti-Stokes, and the molecule is left in a lower energetic state (Fig. 2.25b).

In our experiments, we prepare the colliding CH₄ molecules in the totally symmetric C-H stretch

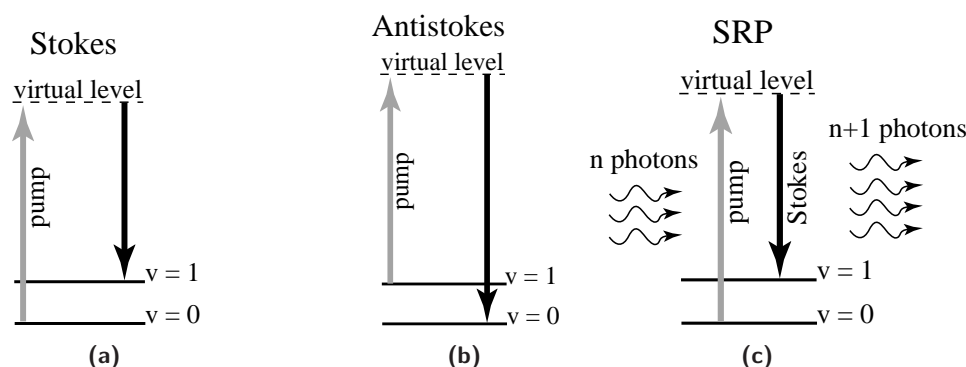


Figure 2.25: Raman Stokes (a) and antistokes (b) processes. The Stokes process leaves the molecule in an excited state. In the SRP process (c), the emission of the Stokes photon is stimulated by the presence of photons having the same frequency of the scattered one.

(ν_1) using stimulated Raman pumping (SRP). In this case, the Raman scattering probability is *enhanced* through the presence of radiation (Stokes laser beam) with the frequency of the scattered photons. Figure 2.25c shows the scheme of the SRP process for a Stokes photon; the emission of the Stokes photon is stimulated by the presence of existing photons with the same frequency of the scattered one. In appendix D we describe the quantum mechanical origin of the SRP process. Experimentally, two superimposed laser beams are focused onto the molecular beam pulses. The molecules will be excited when the difference in frequency of the two laser beams matches the targeted transition frequency. For methane, the difference in energy between ν_1 and the ground state molecules is $\sim 2917 \text{ cm}^{-1}$. If we use as pump a laser beam at 532 nm, then we must use a laser beam at $\sim 630 \text{ nm}$ as Stokes radiation.

Because the Raman pumping process is not particularly efficient, intense laser pulses are needed to drive it into saturation. The optical layout used to produce the required frequencies and intensities is shown in Fig. 2.26. The 532 nm Raman pump beam is produced by generating the second harmonic of an injection-seeded Nd:YAG laser (Spectra Physics, GCR270) operating at 20 Hz with pulse duration of $\sim 8 \text{ ns}$ and pulse energy of 800 mJ. 10% of the 532 nm energy is used to pump a dye laser (Lumonics, HD-500) producing Stokes radiation at 630 nm with a bandwidth of 0.05 cm^{-1} and a pulse energy of $\sim 12 \text{ mJ}$. In order to produce a circular beam shape, a Bethune cell with a diameter of 3.5 mm is installed in the amplifying stage of the dye laser. The dye used is the Exciton DCM in a solution of 20% propylene carbonate/methanol with concentrations of 340 mg/l and 56 mg/l for the oscillator and amplifier, respectively. The size of the dye laser beam ($\varnothing \sim 3 \text{ mm}$) is matched to that of the pump beam ($\varnothing \sim 9 \text{ mm}$) by expanding

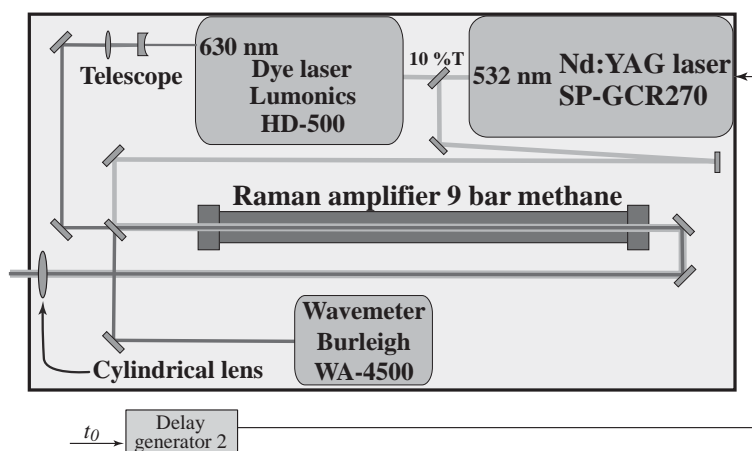


Figure 2.26: Optical setup used for stimulated Raman pumping of CH_4 in the molecular beam.

it about three times using a telescope. The two laser beams are reflected together into a CH_4

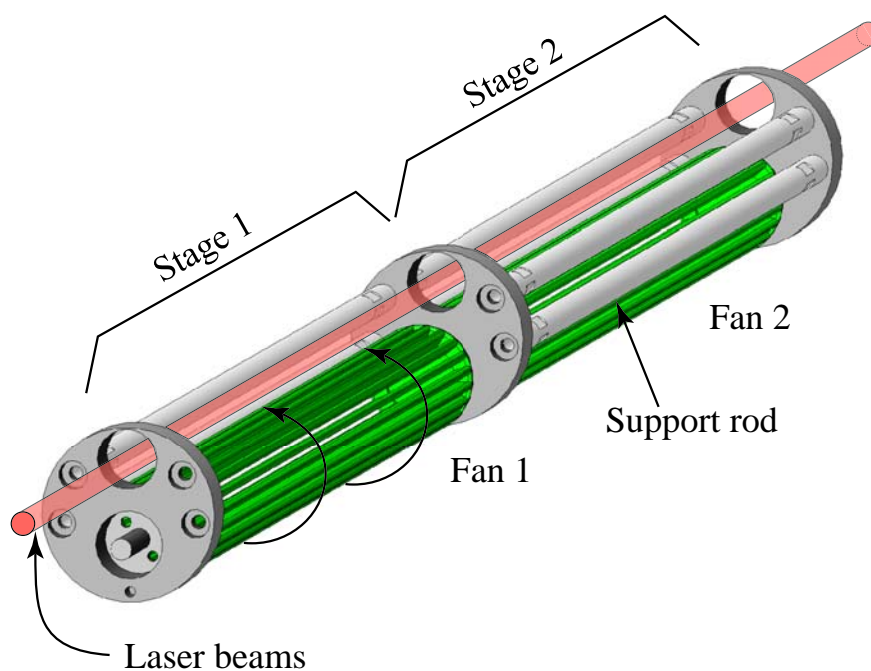


Figure 2.27: Internal part of the Raman amplifier. Two stages among four are shown here. The laser beams fly just above the fans (drawn in green). Each stage is held together by a series of 4 stainless steel rods. The fans rotate at 700 RPM and circulate the gas to avoid thermal lensing.

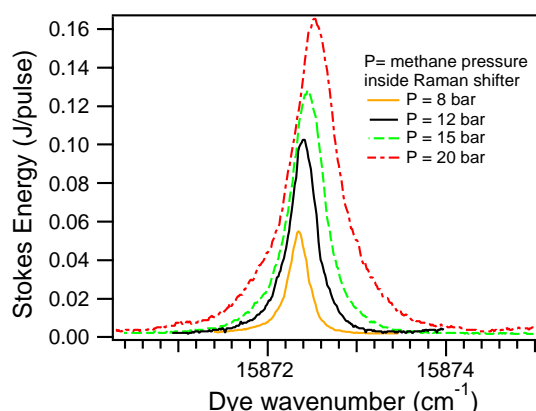


Figure 2.28: Raman gain curves for different methane pressures. The gain curves are measured by monitoring the Stokes beam energy at the output of the Raman amplifier as a function of the dye laser beam frequency. The maximum of the gain curves shifts to higher frequencies by increasing the pressure.

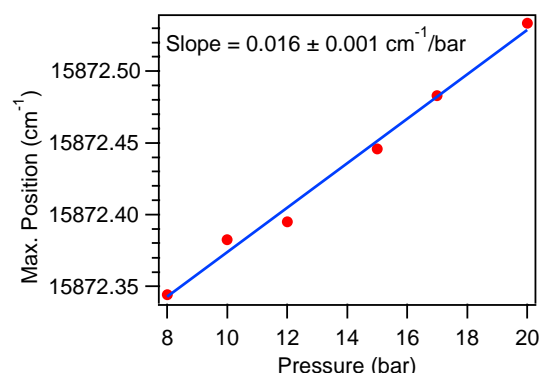


Figure 2.29: Maximum of the gain curves as a function of the methane pressure inside the Raman amplifier. The linear regression is shown as a solid line.

filled 1.7 m long Raman amplifier. When passing through the Raman amplifier, the Stokes beam is amplified and the pump is depleted due to the SRP process. Our homemade Raman amplifier is equipped with 4 fans installed parallel to the path of the laser beams. These fans continuously circulate the CH_4 gas to avoid beam instabilities due to thermal lensing. Figure 2.27 shows the internal part of the Raman amplifier, only two stages among four are shown here, and the fans are green colored. The laser beams pass through the Raman amplifier just above the fans, and to better show the shape of the fans two support rods are removed in the “Stage 1” where “Fan 1” is installed. The fans are rotated by an electric motor which is installed outside the Raman amplifier. A magnetic motion feedthrough transmits the motor torque to the fans and a typical rotation speed is 700 rotations per minute.

We measure the Raman gain curve of our Raman amplifier by recording the Stokes beam energy at the output of the Raman amplifier as a function of the seed laser frequency. With increasing the methane pressure, the maximum of the gain curve shifts towards higher frequency due to elastic and inelastic molecular collisions⁸⁸. Figure 2.28 shows the gain curves recorded using a pump beam energy of 500 mJ/pulse, for different pressures. The shift of the gain curve maximum as a function of the pressure is shown in Fig. 2.29, where a linear regression is

performed on the experimental points and the resulting slope is $0.016 \pm 0.001 \text{ cm}^{-1}/\text{bar}$.

Since the rotational temperature of CH_4 molecules in the molecular beam is $\sim 10 \text{ K}$, only the lowest rotational states $J=0, 1, \text{ and } 2$ are populated (see Chapter 4 for more details). In these conditions only the Q(0), Q(1), and Q(2) transitions of the ν_1 vibrational band can be excited. We use a CH_4 pressure of 9 bar in the Raman amplifier to tune the maximum of the gain profile to overlap the Q(0), Q(1), and Q(2) CH_4 transitions in the molecular beam.

When we pump the Raman amplifier with 700 mJ/pulse at 532 nm, the pump and Stokes beams entering the UHV chamber have energies of 250 mJ/pulse each. Under these conditions, we observe a formation of an opaque spot on the internal face of the input window of the Raman amplifier. The opaque spot is probably formed by the laser decomposed methane molecules in proximity of the window. The opaque spot starts to be visible after ~ 50 hours of operation. We observe a substantial degradation of the laser beam profiles when the opaque spot is formed. The use of different window materials and coatings as BK7-glass, fused silica and quartz AR and non-AR coated does not prevent the spot formation. To avoid the degradation of the laser beam profiles, we change the input window when the spot starts to be visible by eyes.

After the Raman amplifier, the pump and Stokes beams are focused to a line parallel to the molecular beam by a cylindrical lens ($f=300 \text{ mm}$).

The frequency of the dye laser is monitored using a wavemeter (Burleigh, WA-4500) ensuring that the laser beam frequency does not drift during the experiment.

State-resolved reactivity of CD_2H_2 on $\text{Ni}(100)$

3.1 Introduction

Our experiments are designed to explore the effects of different vibrations on a gas-surface reaction. In the case of methane chemisorption on nickel, we want to investigate if there are vibrational states of methane which are more efficient than others in promoting the reaction (vibrational state specificity). For reactions that occur completely in the gas-phase, vibrational state specific reactivity has been observed for several reactions²⁶⁻³¹. For example, Bechtel *et al.*²⁸ have observed that the product state distribution for the reaction of CD_2H_2 with chlorine depends on the initially prepared reactant vibrational state. They have excited the CD_2H_2 to two overtone C-H stretch states which are nearly iso-energetic, but have different nuclear motions: the $|20\rangle^-$ and the $|11\rangle$ state. While in the $|20\rangle^-$ state two quanta of vibrational stretch energy are localized in a single C-H bond, in the $|11\rangle$ state each of the two C-H bonds contains one quantum of vibrational energy. They have found that the $|20\rangle^-$ and $|11\rangle$ states produce CD_2H methyl fragments in completely different vibrational states. The reaction of chlorine with methane excited to the $|20\rangle^-$ state yields methyl radical products in their ground state, whereas the excitation of the $|11\rangle$ state yields methyl radical products that are C-H stretch excited. These results have shown that vibrational energy put into specific modes of methane is not redistributed internally by the interaction during the reactive encounter, but instead contributes in a bond-specific way to promoting the chemical reaction.

For gas-surface reactions, the question of vibrational state specific reactivity is still open. In chapter 1, we have shown that the theoretical treatments of methane chemisorption include both dynamical and statistical approaches^{18,23,24,89,90}. Some dynamical calculations suggest that the reactivity of vibrationally excited methane on nickel should depend on the precise nature of the vibrational state^{23,24}, whereas statistical models predict the complete absence of such effects^{89,90}. At the time of these experiments, there was no reported experimental evidence for mode specificity for methane chemisorption, the results published so far are insufficient to exclude either approach.

In analogy with the experiment of Bechtel *et al.*, in order to test for vibrational state specific behavior in gas-surface reactions, we perform state-resolved chemisorption measurements of CD₂H₂ on Ni(100) with the molecules prepared in the $|20\rangle^-$ and $|11\rangle$ states. In this chapter, we present and discuss the results of these experiments.

3.2 CD₂H₂ laser-off sticking coefficient

As explained in section 2.1, we determine the sticking coefficient of CD₂H₂ without laser excitation ($S_0^{laser-off}$) by exposing the Ni(100) sample to a molecular beam dose. After the deposition, the carbon product is quantified via AES and the sticking coefficient is obtained by eq. 2.1. During the deposition, the crystal surface is held at 473 K to promote methane dehydrogenation and hydrogen recombinative desorption.

We produce CD₂H₂ molecules at different kinetic energies by seeding CD₂H₂ in H₂ carrier gas with different seed ratios and nozzle temperatures. The kinetic energy of the CD₂H₂ molecules is determined via TOF measurements as explained in section 2.3.2. Table 3.1 shows the kinetic energies for different mixtures and nozzle temperatures. The CD₂H₂ used in our experiments was obtained from Cambridge Isotope Laboratories and has an isotope purity of 98% and chemical purity of only around 96%. Using our QMS, we detect some impurities such as heavier hydrocarbons and oxygen in the CD₂H₂/H₂ mixture. Due to the high reactivities of heavier hydrocarbons, these impurities can perturb and invalidate the laser-off sticking coefficient measurements. In order to remove these contaminations, we installed a catalytic trap (Supelco, SuperpureTM O, 2-2450-U) in the gas line. We test the efficacy of the trap by observing that the mass peaks associated with heavier hydrocarbons and oxygen disappear after its installation. We additionally verify that the catalytic trap is able to completely remove the contaminations by installing a second trap in series with respect to the first one. The sticking coefficient ob-

CD ₂ H ₂ /H ₂ Seed ratio(%)	T_{nozzle} (K)	Kinetic energy (kJ/mol)
18	423	41 ± 1
10	423	57 ± 1
1.8	373	80 ± 2
1.8	423	93 ± 2
1.8	473	105 ± 2

Table 3.1: Mixtures used for the CD_2H_2 sticking coefficient measurements. The kinetic energies at the respective nozzle temperatures (T_{nozzle}) are reported.

tained with two oxygen traps installed in series is closed to that determined with one oxygen filter meaning that the quantity of carbon deposited on the surface is principally due to the chemisorption of the CD_2H_2 molecules.

During the deposition, the flux of CD_2H_2 molecules is determined by monitoring the QMS signal at 17 amu. We do not use the QMS signal at 18 amu because of the high background due to the presence of H_2O in the chamber. To calibrate the QMS signal in term of molecules/s, we use our calibrated leaks as explained in section 2.3.2. The two leaks are calibrated for CH_4 and not for CD_2H_2 . However, we know that the gas flow can be written as⁹¹:

$$\begin{aligned} \text{Viscous flow: } Q_{vis} &\propto \frac{1}{\eta} P_0^2, \\ \text{Molecular flow: } Q_{mol} &\propto \frac{1}{\sqrt{m}} P_0, \end{aligned} \quad (3.1)$$

where P_0 is the pressure behind the calibrated leak. For our calibrated leaks, the flow is neither viscous nor molecular; in section 2.3.2 we show that $Q = K_1 P_0 + K_2 P_0^2$, that is we have linear and quadratic dependence in P_0 of the flow.

For smooth rigid elastic spherical molecules the viscosity can be written as⁹¹

$$\eta = \frac{5}{16\delta^2} \left(\frac{kmT}{\pi} \right)^{1/2}, \quad (3.2)$$

where δ is the molecular diameter, k the Boltzmann constant, m is the molecular mass, and T the gas temperature. From this equation, we can see that for two gases having approximately equal values of δ , the viscosities should vary as the ratio of the square roots of the molecular masses. Hence viscous and molecular flows are proportional to $1/\sqrt{m}$. Based on this, we modify the

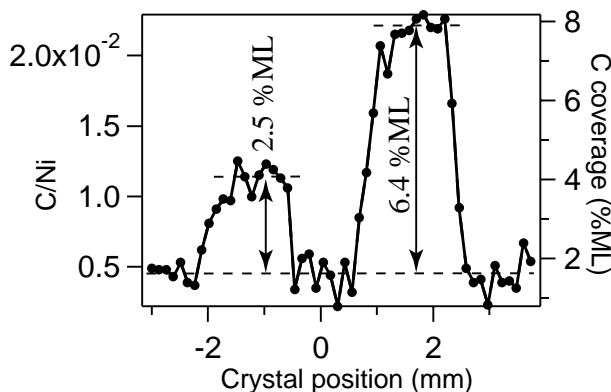


Figure 3.1: Carbon spots on $\text{Ni}(100)$ resulting from the depositions of 1.8% CD_2/H_2 with nozzle temperature of 473 K (kinetic energy of 105 ± 2 kJ/mol). The smaller peak is obtained by exposing the surface to the beam for 30 s, and the higher peak for 60 s.

QMS signal calibration for CD_2H_2 using our leaks by decreasing of $\sqrt{m_2/m_1} = \sqrt{16/18} = 94\%$ the flow values reported in the calibration curves shown in section 2.3.2.

After the deposition, the number of chemisorbed methane molecules is determined by quantifying the carbon coverage across the surface via Auger electron spectroscopy (see section 2.4.1). Figure 3.1 shows two carbon spots on $\text{Ni}(100)$ obtained by depositing 1.8% CD_2/H_2 with a nozzle temperature of 473 K (kinetic energy of 105 ± 2 kJ/mol) for 30 s (left-hand peak) and 60 s (right-hand peak). In order to have a more intense molecular beam, the beam pulses are transmitted through the 25 mm wide slit of our chopper wheel (opening time 333 μs). The carbon coverage is determined by subtracting a baseline (lower dashed line in figure) from the averaged coverage across the center of the peak. We determine the average intensity using the 8 most intense data points. From the $\text{Ni}(100)$ surface density ($1.6 \cdot 10^{15}$ atoms/ cm^2), we calculate a carbon density of $4 \cdot 10^{13}$ atoms/ cm^2 for the smaller peak and $1 \cdot 10^{14}$ atoms/ cm^2 for the higher peak. The molecular beam fluxes measured during the depositions are $2.6 \cdot 10^{14}$ and $3.2 \cdot 10^{14}$ molecules/(cm^2 s) for the small and large carbon peak respectively. The resulting sticking coefficients are $(5.1 \pm 0.3) \cdot 10^{-3}$ and $(5.3 \pm 0.3) \cdot 10^{-3}$ as determined from the small and large carbon peak respectively. The errors reported here are determined considering the uncertainties of the molecular beam intensities (systematic error). We determine the statistical error by repeating the measurement at the same kinetic energy and the total error is calculated as the square-root of the quadrature sum of the statistical and systematic errors.

Table 3.2 reports the laser-off sticking coefficients ($S_0^{\text{laser-off}}$) obtained for different kinetic energies together with the averaged C coverage, dose time, and beam intensity.

Kinetic energy (kJ/mol)	Beam flux (molecules/(cm ² ·s))	Dose time (s)	C coverage %ML	$S_0^{laser-off}$ (-)
41 ± 1	8.2 · 10 ¹⁵ *	6600	1.8	(5.3 ± 1.5) · 10 ⁻⁷
57 ± 1	1.4 · 10 ¹⁶ *	600	8.7	(1.6 ± 0.8) · 10 ⁻⁵
80 ± 2	1.7 · 10 ¹⁴ *	420	1.9	(4.4 ± 1) · 10 ⁻⁴
93 ± 2	2.2 · 10 ¹³	900	2.6	(2.1 ± 0.4) · 10 ⁻³
105 ± 2	2.4 · 10 ¹³	720	6.5	(6 ± 1.5) · 10 ⁻³

Table 3.2: Laser-off sticking coefficient ($S_0^{laser-off}$) for different kinetic energies. The reported beam flux, dose time and carbon coverage are quantities averaged over several experiments. The error bars include the contributions of the statistical (95% of confidence limit) and systematic errors. The molecular beam flux values marked with an * are obtained by transmitting the beam pulses through the wide slit of the chopper wheel.

C_{2v}	E	C_2	$\sigma(xy)$	$\sigma(xz)$	
A_1	1	1	1	1	T_x
A_2	1	1	-1	-1	R_x
B_1	1	-1	1	-1	T_y, R_z
B_2	1	-1	-1	1	T_z, R_y

Table 3.3: Character table of the point group C_{2v} .

Our laser-off measurements represent an upper limit for the reactivity of CD₂H₂ in the vibrational ground state because our analysis neglects a small fraction of thermally vibrationally excited CD₂H₂ in the molecular beam.

3.3 The CD₂H₂ molecule

CD₂H₂ is the only asymmetric rotor of the methane deuterated group. The CD₂H₂ molecule belongs to the symmetry point group C_{2v} for which the character table is shown in Table 3.3. As shown in Fig. 3.2, CD₂H₂ has one C_2 axis and two mutually perpendicular symmetry planes $\sigma(xy)$ and $\sigma(xz)$. The planes $\sigma(xy)$ and $\sigma(xz)$ contain the hydrogen nuclei and the deuterium nuclei respectively. The symmetry axis C_2 coincides with the x axis. If we assume that the three moments of inertia calculated with respect to the three principal axis are $I_a < I_b < I_c$, then I_b is collinear to C_2 axis, I_a is parallel to the z axis and I_c is parallel to the y axis.

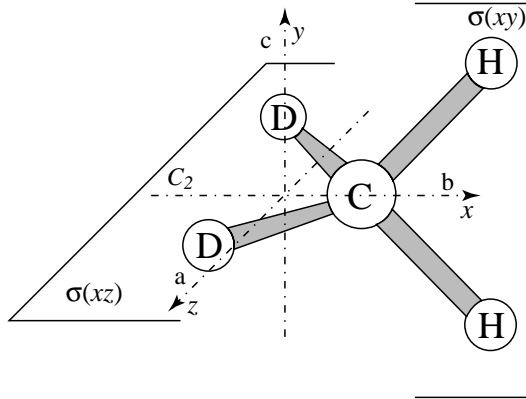


Figure 3.2: Molecular geometry of the CD₂H₂ molecule. The momentum of inertia I_B is collinear to the C_2 axis. The origin of the internal coordinate system sits on the center of mass of the molecule.

3.3.1 Rotational energy levels of an asymmetric-top rotor

Since the CD₂H₂ has three different moments of inertia, it is an asymmetric-top rotor and its rotational Hamiltonian can be written as

$$\hat{H}_{rot} = \frac{\hat{L}_a^2}{2I_a} + \frac{\hat{L}_b^2}{2I_b} + \frac{\hat{L}_c^2}{2I_c}, \quad (3.3)$$

where \hat{L}_i is the angular momentum about the i -th principal axis.

Unlike in the case of symmetric rotors, there are no analytic expressions for the eigenfunctions and eigenvalues of this Hamiltonian. Since the operators \hat{L}_a , does not commute with the Hamiltonian, the quantum number K associated with the eigenvalue of the angular momentum operator along the molecular z -axis ($\hat{L}_z = \hat{L}_a$) is not a good quantum number. However, the square of the angular momentum operator \hat{L}^2 and its projection along the Z component of the laboratory frame \hat{L}_Z both commute with \hat{L}_a^2 , \hat{L}_b^2 and \hat{L}_c^2 . Consequently, the quantum number J associated with the module of the angular momentum operator and the quantum number M associated with the operator \hat{L}_Z are still good quantum numbers. Based on this, each eigenfunction of the rotational Hamiltonian is a linear combination of $2J + 1$ Wigner rotational wave functions⁹² with the same J and M . The rotational eigenfunctions are obtained by performing the diagonalization of the matrices $\langle J, M, K_i | H_{rot} | J, M, K_j \rangle$.

It is convenient to introduce the rotational constants corresponding to each inertial axis as:

$$A = \frac{h}{8\pi^2 I_a c} \quad (3.4)$$

$$B = \frac{h}{8\pi^2 I_b c} \quad (3.5)$$

$$C = \frac{h}{8\pi^2 I_c c}, \quad (3.6)$$

where c is the speed of light in cm/s, and the three constants are expressed in cm⁻¹.

For each asymmetric rotor, an asymmetry parameter can be defined as⁹³:

$$\kappa = (2B - A - C)/(A - C). \quad (3.7)$$

For a prolate symmetric rotor $B = C$ and $\kappa = -1$ and for an oblate symmetric rotor $A = B$ and $\kappa = +1$.

The eigenfunctions of an asymmetric rotor can be labelled with the $J_{K_a K_c}$ notation, where J is the quantum number of the total angular momentum. The meaning of the K_a and K_c indexes can be understood if we consider Fig.3.3, where we show how the rotational levels of an asymmetric-top rotor correlate to that of oblate and prolate symmetric-top rotors. To obtain the graph in Fig.3.3, we calculate the rotational energy levels of an hypothetical asymmetric rotor ($A = 2$, $C = 1$) as a function of the rotational constant B which is varied from A (prolate, $\kappa = 1$) to C (oblate, $\kappa = -1$). It is clear that, if we have an asymmetric-top energy level labelled as $J_{K_a K_c}$, then this level correlates to the prolate symmetric-top level J, K_c when B increases. On the other hand, if B decreases, then the asymmetric-top energy level correlates with that of the oblate level J, K_a .

The CD₂H₂ is a highly asymmetric top molecule with large rotational constants⁹⁴ ($A = 4.30$, $B = 3.51$ and $C = 3.05$ cm⁻¹) and an asymmetry parameter of⁹⁵ $\kappa = -0.27$.

By knowing the rotational constants of the molecule, we can calculate the rotational energy levels by⁹³

$$F(J_{K_a K_c}) = \frac{1}{2}(A + C)J(J + 1) + \frac{1}{2}(A - C)E_{J_{K_a K_c}}(\kappa), \quad (3.8)$$

where $E_{J_{K_a K_c}}(\kappa)$ is a function of the asymmetry parameter κ and it changes for different rotational levels. A list of the $E_{J_{K_a K_c}}(\kappa)$ functions is reported for J up to 3 in table A.1 in Appendix A.

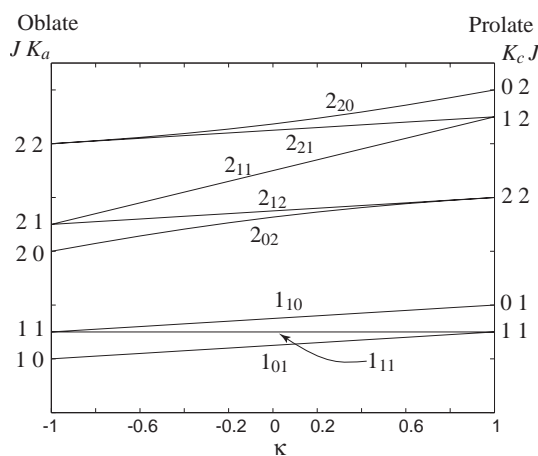


Figure 3.3: Correlation diagram illustrating the energy-level pattern for asymmetric-top rotors. We consider $A = 2C$ and we calculate the energy levels as a function of B that varies from A to C .

3.3.2 Vibrational transitions of CD₂H₂

The CD₂H₂ molecule has $3 \cdot 5 - 6 = 9$ non-degenerate vibrational normal modes. Duncan *et al.*⁹⁴ report the vibrational assignments of the dideutero methane by studying infrared spectra up to 17000 cm^{-1} . Table 3.4 lists the normal modes with their frequencies, symmetries and the vibration states to which they are coupled via Fermi resonance⁹⁴.

For a vibrational transition to be electric dipole allowed, there must be a change of dipole moment during the transition. Translated in term of point group formalism, the direct product between the representations of the wave functions and the representation of one of the dipole moment components must contain a totally symmetric species⁹³:

$$\Gamma(\psi'_\nu) \otimes \Gamma(T_x) \otimes \Gamma(\psi''_\nu) \supset A \quad (3.9)$$

$$\text{and/or } \Gamma(\psi'_\nu) \otimes \Gamma(T_y) \otimes \Gamma(\psi''_\nu) \supset A \quad (3.10)$$

$$\text{and/or } \Gamma(\psi'_\nu) \otimes \Gamma(T_z) \otimes \Gamma(\psi''_\nu) \supset A, \quad (3.11)$$

where ψ''_ν and ψ'_ν are the wave functions of the lower and upper state respectively.

Since CD₂H₂ belongs to the C_{2v} point group, the dipole moment change must be along one of the principal axes of the molecule and we have that, for transitions from the ground state, the representation of the wave function of the excited state ψ'_ν must be equal to one of the

Mode	Vibrational mode	Energy (cm ⁻¹)	Fermi resonance	Symmetry	Band type
ν_1	CH ₂ sym. stretch	2975.49	$2\nu_3$	A_1	b
ν_2	CD ₂ sym. stretch	2146.4/2203.22	$2\nu_7$	A_1	b
ν_3	CH ₂ scissor	1435.13		A_1	b
ν_4	CD ₂ scissor	1033.06		A_1	b
ν_5	Torsion	1331.28		A_2	Inactive
ν_6	CH ₂ antisym. stretch	3012.26		B_1	c
ν_7	CH ₂ rock	1091.22		B_1	c
ν_8	CD ₂ antisym. stretch	2234.7/2285.98	$\nu_4 + \nu_9$	B_2	a
ν_9	CH ₂ wag	2234.7/2285.98		B_2	a

Table 3.4: Energy levels of the vibrational modes of CD₂H₂ molecule. The "Band type" column lists the components of the dipole moment along the a-, b- and c-axis that changes in the transition from the ground state. These values are from the work of Duncan *et al.*⁹⁴.

representations of the dipole moment components⁹³:

$$\Gamma(\psi'_\nu) = \Gamma(T_a) \text{ or } \Gamma(T_b) \text{ or } \Gamma(T_c), \quad (3.12)$$

where $T_a \equiv T_z$, $T_b \equiv T_x$, and $T_c \equiv T_y$ as shown in Fig. 3.2. If we take in consideration the ν_3 mode of the CD₂H₂ molecule (see table 3.4), then its representation ($\Gamma(\nu_3)$) is A_1 and only the direct product with the component of the dipole moment along the b-axis gives a totally symmetric species:

$$\Gamma(\nu_3) \otimes \Gamma(T_b) = A_1 \otimes A_1 = A_1. \quad (3.13)$$

For this reason, the transition from the ground state to the ν_3 level is called "b-type". In the last column of table 3.4, we report the transition type associated at each normal mode.

The rotational selection rules for the rovibrational transitions are listed in Table 3.5. The rotational level are labelled as "oo", "eo", "oe" and "ee", where the first and second letter indicate the parity or the oddness of the quantum numbers K_a and K_c respectively.

Direction of dipole moment	Selection rule	
a-Type	ee↔eo	} and ΔJ = 0, ±1
	oe↔oo	
b-Type	ee↔oo	
	oe↔eo	
c-Type	ee↔oe	
	eo↔oo	

Table 3.5: Rotational selection rules of asymmetric-top rotors for rovibrational transitions of a-, b- and c-type. The rotational levels are labelled as “eo”, “oe”, “ee”, or “oo”, where the first and second letter indicates the parity or the oddness of the quantum numbers K_a and K_c respectively. The double arrow \leftrightarrow implies that the transition is allowed whichever of the two states involved is the upper state⁹³.

For an a-type band, we have the following selection rules:

$$\begin{aligned}\Delta K_a &= 0, \pm 2, \pm 4 \dots \\ \Delta K_c &= \pm 1, \pm 3, \pm 5 \dots \\ \text{and } \Delta J &= 0, \pm 1.\end{aligned}$$

Usually the transitions obeying the symmetric rotor selection rules $\Delta K_a = 0$ (prolate limit, parallel band) and $\Delta K_c = \pm 1$ (oblate limit, perpendicular band) are the most important and account for the bulk of the intensity.

For a b-type band, we have the following selection rules:

$$\begin{aligned}\Delta K_a &= \pm 1, \pm 3, \pm 5 \dots \\ \Delta K_c &= \pm 1, \pm 3, \pm 5 \dots \\ \text{and } \Delta J &= 0, \pm 1,\end{aligned}$$

the transitions with $\Delta K_a = \pm 1$ and $\Delta K_c = \pm 1$ are the most intense.

$J''_{K_a K_c} \rightarrow J'_{K_a K_c}$	Notation	Energy (cm ⁻¹)
0 ₀₀ → 1 ₁₁	^b R ₀₀ (0)	6006.41
1 ₀₁ → 1 ₁₀	^b Q ₀₁ (1)	6000.29
1 ₁₀ → 1 ₀₁	^b Q ₁₀ (1)	5997.81

Table 3.6: Transitions of the 2ν₆ band. $J''_{K_a K_c}$ corresponds to the rotational level of the vibrational ground state. $J'_{K_a K_c}$ is the rotational level of the vibrational excited state. The second column lists the spectroscopic notation for the corresponding transition. The letter in the superscript is the transition type (*a*, *b*, or *c*). The numbers in the subscript are the K_a and K_c values of the starting level and the number in the brackets is the J value of the starting level.

Finally, for a c-type band, we have:

$$\Delta K_c = 0, \pm 2, \pm 4 \dots$$

$$\Delta K_a = \pm 1, \pm 3, \pm 5 \dots$$

$$\text{and } \Delta J = 0, \pm 1,$$

and the transitions with $\Delta K_a = \pm 1$ and $\Delta K_c = 0$ are the most intense.

The 2ν₆ band

The transitions of CD₂H₂ in the region 5880-6136 cm⁻¹ were assigned to the 2ν₆ band by Dowling *et al.*⁹⁶ in 1969. 2ν₆ is a b-type band and the rotational constants of the excited state are $A' = 4.247$, $B' = 3.462$ and $C' = 3.025$ cm⁻¹ as determined by Dowling *et al.* The band center is located at 5999.126 cm⁻¹. Due to the rotationally cold molecules (~ 10 K) produced in the supersonic expansion, only transitions that involve rotational states with $J = 0$ and 1 are recorded using our cavity ring-down spectroscopy (CRD) setup. For such low values of J , the centrifugal distortion constants produce a shift in energy in the order of 10⁻⁴ cm⁻¹. Since our IR beam has a bandwidth of 0.02 cm⁻¹, we neglect the centrifugal distortion terms in the calculation of the rovibrational levels. Using the free software SpecView (by Vadim Stakhursky, www.chemistry.ohio-state.edu/~vstakhur/), we calculate the energies of the rovibrational transitions of the 2ν₆ band. Table 3.6 shows the transitions and their calculated energies. We record the CRD spectra of the three transitions and the results are shown in Fig 3.4. The measured transition frequencies are slightly shifted toward the red (0.05 cm⁻¹) with respect to

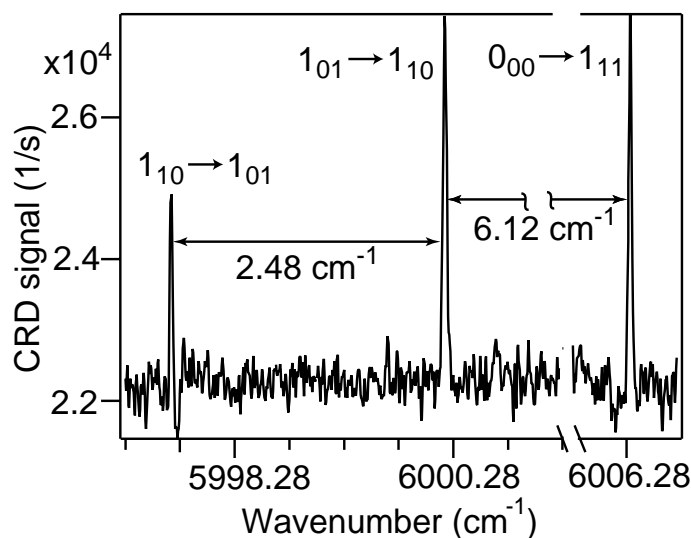


Figure 3.4: CRD spectra of the $0_{00} \rightarrow 1_{11}$, $1_{01} \rightarrow 1_{10}$ and $1_{10} \rightarrow 1_{01}$ transitions of the CD₂H₂ $2\nu_6$ band. These spectra are recorded by expanding a 10% CD₂H₂/H₂ mixture.

the calculated frequencies. However, the energy differences between the transitions are in good agreement with the energy differences obtained using the values in Table 3.6.

The $\nu_1 + \nu_6$ band

The transitions between the vibrational ground states and the $\nu_1 + \nu_6$ states represent a c-type band. The $\nu_1 + \nu_6$ has the band origin at 5879 cm^{-1} and it has an anharmonic resonance with the lower frequency band $\nu_6 + 2\nu_3$ (5827 cm^{-1})⁹⁴.

The rotational constants of the $\nu_1 + \nu_6$ band are determined by knowing that the vibrational dependence of A , B and C is given by⁹³

$$A_\nu = A_e - \sum_i \alpha_i^A \left(\nu_i + \frac{1}{2} \right) \quad (3.14)$$

$$B_\nu = B_e - \sum_i \alpha_i^B \left(\nu_i + \frac{1}{2} \right) \quad (3.15)$$

$$C_\nu = C_e - \sum_i \alpha_i^C \left(\nu_i + \frac{1}{2} \right), \quad (3.16)$$

where the A_e , B_e and C_e are the rotational constant values corresponding to the molecule in the classical equilibrium configuration, that is at the bottom of the potential energy surface. The

$J''_{K_a K_c} \rightarrow J'_{K_a K_c}$	Notation	Energy (cm^{-1})
$0_{00} \rightarrow 1_{10}$	${}^cR_{00}(0)$	5886.72
$1_{01} \rightarrow 1_{11}$	${}^cQ_{01}(1)$	5879.71
$1_{11} \rightarrow 1_{01}$	${}^cQ_{11}(1)$	5878.15

Table 3.7: Transitions of the $\nu_1 + \nu_6$ band. $J''_{K_a K_c}$ corresponds to the rotational level of the vibrational ground state. $J'_{K_a K_c}$ is the rotational level of the vibrational excited state. The second column lists the spectroscopic notation for the corresponding transition. The letter in the superscript is the transition type (a, b , or c). The numbers in the subscript are the K_a and K_c values of the starting level and the number in the brackets is the J value of the starting level.

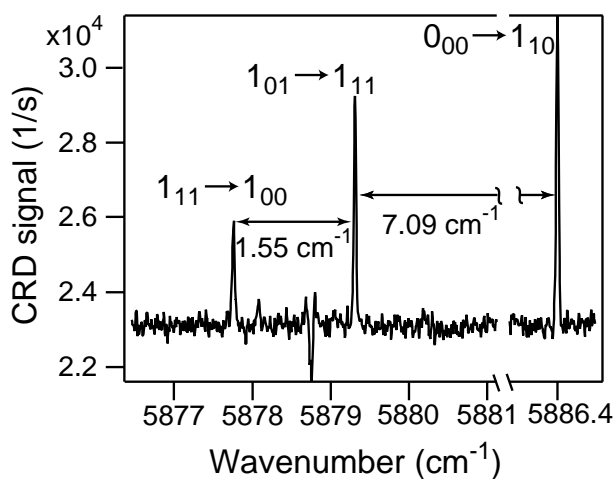


Figure 3.5: CRD spectra of the $0_{00} \rightarrow 1_{10}$, $1_{01} \rightarrow 1_{11}$ and $1_{11} \rightarrow 1_{01}$ transitions of the CD_2H_2 $\nu_1 + \nu_6$ band. These spectra are recorded by expanding a 18% CD_2H_2/H_2 mixture.

summation is over the normal modes of the molecule (9 normal modes for the CD_2H_2 molecule) and ν_i is the number of quanta contained in the vibrational mode i . We use the vibrational constants of the ground state⁹⁶, ν_6 and ν_1 states⁹⁷ to determine the rotational constant of the $\nu_1 + \nu_6$ state. Using eq. 3.14, 3.15 and 3.16 we find that A , B and C for the excited state $\nu_1 + \nu_6$ are 4.244, 3.472 and 3.03 cm^{-1} respectively. The $0_{00} \rightarrow 1_{10}$, $1_{01} \rightarrow 1_{11}$ and $1_{11} \rightarrow 1_{01}$ transitions calculated by the SpecView software are reported in Table 3.7. The CRD spectrum of the three transitions is shown in Fig.3.5. As in the case of the $2\nu_6$ band, the energy differences between the measured transitions are in good agreement with the energy differences obtained by the calculated transitions.

From normal modes to local modes

The concept of the normal modes plays an important part in molecular vibrations. If we consider a molecule with N nuclei that oscillate around their equilibrium positions, normal mode theory predicts that, in the harmonic approximation, there are $3N - 6$ linear combinations of the mass weighted cartesian coordinates that transform the vibrational Hamiltonian into $3N - 6$ uncoupled harmonic oscillator Hamiltonians. The new set of coordinates found by these linear combinations is called the normal coordinates. The vibrational modes that corresponds to the $3N-6$ normal coordinates are the normal modes. Since the Hamiltonian is decomposed into $3N-6$ terms, the total eigenstate can be written as a product of eigenstates which are the solutions of the $3N-6$ harmonic oscillators (normal mode basis set). However, in a real molecule, the interactions between pairs of nuclei are not harmonic and the anharmonicity is more pronounced when the stretching vibrations become highly excited. Therefore, for highly excited vibrational states, the normal mode basis set is not suitable anymore for describing the molecular vibrations.

When more than one quantum of vibrational energy is excited in the stretching of a C-H bond, the anharmonicity effects become important and an alternative way to treat the molecular vibrations is to use a local mode model (LM). For CD₂H₂, the simplest LM model treats the two pairs of C-H and C-D bonds as independent anharmonic (Morse) diatomic oscillators, harmonically coupled to each other. The vibrational states used as basis set are defined in terms of the number of quanta in each C-H and C-D bond, e.g. $|H_1, H_2, D_1, D_2\rangle$, where H_1 and H_2 are the number of quanta in each C-H bond and D_1, D_2 are the number of quanta in the C-D oscillators. We consider only the local mode states where the C-H bond are excited, then we can write the local mode states as $|H_1, H_2\rangle = |H_1, H_2, 0, 0\rangle$. We are interested in the local mode states $|2, 0\rangle$ and $|1, 1\rangle$. If the two C-H bonds of CD₂H₂ were uncoupled, then the two states $|2, 0\rangle$ and $|0, 2\rangle$ would have the same eigenvalue. However, the coupling between these two bonds removes the degeneracy and generates two eigenstates $|2, 0\rangle^\pm$ with two different energies. The $|2, 0\rangle^+$ and $|2, 0\rangle^-$ are the symmetric and antisymmetric combinations of the $|2, 0\rangle$ and $|0, 2\rangle$ states. The $|2, 0\rangle^+$ has a lower energy than the $|2, 0\rangle^-$.⁹⁸

The true eigenstates for a vibrating molecule should be understood as something between the limiting situation represented by either models, as determined by the competition between anharmonicity (which favours the local mode picture) and kinetic and potential coupling between the local bond oscillators (which favours the normal mode picture). This picture of the true eigenstates as a compromise between the two limiting models, depending on the relative

magnitudes of anharmonicity and interbond coupling, can be illustrated by correlation diagrams between normal mode states and local mode states⁹⁹. For CD₂H₂, the $|2, 0\rangle^+$ local mode state correlates to the first overtone of the CH₂ symmetric stretch $2\nu_1$ (band origin = 5873 cm⁻¹), the $|2, 0\rangle^-$ correlates to the combination band $\nu_1 + \nu_6$ (band origin = 5879 cm⁻¹), and the $|1, 1\rangle$ state corresponds to the first overtone of the CH₂ antisymmetric stretch $2\nu_6$ (band origin = 5999.1 cm⁻¹).⁹⁴

3.4 State-resolved sticking coefficients

We are able to determine state-resolved sticking coefficients by performing deposition experiments with and without laser excitation under otherwise identical conditions. From the observed change in the reactivity upon laser excitation, we calculate the sticking coefficient of the excited state S_0^{exc} using the known fraction of excited molecules in the beam f_{exc} as well as the ground state sticking coefficient of $S_0^{\nu=0}$ according to²¹:

$$S_0^{exc} = \frac{S_0^{laser-on} - S_0^{laser-off}}{f_{exc}} + S_0^{\nu=0}, \quad (3.17)$$

where $S_0^{laser-on}$ is the average initial sticking coefficient with laser excitation and $S_0^{laser-off}$ is the corresponding quantity without laser excitation. The method is applicable as long as there is an observable change in the averaged reactivity ($S_0^{laser-on} - S_0^{laser-off}$) upon laser excitation of the molecular beam.

For the determination of the sticking coefficient of the laser excited molecules, the fraction of excited molecules f_{exc} must be known. f_{exc} can be expressed as the product⁵⁴

$$f_{exc} = f_{overlap} \cdot f_{exc}^{laser}, \quad (3.18)$$

where $f_{overlap}$ is the fraction of the molecular beam pulse that is illuminated by the line focus of the laser beam, and f_{exc}^{laser} is the fractional number of irradiated molecules that are promoted to the upper state.

The fraction $f_{overlap}$ is obtained by dividing the length of the laser line focus by the length of the molecular beam pulses. The length of the laser spot at the line focus is defined by placing a beam shaping aperture into the expanded laser before the cylindrical lens. We characterize the intensity distribution seen by the molecular beam using a knife edge mounted on a translation

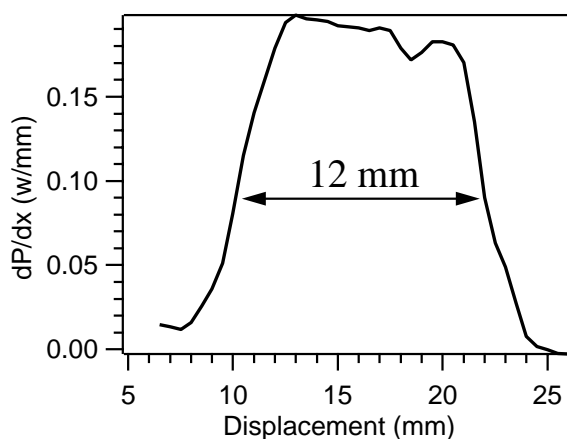


Figure 3.6: IR laser intensity distribution along the line focus of a 160 cm cylindrical lens measured using a knife edge mounted on a translational stage and a power meter. A 12 mm wide beam shaping aperture is placed into the expanded beam before the cylindrical lens (see appendix B).

stage and a power meter as a simple beam profiler (see Fig. 3.6).

The length of the molecular-beam pulse is calculated from the molecular-beam velocity and the $26.6 \mu\text{s}$ opening time of the narrow slit in the chopper wheel (see section 2.3.2).

To determine f_{exc}^{laser} , we decompose it further into three terms:

$$f_{exc}^{laser} = f_{pop} \cdot f_{exc,max}^{laser} \cdot f_{saturation}, \quad (3.19)$$

where f_{pop} is the fractional population of the lower state of the target transition, $f_{exc,max}^{laser}$ is the maximum fractional population that can be transferred to the upper state, as determined by the number of sub-levels that are connected by the laser field, and $f_{saturation}$ is the degree of saturation of the optical transition, ranging from zero to unity. The first term, f_{pop} is calculated from the rotational temperature of the beam determined by cavity ring-down spectroscopy as described in section 3.4.1. The second term, $f_{exc,max}^{laser}$, is calculated from the degeneracy of the states involved in the optical transition, taking into account the selection rules for our linearly polarized excitation laser (section 3.4.2). We determine $f_{saturation}$ for the first overtone of the antisymmetric stretch of CH_4 ($2\nu_3$) from the fluence dependence of the laser-on carbon coverage in previous work⁵⁴. By comparing the transition strength of CH_4 $2\nu_3$ band with those of CD_2H_2 $\nu_1 + \nu_6$ and $2\nu_6$, we calculate the degree of saturation for the two transitions of the CD_2H_2 molecules. More details on these calculations will be given in section 3.4.2.

3.4.1 CD₂H₂ rotational temperature

We determine the rotational temperature of the supersonically expanded CD₂H₂ using the intensity of the transitions acquired with our CRD spectroscopy setup. We record CRD spectra at a sufficiently large distance from the nozzle opening ($x/d > 10$), where the rotational cooling is nearly complete and the observed rotational temperature should give a close upper limit for the rotational temperatures of the molecular beam.

Nuclear spin statistics

In order to correctly identify the statistical weights involved in the absorption spectra of the CD₂H₂ molecule, we need to consider the influence of the nuclear spins of the two pairs of hydrogen and deuterium atoms. In the limit where the electronic, vibrational, and rotational degrees of freedom are separable, a total molecular wave function of CD₂H₂ can be written as $\psi = \psi_e \psi_v \psi_r \psi_{ns}$, where ψ_e , ψ_v and ψ_r are the electronic, vibrational and rotational wave functions and ψ_{ns} is the nuclear spin wave function. From the Pauli principle, the exchange of the two H atoms (fermions) results in a change of sign of the total wave function ψ , which is said to be antisymmetric for the H nuclei exchange. On the other hand, if the deuterium nuclei (bosons) are exchanged, then ψ needs to be symmetric.

We consider now that the CD₂H₂ molecule is in the electronic and vibrational ground state, that is the representations of these two wave functions are totally symmetric: $\Gamma(\psi_e) = A_1$ and $\Gamma(\psi_v) = A_1$. Therefore, we need to consider only the behavior of $\psi_r \psi_{ns}$. As stated earlier in this chapter, the CD₂H₂ point group symmetry is C_{2v} , the unique C_2 axis is along the principal axis b. The rotational group of this molecule is the C_2 group and the only rotation that permutes the nuclei leaving the molecule unchanged is the C_2 rotation along the b-axis. By performing this operation, we permute at the same time the pairs of deuterium and hydrogen nuclei and the total wave function must be antisymmetric with respect to the C_2 . We seek the number of combinations of $\psi_r \psi_{ns}$ that satisfy the required symmetry.

The nuclear spin functions are $3 \cdot 3 \cdot 2 \cdot 2 = 36$ -fold degenerate. In order to obtain the wave functions with the proper symmetry with respect to C_2 , it is necessary to form linear combinations of these degenerate nuclear spin functions. With these 36 nuclear spin states we can create 21 symmetric and 15 antisymmetric combinations with respect to the rotation C_2 ⁹⁵.

We know that the rotational wave functions J_{ee} , J_{oo} are symmetric and J_{eo} , J_{oe} are antisymmetric with respect to the rotation C_2 . In order to have an antisymmetric wave function, the

symmetric combinations of the nuclear spin wave functions must be combined with the anti-symmetric rotational wave functions and vice versa. We finally obtain that the spin statistic weights are:

15 for the levels *ee* and *oo*
and 21 for the levels *eo* and *oe*.

Initial state populations of CD₂H₂ in a jet

Because nuclear spin species do not interconvert in a supersonic jet expansion¹⁰⁰, the rotational cooling occurs independently for each spin species within the stack of rotational levels corresponding to their nuclear spin symmetry. In the case of CD₂H₂, molecules that are in a *ee* or *oo* rotational state can relax only into rotational levels that have *ee* or *oo* symmetries. In the same manner, molecules in a *eo* or *oe* rotational states can relax into levels with *eo* or *oe* symmetries. We refer to the stack that contains the *ee* and *oo* rotational states as symmetric stack. The stack named antisymmetric includes the *eo* and *oe* rotational states. The rotational population of a certain rotational state $p(J_{K_a K_c})$ after a jet expansion at a given rotational temperature T for the two different stacks can be calculated as:

$$p(J_{K_a K_c}) = \chi_i \cdot g_i \cdot (2J + 1) \cdot \exp\left(\frac{-E(J_{K_a K_c})}{kT}\right) / Q_i(T). \quad (3.20)$$

Where i is replaced by A and B for the symmetric and antisymmetric stacks. χ_i is the high-temperature limit mole fraction of nuclear spin specie contained in the stack i and g_i the effective nuclear spin weight. For $i = A$ and B we have that g_i is 15 and 21 respectively (see previous section). $E(J_{K_a K_c})$ is the energy of the rotational state $J_{K_a K_c}$ and Q_i is the rotational partition function of the stack i and can be written as:

$$Q_i(T) = \sum_{J, K_a, K_c} g_i \cdot (2J + 1) \cdot \exp\left(\frac{-E(J_{K_a K_c})}{kT}\right). \quad (3.21)$$

When $i = A$, the summation spans only the *ee* and *oo* rotational states. If $i = B$, then the summation is performed over the *eo* and *oe* states. The mole fractions at room temperature for

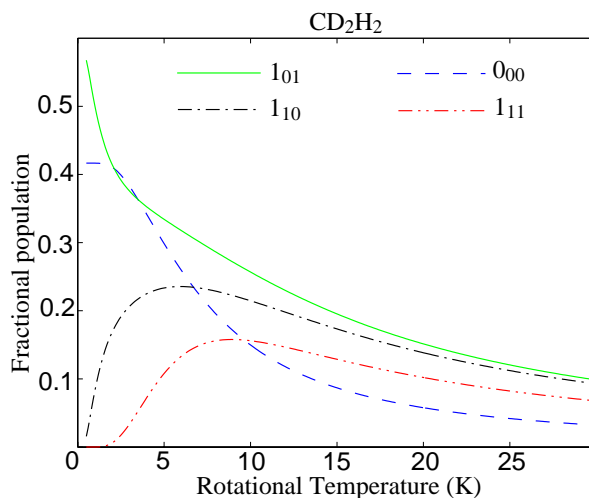


Figure 3.7: Fractional populations of the CD_2H_2 0_{00} , 1_{11} , 1_{01} and 1_{01} rotational levels as a function of the rotational temperature.

the two stacks of rotational levels are:

$$\chi_A = \frac{15}{15 + 21}$$

$$\chi_B = \frac{21}{15 + 21}.$$

Using eq. 3.20 and 3.21, we can calculate the fractional population of the CD_2H_2 0_{00} , 1_{11} , 1_{01} and 1_{01} rotational levels. Figure 3.7 shows the fractional populations of these levels as a function of the rotational temperature. The 0_{00} and 1_{01} are the lowest levels of the two stacks. At 0 K, the fractional populations of 0_{00} and 1_{01} levels are $15/36$ and $21/36$ respectively.

Determination of the rotational temperature

We determine the rotational temperature of the supersonically expanded CD_2H_2 molecules using the intensities of the $\nu_1 + \nu_6$ ${}^c\text{R}_{00}(0)$, ${}^c\text{Q}_{01}(1)$ and ${}^c\text{Q}_{11}(1)$ transitions.

The intensity of a transition $I_{a \rightarrow b}$ from a state a to b is proportional to the population of the starting level $p_a(T)$ and can be written as:

$$I_{a \rightarrow b} \propto p_a(T) |\mu_{ab}|^2 \propto p_a(T) \frac{S_{ab}}{2J_a + 1}, \quad (3.22)$$

where $|\mu_{ab}|^2$ is the squared module of the transition dipole moment matrix element, S_{ab} is the

$J''_{K_a k_c} \rightarrow J'_{K_a k_c}$	Transition strength (-)
0 ₀₀ → 1 ₁₀	1
1 ₀₁ → 1 ₁₁	1.5
1 ₁₁ → 1 ₀₁	1.5

Table 3.8: Rotational transition strengths for the transitions of the $\nu_1 + \nu_6$ band recorded with our CRD setup.

rotational transition strength¹⁰¹ and J_a is the angular momentum quantum number of the state a . The values of S_{ab} for the asymmetric top molecules are tabulated as a function of κ in the appendix V of *Microwave spectroscopy* by C.H. Townes and A.L. Schawlow¹⁰¹. The rotational transition strengths for the three $\nu_1 + \nu_6$ transitions recorded with our CRD setup are shown in Table 3.8.

The ratio between the intensities of the 0₀₀ → 1₁₀ and 1₀₁ → 1₁₁ gives rise to the following equation:

$$\frac{I_{0_{00} \rightarrow 1_{10}}}{I_{1_{01} \rightarrow 1_{11}}} = \frac{p_{0_{00}}(T) \cdot S_{0_{00} \rightarrow 1_{10}} \cdot (2 \cdot 1 + 1)}{p_{1_{01}}(T) \cdot S_{1_{01} \rightarrow 1_{11}} \cdot (0 \cdot 1 + 1)}. \quad (3.23)$$

Using the experimentally measured transition intensities, we can determinate the rotational temperature of the CD₂H₂ molecules by solving eq. 3.23 with respect to T . We calculate the rotational temperature also via the ratio between the 1₁₁ → 1₀₁ and 0₀₀ → 1₁₀ transition intensities and we average the two results. For the three mixtures used (18%, 10% and 1.8% CD₂H₂/H₂), we measure a rotational temperature of 8 ± 1 K which corresponds to the following fractional populations:

$$p_{0_{00}} = 0.19, \quad p_{1_{01}} = 0.28, \quad p_{1_{10}} = 0.23 \quad \text{and} \quad p_{1_{11}} = 0.16. \quad (3.24)$$

At this temperature, 86% of the molecules are in the 0₀₀, 1₀₁, 1₁₀ and 1₁₁ states.

Because of the higher population in the 1₀₁ state, we perform our state-resolved reaction probability experiments by exciting the Q₀₁(1) transition of the 2 ν_6 and $\nu_1 + \nu_6$ bands.

3.4.2 Number of molecules excited in the molecular beam

Once the fractional population of the starting level corresponding to the targeted transition is known, the number of excited molecules in the molecular beam can be determined by eq. 3.18

if $f_{exc,max}^{laser}$ and $f_{saturation}$ are known. This section explains how we determine these two factors.

Determination of $f_{exc,max}^{laser}$

For laser excitation with linearly polarized light, the selection rules for the quantum number M describing the orientation of \mathbf{J} with respect to the laser polarization are:

$$\text{P, R branch } (\Delta J = \pm 1): \Delta M = 0 \quad (3.25)$$

$$\text{Q branch } (\Delta J = 0): \Delta M = 0 \text{ and } M \neq 0 \quad (3.26)$$

These selection rules come from the coupling of the molecular total angular momentum \mathbf{J} with that of the photon, which for linearly polarized light is $J_{photon} = 1$, $M_{photon} = 0$ when the quantization axis is chosen along the electric field of the radiation. The transition probabilities are proportional to the square of the Clebsch-Gordan coefficients $\langle J'' M'', J_{photon} M_{photon} | J' M' \rangle^{102, 103}$, where the quantum numbers marked with double prime ($''$) and prime ($'$) are referred to the excited and ground states respectively. The analytical expressions of the Clebsch-Gordan coefficients are¹⁰²:

$$\text{R-branch: } |\langle JM, 10 | (J+1)M \rangle|^2 = \frac{(J-M+1)(J+M+1)}{(2J+1)(J+1)} \quad (3.27)$$

$$\text{Q-branch: } |\langle JM, 10 | JM \rangle|^2 = \frac{M^2}{J(J+1)} \quad (3.28)$$

$$\text{P-branch: } |\langle JM, 10 | (J-1)M \rangle|^2 = \frac{(J-M)(J+M)}{J(2J+1)}, \quad (3.29)$$

where the double primes denoting the initial state have been dropped for clarity. For Q(1) transitions we have that the transition probabilities for $M = 1$ and -1 are the same.

Based on these selection rules, for a Q-branch excitation, all M'' levels in the ground states combine with all the M' levels except for $M' = 0$ which is not depopulated. At saturation, half of the molecules in the levels corresponding to $M'' \neq 0$ are excited to the upper states, consequently $f_{exc,max}^{laser} = 1/2 \cdot 2J/(2J+1)$. Figure 3.8 shows the level scheme for a Q(1) transition where, at complete saturation, 1/3 of the molecules in the ground state can be transferred to the excited state ($f_{exc,max}^{laser} = 0.33$).

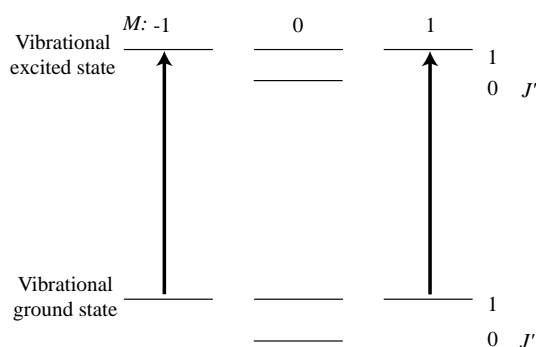


Figure 3.8: Level scheme for a CD₂H₂ Q(1) transition. Because linearly polarized light can induce only $\Delta M = 0$ with $M \neq 0$, the excited level with $M = 0$ is not populated and at complete saturation of the transition 1/3 of the molecules in the ground state are transferred to the upper vibrational state.

Determination of $f_{saturation}$

Exciting vibrational overtone transitions requires high radiation intensities, making pulsed lasers the tool of choice. In previous work, we report our ability to saturate the first overtone of the antisymmetric stretch of methane ($2\nu_3$) by direct optical pumping with a pulsed laser beam^{54,71}. The extent to which an infrared transition can be saturated can be calculated from¹⁰⁴:

$$f_{saturation} = 1 - \exp \left[-\rho \left(\frac{g_1 + g_2}{g_2} \right) B_{12} t \right], \quad (3.30)$$

where B_{12} is the absorption Einstein coefficient ($\text{m}^3\text{J}^{-1}\text{s}^{-2}$) for the transition, g_1 and g_2 are the degeneracy of the lower and upper state respectively, ρ is the radiation density and t is the interaction time between the radiation and the sample.

It is important to note that this calculation is based on the description of a two-level system using the rate equations, which neglect coherence effects. For coherent excitation with a single-mode laser, the excitation process is described by the optical Bloch equations¹⁰⁵. If the relaxation terms are slow compared to the excitation rate, then the excited state population will not approach the saturation value as predicted by eq. 3.30, but oscillates periodically between 0% and 100% with the Rabi frequency given by:

$$\Omega_{\text{Rabi}} = \frac{\mu_{12} E_0}{\hbar}, \quad (3.31)$$

where μ_{12} is the transition dipole moment obtained from the Einstein coefficient B_{12} and E_0

is the electric field strength of the laser in the excitation region. Using an ideal laser with the proper pulse duration, one could produce a so-called π pulse, which completely inverts the initial population and leaves all molecules in the excited state. However, the less than perfect coherence properties of our pulsed dye laser, which typically operates on at least two longitudinal modes, and the variation of the laser intensity across the focus make this π -pulse excitation over the entire focal volume impossible. In fact, we believe that the spatial variation in our laser intensity, when integrated over several Rabi cycles, effectively averages the excited state population so that the fraction of excited molecules produced is consistent with the value predicted by the rate equations.

For the CH_4 $2\nu_3$ R(1) transition, we determine $f_{\text{saturation}} = 98\%$ with a laser pulse energy of 120 mJ from the laser fluence dependence of laser-on carbon coverage^{22,54,71}. We can determine $f_{\text{saturation}}$ for the CD_2H_2 transitions at a given laser intensity by comparing the Einstein coefficients of the CD_2H_2 transitions with that of the CH_4 $2\nu_3$ R(1) transition.

Since the Einstein coefficients of the CD_2H_2 rovibrational transitions are not tabulated in literature, we determine them by comparing the intensities of the CD_2H_2 $2\nu_6$ and $\nu_1 + \nu_6$ $\text{Q}_{01}(1)$ transitions to that of the CH_4 $2\nu_3$ R(1) transition recorded using our CRD spectroscopy setup. For a two-level system, with a negligible population in the excited state, the Einstein coefficient can be expressed as a function of the absorption coefficient $K(\nu)$:

$$B_{12} = \frac{K(\nu)\delta\nu}{h\nu N_1}, \quad (3.32)$$

where $\delta\nu$ is the radiation bandwidth, ν the frequency, and N_1 the population of the ground state. The integrated absorption coefficient K (m^2s^{-2}) over a single line is:

$$K = B_{12}N_1h\nu_0, \quad (3.33)$$

where ν_0 is the central frequency of the transition. The relation between the Einstein coefficients of different transitions and the absorption intensities measured by CRD spectroscopy is:

$$B_{12}^{2\nu_6, b\text{Q}_{01}(1)} = B_{12}^{2\nu_3, \text{R}(1)} \cdot \frac{\nu_{2\nu_3, \text{R}(1)} \cdot N_{2\nu_3, \text{R}(1)} \cdot A_{2\nu_6, b\text{Q}_{01}(1)}}{\nu_{2\nu_6, b\text{Q}_{01}(1)} \cdot N_{2\nu_6, b\text{Q}_{01}(1)} \cdot A_{2\nu_3, \text{R}(1)}}, \quad (3.34)$$

where $A_{2\nu_6, b\text{Q}_{01}(1)}$ and $A_{2\nu_3, \text{R}(1)}$ are the integrated peak heights in the CRD spectra. By knowing that $B_{12}^{2\nu_3, \text{R}(1)} = 2.98 \cdot 10^{14}$ (HITRAN¹⁰⁶), we determine that $B_{12}^{2\nu_6, b\text{Q}_{01}(1)} = (8.1 \pm 0.6) \cdot 10^{13}$ and $B_{12}^{\nu_1 + \nu_6, b\text{Q}_{01}(1)} = (4.8 \pm 0.3) \cdot 10^{13}$ ($\text{m}^3\text{J}^{-1}\text{s}^{-2}$).

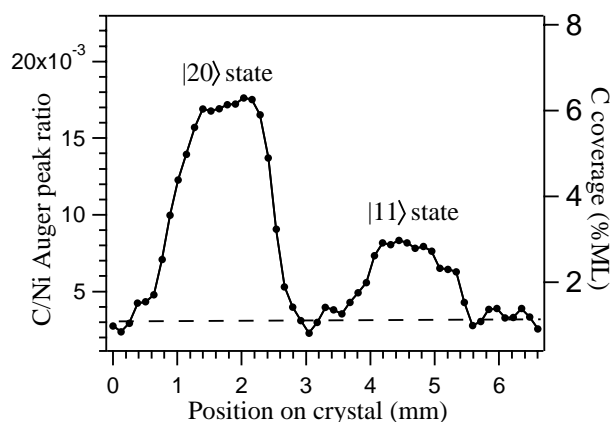


Figure 3.9: Surface carbon Auger signal for identical doses of CD_2H_2 excited to the $|20\rangle^-$ and $|11\rangle$ vibrational states incident on a $\text{Ni}(100)$ surface at kinetic energy of 41 kJ/mol. The dashed line indicates the background level of carbon accumulated during the deposition and analysis time.

Since the Einstein coefficients of the CD_2H_2 $2\nu_6$ and $\nu_1 + \nu_6$ $Q_{01}(1)$ transitions are approximately 3 and 5 times smaller than that of CH_4 $2\nu_3$ $R(1)$ transition, we are not able to saturate the CD_2H_2 transitions. The values of $f_{\text{saturation}}$ are 0.43 ± 0.04 and 0.3 ± 0.03 for $2\nu_6$ and $\nu_1 + \nu_6$ $Q_{01}(1)$ transitions respectively using a laser energy of 120 mJ/pulse.

3.4.3 Calculation of state-resolved sticking coefficients

To compare the reactivities of CD_2H_2 excited to the $|20\rangle^-$ and $|11\rangle$, we direct a molecular beam containing 18% CD_2H_2 in H_2 at normal incidence for 15 minutes at two different positions on the initially clean $\text{Ni}(100)$ surface. The result of this experiment is shown in Fig. 3.9. For the first deposition (left-hand peak), the $|20\rangle^-$ state of CD_2H_2 with $J = 1$ was excited by tuning the IR 120 mJ pulses to the ${}^cQ_{01}(1)$ transition (5879.7 cm^{-1}), and for the second deposition (right-hand peak), the $J = 1$ level of the $|11\rangle$ state was prepared using the same IR pulse energy to excite the corresponding ${}^bQ_{01}(1)$ transition at 6000.3 cm^{-1} . Although the transition used to prepare the $|20\rangle^-$ level is weaker by a factor 1.7 ± 0.1 than the one used to excite the $|11\rangle$ level, the former leads to a carbon signal at least three times as large, indicating clear mode-specific reactivity. Control experiments such as reversing the order and surface location of the deposition did not change the result. For this incident kinetic energy (41 kJ/mol), the *laser-off* sticking coefficient is so small ($5 \cdot 10^{-7}$) that no carbon is detected above the background on the surface when we perform the experiments under the identical beam conditions but without laser

excitation.

We calculate the state-resolved sticking coefficients of CD_2H_2 excited to the $|20\rangle^-$ and $|11\rangle$ states using eq. 3.17 and 3.18. As example, we report the sticking coefficient calculations for the deposition of 18% $\text{CD}_2\text{H}_2/\text{H}_2$ with nozzle temperature of 423 K. The fraction of the molecular beam pulse illuminated by the laser (f_{overlap}) corresponds to:

$$f_{\text{overlap}} = \frac{\text{laser pulse width}}{\text{molecular-beam pulse width}} = \frac{12 \cdot 10^{-3} \text{ m}}{2147 \text{ m/s} \cdot 26.6 \cdot 10^{-6} \text{ s}} = 0.21. \quad (3.35)$$

From sections 3.4.1 and 3.4.2, we have $f_{\text{pop}} = 0.28$ and $f_{\text{exc,max}}^{\text{laser}} = 1/3$. The fractional saturation of the transitions ($f_{\text{saturation}}$) are 0.3 and 0.43 for the $|20\rangle^-$ and $|11\rangle$ states, as determined in section 3.4.2. Finally, we calculate $f_{\text{exc}} = (2.3 \pm 0.2)\%$ and $(3.4 \pm 0.3)\%$ for the $|20\rangle^-$ and $|11\rangle$ states respectively.

We assume $S_0^{\text{laser-off}}$ being an upper limit for the $S_0^{v=0}$ and we calculate the following sticking coefficients:

$$\begin{aligned} S_0^{|20\rangle^-}(41.6 \text{ kJ/mol}) &= (8.5 \pm 2.5) \cdot 10^{-2} \text{ for } \text{CD}_2\text{H}_2 \text{ in the } |20\rangle^- \text{ state,} \\ S_0^{|11\rangle}(41.6 \text{ kJ/mol}) &= (1.7 \pm 0.6) \cdot 10^{-2} \text{ for } \text{CD}_2\text{H}_2 \text{ in the } |11\rangle \text{ state,} \end{aligned}$$

where the uncertainties represent the combination of 95% of confidence limit obtained for repeated measurements with our estimation of the overall accuracy for the experiment.

3.5 Results and discussion

Laser-on and laser-off measurements are made for a series of incident kinetic energies. Figure 3.10 shows the state resolved sticking coefficients for CD_2H_2 determined from these measurements. At 41 kJ/mol, we find that CD_2H_2 is 5.4 times more reactive when promoted to the $|20\rangle^-$ state than when it is excited to the $|11\rangle$ state. The reactivity for both states is enhanced by several orders of magnitude with respect to incident molecules in the ground vibrational state with the same kinetic energy. The difference in reactivity for the $|20\rangle^-$ and $|11\rangle$ state decreases with increasing kinetic energy, reaching a factor of 2 at a kinetic energy of 80 kJ/mol. At still higher kinetic energy we observe a continuation of this trend, although an accurate determination of the absolute reactivity becomes increasingly difficult as a result of the higher reactivity of the ground-state molecules. This decrease in mode specificity is likely due to the increase of the

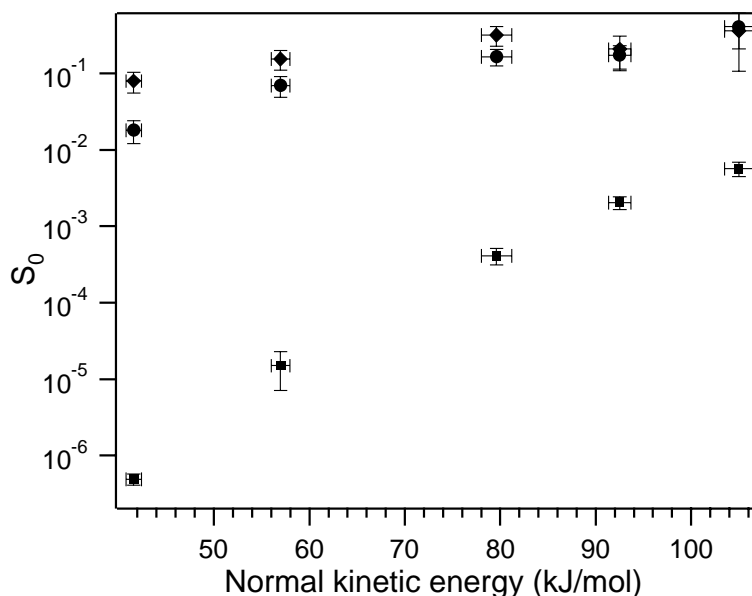


Figure 3.10: State-resolved sticking coefficients for CD_2H_2 in (from top to bottom) the $|20\rangle^-$ (\blacklozenge), $|11\rangle$ (\bullet), and ground (\blacksquare) vibrational states on Ni(100) as a function of incident kinetic energy normal to the surface. The surface temperature is 473 K.

total amount of available energy relative to the reaction barrier. As the reaction probability approaches its asymptotic value, the difference between the two vibrational modes is expected to decrease. On the other hand, the mode selectivity should be even larger at lower kinetic energy.

The larger reactivity of the $|20\rangle^-$ state relative to the $|11\rangle$ state can be rationalized in terms of their different vibrational amplitudes: the former contains two quanta of stretch vibration in a single C-H bond, whereas the latter contains one quantum in each C-H bond. In order to break one of the C-H bonds in CD_2H_2 , our results show that it is more efficient to stretch one of the bond as much as possible by placing two quanta of vibrational excitation in a single bond rather than one quantum in each C-H bond. In the gas-phase reaction of CD_2H_2 with chlorine, the product state distributions observed by Kim *et al.*¹⁰⁷ confirm this local mode description by demonstrating that one of the two bonds acts as spectator during the reaction¹⁰⁸. They have found that the excitation of CD_2H_2 to the $|20\rangle^-$ state, prior the collision with chlorine, yields methyl radical products primarily in their ground state, whereas the excitation of the $|11\rangle$ state yields methyl radical products that are C-H stretch excited. Their results have shown as well that the excitation of the first C-H overtone of CD_2H_2 leads to a preference for hydrogen

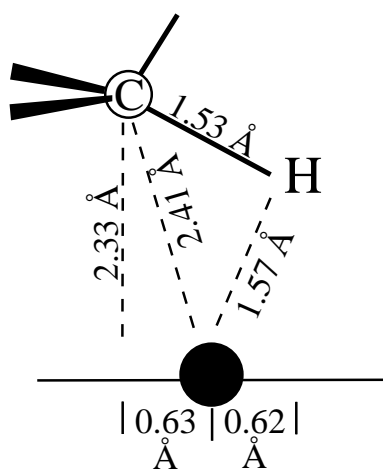


Figure 3.11: The transition state of methane on Ni(111) shows an elongated C-H bond, whereas the methyl geometry is unperturbed¹⁶.

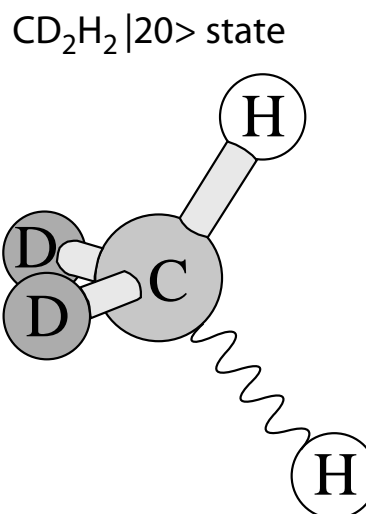


Figure 3.12: The $|20\rangle$ state of CD_2H_2 resembles the configuration of methane on Ni(100) at the transition state as shown in Figure 3.11.

abstraction over deuterium abstraction, and vice versa (bond-specific reactivity). These results have been interpreted with a simple spectator model: the Cl reacts with a single C-H oscillator and the rest of the methane molecule does not participate in the reaction.

The same description of bond-specific reactivity and spectator model also rationalizes our observations. If we assume that the surface reacts with a single C-H bond of CD_2H_2 , the $|20\rangle^-$ state is more reactive than the $|11\rangle$ because it has a larger vibrational amplitude along the C-H bond relative to $|11\rangle$. In the case of CD_2H_2 excited in the $|20\rangle^-$ state, the bond-specific reactivity implies that the vibrationally excited C-H bond is preferentially broken in the reaction with the surface

The difference in reactivity between these two vibrational states implies that the C-H bond stretch has a substantial projection on the reaction coordinate, in agreement with ab-initio calculations of the transition-state structure¹⁶. Figure 3.11 shows the transition state of methane on Ni(111) as calculated by Yang *et al.*¹⁶, where the C-H bond close to the surface is predicted to be elongated, whereas the methyl is unperturbed. One can observe that the $|20\rangle$ state resembles the transition state configuration as shown in Figure 3.12.

Our results show that vibrational excitation of CD_2H_2 significantly influence the dynamics of CD_2H_2 chemisorption on Ni(100). We show that CD_2H_2 excited to the $|20\rangle^-$ state is more

reactive than CD₂H₂ excited to the |11⟩ state on a nickel surface despite the fact that these have nearly the same energy.

This is the first time that vibrational state specificity is observed in a gas-surface reaction. Our results have important implications for theoretical treatments of this process. Bond-specific reactivity is inconsistent with the statistical model proposed by Bukoski *et al.*⁸⁹. Their model assumes complete intramolecular redistribution of the initial vibrational energy in methane as the molecule transiently resides in a local “hot spot” and interacts with a limited number of surface atoms, and it determines rates for desorption and dissociation according to the Rice-Ramsperger-Kassel-Marcus (RRKM) microcanonical rate theory. As a result, it predicts a reactivity that scales with the total available energy independent of vibrational state, which is inconsistent with our experimental results. In contrast to the assumptions of this (or any) statistical model, our observation that CD₂H₂ retains a clear memory of the initially prepared quantum state indicates that its interaction with the metal surface does not induce extensive intramolecular energy redistribution (IVR) before the reaction occurs. We can estimate that a CD₂H₂ molecule approaching on a metal surface with a speed of 1000 m/s takes ~ 200 fs to fly through the interaction region (~ 2 Å). Our results show that the IVR should occur in a timescale in the order of or longer than 200 fs.

In addition to excluding statistical assumptions, the observation of state specificity in the reaction probability provides guidance for dynamical models. In the investigation of molecular dynamics, the knowledge of the potential energy surface (PES) of the system under consideration is a necessary prerequisite. However, the interaction between a polyatomic molecule and a surface depends on many degrees of freedom that a complete description of the system requires substantial computational efforts. The main strategy to face this kind of problems has been to develop reduced-dimensional dynamical models by decreasing the degrees of freedom in the PES. For CH₄ on transition metal surfaces, one simplifying model assumption has been to treat the molecule as quasidiatomic (R-H, with R=CH₃)¹⁷⁻¹⁹. This corresponds to attribute the vibrational activation to a C-H stretch mode. This assumption was justified by the fact that HREELS experiments have found CH₃ and adsorbed hydrogen atoms to be the primary products of methane chemisorption on a nickel surface¹⁴⁻¹⁶ as well as by Ni cluster calculations showing a transition state with one elongated C-H bond^{16,46} (on Ni(100) the methane R-H bond length changes from 1.09 to 1.51 Å at the transition state). Luntz *et al.* have developed a quasidiatomic model for the chemisorption of methane on a Ni(100) surface^{17,18} (“surface mass model”). In their model, they consider the interaction between the surface and the molecule

as a simple semi-empirical 2-dimensional PES $V(z, d)$, where z is the molecule-surface distance and d is the R-H bond distance. In order to simulate the surface temperature dependence of the reaction probability, the PES was coupled to the recoil of the vibrating surface via an harmonic oscillator: $V(z - y, d)$, where y represents the deviation of the oscillating surface from its equilibrium position. The results of this model are in qualitative agreement with the experimental data for CH₄ chemisorption on Ni(100)²⁰. However, the calculated increase in sticking coefficient with incident energy was much steeper than that of experiments²⁰. This discrepancy was attributed to the low dimensionality of the model. Luntz *et al.* approximately included the multidimensionality through the so-called “hole model”¹⁸. This model does not take into account any dynamic coupling of the neglected parameters to the reaction path, but it does describe approximately the effect of the distribution of impact parameter such as the steric effects and the internal vibrational structure of CH₄. The results of this model has been shown to be in good agreement with the experimental molecular beam data obtained by Holmblad *et al.*²⁰.

In order to avoid the rather arbitrary distribution of barriers of the “hole model”, Carré and Jackson extended the “surface mass” model by considering the molecular orientations¹⁹. They adjusted the PES surface to reflect *ab initio* calculations and experimental data. Using this model, except for the isotope effect and the extracted vibrational efficacy, semi-quantitative agreements were found between the theoretical results and the molecular beam experiments of Holmblad *et al.*²⁰.

Recent state-resolved experiments investigated the reactivity of CH₄ excited to the antisymmetric stretch fundamental vibration (ν_3)²¹ and first overtone ($2\nu_3$)^{22, 71} on Ni(100). Juurlink *et al.*²¹ have shown that the thermally prepared fraction of molecules in ν_3 in a hot nozzle beam could not account for more than 2% of the measured sticking probability²⁰. They argue that vibrational modes other than ν_3 must play a significant role for the reactivity of vibrationally excited CH₄. Our results of mode specificity presented in this chapter, together with those of CH₄ prepared in the antisymmetric stretches, show that the quasidiatomic models can not correctly describe the mechanisms of methane chemisorption on a metal surface. Our results suggest that a realistic description of the chemical dynamics will need to go beyond low dimensionality models.

Calculation including more than one vibrational degree of freedom are starting to become feasible^{23–25}. Milot *et al.*²³ have performed wave packet simulations of oriented methane molecules scattered from a flat surface including all nine internal vibrations. Their results showed that the

translational energy loss depends on the vibrational state of the incident molecule following the trend: $\nu_1 > \nu_3 > \nu_4 > \text{ground state}$. Based on this inelasticity, the authors suggested that the ν_1 symmetrical stretch mode will be more effective than the antisymmetrical stretch ν_3 in promoting dissociation because it makes more translational energy available for the reaction. Similar conclusions were obtained by Halonnen et al.²⁴, who have calculated the shift in vibrational energies of CH_4 as the molecule adiabatically approaches a flat metal surface. They predict that the vibrational energy of the symmetric and antisymmetric stretches becomes localized in the proximal and distal C-H bonds respectively during the adiabatic approach toward the surface. While the proximal C-H bond points towards the surface, the three distal distal C-H bonds point outside the surface. Based on this, they suggest that $\text{CH}_4(\nu_1)$ should be significantly more reactive than $\text{CH}_4(\nu_3)$ in the adiabatic limit. In order to test the predictions of these models, we determine the reactivity of CH_4 excited to the ν_1 state on $\text{Ni}(100)$. The experimental details and the results of this experiment are shown in the next chapter.

State-resolved reactivity of $\text{CH}_4(\nu_1)$ on Ni(100)

4.1 Introduction

Recent state-resolved experiments have investigated the reactivity on Ni(100) of methane excited to the antisymmetric stretch $\text{CH}_4(\nu_3)^{21}$ and to its first overtone $\text{CH}_4(2\nu_3)^{22,71}$. The results show that energy in ν_3 promotes the reactivity with similar efficacy as kinetic energy along the surface normal. Furthermore, Juurlink *et al.*²¹ show that CH_4 with excitation in ν_3 contributes less than 2% to the activated chemisorption of thermally excited methane²⁰. They conclude that vibrational modes other than ν_3 must play a significant role in methane reactivity under thermal conditions. Simplified dynamical calculation for the reaction of CH_4 on Ni(100) suggest that methane excited to the fundamental symmetric stretch $\text{CH}_4(\nu_1)$ should be more reactive than $\text{CH}_4(\nu_3)^{23,24}$. For reactions that occur entirely in the gas phase, more realistic dynamical calculations find that the symmetric stretch vibration is generally more efficient than the antisymmetric stretch in promoting reactions^{29,34,56–60}, and this has been confirmed, in part, by experiments^{29,31}.

In Chapter 3, we reported vibrational state specific chemisorption of CD_2H_2 on Ni(100), where we demonstrate the difference in reactivity of two nearly isoenergetic overtone levels¹⁰⁹. However, testing the prediction of higher reactivity for the symmetric stretch relative to the antisymmetric stretch in methane is more challenging, since direct IR excitation cannot be used to excite CH_4 to a totally symmetric vibration such as ν_1 .

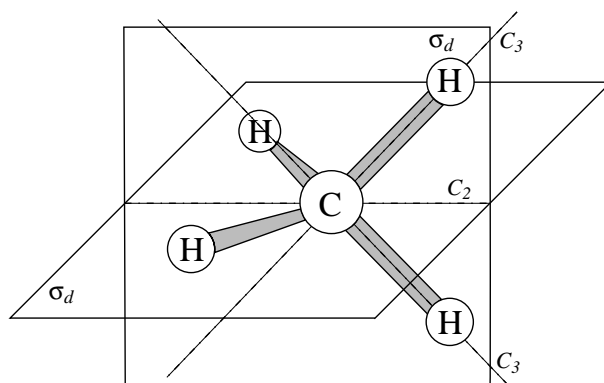


Figure 4.1: Molecular geometry of the CH_4 molecule. One of the 3 C_2 axes and two of the 6 σ_d planes are shown.

In this chapter, we report the first use of stimulated Raman pumping (SRP) to measure the state-resolved surface reactivity of $\text{CH}_4(\nu_1)$ on $\text{Ni}(100)$. Both SRP and IR excitation have been used previously to study the gas-phase reaction of CH_4 with chlorine atoms to compare the effects of ν_1 and ν_3 excitations on the dynamics¹⁰⁸. While no significant difference was observed in the rovibrational product state and angular distributions for the two states, the study did not exclude the possibility of different reaction cross sections.

In the first part of this chapter, we give a description of the methane molecule. In particular, we describe its rotational states with their decompositions into direct sum of irreducible representations. These decompositions will be used for the determination of the rotational temperature of supersonically expanded CH_4 and for the calculation of the sticking coefficients. In the second part of this chapter, we show the results of the SRP experiments and explain how we determine the sticking coefficients of methane molecules prepared in the symmetric stretch.

4.2 The CH_4 molecule

The methane molecule is formed by four hydrogen atoms arranged in a tetrahedral structure around the carbon atom as shown in Fig. 4.1. It belongs to the T_d point group whose character table is shown in Table C.3 of appendix C. The T_d point group contains four C_3 axis, three C_2 axis and six σ_d planes. The C_3 axis are along the directions of each of the C-H bonds. The σ_d are the six planes of all the possible CH_2 fragments. The C_2 axis are along the line generated by the intersection of any two mutually perpendicular σ_d planes.

Under the Born-Oppenheimer approximation, the total wave function of the molecule can be

decomposed as a product of component wave functions

$$\psi = \psi_e \psi_v \psi_r \psi_{ns}, \quad (4.1)$$

where ψ_e , ψ_v and ψ_r are the electronic, vibrational and rotational wave functions and ψ_{ns} is the nuclear spin wave function.

4.2.1 Molecular rotations

Since the CH₄ molecule has three equivalent moments of inertia, it is a spherical-top rotor. Its rotational Hamiltonian can be written as:

$$\hat{H}_{rot} = \frac{\hat{L}_x^2}{2I} + \frac{\hat{L}_y^2}{2I} + \frac{\hat{L}_z^2}{2I} = \frac{|\hat{\mathbf{L}}|^2}{2I}, \quad (4.2)$$

where I is the moment of inertia calculated with respect to whatever axis passing through the center of mass. The eigenfunctions of this Hamiltonian are the Wigner rotational wave functions $\psi_r = |JKM\rangle$ ⁹². In the rigid rotor limit, the rotational energy levels E_r are expressed as a function of the rotational quantum number J by:

$$E_r(J) = B_i J(J+1), \quad (4.3)$$

where B_i is the rotational constant of the i -th vibrational state. The additional term $-D_i J^2(J+1)^2$ can be added to eq. 4.3 to include the centrifugal distortion effects. D_i is called the centrifugal constant corresponding to the vibrational state i . Each rotational energy level is $(2J+1)(2J+1)$ -fold degenerate due to the $2J+1$ possible orientations of the angular momentum operator in the laboratory frame (M quantum number) and in the molecular frame (K quantum number). The rotational B_0 and the centrifugal D_0 constants for the vibrational ground state are 5.241035 and $1.11 \cdot 10^{-4} \text{ cm}^{-1}$ respectively¹¹⁰.

The symmetry properties of the rotational wave functions can be determined using the rotational sub-group T of the point group T_d . The rotational sub-group contains only the symmetry axis and the eigenfunctions species A_1 and A_2 in T_d belong to A in T . F_1 and F_2 belong to F in T . The characters for the representation of T formed by the $|JKM\rangle$ basis set are shown in Table 4.1¹¹¹, where p and k can take the values $0, 1, 2, \dots$. Since the rotational sub-group elements rotate the molecular frame and the laboratory frame is not touched, each character has to be multiplied by a factor $2J+1$ due to the degeneracy of the M quantum number. The

	χ'_E	χ'_{C_2}	χ'_{C_3}	$\chi'_{C_3'}$
$J = 6p + k$	$12p + 2k + 1$	$(-1)^k$	$2/\sqrt{3} \sin \left[\frac{2}{3}(1 - k) \right]$	$2/\sqrt{3} \sin \left[\frac{2}{3}(1 - k) \right]$

Table 4.1: Characters for the representation of T formed by the $|JKM\rangle$ basis set¹¹¹. $p, k = 0, 1, 2, \dots$, all characters must be multiplied by $2J + 1$.

Irreducible representation		Irreducible representation	
J	combination	J	combination
0	A	3	$A + 2F$
1	F	4	$A + E + 2F$
2	$E + F$	5	$E + 3F$

Table 4.2: Symmetries of the rotational functions with J up to 5¹¹¹.

decomposition of this representation in a direct sum of irreducible representations is shown in Table 4.2 for $J = 0$ to 5. The formulae for a generic J are reported by Wilson *et al.*¹¹¹.

The rotational sub-group T is sufficient for describing the nuclear spin isomers and nuclear spin statistical weight, but for the determination of the rotational temperature it is useful to introduce the representation of the T_d point group formed by the $|JKM\rangle$ basis set. Hippler *et al.*¹¹² report the frequency of occurrence G of T_d species for a given J :

$$\begin{aligned}
 G(J, A, \rho) &= \frac{1}{24} (2J + 1 + 3(-1)^J + (-1)^{\rho+J} [6 + g_1(J)] + g_2(J)), \\
 G(J, E) &= \frac{1}{24} (4J + 2 + 6(-1)^J - g_2(J)), \\
 G(J, F, \rho) &= \frac{1}{24} (6J + 3 - 3(-1)^J + (-1)^{\rho+J} [6 - g_1(J)]),
 \end{aligned} \tag{4.4}$$

with:

$$\begin{aligned}
 g_1 &= 6(-1)^J \left[\sin \left(\frac{1}{2} J \pi \right) + \cos \left(\frac{1}{2} J \pi \right) \right], \\
 g_2 &= 8 \left[3^{-1/2} \sin \left(\frac{2}{3} J \pi \right) + \cos \left(\frac{2}{3} J \pi \right) \right],
 \end{aligned}$$

where $\rho = 1$ for A_2 or F_1 , and $\rho = 2$ for A_1 or F_2 .

Other perturbation terms that contain some non-spherical components could be added to the Hamiltonian written in eq. 4.2¹¹³. As a consequence these terms remove the degeneracy of the J quantum states. For a given J value, the allowed states split according to their irreducible

representation indices. However, the energy shifts induced by these terms are in the order of 0.002 cm^{-1} for $J = 2$, which can be neglected due to a spectral width of our dye laser beam (0.05 cm^{-1}).

4.2.2 Molecular vibrations

The CH₄ molecule contains nine internal degrees of freedom that are grouped in four distinct normal vibrations, ν_1 , ν_2 , ν_3 and ν_4 . The representations of the CH₄ normal modes are shown in Fig. 4.2. The symmetric stretch (ν_1) is non degenerate, the symmetric bend ν_2 is 2-fold degenerate, the antisymmetric stretch (ν_3) and bending (ν_4) modes are 3-fold degenerate.

The ν_4 and ν_3 modes are IR active and both have F_2 symmetry. The band origins for ν_4 and ν_3 are 1306.2 cm^{-1} and 3020.3 cm^{-1} , respectively¹¹⁴. The nuclei displacements for the three degenerate ν_3 modes is shown in Fig. 4.2. The hydrogen nuclei oscillate along one of the cartesian coordinates and their motion is counterbalanced by the displacement of the carbon nucleus in such a way that the center of mass of the molecule does not moves.

The ν_2 vibration is the symmetric bend (band origin= 1523.8 cm^{-1})¹¹⁴, in which the hydrogen nuclei move upon the surface of the sphere which passes through the four corners of the regular tetrahedron. Two of the hydrogen nuclei approach each other while at the same time the other two hydrogen nuclei approach each other by an equal amount. This mode is doubly degenerate and has E symmetry. The carbon nucleus does not take part in the motion and no change of dipole moment occurs during the oscillation, so the ν_2 mode is IR inactive. The first overtone of this mode resonates weakly with the intense Raman line of ν_1 ¹¹⁵.

For the normal mode ν_1 , the hydrogen nuclei oscillate in phase along their C-H bond axis. ν_1 has A_1 symmetry and it is IR inactive but Raman active. Its band center is around 2917 cm^{-1} .¹¹⁰ This is the normal mode of interest in our work. The rotational constants of the ν_1 vibrational states are $B_{\nu_1} = 5.25$ and $D_{\nu_1} = 1.7 \cdot 10^{-4} \text{ cm}^{-1}$.¹¹⁰ The rotational selection rules corresponding to the Raman transition are not found from group theory, but from the fact that each photon that is destroyed or created changes the angular momentum by ± 1 . Since in the Raman process two photons interact with the molecule, the allowed changes for J are $\Delta J = 0, \pm 2$. In this work we are concerned with the Q branch Raman transitions ($\Delta J = 0$). Due to the low rotational temperature ($\sim 8 \text{ K}$) in our molecular beam, the only available transitions are: $Q(0)$, $Q(1)$, and $Q(2)$.

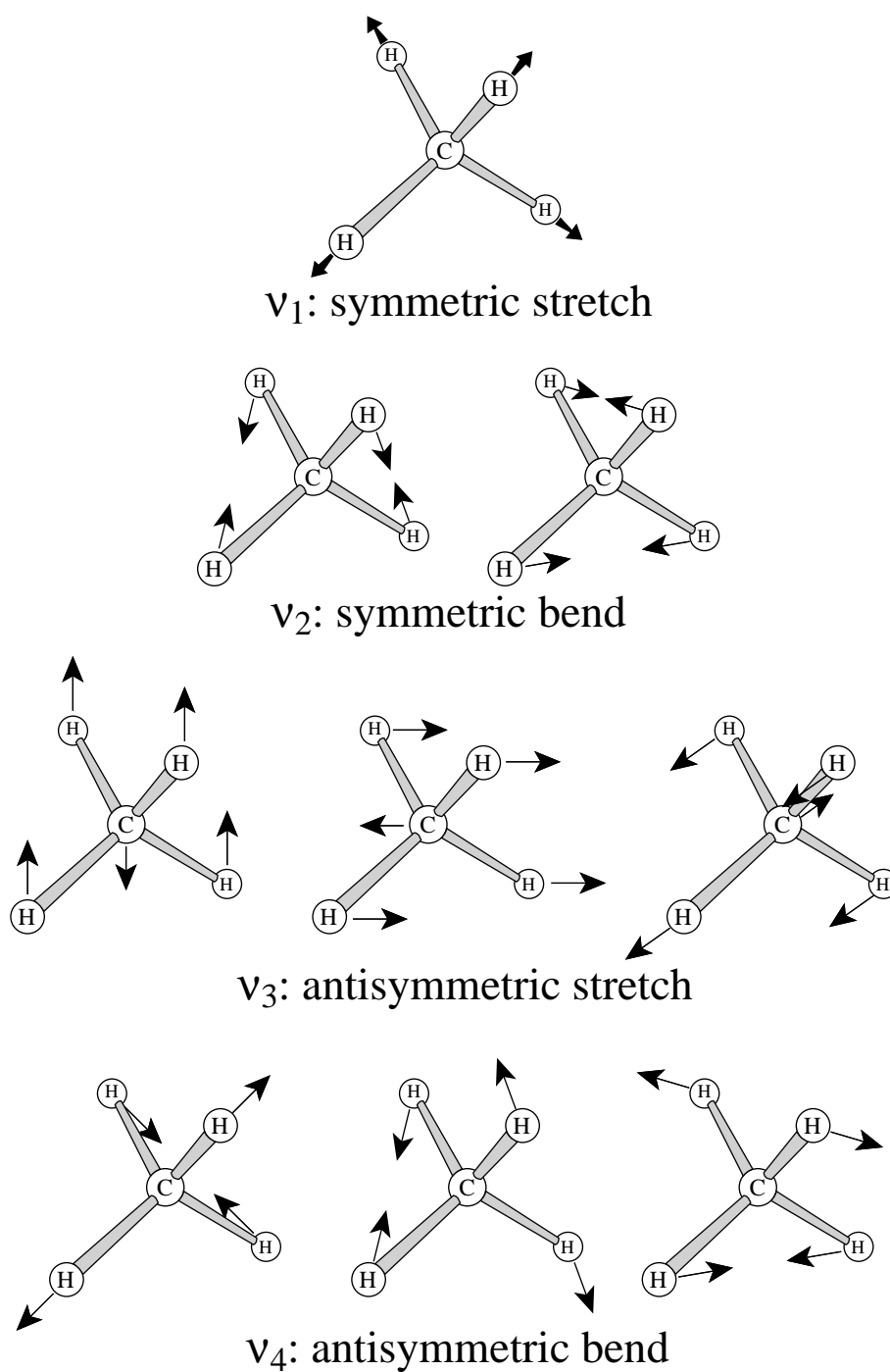


Figure 4.2: Representations of the CH_4 normal modes.

J	Γ	Frequency shift (cm^{-1})
0	A_1	2916.47
1	F_1	2916.49
2	$E + F_2$	2916.53

Table 4.3: Experimentally determined Raman shift frequencies of the $Q(0)$, $Q(1)$, and $Q(2)$ transitions of the ν_1 band¹¹⁰. Γ is the irreducible representation of the ground state level.

4.3 Sticking coefficient of $\text{CH}_4(\nu_1)$ on $\text{Ni}(100)$

Since the symmetric stretch ν_1 of methane is IR inactive, we prepare the $\text{CH}_4(\nu_1)$ molecules in the molecular beam by stimulated Raman pumping (SRP). In this scheme, two focused and superimposed laser beams interact with the molecules when the difference between the two laser frequencies matches the energy difference between the vibrational ground state level and the ν_1 level ($\sim 2917 \text{ cm}^{-1}$). The optical layout we use to perform these measurements is shown in Fig. 2.26 of section 2.7.

The rotational temperatures of the supersonically expanded CH_4/H_2 mixtures used for our experiments are below 10 K (see section 4.3.1). At this temperature only the $J = 0, 1$ and 2 levels of the vibrational ground state are populated. While for an infrared excitation, we can not have a rovibrational transition $Q(0)$, for a Raman process, $Q(0)$ is allowed. Hence, the available Raman transitions in the molecular beam are: $Q(0)$, $Q(1)$, and $Q(2)$. We record a photoacoustic Raman (PAR) spectrum^{116,117} of static methane (30 Torr) at 293 K, and the result is shown in Fig. 4.3. With the bandwidth of our dye laser, we are not able to resolve individual rotational transitions and the resulting PAR spectrum is the convolution of the laser spectral profile and the Raman transitions. The transition frequencies and intensities for the ν_1 band as calculated by the spherical top data system (STDS) software¹¹⁸ at 293 K are reported with stick plots in Fig. 4.3 under the PAR spectrum. The transitions with $J \leq 3$ are labelled. The methane pressure of 9 bar in the Raman amplifier is chosen to tune the maximum of the Raman gain curve (see section 2.7) to overlap the $Q(0)$, $Q(1)$, and $Q(2)$ transitions used to excite the methane molecules in the molecular beam (Fig. 4.3 dashed line). Since the 0.05 cm^{-1} bandwidth of the Stokes radiation is insufficient to resolve the transitions listed in Table 4.3, we assume in our analysis that the Raman excitation takes place simultaneously on all three transitions. We assume also that the degree of saturations of the three transitions are the same.

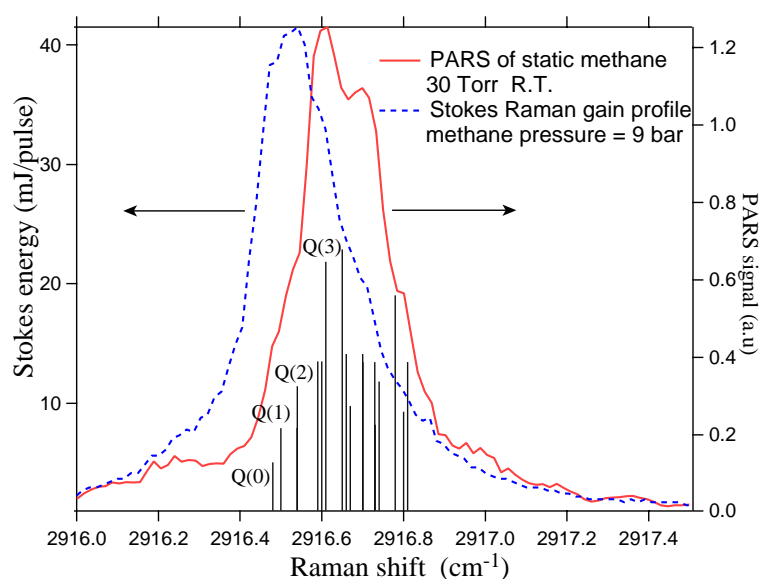


Figure 4.3: Photoacoustic Raman spectrum of 30 Torr static CH_4 at 293 K (solid line). The stick plots are the Q branch transitions as calculated by the STDS software¹¹⁸. The maximum of the Raman gain curve (dashed line) overlaps the $Q(0)$, $Q(1)$, and $Q(2)$ transitions used to excite the methane molecules in the molecular beam.

In order to saturate the Raman transitions, the pump and Stokes beams are focused in a line parallel to the molecular beam axis by a cylindrical lens ($f=300$ mm) as shown in Fig. 4.4 where

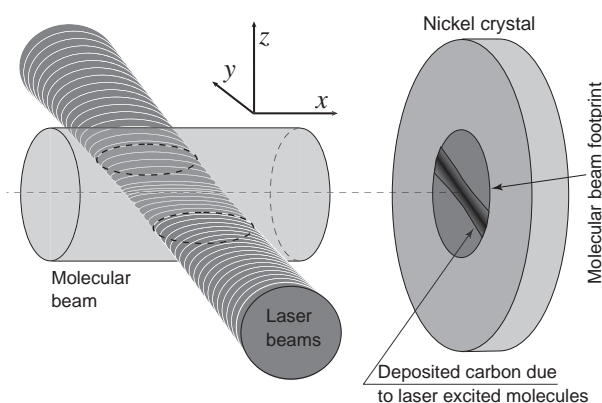


Figure 4.4: Schematic of the excitation region. The laser beams are focused in a line parallel to the molecular beam by a cylindrical lens (not shown) with a focal length of 300 mm. The widths of the laser beams along the z direction are smaller than the molecular beam diameter. The black part on the nickel crystal surface is the part of carbon deposited due to the CH_4 molecules excited in the molecular beam.

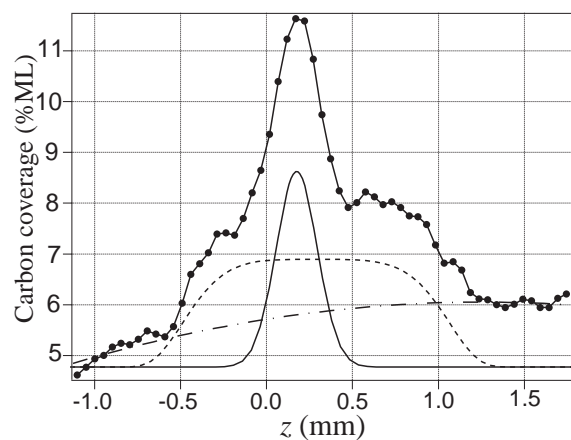


Figure 4.5: Auger analysis of deposited carbon. The individual contributions of the carbon signal from the electron beam induced carbon formation during the Auger analysis (dashed-dotted line), the unexcited molecular beam (dashed line) and the laser excited beam (solid line) are shown separately. These data are obtained at a molecular beam kinetic energy of 63.5 kJ/mol with laser energies of 250 mJ/pulse for both the pump and Stokes radiation.

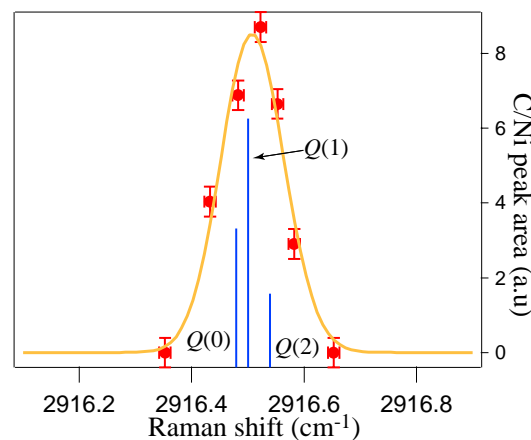


Figure 4.6: Carbon signal on the surface as a function of the Raman shift ($\nu_{Y2} - \nu_{dye}$). The three Q transitions available in the molecular beam are reported with their intensities as stick plots. The best fit to the experimental point of the convolution between a gaussian with the Q transitions is reported as solid line.

the widths of the laser beams along the z direction are much smaller than the molecular beam diameter. The black part in Fig. 4.4 represents the carbon on the nickel surface due to the laser excited CH_4 molecules in the molecular beam.

To perform state-resolved gas/surface reactivity measurements, we expose the $\text{Ni}(100)$ to the laser-excited molecular beam for a predetermined time while monitoring the CH_4 flux with a calibrated quadrupole mass spectrometer. After the deposition, we detect the carbon produced on the surface by performing an AES surface scan along the z direction. Figure 4.5 shows the results of a z scan obtained after a 90 min deposition with a molecular beam kinetic energy of 63.5 kJ/mol and laser energies of 250 mJ/pulse for both the pump and the Stokes radiation. The tight focusing of the laser beams within the molecular beam generates several distinct regions in this profile. The narrow peak in the center is due to the reaction of both laser excited (“laser-on”) and unexcited (“laser-off”) CH_4 molecules. The broad shoulders on either sides of this peak represent the carbon footprint of the molecular beam ($\varnothing = 1.7$ mm) due to chemisorption of unexcited CH_4 as shown in Fig. 4.4. The carbon signal outside the molecular-

beam footprint is due to carbon adsorbed from the background pressure in the chamber ($3 \cdot 10^{-10}$ mbar) during the 90 min deposition time. The rise in the carbon baseline is due to the electron beam induced carbon formation during the 30 min Auger analysis. For the calculation of the state resolved reactivity, we subtract an extrapolated “laser-off” baseline from the central peak and integrate the resulting “laser-on” carbon peak along the z direction. The width of this peak is significantly larger than the $\sim 50 \mu\text{m}$ width of laser focus along the z direction (see section 4.3.2). This difference results from angular misalignment between the laser focal lines and the molecular beam, the finite size of the Auger electron beam (FWHM = $140 \mu\text{m}$) and the spatial jitter of the two laser beams along the z direction. Due to the broadening, we use the C/Ni AES peak integral rather than peak height in our analysis of the state-resolved sticking coefficient.

To verify that the “laser-on” carbon peak is due to the excitation of the ν_1 transitions of the CH₄ molecules in the molecular beam, we repeat the deposition experiment under nearly the same molecular beam and laser energy conditions, but different Stokes frequencies. We obtain nearly the same Stokes energy for different dye laser frequencies by changing the methane pressure in the Raman amplifier in such a way that the maximum of the gain corresponds to the dye frequency at which we perform the deposition experiment. For example, for the depositions with dye frequencies of 15872.25 and 15872.55 cm^{-1} , we use methane pressures of 7 and 19 bar respectively. The normalized C/Ni AES peak integral (solid circle) resulting from these experiments is shown in Fig. 4.6 as a function of the Raman shift (difference between the second harmonic of the Nd:YAG laser frequency and the dye laser frequency). Table 4.4 shows pump and Stokes beam energies for the dye frequencies used to obtain the “laser-on” carbon peak integral values shown in Fig. 4.6. In Fig. 4.6, we show also the $Q(0)$, $Q(1)$, and $Q(2)$ transitions (stick plots) with their intensities at 8 K. We fitted the experimental points with a fitting function generated by the sum of three gaussians centered on the $Q(0)$, $Q(1)$, and $Q(2)$ transitions:

$$f(\nu) = A \left[I_0 \cdot e^{-\left(\frac{\nu-\nu_{Q(0)}}{B}\right)^2} + I_1 \cdot e^{-\left(\frac{\nu-\nu_{Q(1)}}{B}\right)^2} + I_2 \cdot e^{-\left(\frac{\nu-\nu_{Q(2)}}{B}\right)^2} \right], \quad (4.5)$$

where I_0 , I_1 , I_2 are the fractional populations of the $J = 0, 1$ and 2 ground state rotational levels for a rotational temperature of 8 K. $\nu_{Q(0)}$, $\nu_{Q(1)}$ and $\nu_{Q(2)}$ are the transition frequencies, and ν is the Raman shift. A and B are the fitting parameters. The former is a proportionality parameter that relates the Raman transition intensities to the C/Ni peak area. The latter represents the

dye frequency (cm^{-1})	Stokes energy (mJ)	Pump energy (mJ)	methane pressure (bar)
15872.25	210	270	7
15872.32	260	250	8
15872.35	250	250	8
15872.38	230	310	10
15872.42	230	230	12
15872.47	230	240	15
15872.55	220	250	19

Table 4.4: Pump and Stokes laser energies at the output of the Raman amplifier for different methane pressures and dye laser frequencies used to measure the “laser-on” carbon peak integral values shown in Fig.4.6.

laser bandwidth. The solid line in Fig. 4.6 represents the best fit to the experimental data. From the best fit, we obtain a laser beam bandwidth of $\sim 0.1 \text{ cm}^{-1}$, which is larger than the 0.05 cm^{-1} as determined using a spectrum analyzer. This difference is probably due to the power broadening of the Q -branch transitions in the molecular beam. We have observe a similar effect on the excitation of the $2\nu_3$ in the molecular beam⁵⁴. Figure 4.6 shows that no “laser-on” carbon peaks are detected if the difference between the two laser frequencies is not in resonance with the Q -branch transitions of ν_1 . With the results shown in Fig. 4.6, we are sure that with our lasers we excite the CH_4 molecules to the ν_1 state.

We calculate the state-resolved sticking coefficient by

$$S_0^{\nu_1} = \frac{N_{ads}}{N_{exc}}, \quad (4.6)$$

where N_{ads} is the integral of the “laser-on” carbon peak and N_{exc} is the density of molecules excited in the molecular beam.

In the next sections, we describe how we determine the rotational temperature of the CH_4 molecules in the molecular beam and N_{exc} .

4.3.1 CH_4 rotational temperature

For the determination of the reaction probability of CH_4 (ν_1) on $\text{Ni}(100)$, we need to know the number of molecules excited to ν_1 by SRP in the molecular beam. This depends on the fluence

of the laser beams crossing the molecular beam, on the fractional saturation of the transition and on the population of the initial level involved in the transition.

The latter is obtained by determining the populations of rotational levels in the vibrational ground state from measurements of the rotational temperatures of the jet expanded molecules with our CRD setup⁷¹.

For a correct interpretation of the transition intensities, the statistical weights of the starting levels of the corresponding transitions must be considered. In the previous sections, we report the degeneracies of the rotational wave functions. We need to include also the nuclear-spin statistic weight by considering the symmetry of the molecular wave function.

Nuclear spin statistics

The CH₄ molecule has four identical hydrogen nuclei with nuclear spin $\frac{1}{2}$. As these are fermions, the Pauli principle states that the exchange of two hydrogen nuclei results in a change of sign of the total wave function. From Figure 4.1, it can be seen that the effect of performing a \widehat{C}_3 or \widehat{C}_2 symmetry operation is equivalent to exchanging two pairs of hydrogen nuclei. Therefore, the total wave function should be symmetric under the \widehat{C}_3 and \widehat{C}_2 symmetry operations. From the character table of the T_d point group (table C.3 shown in Appendix C), one can observe that the A_1 and A_2 irreducible representations are the only ones that indicates a +1 eigenvalue for these symmetry operations. Therefore, the representation of the total wavefunction must contain a A_1 or A_2 irreducible representation in order to be consistent with the properties of hydrogen nucleus exchanges. Since we are concerned with the electronic and vibrational ground state ($\Gamma(\psi_e) \otimes \Gamma(\psi_v) = A_1$), only the symmetries of the rotational wave functions and the spin states have to be considered. The problem reduces to finding the combination of the irreducible representations for the rotational wavefunctions and spin states such that their direct product contains either A_1 or A_2 irreducible representation. Wilson has shown that this can be done by considering only the rotational sub-group T of the point group T_d ¹¹¹. In this case, the direct product between the representations of ψ_r and ψ_{ns} must satisfy:

$$\Gamma(\psi_r) \otimes \Gamma(\psi_{ns}) \supset A. \quad (4.7)$$

In Section 4.2.1, we have shown the decompositions in irreducible representations of the T sub-group representation formed by the rotational wave functions. Table 4.2 shows the symmetries of some of the rotational wave functions. In order to obtain the right symmetry, these functions

have to be combined with the spin states.

The hydrogen nuclear spins generate a set of $2^4 = 16$ spin states. The representation of the T group formed by the spin states is¹¹¹ $\Gamma(\psi_{ns}) = 5A + E + 3F$. We can observe three nuclear spin isomers: meta-methane (species A) has a total spin $I = 2$ and a degeneracy of $2I + 1 = 5$ (quintet); para-methane (E) is a nuclear singlet with $I = 0$; and ortho-methane (species F) has a total nuclear spin $I = 1$ and a degeneracy of 3 (nuclear spin triplet);

The nuclear spin weights for the allowed states are determined by multiplying the symmetries of the rotational wave functions with that of the nuclear spin isomers and by taking only the symmetric part of the resulting product. With the help of Table C.2 in Appendix C, we can observe that the spin states A combine with the rotational wave functions that include A symmetry (generate one allowed wave function). The spin states E combine with rotational wave functions that contain E symmetry and give rise to two allowed total wave functions ($E \otimes E = 2A + E$, only the two A species are allowed). The spin states F combine with the rotational wave functions that include the F symmetry and generate one allowed wave function.

Using the irreducible representations of the T_d point group, we can observe that the nuclear spin weights for the rotational wave functions are $g_I = 5$ for the A_1 and A_2 rotational levels, $g_I = 2$ for the E rotational levels and $g_I = 3$ for the F_1 and F_2 rotational levels. We can rewrite these results with the following equation:

$$g_I(\Gamma) = \begin{cases} 5 & \text{for } \Gamma = A_1 \text{ or } A_2 \\ 2 & \text{for } \Gamma = E \\ 3 & \text{for } \Gamma = F_1 \text{ or } F_2. \end{cases} \quad (4.8)$$

We can see that the rotational state with $J = 0$ (A_1 symmetry) is allowed only for meta isomer, $J = 1$ (F_1 symmetry) for the ortho isomer, and $J = 2$ ($E + F_1$ symmetries) is populated by both ortho and para isomers.

Determination of the rotational temperature

As described in Section 3.4.1, during the cooling process in a supersonic expansion, spin species do not inter-convert. In the case of CH_4 , we can consider the 3 different spin species as different molecules that cool down during the expansion with 3 different sets of rotational levels:

1. Meta-methane, with rotational states having symmetries A_1 or A_2 ($I = 2$).

2. Para-methane, with rotational states having symmetry E ($I = 0$).
3. Ortho-methane, with rotational states having symmetries F_1 or F_2 ($I = 1$).

One has to observe that a rotational state J can be populated by different spin species, e.g. the rotational state $J = 2$ is populated by the ortho- and para-methane spin isomers. Therefore, the fractional population of the rotational level J at a given temperature T , in a jet expansion, will be given by the sum of the fractional populations of each spin species contained in the rotational state J . This can be expressed with the following equation:

$$\begin{aligned}
 p(J, T) = & \chi_{meta} \sum_{\Gamma_{meta}=A_1, A_2} G(J, \Gamma_{meta}) g_I(\Gamma_{meta}) (2J + 1) \exp\left(-\frac{\epsilon(J, \Gamma_{meta})}{kT}\right) / Q_{meta}(T) \\
 & + \chi_{para} G(J, E) g_I(E) (2J + 1) \exp\left(-\frac{\epsilon(J, E)}{kT}\right) / Q_{para}(T) \\
 & + \chi_{ortho} \sum_{\Gamma_{ortho}=F_1, F_2} G(J, \Gamma_{ortho}) g_I(\Gamma_{ortho}) (2J + 1) \exp\left(-\frac{\epsilon(J, \Gamma_{ortho})}{kT}\right) / Q_{ortho}(T).
 \end{aligned} \tag{4.9}$$

The summations account for the cases where different nuclear spin isomers contribute to the population of a particular J state (e.g. $\Gamma(J = 2) = E + F_2$). In eq. 4.9, we have different terms:

- $G(J, \Gamma)$ is the frequency of occurrence of the irreducible representation Γ in the rotational level J (see eq. 4.4).
- $\epsilon(J, \Gamma)$ is the energy of the state (J, Γ) .
- $Q_{meta}(T)$, $Q_{para}(T)$ and $Q_{ortho}(T)$ are the rotational partition functions at temperature t of the spin species *meta*, *para*, and *ortho*, respectively.
- χ_{meta} , χ_{para} and χ_{ortho} are the high-temperature limit molar fractions of the spin species.

At room temperature, the number of populated rotational states is sufficiently large that the average density of occupied states of a given spin species corresponds to the sum of the dimensions for all the levels giving rise to a particular spin isomer. For the meta-methane: $[A_1] + [A_2] = 2$, for para-methane: $[E] = 2$, and for ortho-methane: $[F_1] + [F_2] = 6$. The molar fraction of different spin species at room temperature is given by the product of the nuclear spin weight g_I

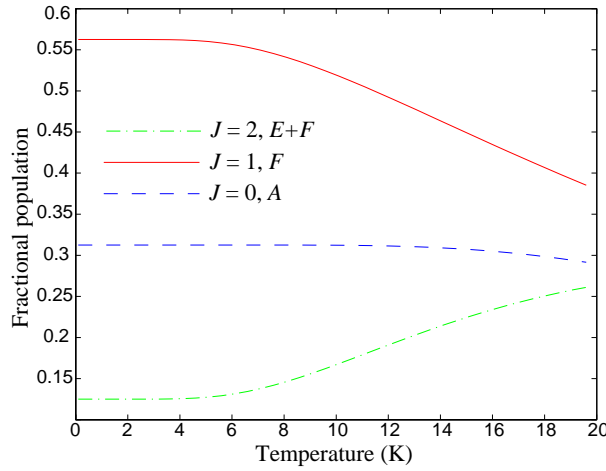


Figure 4.7: Fractional populations of the $J = 0, 1,$ and 2 rotational levels as a function of the rotational temperature after a supersonic expansion. The level $J = 2$ is formed by two nuclear spin species: the singlet (E) and the triplet (F).

with the density of occupied state for each species:

$$\begin{aligned}
 \chi_{meta} &= 5/16, \\
 \chi_{para} &= 2/16, \\
 \chi_{ortho} &= 9/16.
 \end{aligned}
 \tag{4.10}$$

The rotational partition functions for the different spin isomers can be written as:

$$\begin{aligned}
 Q_{meta}(T) &= \sum_J \sum_{\Gamma_{meta}=A_1, A_2} G(J, \Gamma_{meta}) g_I(\Gamma_{meta}) (2J+1) \exp\left(-\frac{\epsilon(J, \Gamma_{meta})}{kT}\right), \\
 Q_{para}(T) &= \sum_J G(J, E) g_I(E) (2J+1) \exp\left(-\frac{\epsilon(J, E)}{kT}\right), \\
 Q_{ortho}(T) &= \sum_J \sum_{\Gamma_{ortho}=F_1, F_2} G(J, \Gamma_{ortho}) g_I(\Gamma_{ortho}) (2J+1) \exp\left(-\frac{\epsilon(J, \Gamma_{ortho})}{kT}\right).
 \end{aligned}
 \tag{4.11}$$

The energies of the rotational levels are calculated using eq. 4.3 with the inclusion of the centrifugal distortion term. The fractional populations of the $J = 0, 1,$ and 2 rotational levels are shown as a function of the rotational temperature in Fig. 4.7.

	T_{rot} (K)	$J = 0$	$J = 1$	$J = 2$	$J = 3$
6% CH ₄ /H ₂ $T_{nozzle} = 423$	6 ± 1	0.31	0.56 ± 0.01	0.13 ± 0.01	0
12% CH ₄ /H ₂ $T_{nozzle} = 423$	8 ± 1	0.31	0.54 ± 0.01	0.15 ± 0.01	0

Table 4.5: Rotational temperatures measured for the two mixtures we use in our experiments. The fractional populations of the $J = 0, 1, 2,$ and 3 rotational levels are reported for the corresponding rotational temperature.

The intensity of a rotational transition from the initial state J'' to the final state J' are approximately given by¹⁰⁰:

$$I \propto p(J'', t)A(J'', J'), \quad (4.12)$$

where $A(J'', J')$ is the rotational factor:

$$A(J'', J') = \frac{2J' + 1}{2J'' + 1}. \quad (4.13)$$

For the Q branch transitions, the rotational factor is 1 and the transition intensities scales directly with the population of the initial level. We use the intensities of the $Q(1)$ and $Q(2)$ $2\nu_3$ band transitions to determine the temperature of the supersonically expanded CH₄ molecules. Using eq. 4.9, we calculate the population of the ground state rotational levels. In our deposition experiments, we use the 6% and 12% CH₄/H₂ mixtures both expanded at a nozzle temperature of 423 K. Table 4.5 shows their rotational temperatures (T_{rot}) and the corresponding populations of the $J \leq 3$ levels.

4.3.2 Number of molecules excited in the molecular beam

The number of CH₄ molecules excited to ν_1 depends on the saturation parameter of the Raman transitions, on the laser beam intensity profiles, and the laser energies and on the population of the initial level involved in the transition. In the previous section, we have explained how we determine the populations of the rotational levels in the vibrational ground state. In this section, we explain how we determine the other factors.

The laser beam intensity profiles

We determine the laser beam intensity profiles at the position of the molecular beam using a CCD camera (Gentec, WinCamD). Figure 4.8 shows the setup used to determine the sizes of the

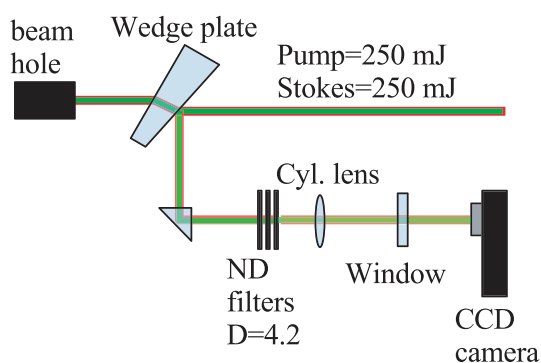


Figure 4.8: Optical setup used to record the laser beam profiles. We reproduce the same optical path between the lens and the molecular beam by placing an IR-SiO₂ window identical to that installed in the surface science chamber (6 mm thickness) after the cylindrical lens.

laser beam in the focal point. We split 10% of the pump and Stokes beam energies by reflecting the beam from a wedge plate. Some neutral density filters (OD=4.2) are installed before the lens to additionally reduce the beam intensities. We set the distance between the lens and the CCD detector equal to that between the lens and the molecular beam used during the deposition experiments (298 ± 0.5 mm). In order to reproduce the same optical path of the deposition experiments, we place a 6 mm thickness IR-SiO₂ window between the lens and the molecular beam. This window is identical to that installed in the surface science UHV chamber. We measure the laser beam profiles by recording 100 laser shots averaged images, which are saved and subsequently analyzed using MatLab 6.5. Figure 4.9 shows one 100 laser-shots averaged image. In order to measure the intensity profiles of the pump and the Stokes radiation, the two laser beams are intentionally misaligned, the pump is displayed below the Stokes beam. The x direction is parallel to the molecular beam axis and z is the focusing direction (see Fig. 4.4). We determine the sizes of the laser beams from the image shown in Fig. 4.9 by knowing that each pixel has an area of $4.3 \times 4.3 \mu\text{m}^2$. The sizes of the two beams along the z direction is obtained by fitting two gaussians to the vertical section of the image in Fig. 4.9. The fitting results together with the experimental points are shown in Fig. 4.10a.

The FWHM of the beams along the z direction for a lens-CCD distance of 298 ± 0.5 mm are 55.6 ± 0.7 and $34.7 \pm 0.8 \mu\text{m}$ for the Stokes and pump beam respectively. Along the x direction the intensity profiles of the two laser beams can not be fitted with simple gaussian. This is due to the “pear-like” shape of the pump beam before entering in the Raman amplifier. In order to fit correctly the intensity profile along the x direction, the sum of three gaussians with a linear baseline is used as a fit function. The best fit of the pump beam intensity along the x direction

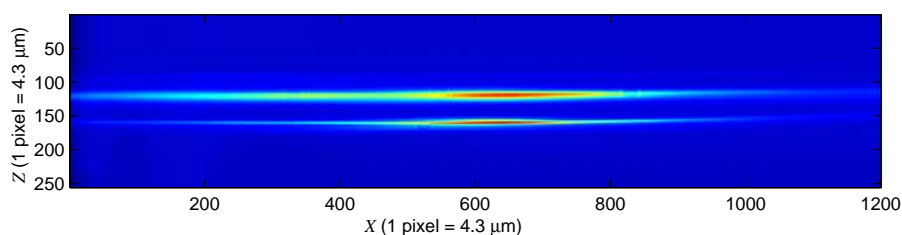
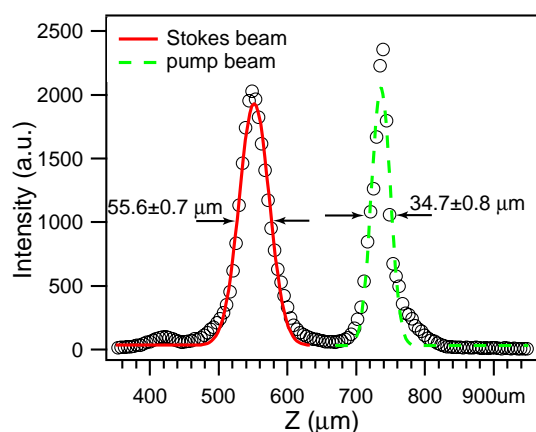
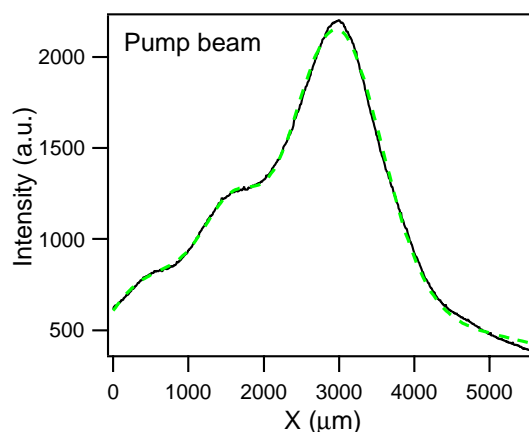


Figure 4.9: Pump (lower part) and Stokes (upper part) beam intensities as recorded by the CCD camera. The x direction is parallel to the molecular beam axis and the z is the focusing direction (see Fig. 4.4). Each pixel has a dimensions of $4.3 \times 4.3 \mu\text{m}^2$. The distance between the lens and the CCD detector is $298 \pm 0.5 \text{ mm}$.



(a) Pump (dashed line) and Stokes (solid line) beam intensity profiles along the z direction.



(b) Intensity profile of the pump laser beam section along the x direction (solid line). The dashed line is the best fit to the experimental points. The fitting function is the sum of three Gaussians.

Figure 4.10: Analysis of the image in Fig. 4.9. Figures (a) and (b) are the sections along the x and z directions respectively.

(dashed line) is shown in Fig. 4.10b together with the experimental points (solid line). The fit results for the beam intensities along the x direction are shown in Table 4.6. In this table, “Gaussian 1” is set by definition to be the most intense (Rel. int.=1) and centered in the origin.

We determine the confocal parameter of the focused beams by recording images as a function of lens-CCD distance. The result is shown in Fig. 4.11. The confocal parameters as deduced by the best fits to the experimental points are 5 and 8 mm for the Stokes and pump beams respectively.

<i>x</i> direction fitting results				
pump beam		Gaussian 1	Gaussian 2	Gaussian 3
	Rel. int.	1	0.36 ± 0.01	0.192 ± 0.008
	Center (cm)	0 ± 0.0003	-0.142 ± 0.002	-0.238 ± 0.002
	FWHM (cm)	0.149 ± 0.001	0.092 ± 0.003	0.11 ± 0.01
Stokes beam		Gaussian 1	Gaussian 2	Gaussian 3
	Rel. int.	1	0.624 ± 0.001	0.260 ± 0.001
	Center (cm)	0 ± 0.0003	-0.137 ± 0.002	-0.233 ± 0.002
	FWHM (cm)	0.173 ± 0.001	0.090 ± 0.003	0.085 ± 0.01

Table 4.6: Fit results for the beam intensities along the *x* direction. Rel. int. are the relative intensities of the gaussians in the fit, Gaussian 1 is set by definition to be the most intense and centered in the origin.

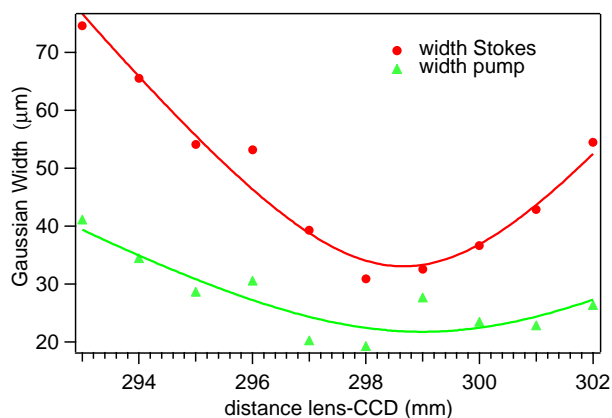


Figure 4.11: Gaussian width for Stokes (●) and pump (Δ) beams are reported as a function of lens-CCD distance.

The saturation parameter of the Raman transitions

The fractional saturation of the Raman transitions is determined by fitting a numerical model of the Raman excitation process, including the laser beam profiles, to the fluence dependence of the “laser-on” carbon signal. We change the laser beam energies by placing up to 10 glass windows before the cylindrical lens. Using our CCD camera, we verify that placing glass windows in the laser beams does not change the sizes of the beams in the focal points and does not shift one beam with respect to the other.

For SRP, the number of excited molecules in a sample illuminated by 2 laser beams depends

on the product of the two laser beam intensities (I_p , I_s), and can be expressed via the formula¹¹⁹ (see appendix D, eq. D.45):

$$\Delta N = \Delta N_0 \exp^{-AI_p I_s \frac{\Gamma}{\Delta\omega^2 + \Gamma^2} \Delta t}, \quad (4.14)$$

where

$$A = \frac{8\pi^2 c^2}{\hbar^2 \omega_p \omega_s^3} \frac{d\sigma}{d\Omega}. \quad (4.15)$$

I_p and I_s are the intensities of the pump and Stokes beams, ΔN corresponds to the population difference, and ΔN_0 to the initial population difference (without laser beams). $\Delta\omega$ is the laser detuning, Δt the interaction time, Γ the convolution of the laser width and transition width, ω_p and ω_s are respectively the pump and Stokes photon frequency, and $d\sigma/d\Omega$ is the transition cross section. However, a real laser beam has a certain spatial intensity distribution ($I_p(\mathbf{r})$, $I_s(\mathbf{r})$), under these circumstances equation 4.14 is valid locally and ΔN depends on the spatial coordinates \mathbf{r} . Using eq. 4.14 the local excited fraction of molecules $f(x, z)$ can be written as:

$$f(x, z) = f_{exc,max}^{laser} (1 - \exp\{-AI_p(x, z)I_s(x, z)[\Gamma/(\Delta\omega^2 + \Gamma^2)]\Delta t\}), \quad (4.16)$$

where $f_{exc,max}^{laser}$ is the maximum fractional population that can be transferred to the upper state at saturation. The x direction is parallel to the molecular beam axis and the z direction is parallel to the focusing direction of the cylindrical lens (see Fig. 4.4). During the fluence dependence experiments, we monitor the energies of the laser beams and not the intensities. However, we can express the laser beam intensities as a function of the laser beam energies E_p and E_s by

$$I_p(x, z) = E_p \cdot g_p(x, z) \text{ and } I_s(x, z) = E_s \cdot g_s(x, z), \quad (4.17)$$

where $g_p(x, z)$ and $g_s(x, z)$ are the normalized intensity distributions of the pump and Stokes beams as determined with the CCD camera (see previous section). We can rewrite eq. 4.16 in terms of laser beam energies E_s , and E_p :

$$f(x, z) = f_{exc,max}^{laser} [1 - \exp(-\beta E_p E_s g_p(x, y) g_s(x, y))], \quad (4.18)$$

where

$$\beta = A \frac{\Gamma}{\Delta\omega^2 + \Gamma^2} \Delta t. \quad (4.19)$$

We call β the *saturation parameter*.

If D is the number of molecules per unit volume in the molecular beam, and it is considered uniform in the molecular beam pulse, then the number of molecules excited N_{exc} in the molecular beam per unit of length can be expressed via:

$$N_{exc} = D \int \int f(x, z) dx dz \quad (4.20)$$

In order to integrate equation 4.20, the intensity profiles can be subdivided in intervals $(\Delta x \Delta z)$ small enough to consider $I_p(x, z)$ and $I_s(x, z)$ constant inside each interval. With this approximation, the integrals in equation 4.20 can be replaced with summations :

$$N_{exc} = D \Delta x \Delta z \sum_{ij} f^{ij}, \quad (4.21)$$

where f^{ij} is:

$$f^{ij} = f_{exc,max}^{laser} [1 - \exp(-\beta E_p E_s g_p^{ij} g_s^{ij})]. \quad (4.22)$$

Where g_p^{ij} and g_s^{ij} are the intensity distribution values inside the interval ij . For these experiments the sizes chosen for Δx and Δz are respectively 50 μm and 1 μm . Decreasing the step sizes does not change significantly the integral values, but increases the computing time.

The equation used to fit the “laser-on” carbon signal as a function of the product of the two laser energies ($E_s \cdot E_p$) is:

$$C(E_s \cdot E_p) = \alpha \Delta x \Delta z \sum_{ij} [1 - \exp(-\beta E_s E_p g_s^{ij} g_p^{ij})], \quad (4.23)$$

where α and β are the fitting parameters.

Figure 4.12 shows the normalized C/Ni AES peak area as a function of the product of the pump and Stokes beam energies.

We fit eq. 4.23 to the experimental points reported in Fig. 4.12 using a program written for MatLab 6.5 (see Appendix E for the program source). This program numerically evaluates $C(E_s \cdot E_p)$ in eq. 4.23 for given $E_s \cdot E_p$, α , and β . The best-fitting curve to the experimental data points is found by minimizing the sum of the squares of the offsets (“the residuals”) of the experimental data points from the calculated curve. The program iteratively changes α and β until convergence is achieved, that is when the minimum value of the sum of the squared offsets is found. The solid line in Fig 4.23 is the best-fitting curve obtained. The determined saturation

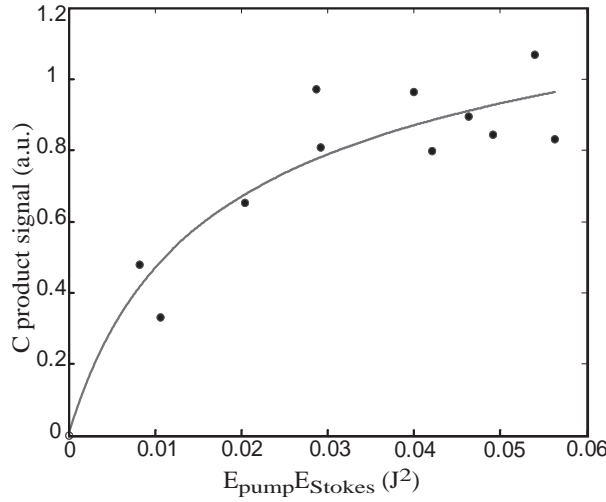


Figure 4.12: Fluence dependence of laser-on carbon signal produced by chemisorption of $\text{CH}_4(\nu_1)$.

parameter is $\beta = 305 \text{ cm}^4/\text{J}^2$.

The number of excited molecules per unit length in each molecular beam pulse is then calculated by replacing the value of β in eq. 4.21. Alternatively, we calculate the saturation parameter using eq. 4.19 by replacing: $\Gamma = 0.11 \text{ cm}^{-1}$ (convolution between the three transitions $Q(0)$, $Q(1)$ and $Q(2)$, and the laser width, see Fig. 4.6), $d\sigma/d\Omega = 1.85 \cdot 10^{-30} \text{ cm}^2/(\text{mol}\cdot\text{ster})$,¹²⁰ $\omega_p = 3.5408 \cdot 10^{15} \text{ 1/s}$, $\omega_s = 2.9995 \cdot 10^{15} \text{ 1/s}$, and $\Delta t = 9 \cdot 10^{-9} \text{ s}$. We find that $\beta_{\text{calculated}} = 613 \text{ cm}^4/\text{J}^2$.

We calculate the state-resolved sticking coefficient using both values of β and we found that the difference between the sticking coefficients is less than 10%.

The molecular density D in each beam pulse can be calculated by:

$$D = \frac{\phi}{v_0 \tau_{\text{pulse}}} \frac{1}{\nu_{\text{pulse}}} \left[\frac{\text{molecules}}{\text{cm}^3} \right], \quad (4.24)$$

where ϕ is the molecular beam flux in $\text{molecules}/(\text{s}\cdot\text{cm}^2)$, v_0 , τ_{pulse} and ν_{pulses} are the beam velocity, the pulse duration and the repetition rate of the molecular beam pulses (see Chapter 2). We calculate the number of excited molecules per centimeter sent on the surface during the deposition using eq. 4.21 and 4.24:

$$N_{\text{exc}} = f_{\text{exc,max}}^{\text{laser}} \cdot D \cdot t_{\text{dose}} \cdot \nu_{\text{pulse}} \cdot \Delta x \cdot \Delta z \cdot \sum_{ij} f^{ij} \left[\frac{\text{Excited molecules}}{\text{cm}} \right], \quad (4.25)$$

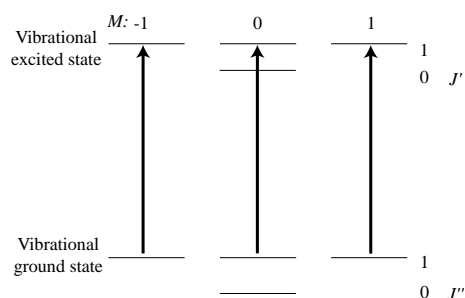


Figure 4.13: Level scheme for a CH_4 Q(1) Raman transition. Because linearly polarized light can induce $\Delta M = 0$, all the excited levels are populated and at complete saturation of the transition, 0.5 of the molecules in the ground state are transferred to the upper vibrational state.

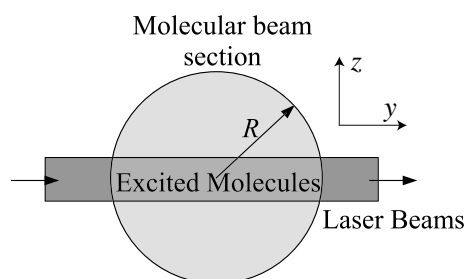


Figure 4.14: Section perpendicular to the molecular beam direction of the excitation region. Laser beams fly from left to right.

where t_{dose} is the exposure time. $f_{exc,max}^{laser}$ represents the maximum fraction of molecules that can be excited at saturation. Since for a Raman transition with $\Delta J = 0$ we have that $\Delta M = 0$,¹²¹ all levels of the ground state combine with all the levels of the excited state and at saturation half of the ground state molecules can be excited to the upper vibrational state (see Fig. 4.13).

If one wants to determine the total number of molecules excited in the molecular beam, the quantity N_{exc} has to be multiplied by the diameter ($2R$) of the molecular beam, which corresponds more or less to the length that the two laser beams travel inside the molecular beam (see figure 4.14). However this length does not play a role in the calculation of S_0 . In the surface analysis, a number of molecules per unit length is obtained as well, and the ratio between the number of attached molecules and N_{exc} cancels the length dimension mentioned above. For a 12% CH_4/H_2 mixture with nozzle temperature of 423 K (average speed = 2470 ± 20 m/s), using eq. 4.25, we calculate that $\sim 0.1\%$ of the molecules in the molecular beam pulses are excited by the SRP lasers. If we assume that the laser beam intensity profiles are constant

in the illuminated region, we can estimate the fraction of molecules excited in the molecular beam by the ratio between the volume of illuminated molecules and the molecular beam pulse volume. The former can be approximately written as:

$$V_{ill.} = w \cdot l \cdot 2R = 50 \cdot 10^{-3} \cdot 2 \cdot 1.9 \sim 0.2 \text{ mm}^3,$$

where w and l are the FWHMs of the beam intensity profiles along z and x directions as determined by the CCD camera, and R is the radius of the molecular beam. The volume of a molecular beam pulse that flies at 2470 m/s is:

$$V_{pulse} = 2470 \cdot \tau_{pulse} \cdot \pi \cdot R^2 = 2470 \cdot 26.6 \cdot 10^{-6} \cdot (0.95)^2 = 184 \text{ mm}^3.$$

If we assume that the transitions are completely saturated, then half of the molecules in the illuminated region are excited by the laser beams. We can estimate the fraction of excited molecules from

$$\frac{V_{ill.} \cdot 0.5}{V_{pulse}} \sim 0.05\%.$$

The fraction of excited molecules in the molecular beam that we calculate from eq. 4.25 is larger than 0.05% because of the power broadening of the illuminated region.

Laser beam widths and carbon peak width along the z direction

We have already mentioned that there is a substantial difference between the sizes of the laser beams in the focal point and the observed carbon peak width. This difference is due to the following factors:

- spatial jitter of the two laser beams along the z direction, included in the CCD measurements if sufficient averaging,
- angular misalignment between the laser focal line and the molecular beam axis,
- molecular beam divergence,
- finite size of the Auger electron beam (step size in analysis= 50 μm).

If these broadening factors are not present, the carbon profile on the surface would be equal to the profile of the excited fraction along the z direction $f(z)$. Due to power broadening, $f(z)$ is wider than the laser beam intensity distributions. Using the value of β found in the previous

section and eq. 4.18, we calculate that the width of $f(z)$ is $\sim 60 \mu\text{m}$, which is the width of the carbon spot we would expect if no other broadening factors take place.

We determine the spatial jitter of our laser beams using our CCD beam profile analyzer. We record an image made by averaging up to 8000 laser shots and we find that the width of the laser beams determined from this image is $\sim 50 \mu\text{m}$ larger than the laser beam widths determined by acquiring a 100 shots averaged image. The width difference is due to the displacements of the laser beams (spatial jitter) while we acquire the averaged image. We verify that the beam width obtained with a single-shot image is equivalent to that obtained from a 100 shots averaged image. The laser beam dimensions along the x direction are $\sim 2.5 \text{ mm}$, assuming a misalignment of 1° we have a broadening of around $40 \mu\text{m}$. The divergence of the molecular beam is estimated by knowing that the aperture that transmits the molecular beam pulses in the UHV chamber has a diameter of 1 mm and that 100 mm downstream the molecular beam foot print on the crystal has a diameter of $\sim 2 \text{ mm}$ (see Fig. 2.2 in chapter 2). Since the distance between the excitation region and the crystal surface is $\sim 40 \text{ mm}$, we expect a change in width of $\sim 25\%$. The carbon peak on the surface is additionally broadened during the surface analysis due to the finite size of the electron beam ($140 \mu\text{m}$) of our Auger spectrometer. Starting from a $60 \mu\text{m}$ width, due to power broadening, and adding each broadening factor we find a carbon peak width of $\sim 240 \mu\text{m}$. The width of the C/Ni AES peak is $300 \pm 40 \mu\text{m}$ on the nickel surface, which corresponds to an angular misalignment of $\sim 2^\circ$. We have performed deposition experiments for different lens angles and we have not observed measurable differences in the width of the C/Ni AES peak. We can explain this by assuming that the other broadening factors are predominant and hide the angular dependence of the cylindrical lens in C/Ni AES peak width. An additional broadening factor comes from the fact that the cylindrical lens is fixed on the UHV chamber and not on the optic table. Since the vacuum pumps induce some vibrations on the UHV chamber, an additional spatial jitter of the laser beams can be introduced by the vibration of the lens.

These estimations of the broadening effects show how it is important to determine the state-resolved sticking coefficient from the area of the “laser-on” carbon peak and not from the peak height. Whatever broadening we can have the area of the “laser-on” carbon peak is conserved. On the other hand, it complicates the determination of the sticking coefficient because the intensity distributions of the laser beams along the z direction must be determined.

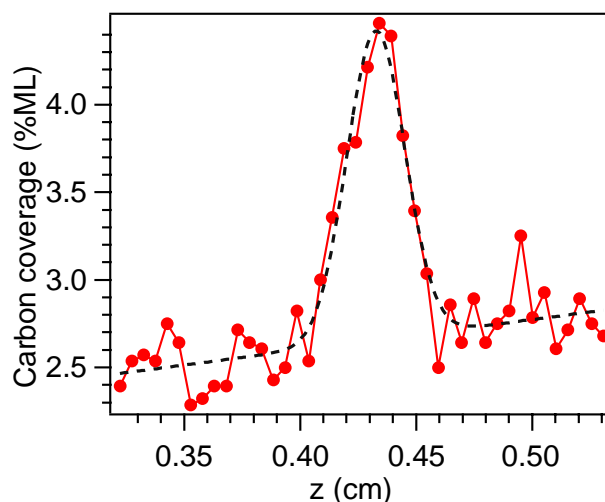


Figure 4.15: Surface analysis after the deposition. A function given by the sum of a straight line (baseline) and a gaussian (“laser on” peak) is fitted to the experimental points. The dashed line represents the best fit.

4.3.3 Calculation of the state-resolved sticking coefficients

As example, we report the calculation of the sticking coefficient of the 12% CH_4/H_2 mixture with nozzle temperature of 423 K. Using our TOF setup, we measure an average speed of 2470 ± 20 m/s ($\Delta V/\langle V \rangle = 0.06$). The molecular beam is pulsed at 20 Hz and the pulse duration is $(26.6 \pm 0.1) \times 10^{-6}$ s. The Ni(100) crystal is exposed for 5400 ± 1 s to the molecular beam, and during the deposition, the QMS measures an average of 2045 ± 10 counts/s at 16 amu, corresponding to a beam flux of $(1.01 \pm .02) \times 10^{14}$ molecules/(cm^2s). The overall density of methane molecules generated by the total number of molecular beam pulses during the deposition corresponds to $D \cdot t_{dose} \cdot \nu_{pulse} = (9.04 \pm 0.04) \times 10^{16}$ molecules/ cm^3 (see eq. 4.24). The laser beam energies are 259 ± 20 mJ for the Stokes and 217 ± 20 mJ for the pump. Using equation 4.25, we determine the fraction of excited molecules in the entire molecular beam to be 0.1% and the number of excited molecules incident on the surface during the deposition is $N_{exc} = (8.4 \pm 1.1) \times 10^{13}$ molecules/cm. Figure 4.15 shows the AES scan results. In this case, the footprint of the molecular beam is not observed because the sticking coefficient of the unexcited molecules is too low²² ($\sim 10^{-5}$) to produce a detectable quantity of carbon.

From the AES scan result shown in Fig. 4.15, we find a carbon density (“laser-on” peak

integral) of $N_{ads} = (9 \pm 1.2) \times 10^{11}$ atoms/cm. The sticking coefficient found is:

$$S_0^{\nu_1} = N_{ads}/N_{exc} = 0.011 \pm 0.0045. \quad (4.26)$$

The uncertainties for these measurements are calculated by combining the statistical and systematic errors. The statistical uncertainties are determined by the standard deviation of repeated measurements. The systematic error is obtained from the uncertainty propagations of the terms that we use to calculate $S_0^{\nu_1}$. The major source of uncertainty comes from our estimation of the focal volume. We estimate that the $S_0^{\nu_1}$ values have the relative uncertainty of 40%.

4.4 Results and discussion

The state-resolved sticking coefficient $S_0^{\nu_1}$ obtained from the ratio between the integrated carbon signal and the incident dose of $\text{CH}_4(\nu_1)$ is shown in Fig. 4.16 for 49 and 63.5 kJ/mol of translational energy. For comparison, we show state-resolved sticking coefficients for the anti-symmetric stretch, $S_0^{\nu_3}$, reported by Juurlink *et al.*^{21,64}, as well as our previous measurements²² of $S_0^{2\nu_3}$ and of $S_0^{laser-off}$. Experimental limitations prevented us from measuring $S_0^{\nu_1}$ at higher and lower kinetic energies: for the higher kinetic energies, the difference in reaction probability between unexcited and laser-excited molecules decreases rapidly, making the "laser-on" peak too difficult to detect above the "laser-off" background; for lower kinetic energy, the reactivity of the laser-excited beam is too low to produce a detectable carbon signal above that from the residual gas in the chamber.

For the two kinetic energies investigated, we found $S_0(\nu_1)$ to be almost equal to $S_0^{2\nu_3}$ measured previously with our setup using IR overtone excitation²², despite the fact that the former has half the amount of vibrational energy. Moreover, comparison of our results for $S_0^{\nu_1}$ with those for $S_0^{\nu_3}$ obtained by Juurlink *et al.*^{21,64} shows that excitation of CH_4 to the symmetric stretch (ν_1) increases the reactivity approximately 10 times more than excitation to the antisymmetric stretch (ν_3). Such a large difference in reactivity between two nearly isoenergetic states is a clear sign of mode-specific chemisorption of CH_4 on Ni(100) and is totally inconsistent with a statistical description of the reaction^{89,90}. We have previously observed vibrational mode specificity in the reaction of CD_2H_2 on Ni(100), where excitation of the combination band ($\nu_1+\nu_6$) containing one quantum each of symmetric and antisymmetric CH stretch vibration increases

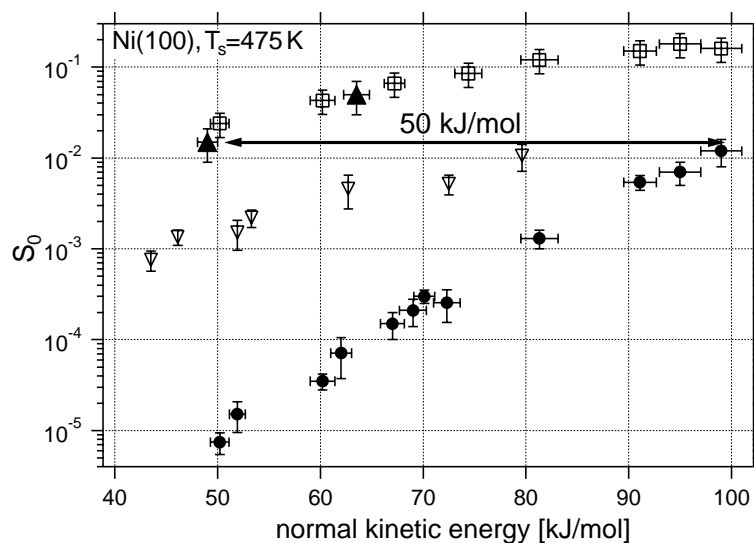


Figure 4.16: State-resolved sticking coefficients for CH_4 in the ν_1 (▲), $2\nu_3$ (□)²², ν_3 (▽)⁶⁴, and ground (●)²² vibrational states on Ni(100) as a function of incident kinetic energy normal to the surface. The error bars represent the 95% confidence interval of the convolute uncertainties. The major source of uncertainty comes from our estimation of the focal volume.

the reactivity up to 5 times more than the antisymmetric stretch overtone ($2\nu_6$)¹⁰⁹. In this case, the difference in reactivity for the two isoenergetic states of CD_2H_2 could be rationalized by the different vibrational amplitudes of the two CH bonds for the initially prepared quantum states. This is consistent with a number of gas phase examples of bond-specific chemistry where the reactivity of a bond is directly related to its amount of stretch excitation^{27,28}.

For CH_4 , the observed difference in reactivity between ν_1 and ν_3 cannot be explained simply in terms of bond specific laser excitation, since all four CH bonds initially carry amplitude for both states. However, recent theoretical models based on a vibrationally adiabatic treatment^{24,34,56,58-60} suggest that the interaction with the approaching reaction partner can lead to energy localization which is different for different initial states, resulting in mode-specific reactivity, and this has been confirmed by experimental results in gas-phase reactions^{29,31}. Halonen et al.²⁴ used this vibrationally adiabatic model to simulate the interaction of a vibrating CH_4 molecule with a flat nickel surface. They calculate how the vibrational energies of the symmetric and antisymmetric stretches of CH_4 change as the molecule adiabatically approaches onto the metal surface. To perform this calculation, several approximations are made. First, the HCH valence angle is considered constant, then the bending motions are neglected. Second, the molecular orientation with respect to the surface is kept constant with one C-H bond pointing

the surface and the other three are considered equivalent. Finally, the interaction between the surface and the molecule occurs only via the unique C-H bond. Specifically, the potential is treated as a function of the Ni-H and Ni-CH₃ pseudo-diatomic distances. They predict that the vibrational energy of the symmetric and antisymmetric stretches becomes localized in the unique C-H bond pointing the surface (proximal) and in the three C-H bonds pointing outside the surface (distal) respectively during the adiabatic approach toward the surface. Based on this, they suggest that CH₄(ν_1) should be significantly more reactive than CH₄(ν_3) in the adiabatic limit. In calculations for gas-phase reactions^{34,56-60}, similar vibrational adiabatic models are used to investigate the reactivity of vibrationally excited molecules. All these calculations show that the symmetric stretch of the reactant transforms adiabatically into the stretching of the bond that breaks during the reaction. In fact, Halonen et al. suggested that the experimentally observed increase in reactivity for CH₄ upon excitation of ν_3 is due to curve-crossing to the reactive ν_1 state at incident speed above the Massey velocity²⁴. The large difference between $S_0^{\nu_1}$ and $S_0^{\nu_3}$ that we observe would indicate that the mixing due to the curve crossing is far from complete at the kinetic energies of our experiment. Although the predictive capabilities of the vibrationally adiabatic model alone may be limited due to its strongly simplifying assumptions, it is reinforced by the experimental observation of a large difference in reactivity for the symmetric and antisymmetric stretch vibrations. Moreover, the experimentally confirmed prediction of the vibrationally adiabatic model should encourage efforts to develop more sophisticated dynamical treatments of methane chemisorption. On the other hand, our results are clearly inconsistent with statistical theories, which assume rapid intramolecular energy randomization and predict reactivities that scale with total internal energy independent of the initially excited vibrational state.

Yoon *et al.* introduced a simple model to explain the difference in reactivity between the symmetric and antisymmetric stretches²⁹. In this model, the vibrations are described in terms of symmetry coordinates. Table 4.7 shows the symmetry coordinates for the degenerate ν_3 vibrations (F_2) and the ν_1 vibration (A_1) of isolated CH₄ (T_d symmetry) in terms of the extensions of the four C-H bonds (r_1 , r_2 , r_3 and r_4)¹²². The approaching of one C-H bond towards the surface changes the symmetry from T_d to C_{3v} . This external perturbation changes also the symmetries of the vibrations of CH₄ and allows the two asymptotically isolated vibrational states to interact. In the reduced symmetry, ν_{3a} and ν_{3b} become the vibrations with symmetry E and ν_{3c} and ν_1 acquire A_1 symmetry. The interaction of the A_1 component of ν_3 vibrational state with ν_1 produces two adiabatically coupled states corresponding to the coordinates $S_p = r_1$ and

$\text{CH}_4 (T_d)$		$\text{Ni} \cdots \text{H-CH}_3 (C_{3v})$	
F_2	$\nu_{3a} : S_{3a} = \frac{1}{2}(r_1 - r_2 + r_3 - r_4)$	$\left\{ \begin{array}{l} E \\ A_1 \\ A_1 \end{array} \right\}$	$S_a = \frac{1}{\sqrt{6}}(2r_2 - r_3 - r_4)$
	$\nu_{3b} : S_{3b} = \frac{1}{2}(r_1 - r_2 - r_3 + r_4)$		$S_b = \frac{1}{\sqrt{2}}(r_3 - r_4)$
	$\nu_{3c} : S_{3c} = \frac{1}{2}(r_1 - r_2 - r_3 - r_4)$		$S_d = \frac{1}{\sqrt{3}}(r_2 + r_3 + r_4)$
A_1	$\nu_1 : S_1 = \frac{1}{2}(r_1 + r_2 + r_3 + r_4)$		$S_p = r_1$

Table 4.7: Correlation of the symmetric and antisymmetric stretching vibrations of the reactant in T_d point group to the localized vibrations in curvilinear symmetry coordinates.

$S_d = 1/\sqrt{3} \cdot (r_2 + r_3 + r_4)$ shown in the right-hand side of Table 4.7. The S_p and S_d states have their vibrational motion localized in the reactive proximal bond and in the spectator distal bonds, respectively. For a vibrationally adiabatic reaction, the symmetric stretching vibration of the reactant, which usually lays lower in energy than the antisymmetric stretching vibration, correlates to localized excitation in the proximal bond and the antisymmetric stretching vibrations correlate to localized excitation in the distal bonds. Then, in the adiabatic limit, the symmetric stretch should promote the reaction better than antisymmetric stretching excitation in T_d molecules having a symmetric stretch lower in energy than the antisymmetric stretch²⁹. In these cases, the state specificity has a more profound sense than that showed in the experiments with CD_2H_2 . The difference in reactivity between two different vibrational states does not only depend on the quantity of vibrational energy contained in each bonds, but it is influenced also by the symmetries of the vibrational states excited (mode-specific reactivity). Since the ν_1 and ν_3 states have similar energies and vibrational motions that differ primarily by the phase of the C-H bond stretches (different symmetries), our results give a clear example of mode-specific reactivity.

Using a different approach than vibrationally adiabatic models previously cited, Milot et al.²³ have performed wave packet calculations of methane scattered from a flat surface, including all nine internal vibrations and with three C-H bonds pointing the surface. Based on the calculated kinetic energy loss during the collision, they predicted the same trend in reactivity: $\nu_1 > \nu_3 > \nu_4 > \text{ground state}$.

In addition to comparing the effect of different vibrational modes on the reactivity of methane on nickel, we can compare the effect of vibrational energy in ν_1 with that of translational energy. One can see from Fig. 4.16 that putting 35 kJ/mol of vibrational energy in ν_1 results in the

same increase in reactivity as adding 50 kJ/mol of kinetic energy normal to the surface. This indicates that energy in ν_1 is 1.4 times more efficient than translational energy in promoting the reaction. A similar effect has been observed for $\text{CH}_4(\nu_3)$ on $\text{Ni}(111)$ ¹²³, where the relative efficacy of ν_3 was found to be 1.25 compared to translational energy. Smith et al. have argued that an efficacy larger than one can result either from lattice recoil, where some translational energy is lost to the motion of the surface¹⁸, or from non-adiabatic dynamics, where ground state molecules do not follow the minimum energy path due to coupling between translation and vibration¹²³.

In conclusion, we have used stimulated Raman pumping to measure for the first time the state-resolved surface reactivity of CH_4 in its totally symmetric CH stretch vibration (ν_1). We found that the reactivity of the symmetric-stretch excited CH_4 is about an order of magnitude higher than that of methane excited to the antisymmetric stretch (ν_3) reported by Juurlink *et al.*²¹ and is similar to that we have previously observed for the excitation of the first overtone ($2\nu_3$). A comparison of our results with those using direct IR excitation of the ν_3 and $2\nu_3$ vibrations confirms the qualitative predictions of simple vibrational adiabatic calculations and wave packet simulations^{23,24} and suggests that quantitative predictions of methane reactivity will require dynamical calculations on a realistic multi-dimensional potential energy surfaces²⁵. Our results clearly indicate that statistical models do not capture the essential physics of the reactive encounter and therefore can neither qualitatively nor quantitative predict methane chemisorption.

Discussion and outlook

5.1 Discussion

For the first time, our experimental results show the evidence of vibrational state specificity in a gas-surface reaction. We have measured the reactivity of CD_2H_2 prepared in two vibrational states that have almost the same vibrational energy, but correspond to different motions of nuclei: the $\nu_1 + \nu_6$ (5879 cm^{-1}) and $2\nu_6$ (5999 cm^{-1}) vibrational states.

Our results show that, for the lowest kinetic energy investigated (41 kJ/mol), the CD_2H_2 molecules prepared in the $\nu_1 + \nu_6$ state are 5.4 times more reactive than those prepared in the $2\nu_6$ state.

We have rationalized our results in terms of a spectator model and bond-specific reactivity. Molecules excited to the $\nu_1 + \nu_6$ state are more reactive than those excited to the $2\nu_6$ state because the former contains two quanta of stretching vibration in a single C-H bond, whereas the latter contains two quanta in each C-H bond. The difference in reactivity between the molecules excited to the $\nu_1 + \nu_6$ and $2\nu_6$ states has suggested that the C-H bond stretch has a substantial projection on the reaction coordinate, in agreement with ab-initio calculations of the transition-state structure which is predicted to have a single C-H bond pointing towards the surface largely elongated ($\sim 0.5\text{ \AA}$)¹⁶.

Our measurements are inconsistent with the statistical model developed by Bukoski *et al.*^{52,89}, where the initial vibrational energy in methane is randomized via intramolecular energy redistribution (IVR) as the molecule transiently resides in a local “hot-spot” and interacts with a limited number of surface atoms. This model predicts the reactivity to scale only with the total

available energy independent of vibrational state. In contrast to the assumptions of the statistical model, our observation that CD_2H_2 retains a clear memory of the initially prepared quantum state has confirmed that its interaction with the metal surface does not induce complete IVR before the reaction occurs. We estimate that the CH_4 -surface collision complex has a lifetime of $\sim 10^{-13}$ s. Our results show that the IVR process at the transition state occurs on a timescale slower than 10^{-13} s.

In this work, we have also reported the state-resolved reactivity on Ni(100) of methane prepared in the symmetric stretch $\text{CH}_4(\nu_1)$. Our results show that the $\text{CH}_4(\nu_1)$ molecules are 10 times more reactive than the molecules prepared in the antisymmetric stretch $\text{CH}_4(\nu_3)$. As in the case of CD_2H_2 , such a large difference in reactivity between two nearly iso-energetic states is direct evidence of state specific chemisorption of CH_4 on Ni(100), which is inconsistent with a statistical model of the reaction⁸⁹. Since the ν_1 and ν_3 states have similar vibrational motions which differ by the oscillating phase of the C-H bond stretches, we cannot explain the difference in reactivity between $\text{CH}_4(\nu_1)$ and $\text{CH}_4(\nu_3)$ in terms of vibrational energy localized in each C-H bond. However, a simple model using symmetry coordinates and vibrational adiabaticity qualitatively describes the enhanced reactivity for CH_4 molecules with excited symmetric stretching vibrations^{29,58}. The perturbation of the surface splits the degenerate antisymmetric stretch into two components, one of which has the correct symmetry to interact with the perturbed symmetric stretch to form two localized vibrational states. Because ν_1 of methane has lower energy compared to ν_3 , it correlates adiabatically to a state where the vibrational excitation is localized in the active bond pointing towards the surface, promoting the chemisorption. Conversely, the ν_3 correlates to the state where the vibrational energy is localized in the three C-H bonds pointing outwards the surface. Calculations based on vibrational adiabatic approach of the molecules on the surface have confirmed the description of this simple model²⁴.

Our $\text{CH}_4(\nu_1)$ state-resolved measurements show that the reactivity of a vibrational state does not only depend on the vibrational energy initially localized in the bonds, but it is also influenced by the symmetry of the vibrational state excited (*mode-specific reactivity*). The experimentally confirmed predictions of the vibrationally adiabatic model should encourage efforts to develop more sophisticated dynamical treatments of methane chemisorption and suggest that quantitative predictions of methane reactivity will require dynamical calculations on a realistic multidimensional potential energy surface²⁵.

Alternatively, we could explain the higher reactivity of ν_1 compared to ν_3 in terms of different couplings between the CH_4 vibrational states and the lattice motion. The energy quenching due

to lattice recoil could be more significant for ν_3 than for ν_1 , favoring the energy loss into the lattice. In this context, one could speculate that the difference in the coupling with the surface motion is due to the dipole moment of the $\text{CH}_4(\nu_3)$ molecules.

During the four years of my Ph.D. thesis, other experimental results have confirmed the non-statistical dynamics and mode-specificity of the CH_4 chemisorption on nickel. Smith *et al.*¹²³ have shown that the excitation of the antisymmetric stretch is 1.25 times more efficient than translational energy in promoting the chemisorption of CH_4 on Ni(111). This result is in contrast with the predictions of the statistical models. Recently, Juurlink *et al.*¹²⁴ have reinforced the idea of vibrational mode-specificity of methane chemisorption on nickel. They have shown that the the second overtone of the bending motion $3\nu_4$ is significantly less effective than the ν_3 in promoting the dissociative chemisorption of methane on Ni(111), even though $3\nu_4$ contains 30% more energy.

It is interesting to evaluate the contribution of ν_1 sticking coefficient ($S_0^{\nu_1}$) on the thermal reactivities of CH_4 measured from molecular beam experiments. Holmblom *et al.* have reported CH_4 sticking coefficient (S_0^t) as a function of valve temperature (T_v) and incident kinetic energy normal to the surface²⁰. We calculate the contribution of $S_0^{\nu_1}$ to S_0^t for the kinetic energy of 50 kJ/mole by multiplying the $S_0^{\nu_1}$ with the fractional population of ν_1 at a given T_v ($p_{\nu_1}(T_v)$). If we assume that the vibrational states do not relax during the supersonic expansion, we can determine the number of molecules in each vibrational state using the Boltzmann distribution (see Appendix F for the vibrational energy levels and degeneracies). Table 5.1 shows $S_0^t(50 \text{ kJ/mole})$ ²⁰, the populations of ν_1 and the contributions of $S_0^{\nu_1}$ to S_0^t for different valve temperatures. We observe a maximum contribution of 11 % for $T_v = 650 \text{ K}$. At higher valve temperatures, the effect of $S_0^{\nu_1}$ on S_0^t decreases progressively, meaning that states at higher vibrational energies have larger contributions to S_0^t .

We can also include the effects of the other vibrational states on S_0^t . We have previously reported the state-resolved reactivity of $2\nu_3$ and the group of Utz measured the reactivity of ν_3 .^{22,54,64,71} Figure 5.1 shows the two sets of data as a function of the total energy in the molecule (kinetic energy + vibrational energy). One can observe that the $2\nu_3$ data set seems to extend the ν_3 data points. We fit the total energy dependence of the sticking coefficient using an empirical ‘‘S-shape’’ function²⁰:

$$S_0^\nu(E) = \frac{A(\nu)}{2} \left(1 + \operatorname{erf} \left[\frac{E - E_0(\nu)}{W(\nu)} \right] \right), \quad (5.1)$$

T_v (K)	S_0^t	p_{ν_1}	contribution %
350	$8 \cdot 10^{-6}$	$6.0 \cdot 10^{-6}$	1
650	$3.1 \cdot 10^{-4}$	$1.2 \cdot 10^{-3}$	11
750	$7.7 \cdot 10^{-4}$	$2.5 \cdot 10^{-3}$	9
850	$1.8 \cdot 10^{-3}$	$4.2 \cdot 10^{-3}$	7
950	$3.6 \cdot 10^{-3}$	$5.8 \cdot 10^{-3}$	2
1050	$6.4 \cdot 10^{-3}$	$7.5 \cdot 10^{-3}$	< 2

Table 5.1: Sticking coefficient on Ni(100) of CH₄ at 50 kJ/mole of incident energy S_0^t for different valve temperatures T_v as measured by Holmblaud *et al.*. The contributions of $S_0^{\nu_1}$ to S_0^t are obtained by multiplying the fractional populations p_{ν_1} with $S_0^{\nu_1}$.

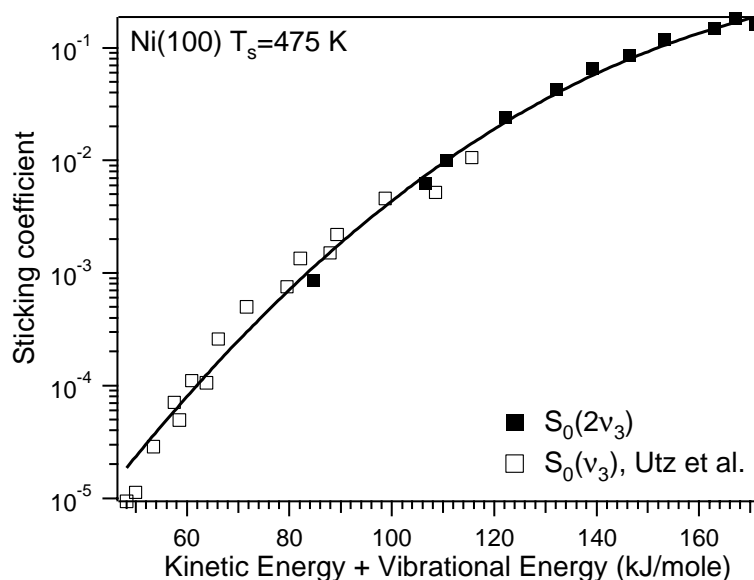


Figure 5.1: State-resolved reactivities for CH₄ in the ν_3 (\square) and $2\nu_3$ (\blacksquare) vibrational states on Ni(100) as a function of total energy of the molecule (kinetic energy + vibrational energy). The solid curve is the best fit of an “S-shape” curve to the experimental points .

where $A(\nu)$, $E_0(\nu)$ and $W(\nu)$ are the fitting parameters for the vibrational quantum state ν and represent the asymptotic value of S_0 at high translational energy, the “center-point” energy where S_0 has risen to 50% of the asymptote, and the steepness of the rise respectively. The solid line shown in Fig. 5.1 is the best fit of the “S-shape” curve to the data points of ν_3 and $2\nu_3$. The fit result is: $A = 0.4 \pm 0.1$, $E_0 = 170 \pm 8$ and $W = 45 \pm 2$. Juurlink *et al.* recently reported the

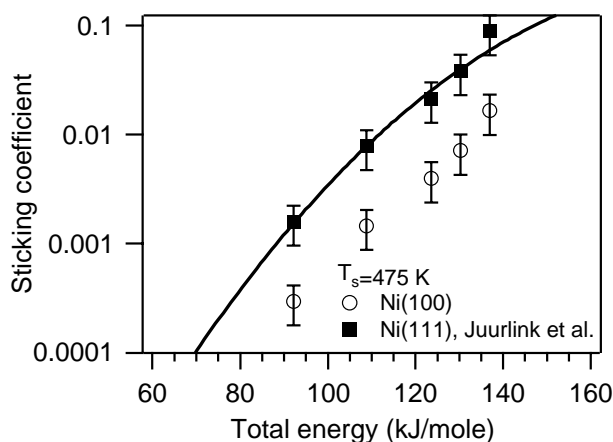


Figure 5.2: State-resolved reactivities for CH_4 in the $3\nu_4$ vibrational state on Ni(111) (○) and Ni(100) (■) as a function of total energy of the molecule (kinetic energy + vibrational energy). The reactivity on Ni(100) are obtained by multiplying the sticking coefficients on Ni(111) by a factor 5.8. The solid curve is the best fit of an “S-shape” curve to the sticking coefficients on Ni(100).

reactivity of CH_4 in the $3\nu_4$ state on Ni(111) as a function of kinetic energy. The open squares in Fig. 5.2 represent these data points as a function of the total energy of the molecule. In our lab, we have determined that ground state CH_4 molecules are approximately 5.8 times more reactive on Ni(100) than on Ni(111). We estimate that the $3\nu_4$ reactivities on Ni(100) are 5.8 times larger than the experimental values for Ni(111). The filled squares in Fig. 5.2 represent our estimations for the $3\nu_4$ reactivities on Ni(100). The solid black line represented in Fig. 5.2 is the best fit of the “S-shape” curve to the reactivities on Ni(100). For the fitting procedure, we keep constant A to the value of 0.4 obtained from ν_3 and $2\nu_3$ data point fitting. The fit result is: $E_0 = 166 \pm 8$ and $W = 40 \pm 5$. In analogy with the ν_3 and $2\nu_3$ results, we assume that $S_0^{\nu_4}$ and $S_0^{2\nu_4}$ lay on the “S-shape” curve of $3\nu_4$. Therefore, we estimate the values of $S_0^{\nu_4}$, $S_0^{2\nu_4}$ and $S_0^{3\nu_4}$ at 50 kJ/mole by the “S-curve” shown in Fig. 5.2. For example, $S_0^{\nu_4}(50 \text{ kJ/mole})$ corresponds to the value of the “S-curve” at $E_t + E_v = 50 + 15.6 = 65.6 \text{ kJ/mole}$, where E_t and E_v are the kinetic and the vibrational energies respectively. Table 5.2 shows the sticking coefficient values obtained in this way.

We assume that ν_2 is equivalent to ν_4 in promoting the reaction, then the sticking coefficients of methane in the ν_2 state follow the same “S-shape” curve of ν_4 . Under this condition, we can calculate the reactivity at 50 kJ/mole for the ν_2 , $2\nu_2$, $3\nu_2$ and $\nu_2 + \nu_4$ states (see Table 5.3).

We calculate the contribution of every state listed above (including the ground state molecules)

$$\begin{aligned}
 S_0^{\nu_4}(50 \text{ kJ/mole}) &= 5.0 \cdot 10^{-5} \\
 S_0^{2\nu_4}(50 \text{ kJ/mole}) &= 3.6 \cdot 10^{-4} \\
 S_0^{3\nu_4}(50 \text{ kJ/mole}) &= 2.5 \cdot 10^{-3}
 \end{aligned}$$

Table 5.2: Sticking coefficients at 50 kJ/mole of CH₄ in the ν_4 , $2\nu_4$ and $3\nu_4$ states obtained from the “S-shape” curve reported in Fig. 5.2.

$$\begin{aligned}
 S_0^{\nu_2}(50 \text{ kJ/mole}) &= 8.0 \cdot 10^{-5} \\
 S_0^{\nu_2+\nu_4}(50 \text{ kJ/mole}) &= 5.8 \cdot 10^{-4} \\
 S_0^{2\nu_2}(50 \text{ kJ/mole}) &= 8.3 \cdot 10^{-4} \\
 S_0^{3\nu_2}(50 \text{ kJ/mole}) &= 5.4 \cdot 10^{-3}
 \end{aligned}$$

Table 5.3: Sticking coefficients at 50 kJ/mole of CH₄ in the ν_2 , $\nu_2 + \nu_4$, $2\nu_2$ and $3\nu_2$ states obtained from the “S-shape” curve reported in Fig. 5.2.

to S_0^t at 50 kJ/mole by multiplying the sticking probability with the fractional population of every state. We sum all contributions from individual states and calculate S_0 . The results are reported in Table 5.4 together with the total contribution to S_0^t . We can observe that

T_v (K)	S_0^t	calculated S_0	total contribution %
350	$8 \cdot 10^{-6}$	$1.0 \cdot 10^{-5}$	120
650	$3.1 \cdot 10^{-4}$	$5.5 \cdot 10^{-5}$	18
750	$7.7 \cdot 10^{-4}$	$9.6 \cdot 10^{-5}$	13
850	$1.8 \cdot 10^{-3}$	$1.5 \cdot 10^{-4}$	9
950	$3.6 \cdot 10^{-3}$	$2.1 \cdot 10^{-4}$	6
1050	$6.4 \cdot 10^{-3}$	$2.7 \cdot 10^{-4}$	4

Table 5.4: Sticking coefficient S_0^t on Ni(100) of CH₄ at 50 kJ/mole of incident energy for different valve temperatures T_v as measured by Holmblom *et al.*²⁰. The sticking coefficients calculated from the reactivities of the ν_1 , ν_2 , ν_3 , ν_4 , $2\nu_4$, $2\nu_2$, $\nu_2 + \nu_4$, $3\nu_4$, $3\nu_2$ and $2\nu_3$ states are reported with their contributions to S_0^t .

the inclusion of these vibrational states is not sufficient to reproduce S_0^t . It could be that the remaining vibrations are relevant for the calculation of S_0^t . It would be interesting to include the effects of all vibrations in the sticking coefficient calculation. However, for most of the vibrational motions, the reaction probability is unknown. One solution is to assume

that the energy in the remaining states is as efficient as the translational energy in promoting the chemisorption. This means that putting a given amount of energy in a vibrational state results in the same increase in reactivity as adding the same amount of kinetic energy. As a consequence, the “S-shape” curves associated to these states are identical to that of the ground state molecules. The experimentally determined “S-shape” curve parameters for the ground state molecules are: $A = 0.4$, $E_0 = 140 \pm 2$ and $W = 41 \pm 1$. Table 5.5 shows the calculated sticking coefficients, which are in good agreement with S_0^t for valve temperatures in the range

T_v (K)	S_0^t	calculated S_0	contribution %
350	$8 \cdot 10^{-6}$	$1.0 \cdot 10^{-5}$	120
650	$3.1 \cdot 10^{-4}$	$1.4 \cdot 10^{-4}$	44
750	$7.7 \cdot 10^{-4}$	$4.1 \cdot 10^{-4}$	53
850	$1.8 \cdot 10^{-3}$	$1.1 \cdot 10^{-3}$	62
950	$3.6 \cdot 10^{-3}$	$2.5 \cdot 10^{-3}$	69
1050	$6.4 \cdot 10^{-3}$	$5 \cdot 10^{-3}$	78

Table 5.5: Sticking coefficient S_0^t on Ni(100) of CH_4 at 50 kJ/mole of incident energy for different valve temperatures T_v as measured by Holmblaud *et al.*. The calculated S_0 are obtained including all the vibrational states.

of 850-1050 K. At 650 K, only 44% of the reactivity is reproduced. This discrepancy suggests that there are other vibrational states more efficient than translational energy in promoting the reaction. In this context, it would be interesting to measure the reactivity of other CH_4 overtone and combination states.

5.2 Improving the apparatus

For the state-resolved reactivity measurements, we need to determine the number of excited molecules in the molecular beam by measuring the laser focal volume, the laser energy and the extent to which a transition is saturated (saturation parameter). We obtain the saturation parameter by fitting a saturation curve to the fluence dependence of the “laser-on” carbon signal. This kind of measurement is time consuming and represents a bottleneck in our experimental procedure. An alternative is to perform depletion spectroscopy (DS) measurements on methane molecules in the molecular beam. The basic idea of the DS resides in the use of two lasers:

the depletion lasers (DL) and the probe laser (PL). The former is the laser used to excite the molecules to the desired quantum state prior the impact with the surface. The latter probes the effect induced by the DL on the molecules. For methane molecules, the PL is fixed at the frequency corresponding to a transition from ground state to the ν_3 excited state. The photons absorbed by the methane molecules are monitored by measuring the laser beam intensity transmitted through the molecular beam. The frequency of the depletion laser is varied and when it is tuned onto a CH_4 transition, the ground state is depopulated and the absorption of the diode laser beam is depleted. As PL we are going to use a cw diode laser tunable around 3000 cm^{-1} . With this technique it should be possible to detect if the DL is on resonance with the targeted transition and to directly determine the fraction of molecules excited in the molecular beam without knowing the saturation parameter and the laser focal volume. The same technique could be used as well for the SRS experiments, where both the pump and Stokes lasers act as DL. However, in this case, the detection of the absorption depletion could be more difficult than in the IR experiments due to the small fraction of molecules excited in the molecular beam.

For molecules that can be REMPI ionized (H_2 , N_2 , $\text{NH}_3 \dots$), one alternative could be to perform depletion spectroscopy using the REMPI laser as PL^{13,125}. In this case, a ion detector have to be installed in the proximity of the ionization region in order to maximize the ion collection efficacy. The effects of the DL should be observed as a depletion in the ion signal.

Our sticking coefficient determinations are based on the molecular-beam flux measurements. Values of S_0 that exceed 0.01 can be accurately determined using the King and Wells technique¹²⁶. In this case, a flag in the UHV chamber is inserted into the molecular beam which is scattered and produces a pressure rise in the chamber. A QMS monitors the molecular beam intensity as a function of time. At t_0 , the flag is opened and the molecular beam impinges on an initially clean surface. Due to the adsorption of the molecules, the crystal surface acts as a pump. Consequently, the QMS signal initially decreases with time. When the surface starts to be saturated, the QMS signal increases and returns to the initial value (when the flag was blocking the molecular beam). The sticking coefficient is determine by the dip in the QMS signal. This technique does not require the measurements of the molecular beam flux and the quantity of absorbed molecules for S_0 determination. We implemented the King and Wells method in our setup, but at the moment the QMS signal to noise ratio (S/N) is not good enough for a depletion detection of few percent of the QMS counts. We need to work more on it to understand from where the problem comes from and to improve the S/N. It would be useful to compare the sticking coefficients obtained by the King and Wells technique with those obtained using the

method explained in this thesis. With this comparison, we could determine if any systematic error is introduced in our technique.

In our experiments, we use Auger spectroscopy for the detection of reaction products on the surface. Sometimes, it happens that the Auger peak of the product are nearly coincident with an Auger peak of the substrate, e.g. C on Pt. Under this condition, the detection of a small quantity of adsorbate on the surface by Auger spectroscopy is very difficult. An alternative is to use temperature programmed desorption (TPD) for the quantification of the adsorbate on the surface. We have tried to implement TPD in our setup, but experimental limitations prevented us in obtaining good S/N. We think that the major problem is the QMS which is situated too far from the surface and the desorbed species are not efficiently collected. In this configuration, the QMS also records molecules desorbed from the crystal holder. In order to increase the collection efficiency of the molecules desorbed from the crystal surface, it would be useful to have a differentially pumped QMS which can be positioned few millimeters away from the surface.

We are implementing an optical non-resonant reflectivity change method to detect the products on the surface¹²⁷. The basic physics behind this method resides on the perturbation of the surface electronic structure induced by the chemisorbed molecules. This perturbation leads to changes in optical reflectivity (R) of the surface ($\Delta R/R \sim 1\%$ for chemisorbed species). With this technique, we would be able to monitor the adsorbate concentration on the surface as a function of time while we deposit with our molecular beam. The $\Delta R/R$ can be calibrated in terms of ML using our Auger spectrometer. We can determine the sticking coefficient from the slope of the $\Delta R/R$ value displayed as a function of time. Preliminary results show that the reflectivity technique is more sensitive (0.1% ML) than the AES detection.

One of the major constraints of our infrared DFG-OPA setup is the tuning range of our OPA and DFG crystals ($\sim 100 \text{ cm}^{-1}$). To cover a wider frequency range, a series of crystals cut at different angles must be acquired. An alternative is to use an optical parametric oscillator (OPO) system based on a periodically poled lithium niobate crystal (PPLN). Commercial cw PPLN OPO systems start to be available on the market with output power $> 1 \text{ W}$, tunable range from 2500 up to 6000 cm^{-1} and bandwidth of 1 MHz. With such a large tunability, we could cover the CH_4 regions of ν_3 , $2\nu_3$, $\nu_1 + \nu_4$, $\nu_3 + \nu_4$, $2\nu_4$, etc. With this device we could excite also O-H ($\sim 3600 \text{ cm}^{-1}$) and N-H ($\sim 3300 \text{ cm}^{-1}$) stretches, opening the possibility to study other molecules on different surfaces.

5.3 Outlook

In order to answer to questions as: “are there other vibrational states more efficient than translational energy?”, more work has to be done on the chemisorption of methane on Ni. In this context, it would be interesting to explore the effect of the excitation of other vibrational motions on the reactivity of methane on nickel. We are setting up experiments for the determination of the sticking coefficient of methane on Ni with CH₄ excited to the $\nu_1 + \nu_4$ and $\nu_3 + \nu_4$ states ($\sim 4300 \text{ cm}^{-1}$).

While bond-specificity has been observed in gas-phase reactions²⁶⁻²⁸, no direct evidence had been obtained for gas-surface reactions prior to this work. For reactions in the gas-phase, the bond-specific reactivity has been observed by analyzing the product state distribution. For gas-surface systems, we can envision experiments where we do not measure the reactivity, but we analyze the product distributions on the surface. One possible experiment could be to deposit CD₃H with two quanta of C-H stretch excited ($\sim 5900 \text{ cm}^{-1}$) on Ni(100) with low surface temperature ($< 150 \text{ K}$). At this temperature, the adsorbed methyl does not decompose and can be detected using high resolution electron energy loss (HREEL) spectroscopy^{14,15,66}. The bond-specificity implies that only the vibrationally excited bond (C-H) should break in the chemisorption reaction of CD₃H on Ni. Then we should observe the relative intensities of the C-H and C-D stretch HREEL peaks to change for deposition with and without laser excitation. In particular, the ratio between the intensities of the C-D and C-H HREEL peaks measured after the deposition with laser excited CD₃H should be larger than that obtained by depositing CD₃H without laser excitation.

Walker and King measured the reaction probability of CH₄ on Pt using supersonic molecular beams¹²⁸. For low translational energy ($E_t < 10 \text{ kJ/mole}$) of the incoming molecules, they found that the sticking coefficient falls with increasing kinetic energy. At $E_t > 10 \text{ kJ/mole}$, the sticking coefficient rises to a plateau with increasing translational energy. They explain their results by introducing two different processes. For low kinetic energy (2-10 kJ/mole), they proposed two models: precursor mediated and dynamic steering mechanisms. By varying the valve temperature, they argued that the sticking coefficient is increased by ~ 2 orders of magnitude as the vibrational deformation modes are excited (ν_2 and ν_4). At higher kinetic energy, a direct activated process becomes dominant in which the C-H stretch modes of methane are important. It would be interesting to compare the efficacy of ν_4 and ν_3 states in promoting the reaction of CH₄ on Pt(110)(1 \times 2) for low kinetic energies. If Walker and King conclusions

are correct, we should observe that the ν_4 state is more efficient than ν_3 at $E_t < 10$ kJ/mole.

We are preparing experiments for the study of the chemisorption of SiH_4 on Si surfaces. It has been shown that this reaction is a direct process activated by the translational energy¹²⁹. Since the overtone spectroscopy of SiH_4 is well known¹³⁰, with our laser system, we can selectively vibrationally excite molecules in the molecular beam that contain only ^{28}Si , ^{29}Si or ^{30}Si . If vibrational excitation can promote the chemisorption of silane on a silicon surface, one could envision a laser controlled isotope selective deposition of Si on semiconductor surfaces and prepare isotopically pure films of Si. In this case, the product result of Si isotope on the surface is detected using secondary ion mass spectrometry. These kind of studies can open the ways to develop a laser based process for fabrication of isotopically engineered surface structures.

Another interesting experiment could be the determination of the reactivities of vibrationally excited H_2 on $\text{Cu}(100)$. The results obtained with these experiments could be compared with the predictions of the six-dimensional quantum dynamic calculation developed by McCormack *et al.*⁷. In this context, we would use our Raman amplifier to excite the H_2 molecules to $v=1$ prior the collision with the surface.

It is commonly assumed that the energy released in low-energy chemisorption of molecules on metal is dissipated by surface vibrations (phonons). However, recent works have shown reaction-induced surface electron excitations during a gas-surface interaction¹³¹. Using Schottky diodes, they measured e-h pair formations (chemicurrent) created by nonadiabatic energy dissipation due to the reaction of the adsorbate on the surface. It would be interesting to study the effects of molecular vibration excitations on the chemicurrent. For example, one could try to measure if the reaction of vibrationally excited H_2 with Ag or Cu induces formations of e-h pairs.

The overall goal of such a kind of experiments is the physical understanding of gas-surface reaction dynamics. Our results can give detailed information on the roles that vibrational excitations have in the dissociation of molecules on surfaces. This information can be used to test and improve theoretical calculations. Both theoretical and experimental works must be carried out together to obtain a reliable gas-surface interaction description which can lead to new ideas for the development of more efficient and economic catalysts.

Rotational energy levels of an asymmetric rotor

The rotational energy levels of an asymmetric-top rotor can be written as⁹³

$$F(J_{K_a K_c}) = \frac{1}{2}(A + C)J(J + 1) + \frac{1}{2}(A - C)E_{J_{K_a K_c}}(\kappa), \quad (\text{A.1})$$

where $E_{J_{K_a K_c}}(\kappa)$ is a function of the asymmetry parameter κ which is defined by Eq. 3.7. Table A.1 shows the $E_{J_{K_a K_c}}(\kappa)$ functions for different rotational states.

$J_{K_a K_c}$	$E_{J_{K_a K_c}}(\kappa)$	$J_{K_a K_c}$	$E_{J_{K_a K_c}}(\kappa)$
0 ₀₀	0	3 ₃₀	$5\kappa + 3 + 2\sqrt{4\kappa^2 - 6\kappa + 6}$
1 ₁₀	$\kappa + 1$	3 ₃₁	$2\left(\kappa + \sqrt{\kappa^2 + 15}\right)$
1 ₁₁	0	3 ₂₁	$5\kappa - 3 + 2\sqrt{4\kappa^2 + 6\kappa + 6}$
1 ₀₁	$\kappa - 1$	3 ₂₂	4κ
		3 ₁₂	$5\kappa + 3 - 2\sqrt{4\kappa^2 - 6\kappa + 6}$
2 ₂₀	$2\left(\kappa + \sqrt{\kappa^2 + 3}\right)$	3 ₁₃	$2\left(\kappa - \sqrt{\kappa^2 + 15}\right)$
2 ₂₁	$\kappa + 3$	3 ₀₃	$5\kappa - 3 - 2\sqrt{4\kappa^2 + 6\kappa + 6}$
2 ₁₁	4κ		
2 ₁₂	$\kappa - 3$		
2 ₀₂	$2\left(\kappa - \sqrt{\kappa^2 + 3}\right)$		

Table A.1: Asymmetric rotor $E_{J_{K_a K_c}}(\kappa)$ functions for $J = 0, 1, 2, 3$.

Measurement of the IR beam intensity distribution

For the state-resolved reactivity measurements of methane on nickel, the number of excited molecules in the molecular beam must be determined. It depends on the energy of the laser pulses, on the intensity of the molecular beam pulses, on the extent at which the transition is saturated, and on the fraction of molecular beam pulse that is illuminated by the line focus of the laser beam ($f_{overlap}$). Since in the IR deposition experiments we illuminate the entire diameter of the molecular beam, $f_{overlap}$ is obtained by dividing the length of the laser line focus with the length of the molecular beam pulses. The former is obtained by measuring the IR laser beam intensity distribution. We characterize the intensity distribution using a knife edge installed on a translation stage and a power meter (see Fig. B.1). The distance between the cylindrical lens and the knife edge is equal to that between the lens and the molecular beam. To define the laser beam shape, we place an aperture into the expanded laser before the cylindrical lens. For each knife edge position, the transmitted power is recorded and the measurement result is shown in Fig. B.2. Figure B.3 shows the beam intensity distribution as determined by deriving the curve reported in Fig. B.2.

We measure an intensity distribution with a full width half maximum of 12 mm.

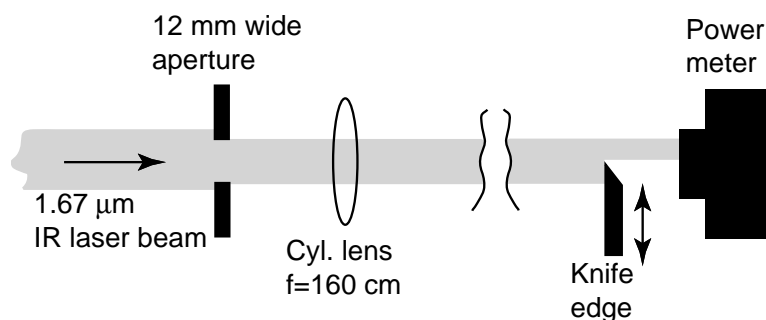


Figure B.1: Setup used for the IR laser beam intensity distribution measurement. For each knife edge position the transmitted power is recorded. The obtained integral of the laser beam intensity distribution is shown in Fig. B.2.

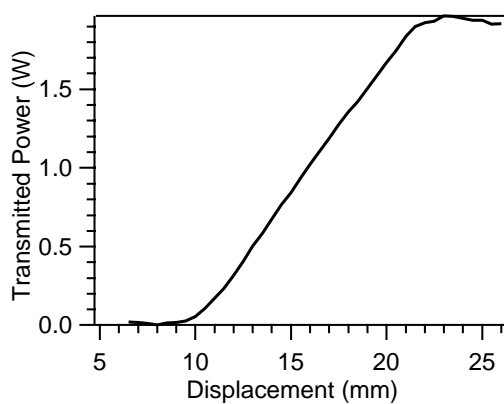


Figure B.2: Integral of the IR laser intensity distribution along the line focus of a 160 cm cylindrical lens measured using a knife edge mounted on a translational stage and a power meter. A 12 mm wide beam shaping aperture is placed into the expanded beam before the cylindrical lens.

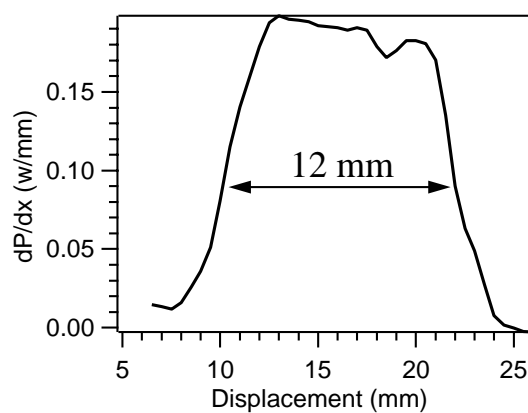


Figure B.3: IR laser intensity distribution along the line focus of a 160 cm cylindrical lens as obtained by deriving the plot in Fig. B.2.

Appendix C

The T and T_d group

<i>T</i>	<i>E</i>	$3C_2$	$4C_3$	$4C_3'$
<i>A</i>	1	1	1	1
{ <i>E</i> ₁	1	1	ω	ω^2
{ <i>E</i> ₂	1	1	ω^2	ω
<i>F</i>	3	-1	0	0
$\omega = e^{2\pi i/3}$				

Table C.1: Irreducible representations of the group T^{111} .

	<i>A</i>	<i>E</i> ₁	<i>E</i> ₂	<i>F</i>
<i>A</i>	<i>A</i>	<i>E</i> ₁	<i>E</i> ₂	<i>F</i>
<i>E</i> ₁	<i>E</i> ₁	<i>E</i> ₂	<i>A</i>	<i>F</i>
<i>E</i> ₂	<i>E</i> ₂	<i>A</i>	<i>E</i> ₁	<i>F</i>
<i>F</i>	<i>F</i>	<i>F</i>	<i>F</i>	$A + E_1 + E_2 + 2F$

Table C.2: Multiplication table for the group T^{111} .

T_d	E	$8C_3$	$3C_2$	$6S_4$	$6\sigma_d$	
A_1	1	1	1	1	1	$\alpha_{xx} + \alpha_{yy} + \alpha_{zz}$
A_2	1	1	1	-1	-1	
E	2	-1	2	0	0	$(\alpha_{xx} + \alpha_{yy} - 2\alpha_{zz}, \alpha_{xx} - \alpha_{yy})$
F_1	3	0	-1	1	-1	(R_x, R_y, R_z)
F_2	3	0	-1	-1	1	(T_x, T_y, T_z) $(\alpha_{xy}, \alpha_{xz}, \alpha_{yz})$

Table C.3: Character table of the T_d point group.

	A_1	A_2	E	F_1	F_2
A_1	A_1	A_2	E	F_1	F_2
A_2		A_1	E	F_2	F_1
E			$A_1 + A_2 + E$	$F_1 + F_2$	$F_1 + F_2$
F_1				$A_1 + E + F_1 + F_2$	$A_2 + E + F_1 + F_2$
F_2					$A_1 + E + F_1 + F_2$

Table C.4: Multiplication table for the T_d group.

Stimulated Raman pumping

The symmetric stretch ν_1 of methane is IR inactive, however we can prepare the $\text{CH}_4(\nu_1)$ molecules in the molecular beam using the stimulated Raman pumping (SRP) process.

The properties of a dielectric medium through which an electromagnetic wave propagates are completely described by the relation between the polarization density vector $\mathbf{P}(\mathbf{r}, \mathbf{t})$ and the electric field vector $\mathbf{E}(\mathbf{r}, \mathbf{t})$. The mathematical relation between $\mathbf{P}(\mathbf{r}, \mathbf{t})$ and $\mathbf{E}(\mathbf{r}, \mathbf{t})$ is called the medium equation and is governed by the characteristics of the medium. A non-linear dielectric medium is characterized by the non-linear relation between the polarization and electric field vectors. Since the electric fields of interest are small ($\sim 10^6$ V/m) compared to the electric fields experienced by the electrons in the atoms or molecules ($\sim 10^9$ V/m), the medium equation can be expanded in Taylor's series about $|\mathbf{E}| = 0$ ¹³²,

$$P_i = \chi_{ij}^{(1)} E_j + \chi_{ijk}^{(2)} E_j E_k + \chi_{ijkl}^{(3)} E_j E_k E_l + \dots, \quad (\text{D.1})$$

where $\chi_{ij}^{(1)}$, $\chi_{ijk}^{(2)}$ and $\chi_{ijkl}^{(3)}$ are the first, second and third order susceptibilities and $\chi_{ij}^{(1)}$ is the susceptibility tensor of ordinary dielectric theory (linear optics). The summations are performed over the repeated indexes. For an isotropic material, such as gas or liquid, $\chi_{ij}^{(1)}$ is diagonal and $\chi_{ijk}^{(2)} = 0$.

The stimulated Raman scattering (SRS) is generated by the third order non-linear susceptibility¹³³. This appendix describes the origin of the SRS from a classical and quantum-mechanical point of view.

D.1 SRS: classical description

In a molecule the nuclei are engaged in vibrational motions. As a consequence, the dipole moment induced by an external electric field will be a function not only of the external field, but also of the instantaneous nuclear position. The non-linear polarization of a molecule arises from its simultaneous dependence on the nuclear coordinates and the electric field. For small amplitudes of vibrations, we can account for this dependence by expanding the polarizability coefficients in powers of the nuclear displacements. We consider a single molecule and let p_i be its electric dipole moment, which depends on the normal modes coordinates X^ν . We can write¹³²:

$$p_i(X^\nu, \mathbf{E}) = p_i^{(0)}(X^\nu) + \epsilon_0 \alpha_{ij}(X^\nu) E_j + \dots, \quad (\text{D.2})$$

where $\alpha_{ij}(X^\nu)$ is the first order polarizability and the summations are performed over the repeated indexes. We use α_{ij} instead of χ_{ij} to emphasize that we are considering a single molecule rather than the dipole moment per unit volume of a macroscopic sample.

We expand the various coefficients in Eq. D.2 in powers of normal modes:

$$p_i^{(0)}(X^\nu) = p_i^{(0)} + \sum_{\nu=1}^{3n-6} \left[\frac{\partial p_i^{(0)}}{\partial X^\nu} \right]_0 X^\nu + \dots, \quad (\text{D.3})$$

The first term in the right-hand side is the permanent dipole moment of the molecule, the second is responsible for the IR transition, that is we can neglect $p_i^{(0)}(X^\nu)$ for our purposes. If we pose $p_i^{(1)}(X^\nu, \mathbf{E}) = \alpha_{ij}(X^\nu) E_j$ we have:

$$\begin{aligned} p_i^{(1)}(X^\nu, \mathbf{E}) &= \epsilon_0 \left[\alpha_{ij}^{(0)} E_j + \sum_{\nu=1}^{3n-6} \left[\frac{\partial \alpha_{ij}}{\partial X^\nu} \right]_0 E_j X^\nu + \dots \right] \\ &= \epsilon_0 \left[\alpha_{ij}^{(0)} E_j + \sum_{\nu=1}^{3n-6} \alpha_{ij\nu}^{(\mathbf{R})} E_j X^\nu + \dots \right], \quad (\text{D.4}) \\ \text{where } \alpha_{ij\nu}^{(\mathbf{R})} &= \left[\frac{\partial \alpha_{ij}}{\partial X^\nu} \right]_0. \end{aligned}$$

The first term in Eq. D.4 generates the Rayleigh scattering of the light. The second term generates the Raman scattering, which will be the focus of our attention.

In order to give a qualitative description of the process, we can greatly simplify the problem

by considering only a one dimensional approach. Under this assumption, we have that:

$$\begin{aligned} p^{(1)}(X, E) &= \epsilon_0 \left[\alpha^{(0)} E + \left(\frac{\partial \alpha}{\partial X} \right)_0 X E \right] \\ &= \epsilon_0 \alpha^{(0)} E + p_{(NL)}(X, E), \end{aligned} \quad (\text{D.5})$$

where $p_{(NL)}(X, E)$ represents the non-linear Raman polarization.

The Raman medium is taken as consisting of N harmonic oscillators per unit volume, each oscillator representing one molecule. The oscillators are independent of each other and are characterized by their positions z in the laboratory frame and the internal normal coordinate $X(z, t)$. The equation of motion for a single oscillator is then¹³³

$$\frac{d^2 X(z, t)}{dt^2} + \gamma \frac{dX(z, t)}{dt} + \omega_\nu^2 X = \frac{F(z, t)}{m}, \quad (\text{D.6})$$

where γ is the damping constant chosen so that the observed spontaneous Raman scattering linewidth is $\Delta\nu = \gamma/2\pi$, ω_ν is the resonance frequency, m is the mass, and $F(z, t)$ is the driving force generated by the electric field. The energy of a polarized dipole in an electric field is¹³³:

$$U = - \int_0^E \mathbf{p}^{(1)} \cdot d\mathbf{E}' = -\epsilon_0 \left\{ \alpha^{(0)} + \frac{1}{2} \left(\frac{\partial \alpha}{\partial X} \right)_0 X \right\} E^2 \quad (\text{D.7})$$

and the force acting on a single molecule is

$$F(z, t) = - \frac{\partial U}{\partial X} = \epsilon_0 \frac{1}{2} \left(\frac{\partial \alpha}{\partial X} \right)_0 \mathbf{E} \cdot \mathbf{E}. \quad (\text{D.8})$$

We want to see how the field-induced excitation of the molecular vibration $X(z, t)$ reacts back on the electromagnetic fields. The dielectric constant of a medium containing N molecules per unit volume is:

$$\epsilon = \epsilon_0 + N p^{(1)} / E = \epsilon_0 \left\{ 1 + N \left[\alpha^{(0)} + \left(\frac{\partial \alpha}{\partial X} \right)_0 X \right] \right\}. \quad (\text{D.9})$$

According to this equation, the molecular vibration at ω_ν causes a modulation of the dielectric constant ϵ at ω_ν . This can lead to energy exchange between electromagnetic fields separated by multiples of ω_ν . We consider the total field as the sum between the Stokes E_s (ω_s) and pump E_p (ω_p) laser fields linearly polarized along z direction:

$$\mathbf{E}(z, t) = \frac{1}{2} \hat{z} E_s(z) e^{i\omega_s t} + \frac{1}{2} \hat{z} E_p(z) e^{i\omega_p t} + \text{c.c.}, \quad (\text{D.10})$$

such that

$$\mathbf{E} \cdot \mathbf{E} = \frac{1}{4} E_p(z) E_s^*(z) e^{i(\omega_p - \omega_s)t} + \text{c.c.}, \quad (\text{D.11})$$

where we have neglected the high frequency terms $(\omega_p + \omega_s)$, which oscillate too fast with respect to ω_ν and consequently are weakly coupled with the oscillator. If we assume that the solution of Eq. D.6 has the form:

$$X(z, t) = \frac{1}{2} X(z) e^{i\omega t} + \text{c.c.}, \quad (\text{D.12})$$

and we replace Eq. D.12, D.11, and D.8 in Eq. D.6 we find that the molecular vibration is driven at a frequency of $\omega_\nu = \omega_p - \omega_s$ with a complex amplitude

$$X(z) = \frac{\epsilon_0 \left(\frac{\partial \alpha}{\partial X} \right)_0 E_p(z) E_s^*(z)}{4m [\omega_\nu^2 - (\omega_p - \omega_s)^2 + i(\omega_p - \omega_s)\gamma]}. \quad (\text{D.13})$$

The non-linear Raman polarization induced in the molecule by the fields is:

$$\begin{aligned} P_{(NL)}(z, t) &= N p_{(NL)} \\ &= \frac{1}{4} \epsilon_0 N \left(\frac{\partial \alpha}{\partial X} \right)_0 \left\{ \frac{\epsilon_0 \left(\frac{\partial \alpha}{\partial X} \right)_0 E_p(z) E_s^*(z) e^{i(\omega_p - \omega_s)t}}{4m [\omega_\nu^2 - (\omega_p - \omega_s)^2 + i(\omega_p - \omega_s)\gamma]} + \text{c.c.} \right\} \\ &\quad \times [E_s(z) e^{i\omega_s t} + E_p(z) e^{i\omega_p t} + \text{c.c.}]. \end{aligned} \quad (\text{D.14})$$

If we multiply the two terms in Eq. D.14, we obtain polarizations that oscillates at ω_s , ω_p , $2\omega_s - \omega_p$, and $2\omega_p - \omega_s$. We consider only the term that oscillates at ω_s and we call it:

$$P_{(NL)}^{(\omega_s)}(z, t) = \frac{1}{2} P_{(NL)}^{(\omega_s)}(z) e^{i\omega_s t} + \text{c.c.}, \quad (\text{D.15})$$

where

$$P_{(NL)}^{(\omega_s)}(z) = \frac{\epsilon_0^2 N \left(\frac{\partial \alpha}{\partial X} \right)_0^2 |E_p|^2}{8m [\omega_\nu^2 - (\omega_p - \omega_s)^2 + i(\omega_p - \omega_s)\gamma]} E_s(z). \quad (\text{D.16})$$

The coefficients relating an induced polarization to the inducing electric fields is the susceptibility (Eq. D.1). We can rewrite Eq. D.16 as

$$P_{(NL)}^{(\omega_s)}(z) = \epsilon_0 \chi_{\text{Raman}}(\omega_s) |E_p|^2 E_s(z), \quad (\text{D.17})$$

with

$$\chi_{\text{Raman}}(\omega_s) = \frac{\epsilon_0^2 N \left(\frac{\partial \alpha}{\partial X} \right)_0^2}{8m [\omega_\nu^2 - (\omega_p - \omega_s)^2 + i(\omega_p - \omega_s)\gamma]}. \quad (\text{D.18})$$

We can write it more generally using the fourth-rank tensor notation:

$$P_i^{(\omega_i=\omega_j-\omega_k+\omega_l)} = \chi_{ijkl}^{(\omega_i=\omega_j-\omega_k+\omega_l)} E_j^{\omega_j} E_k^{\omega_k*} E_l^{\omega_l}, \quad (\text{D.19})$$

where in our special case we have that $\omega_j = \omega_k = \omega_p$ and $\omega_i = \omega_l = \omega_s$. The notations $(\omega_i = \omega_j - \omega_k + \omega_l)$ means that the fourth-rank tensor susceptibility at ω_i is due to the oscillations of the three inducing electric fields at frequencies of ω_j , ω_k and ω_l .

We can divide the $\chi_{\text{Raman}}(\omega_s)$ into its complex and real part:

$$\chi_{\text{Raman}}(\omega_s) = \chi'_{\text{Raman}}(\omega_s) + i\chi''_{\text{Raman}}(\omega_s), \quad (\text{D.20})$$

where

$$\chi'_{\text{Raman}}(\omega_s) \simeq \frac{\epsilon_0^2 N \left(\frac{\partial \alpha}{\partial X}\right)_0^2 (\omega_\nu - \omega_p + \omega_s)}{16m\omega_\nu \left\{ [\omega_\nu - (\omega_p - \omega_s)]^2 + \gamma^2/4 \right\}} \quad (\text{D.21})$$

and

$$\chi''_{\text{Raman}}(\omega_s) \simeq \frac{\epsilon_0^2 N \left(\frac{\partial \alpha}{\partial X}\right)_0^2 \gamma/2}{16m\omega_\nu \left\{ [\omega_\nu - (\omega_p - \omega_s)]^2 + \gamma^2/4 \right\}} \quad (\text{D.22})$$

where we assume that $\gamma \ll \omega_\nu$. The presence of the Raman susceptibility at ω_s changes the propagation constant k_s of the field $E_s(z, t)$ as

$$\begin{aligned} k'_s &= k_s \left[1 + \frac{\chi_{\text{Raman}}(\omega_s)}{2n_s^2} |E_p|^2 \right] \\ &= k_s \left[1 + \frac{|E_p|^2}{2n_s^2} (\chi'_{\text{Raman}}(\omega_s) - i\chi''_{\text{Raman}}(\omega_s)) \right]. \end{aligned} \quad (\text{D.23})$$

The electric field of the Stokes radiation will propagate along the z direction following

$$E_s(z) = E_s(0) \exp \left\{ -iK_s z \left[1 + \frac{|E_p|^2 \chi'_{\text{Raman}}(\omega_s)}{2n_s^2} \right] - k_s z \frac{|E_p|^2 \chi''_{\text{Raman}}(\omega_s)}{2n_s^2} \right\}. \quad (\text{D.24})$$

Since the $\chi''_{\text{Raman}}(\omega_s)$ is negative, this equation shows that the Stokes beam is amplified as it propagates through the Raman medium and that the exponential gain $g(\omega_s)$ coefficient depends

on the energy per unit volume of the pump beam $|E_p|^2$ by

$$\begin{aligned} g(\omega) &= -\frac{k_s}{2n_s^2}|E_p|^2\chi''_{\text{Raman}}(\omega_s) \\ &= \frac{k_s\epsilon_0^2 N \left(\frac{\partial\alpha}{\partial X}\right)_0^2 \gamma |E_p|^2}{32n_s^2 m\omega_\nu \left\{[\omega_\nu - (\omega_p - \omega_s)]^2 + \gamma^2/4\right\}}. \end{aligned} \quad (\text{D.25})$$

The maximum of the gain occurs when the difference in frequency between the pump and Stokes laser beams matches the oscillator frequency $\omega_p - \omega_s = \omega_\nu$. The normalized Raman line shape is a Lorentzian with the maximum at $\omega_p - \omega_s = \omega_\nu$.

D.2 SRS: quantum-mechanical description

For the quantum-mechanical description of this process, we need to consider that the vibrational oscillations of the molecules around their equilibrium positions and the electric fields are quantum systems. Our aim is to derive the transition probability for an isolated molecule (harmonic oscillator) that interacts with the Stokes and pump photons.

We consider only the the normal mode ν of the molecule, then the vibrational Hamiltonian of the harmonic oscillator characterizing the isolated molecule is:

$$H_{\text{mol}} = \hbar\omega_\nu \left(\widehat{b}_\nu^+ \widehat{b}_\nu + \frac{1}{2} \right), \quad (\text{D.26})$$

where \widehat{b}_ν and \widehat{b}_ν^+ are the lowering and raising operators of the harmonic oscillator¹³⁴:

$$\begin{aligned} \text{raising operator: } \widehat{b}_\nu^+ |\nu\rangle &= \sqrt{\nu+1} \cdot |\nu+1\rangle \\ \text{lowering operator: } \widehat{b}_\nu |\nu\rangle &= \sqrt{\nu} \cdot |\nu-1\rangle. \end{aligned}$$

The product $\widehat{b}_\nu^+ \widehat{b}_\nu$ applied to a general state $|\nu\rangle$ with ν quanta in the vibrational mode gives:

$$\widehat{N}_\nu |\nu\rangle = \widehat{b}_\nu^+ \widehat{b}_\nu |\nu\rangle = \nu |\nu\rangle,$$

that is \widehat{N}_ν is the operator that gives the number of vibrational quanta in the vibrational mode.

We can write the hamiltonian for the radiation field as

$$H_{\text{pho}} = \sum_{kj} \hbar\omega_k \left(\hat{a}_{kj}^+ \hat{a}_{kj} + \frac{1}{2} \right), \quad (\text{D.27})$$

where \hat{a}_{kj} and \hat{a}_{kj}^+ are the annihilation and creation operators of a photon of wave vector k and polarization j :

$$\begin{aligned} \text{creation operator: } \hat{a}_{kj}^+ |n_{kj}\rangle &= \sqrt{n_{kj} + 1} \cdot |n_{kj} + 1\rangle \\ \text{annihilation operator: } \hat{a}_{kj} |n_{kj}\rangle &= \sqrt{n_{kj}} \cdot |n_{kj} - 1\rangle. \end{aligned}$$

The operator $\hat{N}_{kj} = \hat{a}_{kj}^+ \hat{a}_{kj}$ gives the number of photons n_{ij} per unit volume of wave vector k and polarization j corresponding to a photon state $|n_{11} \dots n_{kj} \dots\rangle$. In our case, we consider only Stokes n_s and pump n_p photons having the same polarization and we can write the photon state as $|n_s, n_p\rangle$.

The interaction Hamiltonian between the electric field and the molecule can be written in the form:

$$H_I = -\epsilon_0 \frac{1}{2} \left(\frac{\partial \alpha}{\partial X} \right)_0 \hat{X} (\hat{E}_p + \hat{E}_s)^2, \quad (\text{D.28})$$

where \hat{E}_p and \hat{E}_s are the electric field operators for the pump and Stokes photons, and \hat{X} is the spatial operator of the vibrational states.

We can write \hat{X} in term of lowering and raising operators¹³⁴:

$$\hat{X} = \left(\frac{\hbar}{2M\omega_\nu} \right) (\hat{b}_\nu + \hat{b}_\nu^+), \quad (\text{D.29})$$

where M and ω_ν are the effective mass and the frequency of the quantum oscillator. We assume that the molecule is placed at the origin of our reference frame, then the electric field operators acting on the molecule is¹⁰⁵:

$$\mathbf{E}_j = i \sqrt{\frac{2\pi\hbar\omega_j}{V}} \mathbf{e}_j (\hat{a}_j - \hat{a}_j^+), \quad (\text{D.30})$$

where $j = s, p$ for the Stokes and pump field. V is the quantization volume and \mathbf{e}_j is the polarization of the fields. By replacing Eq. D.29 and D.30 into Eq. D.28 and by taking only the terms of interest (terms that do not vanish when we calculate the transition rate) we find¹³²:

$$H_I = \frac{2\pi\hbar}{V} \left(\frac{\partial \alpha}{\partial X} \right)_0 \sqrt{\frac{\hbar}{2M\omega_\nu}} \sqrt{\omega_p \omega_s} \cdot \hat{a}_p \hat{a}_s^+ (\hat{b}_\nu + \hat{b}_\nu^+). \quad (\text{D.31})$$

We consider H_I as a perturbation to the Hamiltonian

$$H = H_{\text{mol}} + H_{\text{pho}}, \quad (\text{D.32})$$

which has unperturbed states defined as $|n_p, n_s, \nu\rangle$. We calculate the transition rate using the Fermi golden rule¹³⁵. If we consider the initial state $|n_p, n_s, \nu = 0\rangle$, we find that the transition probability is non-zero when the final state is $|n_p - 1, n_s + 1, 1\rangle$. The molecule, initially in the state $\nu = 0$, is excited to the state $\nu = 1$ due to the photon scattering; this corresponds to a Stokes event. We find that the transition rate per molecule is

$$\Gamma_{if} = \frac{8\pi^3\omega_s\omega_p}{V^2} \left(\frac{\hbar}{2M\omega_\nu} \right) \left(\frac{\partial\alpha}{\partial X} \right)_0^2 n_p(n_s + 1)\delta(\omega_s - \omega_p + \omega_\nu). \quad (\text{D.33})$$

The transition rate is non-zero when the difference between the pump and Stokes photon frequencies matches the vibrational frequency. The term $n_s n_p$ is responsible for the SRS process and the term n_p describes the spontaneous Raman scattering. We focus our attention on the SRS process. The intensity of a field with a total energy E in a volume V is $I = Ec/V$, for the stimulated case we have that $n_p \gg 1$ and $n_s \gg 1$, hence we can write:

$$I_p = \frac{\hbar\omega_p n_p c}{V} \quad \text{and} \quad I_s = \frac{\hbar\omega_s n_s c}{V}, \quad (\text{D.34})$$

we can write Γ_{if} as

$$\Gamma_{if} = \frac{8\pi^3 I_p I_s}{\hbar c^2 M \omega_\nu} \left(\frac{\partial\alpha}{\partial X} \right)_0^2 \delta(\omega_s - \omega_p + \omega_\nu). \quad (\text{D.35})$$

This is the transition state per molecule, so we can write the transition state per volume by knowing the number of molecules per unit volume ρ :

$$\Gamma_{\text{volume}} = \frac{\rho V 8\pi^3 I_p I_s}{\hbar c^2 M \omega_\nu} \left(\frac{\partial\alpha}{\partial X} \right)_0^2 \delta(\omega_s - \omega_p + \omega_\nu). \quad (\text{D.36})$$

The rate of generation of new Stokes photon in the volume is also equal to this transition rate $\dot{n}_s = \Gamma_{\text{volume}}$, then we obtain:

$$\dot{I}_s = \frac{8\pi^3 \rho \omega_s I_p I_s}{\hbar c M \omega_\nu} \left(\frac{\partial\alpha}{\partial X} \right)_0^2 \delta(\omega_s - \omega_p + \omega_\nu). \quad (\text{D.37})$$

This time derivative can be changed to a space derivative by assuming that the radiations flight

Gas	$\frac{d\sigma}{d\Omega}$ (10^{-30} cm ² /(sr·molec.))
N ₂	0.43
H ₂ (Q(1))	0.69
CH ₄ (ν_1)	1.8
NH ₃ (ν_1)	2.1
H ₂ S(ν_1)	2.7

Table D.1: Raman cross-section for some molecules.

through the Raman medium along the z direction, we obtain:

$$\frac{dI_s}{dt} = \frac{dI_s}{dz} \frac{dz}{dt} = \frac{dI_s}{dz} c. \quad (\text{D.38})$$

Therefore, the rate of change of the Stokes beam due to the Raman transition in the Raman medium is:

$$\frac{dI_s}{dz} = \frac{8\pi^3 \rho \omega_s I_p(z) I_s(z)}{\hbar c^2 M \omega_\nu} \left(\frac{\partial \alpha}{\partial X} \right)_0^2 \delta(\omega_s - \omega_p + \omega_\nu). \quad (\text{D.39})$$

The Raman gain coefficient β is:

$$\beta = \frac{8\pi^3 \rho \omega_s}{\hbar c^2 M \omega_\nu} \left(\frac{\partial \alpha}{\partial X} \right)_0^2 \delta(\omega_s - \omega_p + \omega_\nu). \quad (\text{D.40})$$

Due to the finite lifetime of the excited vibrational state and laser spectral width, the delta function is replaced by a Lorentzian, then the gain coefficient can be written as:

$$\beta = \frac{8\pi^2 \rho \omega_s}{\hbar c^2 M \omega_\nu} \left(\frac{\partial \alpha}{\partial X} \right)_0^2 \frac{\gamma_\nu}{(\omega_s - \omega_p + \omega_\nu)^2 + \gamma_\nu^2}, \quad (\text{D.41})$$

where γ_ν is the convolution between the transition line width and the laser spectral width. The Raman gain is often expressed as a function of the spontaneous Raman cross-section $\frac{d\sigma}{d\Omega}$ by¹³⁶:

$$\beta = \frac{8\pi^2 \rho c^2}{n^2(\omega_s) \hbar \omega_s^2 \omega_p} \left(\frac{d\sigma}{d\Omega} \right) \frac{\gamma_\nu}{(\omega_s - \omega_p + \omega_\nu)^2 + \gamma_\nu^2}, \quad (\text{D.42})$$

where $n(\omega_s)$ is the diffraction index of the Raman medium at the frequency ω_s . From the

comparison of Eq. D.42 and D.41 we find

$$\left(\frac{d\sigma}{d\Omega}\right) = \frac{\omega_s^3 \omega_p}{c^4 n^2(\omega_s)} \frac{\left(\frac{\partial\alpha}{\partial X}\right)_0^2}{M\omega_\nu}. \quad (\text{D.43})$$

From this equation we can express $\left(\frac{\partial\alpha}{\partial X}\right)_0^2$ as a function of the cross-section and we can replace it in Eq. D.35. After substitution, we find the transition rate as a function of the laser beam intensities and cross-section:

$$\Gamma_{if} = \frac{8\pi^2 I_p I_s c^2 n^2(\omega_s)}{\hbar \omega_s^3 \omega_p} \left(\frac{d\sigma}{d\Omega}\right) \frac{\gamma_\nu}{(\omega_s - \omega_p + \omega_\nu)^2 + \gamma_\nu^2}. \quad (\text{D.44})$$

The change in population ΔN between the vibrational ground and excited molecular states induced by the pump and Stokes laser beams can be written as:

$$\Delta \dot{N} = -\Gamma_{if} \Delta N. \quad (\text{D.45})$$

We use this equation in chapter 4 to calculate the fractional saturation of the Stokes transition.

In table D.1 we show the Raman cross-sections for H₂, N₂, NH₃, H₂S and CH₄. We can observe that methane is a good Raman scattering medium compared to hydrogen and nitrogen. Using Eq. D.45 and the value of the methane Raman cross-section we can calculate the number of molecules that we excite in our molecular beam as a function of the laser beam intensities (see chapter 4).

Appendix E

Program for saturation curve fitting

```
1 % Program used to fit the fluence dependence of the
2 % ‘‘laser-on’’ C/Ni peak area.
3 % The saturation model considers the intensity
4 % profiles of the laser beams along the x and z directions,
5 % which have been measured with the CCD. To reproduce
6 % the laser beam Intensity profiles along the x direction,
7 % I have used 3 gaussians.
8 % Plinio Maroni, February 2005
9
10 function out=FitSaturation(varargin)
11     clear all % clean the memory and plots
12     Alfa0=4e-9 ;%starting point for the fit procedure
13     Beta0=2e2 ;%starting point for the fit procedure
14
15     %Experimental data points
16     EsEp=[0 56326.1 29228.1 28728.8 53988.6 20376 49181 10604 42126 \
17     →46299 40000 8253]./1e6; %energy per pulse of the Pump and \
18     →Stokes beams in J^2
19     Experiment=[0 8.30517e-10 8.07792e-10 9.72033e-10 1.06943e-09 \
20     →6.51339e-10 8.43635e-10 3.3e-10 7.96817e-10 8.95355e-10 9.64285\
21     →e-10 4.78839e-10]; %[a.u] Normalized AES C/Ni peak area for \
```

```

18
19
20 %fitting procedure: lsqcurvefit is a matlab procedure
21 %to perform non-linear fit.
22 x0=[Alfa0 Beta0];%starting point for the fit
23 OPTIONS=optimset('Display','iter','TolFun',1e-50,'MaxFunEvals'\
→,20000,'TolX',1e-10); %set options
24 [X0,r,res,exitflag,output,lambda,Jacobian]=lsqcurvefit(\
→@SatCurve2D,x0,EsEp,Experiment,[],[],OPTIONS);%run the \
→iteration procedure, SatCurve2D is the fitting function as \
→defined below
25
26 %plot the results
27 plot(EsEp,Experiment,'o') hold on
28 EsEpPlot=min(EsEp):1e-4:max(EsEp);
29
30 plot(EsEpPlot,SatCurve2D(X0,EsEpPlot),'r') X0
31
32 % Saturation function: the intensity profiles
33 % for the two laser beams along the x direction are modelled with
34 % 3 gaussian. For the z direction, I use only one gaussian.
35
36 function sat=SatCurve2D(X0,EsEp)
37 Alfa=X0(1);
38 Beta=X0(2)
39 WidthS=[1.73e-3 0.90e-3 .85e-3]; % [m] FWHMs of the gaussian \
→Stokes beam intensity profile along x direction
40 RelIntS=[1 .624 .26];% relative intensities of the Stokes \
→gaussian peaks found by the fit
41 RelPosS=[0 -1.37e-3 -2.33e-3];% [m] relative positions of the \
→Stokes gaussian peaks along the x direction found by the fit
42 WidthP=[1.49e-3 0.925e-3 1.1e-3]; % [m] FWHMs of the gaussian \

```

```

43  →pump beam intensity profile along x direction
    RelIntP=[1 .36 .192];% relative intensities of the pump gaussian\
    → peaks found by the fit
44  RelPosP=[0 -1.42e-3 -2.38e-3];% [m] relative positions of the \
    →pump gaussian peaks along the x direction found by the fit
45  WidthSz= 55.6e-6; % [m] FWHM of the gaussian Stokes beam \
    →intensity profile along direction perpendicular to the \
    →molecular beam
46  WidthPz= 34.7e-6; % [m] FWHM of the gaussian Pump beam intensity\
    → profile along direction perpendicular to the molecular beam
47
48  x=(-0.5:0.005:.5)/100; %[m] build vector for the laser beam \
    →intensity on molecular beam
49  z=(-.08:0.0001:.08)/100; %[m] build vector for the laser beam \
    →intensity on the direction perpendicular to the mol. beam
50  %calculate gaussian intensity profile for the Pump and Stokes
51  Ip=exp(-4 * log(2) * x.^2 / WidthP(1)^2)+RelIntP(2)*exp(-4 * log\
    →(2) * (x-RelPosP(2)).^2 / WidthP(2)^2)+RelIntP(3)*exp(-4 * log\
    →(2) * (x-RelPosP(3)).^2 / WidthP(3)^2);
52  %function of 3 gaussian with the parameters given above
53  Is=exp(-4 * log(2) * x.^2 / WidthS(1)^2)+RelIntS(2)*exp(-4 * log\
    →(2) * (x-RelPosS(2)).^2 / WidthS(2)^2)+RelIntS(3)*exp(-4 * log\
    →(2) * (x-RelPosS(3)).^2 / WidthS(3)^2);
54  %function of 3 gaussian with the parameters given above
55  IpIs=Ip.*Is;%calculate the product of the intensities along x
56  Ipz=exp(-4 * log(2) * z.^2 / WidthPz^2);
57  Isz=exp(-4 * log(2) * z.^2 / WidthSz^2);
58  IpIsz=Ipz.*Isz;%calculate the product of the intensities along z
59
60
61  %Calculate the number of excited molecules
62  N=zeros(size(EsEp));
63  for i=1:length(EsEp)

```

```
64     for j=1:length(IpIs)
65         for k=1:length(IpIsz)
66             N(i) = N(i) +(x(2)-x(1))*(z(2)-z(1)) * (1 - exp(-Beta * \
                -EsEp(i) * IpIs(j) * IpIsz(k)) ); % integrate over x and \
                → z for each EpEs element
67         end
68     end
69 end
70 end
71 sat= Alfa * N;
```

Methane vibrational energy levels

Table F.1: CH₄ vibrational energy levels indicated by the quanta for ν_1 , ν_2 , ν_3 and ν_4 . The energy levels up to 72 kJ/mole are obtained by work of Schwenke and Partridge¹³⁷. The levels above 72 kJ/mole are from the thesis of Juurlink¹³⁸.

ν_1	ν_2	ν_3	ν_4	Vibrational energy kJ/mol	Degeneracy
0	0	0	0	0	1
0	0	0	1	15.62	3
0	1	0	0	18.23	2
0	0	0	2	29.5	6
0	1	0	1	33.8	6
1	0	0	0	34.9	1
0	0	1	0	36.13	3
0	2	0	0	36.6	3

Continued on next page

ν_1	ν_2	ν_3	ν_4	Vibrational energy kJ/mol	Degeneracy
0	0	0	3	46.6	10
0	1	0	2	49.5	12
1	0	0	1	50.5	3
0	0	1	1	51.7	9
0	2	0	1	52.15	9
1	1	0	0	53.2	2
0	1	1	0	54.3	6
0	3	0	0	54.9	4
0	0	0	4	62.2	15
0	1	0	3	64.6	20
1	0	0	2	65.6	6
0	0	1	2	66.8	18
0	2	0	2	67.1	18
1	1	0	1	68.1	6
2	0	0	0	69	1
0	1	1	1	69.3	18
0	3	0	1	69.6	12
1	0	1	0	70.2	3
1	2	0	0	70.5	3
0	0	2	0	71.4	6
0	2	1	0	71.7	9
0	4	0	0	72.1	5
0	0	0	5	76.9	21
0	1	0	4	79.4	60
1	0	0	3	80.3	10
0	0	1	3	81.5	30
0	2	0	3	81.9	30

Continued on next page

ν_1	ν_2	ν_3	ν_4	Virational energy kJ/mol	Degeneracy
1	1	0	2	82.8	12
2	0	0	1	83.8	3
0	1	1	2	84	36
0	3	0	2	84.4	24
1	0	1	1	85	9
1	2	0	1	85.3	9
0	0	2	1	86.2	18
2	1	0	0	86.2	2
0	2	1	1	86.5	27
0	4	0	1	86.9	15
1	1	1	0	87.4	6
1	3	0	0	87.8	4
0	1	2	0	88.6	12
0	3	1	0	89	12
0	5	0	0	89.4	6
0	0	0	6	91.7	28
0	1	0	5	94.2	42
1	0	0	4	95.1	15
0	0	1	4	96.3	45
0	2	0	4	96.7	45
1	1	0	3	97.6	30
2	0	0	2	98.5	6
0	1	1	3	98.8	30
0	3	0	3	99.2	40
1	2	0	2	100.1	18
0	0	2	2	100.9	36
2	1	0	1	101	6

Continued on next page

ν_1	ν_2	ν_3	ν_4	Vibrational energy kJ/mol	Degeneracy
0	2	1	2	101.3	54
0	4	0	2	101.6	30
3	0	0	0	101.9	1
1	1	1	1	102.2	18
1	3	0	1	102.6	12
2	0	1	0	103.1	3
0	1	2	1	103.4	36
2	2	0	0	103.5	3
0	3	1	1	103.8	36
0	5	0	1	104.1	18
1	0	2	0	104.3	6
1	2	1	0	104.7	9
1	4	0	0	105.1	5
0	0	3	0	105.5	10
0	2	2	0	105.9	18
0	4	1	0	106.3	15
0	0	0	7	106.5	36
0	6	0	0	106.6	7
0	1	0	6	108.9	56
1	0	0	5	109.9	21
0	0	1	5	111.1	63
0	2	0	5	111.4	63
1	1	0	4	112.4	20
2	0	0	3	113.3	10
0	1	1	4	113.6	90
0	3	0	4	113.9	60
1	0	1	3	114.5	45

Continued on next page

ν_1	ν_2	ν_3	ν_4	Virational energy kJ/mol	Degeneracy
1	2	0	3	114.8	45
0	0	2	3	115.7	60
2	1	0	2	115.8	12
0	2	1	3	116	90
3	0	0	1	116.7	3
1	1	1	2	117	36
2	0	1	1	117.9	9
0	1	2	2	118.2	72
2	2	0	1	118.3	9
3	1	0	0	119.2	2
1	2	1	1	119.5	27
0	0	3	1	120.3	30
2	1	1	0	120.4	6
0	2	2	1	120.7	54
2	3	0	0	120.7	4
1	1	2	0	121.6	12
1	3	1	0	121.9	12
0	1	3	0	122.8	20
0	3	2	0	123.1	24
3	0	0	2	131.5	6
2	0	1	2	132.7	18
1	0	2	2	133.9	36
3	1	0	1	134	6
4	0	0	0	134.9	1
0	0	3	2	135.1	60
2	1	1	1	135.1	18
3	0	1	0	136.1	3

Continued on next page

ν_1	ν_2	ν_3	ν_4	Vibrational energy kJ/mol	Degeneracy
1	1	2	1	136.3	36
3	2	0	0	136.4	3
2	0	2	0	137.3	6
0	1	3	1	137.5	60
2	2	1	0	137.6	9
1	0	3	0	138.5	10
1	2	2	0	138.8	18
0	0	4	0	139.7	15
0	2	3	0	140	30
4	0	0	1	149.6	3
3	0	1	1	150.8	9
2	0	2	1	152	18
4	1	0	0	152.1	2
1	0	3	1	153.2	30
3	1	1	0	153.3	9
0	0	4	1	154.4	45
2	1	2	0	154.5	12
1	1	3	0	155.7	20
0	1	4	0	156.9	30
5	0	0	0	167.8	1
4	0	1	0	169	3
3	0	2	0	170.2	6
2	0	3	0	171.4	10
1	0	4	0	172.6	15
0	0	5	0	173.8	21

List of Figures

1.1	Lennard-Jones one-dimensional PES describing the dissociative adsorption of a diatomic molecule on a surface.	3
1.2	Contour plot of a two-dimensional PES used for modelling the H ₂ dissociative adsorption (from Halstead <i>et al.</i> ²).	4
1.3	Classical trajectories on PESs with early and late barriers. From the work of Polanyi ⁴	6
2.1	Overall scheme of our experimental setup.	22
2.2	Schematic overview of the molecular beam source connected to the UHV surface science chamber.	23
2.3	Timing diagram of the optocoupler signal, the master trigger, and the valve trigger.	24
2.4	Scheme of the TOF setup.	28
2.5	Chopper wheel diagram.	30
2.6	Experimental setup used to determine $\Delta t_{chopper}$	30
2.7	Transmitted He-Ne laser beam intensity detected by the photodiode and trigger signal as a function of time.	30
2.8	Transmission function of the narrow slit (dashed line) as measured with the He-Ne laser.	30
2.9	Schematic view of the chopper wheel with the optocoupler and the molecular beam angularly misaligned by α	31
2.10	Arrival time of the Ar supersonic expansion with $T_{nozzle} = 393$ K as a function of the cage voltage.	33

2.11	Ar and He TOF distributions.	34
2.12	Schematic view of the ion source installed in our QMS.	35
2.13	Example of velocity determination of a mixture of CH ₄ in H ₂	36
2.14	Energy distribution of the TOF shown in Fig.2.13.	36
2.15	Factory calibration data points for the CLO-6/7 and CLO-7/8 crimped calibrated leak standards.	37
2.16	Schematic view of the Auger spectrometer.	41
2.17	Auger spectra of the most intense LMM nickel transition and the KLL carbon transition.	43
2.18	Crystal surface mapped in term of deposition coordinates ($Z_{dep.}$, $Y_{dep.}$) and Auger analysis coordinates (Z_{Auger} , X_{Auger}).	44
2.19	Self-limiting chemisorption of ethylene on Ni(100). The saturation value correspond to 0.5 ML on Ni(100) (graph taken from Schmid Ph.D. thesis ⁷¹).	45
2.20	LEED pattern of a clean Ni(100).	46
2.21	2 × 2)p4g reconstruction produced by 0.5 ML of carbon.	47
2.22	LEED pattern of a carbon saturated Ni(100).	47
2.23	Auger electron spectra of a contaminated (upper trace) and clean (lower trace) Ni(100).	47
2.24	Infrared laser setup used to excite CH ₄ overtone and combination CH stretch transitions around 1.7 μm.	48
2.25	Raman Stokes and antistokes processes.	52
2.26	Optical setup used for stimulated Raman pumping of CH ₄ in the molecular beam.	53
2.27	Internal part of the Raman amplifier.	53
2.28	Raman gain curves for different methane pressures.	54
2.29	Maximum of the gain curves as a function of the methane pressure inside the Raman amplifier.	54
3.1	Carbon spots on Ni(100) resulting from the depositions of 1.8% CD ₂ /H ₂ with nozzle temperature of 473 K.	60
3.2	Molecular geometry of the CD ₂ H ₂ molecule.	62
3.3	Correlation diagram illustrating the energy-level pattern for asymmetric-top rotors.	64
3.4	CRD spectra of the 0 ₀₀ → 1 ₁₁ , 1 ₀₁ → 1 ₁₀ and 1 ₁₀ → 1 ₀₁ transitions of the CD ₂ H ₂ 2ν ₆ band.	68

3.5	CRD spectra of the $0_{00} \rightarrow 1_{10}$, $1_{01} \rightarrow 1_{11}$ and $1_{11} \rightarrow 1_{01}$ transitions of the CD_2H_2 $\nu_1 + \nu_6$ band.	69
3.6	IR laser intensity distribution along the line focus of a 160 cm cylindrical lens.	72
3.7	Fractional populations of the CD_2H_2 0_{00} , 1_{11} , 1_{01} and 1_{01} rotational levels as a function of the rotational temperature.	75
3.8	Level scheme for a CD_2H_2 Q(1) transition.	78
3.9	Surface carbon Auger signal for identical doses of CD_2H_2 excited to the $ 20\rangle^-$ and $ 11\rangle$ vibrational states incident on a Ni(100) surface.	80
3.10	State-resolved sticking coefficients for CD_2H_2	82
3.11	Calculated transition state of methane on Ni(111).	83
3.12	The $ 20\rangle$ state of CD_2H_2	83
4.1	Molecular geometry of the CH_4 molecule.	88
4.2	Representations of the CH_4 normal modes.	92
4.3	Photoacoustic Raman spectrum of 30 Torr static CH_4 at 293 K (solid line).	94
4.4	Schematic of the excitation region.	94
4.5	Auger analysis of deposited carbon.	95
4.6	Carbon signal on the surface as a function of the Raman shift ($\nu_{Y2} - \nu_{dye}$).	95
4.7	Fractional populations of the $J = 0, 1$, and 2 rotational levels as a function of the rotational temperature after a supersonic expansion.	101
4.8	Optical setup used to record the laser beam profiles.	103
4.9	Pump and Stokes beam intensities as recorded by the CCD camera.	104
4.10	Analysis of the image in Fig. 4.9.	104
4.11	Gaussian width for Stokes and pump beams as a function of lens-CCD distance.	105
4.12	Fluence dependence of laser-on carbon signal produced by chemisorption of $\text{CH}_4(\nu_1)$	108
4.13	Level scheme for a CH_4 Q(1) Raman transition.	109
4.14	Section perpendicular to the molecular beam direction of the excitation region.	109
4.15	Surface analysis after the deposition.	112
4.16	State-resolved sticking coefficients for CH_4 in the ν_1 , $2\nu_3^{22}$, ν_3^{64} , and ground ²² vibrational states.	114

5.1	State-resolved reactivities for CH ₄ in the ν_3 (□) and $2\nu_3$ (■) vibrational states on Ni(100) as a function of total energy of the molecule (kinetic energy + vibrational energy). The solid curve is the best fit of an “S-shape” curve to the experimental points	122
5.2	State-resolved reactivities for CH ₄ in the $3\nu_4$ vibrational state on Ni(111) (○) and Ni(100) (■) as a function of total energy of the molecule (kinetic energy + vibrational energy). The reactivity on Ni(100) are obtained by multiplying the sticking coefficients on Ni(111) by a factor 5.8 . The solid curve is the best fit of an “S-shape” curve to the sticking coefficients on Ni(100)	123
B.1	Setup used for IR laser beam intensity distribution determination.	134
B.2	Integral of the IR laser intensity distribution along the line focus of a 160 cm cylindrical lens.	134
B.3	IR laser intensity distribution along the line focus of a 160 cm cylindrical lens.	134

List of Tables

2.1	Ion TOF fit results for different gasses.	33
2.2	Neutral flight distance calibration results.	35
2.3	Auger transition for the atomic species that we detect on the surface.	40
2.4	Auger parameters used in each region we scan for surface analysis.	42
2.5	Rotational temperatures of CH ₄ in pulsed jet expansion under various expansion conditions.	51
3.1	Mixtures used for the CD ₂ H ₂ sticking coefficient measurements.	59
3.2	Laser-off sticking coefficient ($S_0^{laser-off}$) for different kinetic energies.	61
3.3	Character table of the point group C_{2v}	61
3.4	Energy levels of the vibrational modes of CD ₂ H ₂ molecule.	65
3.5	Rotational selection rules of asymmetric-top rotors for rovibrational transitions of a-, b- and c-type.	66
3.6	Transitions of the $2\nu_6$ band. $J''_{K_a K_c}$ corresponds to the rotational level of the vibrational ground state.	67
3.7	Transitions of the $\nu_1 + \nu_6$ band.	69
3.8	Rotational transition strengths for the transitions of the $\nu_1 + \nu_6$ band recorded with our CRD setup.	76
4.1	Characters for the representation of T formed by the $ JKM\rangle$ basis set ¹¹¹	90
4.2	Symmetries of the rotational functions with J up to 5 ¹¹¹	90
4.3	Experimentally determined Raman shift frequencies of the $Q(0)$, $Q(1)$, and $Q(2)$ transitions of the ν_1 band ¹¹⁰	93

4.4	Pump and Stokes laser energies at the output of the Raman amplifier for different methane pressures and dye laser frequencies used to measure the “laser-on” carbon peak integral values shown in Fig.4.6.	97
4.5	Rotational temperatures measured for the two mixtures we use in our experiments.	102
4.6	Fit results for the beam intensities along the x direction.	105
4.7	Correlation of the symmetric and antisymmetric stretching vibrations of the reactant in T_d point group to the localized vibrations in curvilinear symmetry coordinates.	116
5.1	Sticking coefficient on Ni(100) of CH_4 at 50 kJ/mole of incident energy S_0^t for different valve temperatures T_v as measured by Holmblaud <i>et al.</i> . The contributions of $S_0^{\nu_1}$ to S_0^t are obtained by multiplying the fractional populations p_{ν_1} with $S_0^{\nu_1}$	122
5.2	Sticking coefficients at 50 kJ/mole of CH_4 in the ν_4 , $2\nu_4$ and $3\nu_4$ states obtained from the “S-shape” curve reported in Fig. 5.2.	124
5.3	Sticking coefficients at 50 kJ/mole of CH_4 in the ν_2 , $\nu_2 + \nu_4$, $2\nu_2$ and $3\nu_2$ states obtained from the “S-shape” curve reported in Fig. 5.2.	124
5.4	Sticking coefficient S_0^t on Ni(100) of CH_4 at 50 kJ/mole of incident energy for different valve temperatures T_v as measured by Holmblaud <i>et al.</i> ²⁰ . The sticking coefficients calculated from the reactivities of the ν_1 , ν_2 , ν_3 , ν_4 , $2\nu_4$, $2\nu_2$, $\nu_2 + \nu_4$, $3\nu_4$, $3\nu_2$ and $2\nu_3$ states are reported with their contributions to S_0^t	124
5.5	Sticking coefficient S_0^t on Ni(100) of CH_4 at 50 kJ/mole of incident energy for different valve temperatures T_v as measured by Holmblaud <i>et al.</i> . The calculated S_0 are obtained including all the vibrational states.	125
A.1	Asymmetric rotor $E_{J_{K_a K_c}}(\kappa)$ functions for $J = 0, 1, 2, 3$	131
C.1	Irreducible representations of the group T^{111}	135
C.2	Multiplication table for the group T^{111}	135
C.3	Character table of the T_d point group.	136
C.4	Multiplication table for the T_d group.	136
D.1	Raman cross-section for some molecules.	145

-
- F.1 CH₄ vibrational energy levels indicated by the quanta for ν_1 , ν_2 , ν_3 and ν_4 . The energy levels up to 72 kJ/mole are obtained by work of Schwenke and Partridge¹³⁷. The levels above 72 kJ/mole are from the thesis of Juurlink¹³⁸. 151
-

Bibliography

- [1] J. E. Lennard-Jones. Processes of adsorption and diffusion on solid surfaces. *Trans. Faraday Soc.*, 28:333–359, 1932.
- [2] D. Halstead and S. Holloway. The influence of potential energy surface topologies on the dissociation of H₂. *The Journal of Chemical Physics*, 93(4):2859–2870, 1990.
- [3] J. C. Polanyi. Some concepts in reaction dynamics - (nobel lecture). *Angewandte Chemie-International Edition in English*, 26(10):952–971, 1987.
- [4] J. C. Polanyi. Some concepts in reaction dynamics. *Science*, 236(4802):680–690, 1987.
- [5] A. Gross, S. Wilke, and M. Scheffler. 6-dimensional quantum dynamics of adsorption and desorption of H₂ at Pd(100) - steering and steric effects. *Physical Review Letters*, 75(14):2718–2721, 1995.
- [6] G. J. Kroes, E. J. Baerends, and R. C. Mowrey. Six-dimensional quantum dynamics of dissociative chemisorption of ($v=0, j=0$) H₂ on Cu(100). *Physical Review Letters*, 78(18):3583–3586, 1997.
- [7] D. A. McCormack, G. J. Kroes, R. A. Olsen, J. A. Groeneveld, J. N. P. van Stralen, E. J. Baerends, and R. C. Mowrey. Quantum dynamics of the dissociation of H₂ on Cu(100): Dependence of the site-reactivity on initial rovibrational state. *Faraday Discussions*, (117):109–132, 2000.
- [8] Jiqiong Dai and John C. Light. Six dimensional quantum dynamics study for dissociative adsorption of H₂ on Cu(111) surface. *The Journal of Chemical Physics*, 107(5):1676–1679, 1997.

-
- [9] S. Wilke and M. Scheffler. Potential-energy surface for H_2 dissociation over Pd(100). *Physical Review B*, 53(8):4926–4932, 1996.
- [10] K. D. Rendulic, G. Anger, and A. Winkler. Wide range nozzle beam adsorption data for the systems H_2 /nickel and H_2 /Pd(100). *Surface Science*, 208(3):404–424, 1989.
- [11] Michael Beutl, Manfred Riedler, and Klaus D. Rendulic. Strong rotational effects in the adsorption dynamics of H_2 /Pd(111): evidence for dynamical steering. *Chemical Physics Letters*, 247(3):249–252, 1995.
- [12] H. A. Michelsen and D. J. Auerbach. A critical examination of data on the dissociative adsorption and associative desorption of hydrogen at copper surfaces. *The Journal of Chemical Physics*, 94(11):7502–7520, 1991.
- [13] E. Watts, G. O. Sitz, D. A. McCormack, G. J. Kroes, R. A. Olsen, J. A. Groeneveld, J. N. P. Van Stralen, E. J. Baerends, and R. C. Mowrey. Rovibrationally inelastic scattering of ($v = 1, j = 1$) H_2 from Cu(100): Experiment and theory. *The Journal of Chemical Physics*, 114(1):495–503, 2001.
- [14] M. B. Lee, Q. Y. Yang, S. L. Tang, and S. T. Ceyer. Activated dissociative chemisorption of CH_4 on Ni(111) - observation of a methyl radical and implication for the pressure gap in catalysis. *Journal of Chemical Physics*, 85(3):1693–1694, 1986.
- [15] M. B. Lee, Q. Y. Yang, and S. T. Ceyer. Dynamics of the activated dissociative chemisorption of CH_4 and implication for the pressure gap in catalysis - a molecular-beam high-resolution electron-energy loss study. *Journal of Chemical Physics*, 87(5):2724–2741, 1987.
- [16] Hong Yang and Jerry L. Whitten. Dissociative chemisorption of CH_4 on Ni(111). *The Journal of Chemical Physics*, 96(7):5529–5537, 1992.
- [17] A. C. Luntz and J. Harris. CH_4 dissociation on metals: a quantum dynamics model. *Surface Science*, 258(1-3):397–426, 1991.
- [18] A. C. Luntz. CH_4 dissociation on Ni(100) - comparison of a direct dynamical model to molecular-beam experiments. *Journal of Chemical Physics*, 102(20):8264–8269, 1995.
- [19] M. N. Carre and B. Jackson. Dissociative chemisorption of CH_4 on Ni: The role of molecular orientation. *Journal of Chemical Physics*, 108(9):3722–3730, 1998.
-

-
- [20] P. M. Holmblad, J. Wambach, and I. Chorkendorff. Molecular-beam study of dissociative sticking of methane on Ni(100). *Journal of Chemical Physics*, 102(20):8255–8263, 1995.
- [21] L. B. F. Juurlink, P. R. McCabe, R. R. Smith, C. L. DiCologero, and A. L. Utz. Eigenstate-resolved studies of gas-surface reactivity: $\text{CH}_4(\nu_3)$ dissociation on Ni(100). *Physical Review Letters*, 83(4):868–871, 1999.
- [22] Mathieu P. Schmid, Plinio Maroni, Rainer D. Beck, and Thomas R. Rizzo. Surface reactivity of highly vibrationally excited molecules prepared by pulsed laser excitation: $\text{CH}_4(2\nu_3)$ on Ni(100). *The Journal of Chemical Physics*, 117(19):8603–8606, 2002.
- [23] R. Milot and A. P. J. Jansen. Bond breaking in vibrationally excited methane on transition-metal catalysts. *Physical Review B*, 61(23):15657–15660, 2000.
- [24] L. Halonen, S. L. Bernasek, and D. J. Nesbitt. Reactivity of vibrationally excited methane on nickel surfaces. *Journal of Chemical Physics*, 115(12):5611–5619, 2001.
- [25] G. J. Kroes, A. Gross, E. J. Baerends, M. Scheffler, and D. A. McCormack. Quantum theory of dissociative chemisorption on metal surfaces. *Acc. Chem. Res.*, 35(3):193–200, 2002.
- [26] Amitabha Sinha, Mark C. Hsiao, and F. Fleming Crim. Controlling bimolecular reactions: Mode and bond selected reaction of water with hydrogen atoms. *The Journal of Chemical Physics*, 94(7):4928–4935, 1991.
- [27] Amitabha Sinha, John D. Thoemke, and F. Fleming Crim. Controlling bimolecular reactions: Mode and bond selected reaction of water with translationally excited chlorine atoms. *J. Chem. Phys.*, 96(1):372–376, 1992.
- [28] Hans A. Bechtel, Zee Hwan Kim, Jon P. Camden, and Richard N. Zare. Bond and mode selectivity in the reaction of atomic chlorine with vibrationally excited CH_2D_2 . *The Journal of Chemical Physics*, 120(2):791–799, 2004.
- [29] Sangwoon Yoon, Robert J. Holiday, Edwin L. Sibert III, and F. Fleming Crim. The relative reactivity of CH_3D molecules with excited symmetric and antisymmetric stretching vibrations. *The Journal of Chemical Physics*, 119(18):9568–9575, 2003.
-

-
- [30] S. Yoon, R. J. Holiday, and F. F. Crim. Vibrationally controlled chemistry: Mode- and bond-selected reaction of CH₃D with Cl. *Journal of Physical Chemistry B*, 109(17):8388–8392, 2005.
- [31] Sangwoon Yoon, Sarah Henton, Aleksandar N. Zivkovic, and F. Fleming Crim. The relative reactivity of the stretch–bend combination vibrations of CH₄ in the Cl(²P_{3/2}) + CH₄ reaction. *The Journal of Chemical Physics*, 116(24):10744–10752, 2002.
- [32] Wendell T. Duncan and Thanh N. Truong. Thermal and vibrational-state selected rates of the CH₄ + Cl ↔ HCl + CH₃ reaction. *The Journal of Chemical Physics*, 103(22):9642–9652, 1995.
- [33] J. Espinosa-Garcia and J. C. Corchado. Analytical potential energy surface for the CH₄ + Cl → CH₃ + ClH reaction: Application of the variational transition state theory and analysis of the kinetic isotope effects. *The Journal of Chemical Physics*, 105(9):3517–3523, 1996.
- [34] J. C. Corchado, D. G. Truhlar, and J. Espinosa-Garcia. Potential energy surface, thermal, and state-selected rate coefficients, and kinetic isotope effects for Cl + CH₄ → ClH + CH₃. *Journal of Chemical Physics*, 112(21):9375–9389, 2000.
- [35] Charles N. Stewart and Gert Ehrlich. Dynamics of activated chemisorption: Methane on rhodium. *The Journal of Chemical Physics*, 62(12):4672–4682, 1975.
- [36] Harold F. Winters. The kinetic isotope effect in the dissociative chemisorption of methane. *The Journal of Chemical Physics*, 64(9):3495–3500, 1976.
- [37] J. T. Yates, J. J. Zinck, S. Sheard, and W. H. Weinberg. Search for vibrational activation in the chemisorption of methane. *Journal of Chemical Physics*, 70(5):2266–2272, 1979.
- [38] Stephen G. Brass, David A. Reed, and Gert Ehrlich. Vibrational excitation and surface reactivity: An examination of the ν_3 and $2\nu_3$ modes of CH₄. *The Journal of Chemical Physics*, 70(11):5244–5250, 1979.
- [39] C. T. Rettner, H. E. Pfnur, and D. J. Auerbach. Dissociative chemisorption of CH₄ on W(110) - dramatic activation by initial kinetic-energy. *Physical Review Letters*, 54(25):2716–2719, 1985.
-

-
- [40] C. T. Rettner, H. E. Pfnur, and D. J. Auerbach. On the role of vibrational energy in the activated dissociative chemisorption of methane on tungsten and rhodium. *The Journal of Chemical Physics*, 84(8):4163–4167, 1986.
- [41] T. P. Beebe, D. W. Goodman, B. D. Kay, and J. T. Yates. Kinetics of the activated dissociative adsorption of methane on the low index planes of nickel single-crystal surfaces. *Journal of Chemical Physics*, 87(4):2305–2315, 1987.
- [42] A. V. Hamza and R. J. Madix. Dynamics of the dissociative adsorption of hydrogen on Ni(100). *Journal of Physical Chemistry*, 89(25):5381–5386, 1985.
- [43] A. C. Luntz and D. S. Bethune. Activation of methane dissociation on a Pt(111) surface. *The Journal of Chemical Physics*, 90(2):1274–1280, 1989.
- [44] D. J. Oakes, M. R. S. McCoustra, and M. A. Chesters. Dissociative adsorption of methane on Pt(111) induced by hyperthermal collisions. *Faraday Discussions*, (96):325–336, 1993.
- [45] A. B. Anderson and J. J. Maloney. Activation of methane on iron, nickel, and platinum surfaces - a molecular-orbital study. *Journal of Physical Chemistry*, 92(3):809–812, 1988.
- [46] Ole Swang, Knut Faegri, Jr, Odd Gropen, Ulf Wahlgren, and Per Siegbahn. A theoretical study of the chemisorption of methane on a Ni(100) surface. *Chemical Physics*, 156(3):379–386, 1991.
- [47] H. Burghgraef, A. P. J. Jansen, and R. A. van Santen. Theoretical investigation of the insertion of nickel in the CH bond of CH₄. electronic structure calculations and dynamics. *The Journal of Chemical Physics*, 98(11):8810–8818, 1993.
- [48] H. Burghgraef, A. P. J. Jansen, and R. A. van Santen. Electronic structure calculations and dynamics of the chemisorption of methane on a Ni(111) surface. *Chemical Physics*, 177(2):407–420, 1993. TY - JOUR.
- [49] H. Burghgraef, A. P. J. Jansen, and R. A. van Santen. Electronic structure calculations and dynamics of methane activation on nickel and cobalt. *The Journal of Chemical Physics*, 101(12):11012–11020, 1994.
- [50] H. Burghgraef, A. P. J. Jansen, and R. A. van Santen. Methane activation and dehydrogenation on nickel and cobalt: a computational study. *Surface Science*, 324(2-3):345–356, 1995. TY - JOUR.
-

-
- [51] I. Chorkendorff, I. Alstrup, and S. Ullmann. XPS study of chemisorption of CH_4 on $\text{Ni}(100)$. *Surface Science*, 227(3):291–296, 1990.
- [52] V. A. Ukraintsev and I. Harrison. A statistical-model for activated dissociative adsorption - application to methane dissociation on $\text{Pt}(111)$. *Journal of Chemical Physics*, 101(2):1564–1581, 1994.
- [53] P. R. McCabe, L. B. F. Juurlink, and A. L. Utz. A molecular beam apparatus for eigenstate-resolved studies of gas-surface reactivity. *Review of Scientific Instruments*, 71(1):42–53, 2000.
- [54] M. P. Schmid, P. Maroni, R. D. Beck, and T. R. Rizzo. Molecular-beam/surface-science apparatus for state-resolved chemisorption studies using pulsed-laser preparation. *Review of Scientific Instruments*, 74(9):4110–4120, 2003.
- [55] J. Higgins, A. Conjusteau, G. Scoles, and S. L. Bernasek. State selective vibrational ($2\nu_3$) activation of the chemisorption of methane on $\text{Pt}(111)$. *Journal of Chemical Physics*, 114(12):5277–5283, 2001.
- [56] Juliana Palma and David C. Clary. Improving reduced dimensionality quantum reaction dynamics with a generalized transition state. application to $\text{CH}_4 + \text{O}(^3\text{P})$. *The Journal of Chemical Physics*, 115(5):2188–2197, 2001.
- [57] Joanna R. Fair, Doug Schaefer, Ronnie Kosloff, and David J. Nesbitt. Intramolecular energy flow and nonadiabaticity in vibrationally mediated chemistry: Wave packet studies of $\text{Cl} + \text{H}_2\text{O}$. *The Journal of Chemical Physics*, 116(4):1406–1416, 2002.
- [58] George C. Schatz. How symmetric stretch excitation in a triatomic molecule can be more efficient than asymmetric stretch excitation in enhancing reaction rates in atomic plus triatom reactions. *The Journal of Chemical Physics*, 71(1):542–543, 1979.
- [59] G. C. Schatz, M. C. Colton, and J. L. Grant. A quasiclassical trajectory study of the state-to-state dynamics of $\text{H} + \text{H}_2\text{O} \rightarrow \text{OH} + \text{H}_2$. *Journal of Physical Chemistry*, 88(14):2971.
- [60] Juliana Palma, Julian Echave, and David C. Clary. The effect of the symmetric and asymmetric stretching vibrations on the $\text{CH}_3\text{D} + \text{O}(^3\text{P}) \rightarrow \text{CH}_3 + \text{OD}$ reaction. *Chemical Physics Letters*, 363(5-6):529–533, 2002.
-

-
- [61] H. Mortensen, L. Diekhoner, A. Baurichter, and A. C. Luntz. CH₄ dissociation on Ru(0001): A view from both sides of the barrier. *The Journal of Chemical Physics*, 116(13):5781–5794, 2002.
- [62] J. H. Larsen, P. M. Holmblad, and I. Chorkendorff. Dissociative sticking of CH₄ on Ru(0001). *The Journal of Chemical Physics*, 110(5), 1999.
- [63] A. C. Luntz. A simple model for associative desorption and dissociative chemisorption. *Journal of Chemical Physics*, 113(16):6901–6905, 2000.
- [64] A. L. Utz. Personal communication.
- [65] J. H. Larsen and I. Chorkendorff. From fundamental studies of reactivity on single crystals to the design of catalysts. *Surface Science Reports*, 35(5-8):165–222, 1999.
- [66] S. T. Ceyer. Translational and collision-induced activation of CH₄ on Ni(111) - phenomena connecting ultra-high-vacuum surface science to high-pressure heterogeneous catalysis. *Langmuir*, 6(1):82–87, 1990.
- [67] X. L. Zhou and J. M. White. Decomposition kinetics of CH₃ (CD₃) on Ni(100). *Chemical Physics Letters*, 142(5):376–380, 1987.
- [68] X. L. Zhou and J. M. White. Adsorption and decomposition of methyl halides on Ni(100) - a tpd, sims and aes study. *Surface Science*, 194(3):438–456, 1988.
- [69] X. Y. Zhu and J. M. White. Hydrogen interaction with Ni(100) - a static secondary ion mass-spectroscopy study. *Journal of Physical Chemistry*, 92(13):3970–3974, 1988.
- [70] K. Christmann, O. Schober, G. Ertl, and M. Neumann. Adsorption of hydrogen on nickel single-crystal surfaces. *Journal of Chemical Physics*, 60(11):4528–4540, 1974.
- [71] Mathieu Philippe Schmid. *Interaction of highly excited molecules with solid surfaces*. PhD thesis, Ecole polytechnique Fédérale de Lausanne, 2002.
- [72] I. Alstrup, I. Chorkendorff, and S. Ullmann. Interaction of hydrogen with carbidic carbon on Ni(100). *Surface Science*, 293(3):133–144, 1993.
- [73] H. He, J. Nakamura, and K. Tanaka. Spectroscopic evidence for the formation of CH_x species in the hydrogenation of carbidic carbon on Ni(100). *Catalysis Letters*, 16(4):407–412, 1992.
-

-
- [74] D. W. Goodman, R. D. Kelley, T. E. Madey, and J. M. White. Measurement of carbide buildup and removal kinetics on Ni(100). *Journal of Catalysis*, 64(2):479–481, 1980.
- [75] David R. Miller. Free jet source. In Giacinto Scoles, editor, *Atomic and molecular beam methods*, volume I, pages 14–53. Oxford University Press, New York, Oxford, 1988.
- [76] S. Dushman. *Scientific Foundations of Vacuum Technique*. Wiley, New York, 2nd edition, 1962.
- [77] Douglas A. Skoog, F. James Holler, and Timothy A. Nieman. *Principle of instrumental analysis*. Saunders College Publishing, Philadelphia, fifth edition, 1998.
- [78] E. N. Sickafus and D. M. Holloway. Specimen position effects on energy shifts and signal intensity in a single-stage cylindrical-mirror analyzer. *Surface Science*, 51(1):131–139, 1975.
- [79] F. C. Schouten, O. L. J. Gijzeman, and G. A. Bootsma. Interaction of methane with Ni(111) and Ni(100); diffusion of carbon into nickel through the (100) surface; an aes-leed study. *Surface Science*, 87(1):1–12, 1979.
- [80] C. Klink, L. Olesen, F. Besenbacher, I. Stensgaard, E. Laegsgaard, and N.D. Lang. Interaction of C with Ni(100): Atom-resolved studies of the "clock" reconstruction. *Physical Review Letters*, 71(26):4350–4353, 1993.
- [81] L. Vattuone, Y. Y. Yeo, R. Kose, and D. A. King. Energetics and kinetics of the interaction of acetylene and ethylene with Pd(100) and Ni(100). *Surface Science*, 447(1-3):1–14, 2000.
- [82] R. Terborg, J. T. Hoeft, M. Polcik, R. Lindsay, O. Schaff, A.M. Bradshaw, R.L. Toomes, N.A. Booth, D.P. Woodruff, E. Rotenberg, and J. Denlinger. Coverage dependence of the local structure of C on Ni(100): A structural precursor to adsorbate-induced reconstruction. *Surface Science*, 446(3):301–313, 2000.
- [83] Julia H. Onuferko, D. P. Woodruff, and B. W. Holland. LEED structure analysis of the Ni(100)(2x2)C(p4g) structure; a case of adsorbate-induced substrate distortion. *Surface Science*, 87(2):357–374, 1979.
- [84] M. A. Vasylyev, A. G. Blaschuk, N. S. Mashovets, and N. Yu. Vilkova. LEED study of Ni(100) and (111) surface damage caused by Ar⁺ ion bombardment with low energy and small doses. *Vacuum*, 57(1):71–80, 2000.
-

-
- [85] D. J. Armstrong, W. J. Alford, T. D. Raymond, A. V. Smith, and M. S. Bowers. Parametric amplification and oscillation with walkoff-compensating crystals. *Journal of the Optical Society of America B-Optical Physics*, 14(2):460–474, 1997.
- [86] Richard L. Sutherland. *Handbook of nonlinear optics*. 1996.
- [87] Gerard Meijer, Maarten G. H. Boogaarts, Rienk T. Jongma, David H. Parker, and Alec M. Wodtke. Coherent cavity ring down spectroscopy. *Chemical Physics Letters*, 217(1-2):112–116, 1994.
- [88] Robert Brian Lopert. *Measured stimulated raman gain in methane*. PhD thesis, University of California, 1983.
- [89] A. Bukoski and I. Harrison. Assessing a microcanonical theory of gas-surface reactivity: Applicability to thermal equilibrium, nonequilibrium, and eigenstate-resolved dissociation of methane on Ni(100). *Journal of Chemical Physics*, 118(21):9762–9768, 2003.
- [90] H. L. Abbott, A. Bukoski, and I. Harrison. Microcanonical unimolecular rate theory at surfaces. ii. vibrational state resolved dissociative chemisorption of methane on Ni(100). *Journal of Chemical Physics*, 121(8):3792–3810, 2004.
- [91] J.M. Lafferty. *Foundations of Vacuum Science*. John Wiley & Sons, Inc, New York, 2nd edition, 1962.
- [92] Jeanne L. McHale. *Molecular spectroscopy*. Prentice Hall, Inc., New Jersey, 1st edition, 1999.
- [93] J. Michael Hollas. *High resolution spectroscopy*. John Wiley & Sons, Inc, New York, 2nd edition, 1998.
- [94] J. L. Duncan and M. M. Law. Vibrational anharmonicity in dideuteromethane: A study of its infrared spectrum up to 17000 cm^{-1} . *Spectrochimica Acta Part A -Molecular and Biomolecular Spectroscopy*, 53(9):1445–1457, 1997.
- [95] J. C. Deroche. Analyse de la bande de vibration-rotation of ν_9 du methane bideutere vers $8\ \mu$. *Journal de physique*, 34:559–569, 1973.
- [96] J. Dowling, J. H. Wray, and A. G. Meister. Analysis of b-type vibration-rotation band of methane D_2 in region $5880\text{--}6136\text{ cm}^{-1}$. *Journal of Physics Part B Atomic and Molecular Physics*, 2(4):499–506, 1969.
-

-
- [97] J. C. Deroche and G. Guelachvili. High-resolution infrared-spectrum of CH_2D_2 - ν_1 and ν_6 fundamental bands near 3000 cm^{-1} . *Journal of Molecular Spectroscopy*, 56(1):76–87, 1975.
- [98] O. Sonnich Mortensen, Bryan R. Henry, and M. Ali Mohammadi. *Journal of Chemical Physics*, 75(10):4800–4808, 1981.
- [99] M S. Child and L. Halonen. *Adv. Chem. Phys.*, 57:1, 1984.
- [100] A. Amrein, M. Quack, and U. Schmitt. High-resolution interferometric fourier-transform infrared-absorption spectroscopy in supersonic free jet expansions - carbon-monoxide, nitric-oxide, methane, ethyne, propyne, and trifluoromethane. *Journal of Physical Chemistry*, 92(19):5455–5466, 1988.
- [101] C. H. Townes and A. L. Schawlow. *Microwave spectroscopy*. Dover publications, inc., New York, first edition, 1975.
- [102] R. N. Zare. *Angular Momentum*. John Wiley & Sons, New York, 1988.
- [103] K. Bergmann. State selection by optical methods. In Giacinto Scoles, editor, *Atomic and molecular beam methods*, volume I, chapter 12. Oxford University Press, Oxford, first edition, 1988.
- [104] R. B. Bernstein. *Chemical dynamics via molecular beam and laser techniques*. Oxford University Press, New York, first edition, 1982.
- [105] R. Loudon. *The quantum theory of light*. Oxford University Press, Oxford, U.K., first edition, 2000.
- [106] L. S. Rothman, A. Barbe, D. C. Benner, L. R. Brown, C. Camy-Peyret, M. R. Carleer, K. Chance, C. Clerbaux, V. Dana, V. M. Devi, A. Fayt, J. M. Flaud, R. R. Gamache, A. Goldman, D. Jacquemart, K. W. Jucks, W. J. Lafferty, J. Y. Mandin, S. T. Massie, V. Nemtchinov, D. A. Newnham, A. Perrin, C. P. Rinsland, J. Schroeder, K. M. Smith, M. A. H. Smith, K. Tang, R. A. Toth, J. Vander Auwera, P. Varanasi, and K. Yoshino. The hitran molecular spectroscopic database: edition of 2000 including updates through 2001. *Journal of Quantitative Spectroscopy & Radiative Transfer*, 82(1-4):5–44, 2003.
-

-
- [107] Z. H. Kim, H. A. Bechtel, and R. N. Zare. Vibrational control in the reaction of methane with atomic chlorine. *Journal of the American Chemical Society*, 123(50):12714–12715, 2001.
- [108] Hans A. Bechtel, Jon P. Camden, Davida J. Ankeny Brown, and Richard N. Zare. Comparing the dynamical effects of symmetric and antisymmetric stretch excitation of methane in the Cl + CH₄ reaction. *The Journal of Chemical Physics*, 120(11):5096–5103, 2004.
- [109] R. D. Beck, P. Maroni, D. C. Papageorgopoulos, T. T. Dang, M. P. Schmid, and T. R. Rizzo. Vibrational mode-specific reaction of methane on a nickel surface. *Science*, 302(5642):98–100, 2003.
- [110] A. Owyong, C. W. Patterson, and R. S. McDowell. Cw stimulated raman gain spectroscopy of ν_1 fundamental of methane. *Chemical Physics Letters*, 59(1):156–162, 1978.
- [111] E. Bright Wilson and Jr. The statistical weights of the rotational levels of polyatomic molecules, including methane, ammonia, benzene, cyclopropane and ethylene. *The Journal of Chemical Physics*, 3(5):276–285, 1935.
- [112] Michael Hippler and Martin Quack. High-resolution fourier transform infrared and cw-diode laser cavity ringdown spectroscopy of the $\nu_2 + 2\nu_3$ band of methane near 7510 cm⁻¹ in slit jet expansions and at room temperature. *The Journal of Chemical Physics*, 116(14):6045–6055, 2002.
- [113] K. T. Hecht. The vibration-rotation energies of tetrahedral XY₄ molecules .1. theory of spherical top molecules. *Journal of Molecular Spectroscopy*, 5(5):355–389, 1960.
- [114] G. Herzberg. *Molecular spectra and molecular structure II: infrared and Raman spectra of polyatomic molecules*. Krieger publishing company, Malabar, Florida, first edition, 1991.
- [115] D.M. Dennison. The infra-red spectra of polyatomic molecules. part ii. *Reviews of Modern Physics*, 12:175–214, 1940.
- [116] J. J. Barrett and M. J. Berry. Photoacoustic raman-spectroscopy (pars) using cw laser sources. *Applied Physics Letters*, 34(2):144–146, 1979.
- [117] G. A. West, D. R. Siebert, and J. J. Barrett. Gas-phase photoacoustic raman-spectroscopy using pulsed laser excitation. *Journal of Applied Physics*, 51(5):2823–2828, 1980.
-

-
- [118] C. Wenger and J. P. Champion. Spherical top data system (stds) software for the simulation of spherical top spectra. *Journal of Quantitative Spectroscopy & Radiative Transfer*, 59(3-5):471–480, 1998.
- [119] M. D. Duncan, P. Oesterlin, F. Konig, and R. L. Byer. Observation of saturation broadening of the coherent anti-stokes raman-spectrum (cars) of acetylene in a pulsed molecular-beam. *Chemical Physics Letters*, 80(2):253–256, 1981.
- [120] Y. Taira, F. Uchikoba, and H. Takuma. Frequency-dependence of raman cross-section of $\text{CH}_4 \nu_1$ line determined with coherent raman-spectroscopy. *Japanese Journal of Applied Physics Part 1-Regular Papers Short Notes & Review Papers*, 26(11):1807–1810, 1987.
- [121] Derek A. Long. *The Raman effect*. John wiley & sons, LTD, West Sussex, England, 2002.
- [122] Xiao-Gang Wang and Edwin L. Sibert III. A nine-dimensional perturbative treatment of the vibrations of methane and its isotopomers. *The Journal of Chemical Physics*, 111(10):4510–4522, 1999.
- [123] R. R. Smith, D. R. Killelea, D. F. DelSesto, and A. L. Utz. Preference for vibrational over translational energy in a gas-surface reaction. *Science*, 304(5673):992–995, 2004.
- [124] L. B. F. Juurlink, R. R. Smith, D. R. Killelea, and A. L. Utz. Comparative study of C – H stretch and bend vibrations in methane activation on Ni(100) and Ni(111). *Physical Review Letters*, 94(20), 2005.
- [125] E. Watts and G. O. Sitz. State-to-state scattering in a reactive system: $\text{H}_2(\nu=1, j=1)$ from cu(100). *Journal of Chemical Physics*, 114(9):4171–4179, 2001.
- [126] David A. King and Michael G. Wells. Molecular beam investigation of adsorption kinetics on bulk metal targets: Nitrogen on tungsten. *Surface Science*, 29(2):454–482, 1972.
- [127] J. Dvorak and H. L. Dai. Optical reflectivity changes induced by adsorption on metal surfaces: The origin and applications to monitoring adsorption kinetics. *Journal of Chemical Physics*, 112(2):923–934, 2000.
- [128] A. V. Walker and D. A. King. Dynamics of dissociative methane adsorption on metals: CH_4 on Pt{110}(1 × 2). *The Journal of Chemical Physics*, 112(10):4739–4748, 2000.
-

-
- [129] M. E. Jones, L. Q. Xia, N. Maity, and J. R. Engstrom. Translationally activated dissociative chemisorption of SiH_4 on the Si(100) and Si(111) surfaces. *Chemical Physics Letters*, 229(4-5):401–407, 1994.
- [130] J. Makowe, O. V. Boyarkin, and T. R. Rizzo. Isotopically selective infrared multiphoton dissociation of vibrationally excited SiH_4 . *Journal of Physical Chemistry A*, 106(21):5221–5229, 2002.
- [131] Brian Gergen, Hermann Nienhaus, W. Henry Weinberg, and Eric W. McFarland. Chemically induced electronic excitations at metal surfaces. *Science*, 294(5551):2521–2523, 2001.
- [132] D. L. Mills. *Nonlinear optics, basic concepts*. Springer, Berlin, second edition, 1998.
- [133] Amnon Yariv. *Quantum electronics*. John Wiley & Sons, New York, third edition, 1989.
- [134] Claude Cohen-Tannoudji, Bernard Diu, and Franck Laloe. *Quantum mechanics*, volume one. John Wiley & Sons, New York, second edition, 1977.
- [135] Claude Cohen-Tannoudji, Bernard Diu, and Franck Laloe. *Quantum mechanics*, volume two. John Wiley & Sons, New York, second edition, 1977.
- [136] P. Lallemand. The stimulated raman effect. In A. Anderson, editor, *The Raman effect*, volume I, pages 287–342. Marcel Dekker, INC., New York, 1971.
- [137] D. W. Schwenke and H. Partridge. Vibrational energy levels for CH_4 from an ab initio potential. *Spectrochimica Acta Part a-Molecular and Biomolecular Spectroscopy*, 57(4):887–895, 2001.
- [138] Ludo B. F. Juurlink. *Eigenstate-resolved measurements of methane dissociation on Ni(100)*. PhD thesis, Tufts University, 2000.
-

Acknowledgments

I would like to address my sincere acknowledgments to all people mentioned below for the contributions they brought to this thesis work.

My thesis advisor *Dr. Rainer Beck* for choosing me as his Ph.D. student, for the guidance he gave me throughout my work and for sharing scientific knowledge as well as for reading and correction of this manuscript.

Prof. Thomas Rizzo for accepting me in his group and for helpful discussions during the progression of this work.

The previous Ph.D. student *Dr. Mathieu Schmid*, who built with Rainer the “astonishing machine”, for having taught me many “tricks” on our setup as well as for the two years spent working together in a constructive and good humor environment.

Dr. Dimitrios Papageorgopoulos for his cooperation in my experiments.

The other students of the “surface project” *Thanh Tung Dang* and *Marco Sacchi*, for their enthusiasm in taking over the work in the lab. Thanks to *Dr. Régis Bisson* for the French version of the abstract, and critical reading.

Prof. Pierre Vogel, *Prof. Giacinto Scoles*, *Prof. Johannes Barth* and *Prof. Harald Brune* for having accepted to be members of my thesis jury.

Amanz Ruf, *Jean-Luc Passard* and *André Fattet* for the valuable suggestions and contributions in the design and machining of the Raman amplifier.

The other members of the mechanical workshop.

The electronic workshop members *Gabriel Roch* and *Olivier Noverraz*, for the realizations and reparations of useful electronic “black boxes”.

My officemates *Richard Bossart* and *Mikhail Polianski*, for the tons of coffee shared together and fruitful discussions. An additional special thank to Richard for useful reading of this thesis.

Anthi Kamariotis, *Monia Guidi* and *Sébastien Mercier* for hosting me in their office during the break times and stressful moments.

Prof. Tino Gäumann, Dr. Andrea Callegari, Dr. Marcel Drabbels, Dr. Oleg Boiarkine, Dr. Aziz Kasimov, Cédric Bovet, Rachele Chianese, Pavel Maksyutenko and Antoine Milon former or current colleagues of the LCPM, for their enjoyable atmosphere.

Our kind secretary *Marianne Dang*, who takes care about administrative stuff.

My friends and flatmates *Andreas Braun, Patrice Theulé* and *Evgeniy Loginov* with whom I have shared moments of fun and happiness.

I wish to thank *Prof. Alberto Di Lieto*, without whom I would not have had the opportunity to come in Lausanne.

My friends and family for their love and support.

Particularly, I would like to express my gratitude to my love *Christine Guibert*, who appeared as a sunshine in the middle of the storm to guide and support me in the accomplishment of this fantastic journey.

CURRICULUM VITAE

Education

- 2001-2005 Ecole Polytechnique Fédérale de Lausanne
Ph.D. in physical chemistry with Dr. Rainer Beck and Prof. Thomas Rizzo. *Bond- and mode-specific reactivity of methane on Ni(000)*.
- 1994-2000 **Degree in Physics**
at the University of Pisa, Italy (evaluation: 110/110 cum laude).
- 1989-1994 **Secondary School degree in Chemistry**
at the National Technical Institute (Istituto Technico Statale) Tito Sarrocchi in Siena, Italy (evaluation: 56/60).

Publications

- P. Maroni, D. C. Papageorgopoulos, M. Sacchi, T. T. Dang, R. D. Beck, and T. R. Rizzo.** State-resolved gas/surface reactivity of methane on the symmetric C-H stretch vibration on Ni(100). *Phys. Rev. Lett.*, **94**:246104 (2005).
- R. D. Beck, P. Maroni, D. C. Papageorgopoulos, T. T. Dang, M. P. Schmid, and T. R. Rizzo.** Vibrational mode-specific reaction of methane on a nickel surface. *Science* **302**:98-100 (2003).
- M. P. Schmid, P. Maroni, R. D. Beck, and T. R. Rizzo.** Molecular-beam/surface-science apparatus for state-resolved chemisorption studies using pulsed-laser preparation. *Review of Scientific Instruments* **74**:4110-4120 (2003).
- B. Baronti, F. Cornacchia, A. Di Lieto, P. Maroni, A. Toncelli, and M. Tonelli.** Room temperature 2 mm Tm,Ho : YLF laser. *Optics and Lasers in Engineering* **39**:277-282 (2003).
- M. P. Schmid, P. Maroni, R. D. Beck, and T. R. Rizzo.** Surface reactivity of highly vibrationally excited molecules prepared by pulsed laser excitation: CH₄ (2ν₃) on Ni(100). *Journal of Chemical Physics* **117**:8603-8606 (2002).
- F. Cornacchia, A. Di Lieto, P. Maroni, P. Minguzzi, A. Toncelli, M. Tonelli, E. Sorokin, and I. Sorokina.** A cw room-temperature Ho,Tm : YLF laser pumped at 1.682
-

μm . *Applied Physics B-Lasers and Optics* **73**:191-194 (2001).

P. Maroni, L. Palatella, A. Toncelli, and M. Tonelli. Fluoride crystals: 2 mm Ho^{3+} laser emission and energy transfer mechanisms in Er^{3+} . *Journal of Crystal Growth* **229**:497-500 (2001).
